

Mathematical Modeling, Prediction and Design Optimization of Wave Energy Converter Devices

THESIS

Submitted in partial fulfillment
of the requirements for the degree of
DOCTOR OF PHILOSOPHY

by

VIPIN V

ID No. 2019PHXF0066H

Under the Supervision of

Prof. Santanu Koley



BITS Pilani
Pilani | Dubai | Goa | Hyderabad


BIRLA INSTITUTE OF TECHNOLOGY AND SCIENCE, PILANI

2024

BIRLA INSTITUTE OF TECHNOLOGY AND SCIENCE, PILANI

CERTIFICATE

This is to certify that the thesis entitled “*Mathematical Modeling, Prediction and Design Optimization of Wave Energy Converter Devices*” submitted by **VIPIN V**, ID No. 2019PHXF0066H in partial fulfillment of the requirements for the degree of DOCTOR OF PHILOSOPHY embodies original work done by him under my supervision.



Supervisor

PROF. SANTANU KOLEY

Associate Professor,

BITS-Pilani, Hyderabad Campus

Date: 14.06.2024

To

my grandfather Raman V and grandmother Janaki V

&

my father Kumaran V

&

my mother Vinitha V

and teachers

for their endless love, support and encouragement

Acknowledgements

Undertaking this research work has been a truly life-changing experience for me and it would not have been possible to do without the support and guidance that I have received from many people.

With immense pleasure and profound sense of gratitude, I take this opportunity to express my sincere indebtedness to my supervisor **Prof. Santanu Koley**. He has been a pillar of strength for me. His affectionate nature and patience throughout the duration of the research work is something I shall cherish throughout my life. It has been a humbling experience and a wonderful honor to be his student. I could not have imagined having a better advisor and mentor for my Ph.D.

I would also like to extend my gratitude to my DAC members, **Prof. Jonnalagadda Jagan Mohan** and **Prof. T S L Radhika**, for their helpful questions, comments, and constant feedback during this research work.

My sincere thanks to the present Head of the Department, **Prof. Pradyumn Kumar Sahoo** and former Head of the Department **Prof. Dipak K Satpathi**, DRC convener, **Prof. Sharan Gopal**, and each faculty member of the Department of Mathematics, BITS-Pilani, Hyderabad Campus, for their help, support, and encouragement to carry out my research work.

With a deep sense of gratitude, I express my sincere indebtedness to **Prof. Trilochan Sahoo**, Professor, Dept. of Ocean Engineering and Naval Architecture, IIT Kharagpur, and **Prof V. Sree Hari Rao**, Director and Principal Research Scientist, Foundation for Scientific Research and Technological Innovation, Hyderabad for their precious suggestions and guidance during my research work.

I wish to thank **Prof. Dipak Kumar Satpathi** for teaching me Statistics and Optimization. Also, I wish to thank my teachers **Mr. Devadas** and **Mr. Vinod** for their support and encouragement.

I would also like to convey my gratitude to my co-authors **Prof. V V Haragopal**, **Prof. Dipak Kumar Satpathi**, **Dr. Kshma Trivedi** and **Dr. Kottala Panduranga** for their contributions and support during my research work.

I express my sincere thanks to the Council of Scientific and Industrial Research (CSIR), India for providing necessary financial support through CSIR junior research fellowship and Senior research fellowships (File No: 09/1026(0030)/2019-EMR-I).

I gratefully acknowledge BITS-Pilani, Hyderabad Campus, for providing me with the necessary facilities to carry out my research work.

I would also like to convey special thanks to my friends Kshma, Amya, Santanu, Kailash, Anjali, Aleena, Faiz, Karthik, Vinod, Amar, Rahul, Amal, Nithin, Sayooj, Ambily, Sreeja, Akhil, Sandeep, Tincy, Shanuz, Cheri, Ashitha, Reetha, Jose, Uma, Sruthi, and Vaishnavi who were with me in both happy and difficult moments during my PhD life.

A special thanks to all my department research scholars for their endless help, companionship, and for making my life more enjoyable and happier in these years.

Most importantly, I would like to thank my father, mother, brother, and sister-in-law, and all my family members for their love, care, and support for my personal life. A very special thanks to my brother Senthil for always supporting me.

Above all, I sincerely pray to my dear Lord Sree Ram and Mahavishnu for their blessings and kindness on me during every phase of my entire life.

Abstract

The thesis focuses on the power generation performance and optimization of the design parameters of piezoelectric and oscillating water column wave energy converter devices. The linear water wave theory is used to formulate the physical problem associated with the power generation. Machine learning models and multivariate statistical methods are employed for the optimization of the parameters related to wave energy converter devices. The performance of the devices is studied under both the regular and irregular wave climates in the frequency domain. Also, the time-dependent piezoelectric plate deflection and the free surface displacement around the piezoelectric plate are studied under the time domain analysis. The physical problem associated with the power generation by the devices contains undulated seabed topography. In this regard, one of the best methods to solve such a problem is the boundary element method. However, the problems with degenerate boundaries have rank deficiency difficulties in the influence matrices when using the boundary element method. So, the dual boundary element method is also used to address this rank deficiency issue. The piezoelectric wave energy converter device is capable of generating electricity to run low-energy electronics. The resonances in the power generation by the piezoelectric wave energy converter device occur for certain incident wave frequencies. However, ocean waves consist of a wider range of frequencies, and therefore, we have studied the hydrodynamics of an oscillating water column wave energy converter device, which will work efficiently for a wider range of incident wave frequencies and can also generate higher power. Further, the prediction and optimization of the wave energy converter devices are studied using machine learning models, interpretable machine learning approaches, and a multivariate statistical method, namely the response surface methodology. The accuracy of a machine learning model is widely recognized to be closely linked to the sampling technique employed. The Latin hypercube sampling methodology is used to construct the most stratified input database for building machine learning models. A deep learning model, namely the multilayer perceptron model, and a tree ensemble model, namely the XGBoost model, are employed to predict the power generation associated with the wave energy converter devices. The importance of features and interaction effects has been studied through interpretable machine learning techniques. Finally, the ranges of design parameters associated with the wave energy energy converter devices are determined.

Keywords: Piezoelectric plate; Oscillating water column device; Wave power; Optimization; Machine learning; Deep learning; Interpretable machine learning.

Contents

CERTIFICATE

i

Acknowledgements

Abstract

Contents

List of Tables

List of Figures

List of Symbols

Abbreviations

| | | |
|----------|--|----------|
| 1 | Introduction | 1 |
| 1.1 | Preamble | 1 |
| 1.2 | State of the art | 4 |
| 1.2.1 | Classification of wave energy converter devices | 5 |
| 1.2.1.1 | Working principle | 5 |
| 1.2.1.2 | Size of the device and direction of the incoming wave | 7 |
| 1.2.1.3 | Location | 7 |
| 1.2.2 | Piezoelectric wave energy converter device | 8 |
| 1.2.3 | Oscillating water column wave energy converter device | 9 |
| 1.2.4 | Hydrodynamics of the piezoelectric wave energy converter device | 10 |
| 1.2.5 | Hydrodynamics of the oscillating water column wave energy converter device | 12 |
| 1.2.6 | Machine learning models to predict the power generation | 13 |
| 1.2.7 | Optimization of the parameters of wave energy converter devices | 14 |
| 1.3 | Motivation and outline of the thesis | 15 |
| 1.4 | Mathematical modeling of wave-structure interaction problems | 19 |

| | | |
|----------|--|-----------|
| 1.4.1 | Basic equations for linear water wave theory | 19 |
| 1.4.2 | Basic equations and edge conditions for floating flexible plate type structures | 22 |
| 1.4.3 | Basic equations and boundary conditions associated with the piezoelectric wave energy converter device | 24 |
| 1.4.4 | Governing equation and boundary conditions associated with the modeling of oscillating water column wave energy converter device | 25 |
| 1.5 | Fundamentals of integral equations | 28 |
| 1.6 | Boundary element method (BEM) | 29 |
| 1.6.1 | Fundamental solution of the Laplace equation and Green's second identity | 29 |
| 1.6.2 | Formulation of the boundary integral equations | 30 |
| 1.6.3 | Discretization of boundary integral equations using constant element approach | 31 |
| 1.6.4 | Evaluation of influence coefficients | 32 |
| 1.7 | Dual boundary element method (DBEM) | 33 |
| 1.8 | Artificial neural networks | 36 |
| 1.8.1 | Background | 36 |
| 1.8.2 | The multilayer perceptron model | 36 |
| 1.8.3 | The elements of a perceptron model | 37 |
| 1.8.4 | Activation function | 38 |
| 1.8.5 | Forward propagation algorithm | 41 |
| 1.8.6 | Back-propagation algorithm | 43 |
| 1.8.7 | Optimization algorithms | 43 |
| 1.9 | Extreme gradient boosting and interpretable machine learning approaches | 45 |
| 1.9.1 | Extreme gradient boosting (XGBoost) | 45 |
| 1.9.2 | Accumulated local effects(ALE) | 47 |
| 1.9.3 | Shapley additive explanations (SHAP) | 48 |
| 1.10 | k-fold cross-validation | 49 |
| 1.11 | Response surface methodology (RSM) | 50 |
| 2 | Mathematical modeling of a breakwater-integrated piezoelectric wave energy converter device placed over an undulated seabed | 52 |
| 2.1 | General introduction | 53 |
| 2.2 | Mathematical formulation | 53 |
| 2.3 | Method of solution | 56 |
| 2.4 | Results and discussions | 58 |
| 2.4.1 | Model validation | 59 |
| 2.4.2 | Numerical convergence | 60 |
| 2.4.3 | PWEC device with fixed edges | 60 |
| 2.4.4 | PWEC device having fixed rear edge and free front edge | 64 |
| 2.4.5 | PWEC device having fixed rear edge and moored front edge | 67 |
| 2.4.6 | Effect of plate lee edge conditions on the power generation | 69 |
| 2.5 | Conclusions | 71 |
| 3 | Performance and optimization of design parameters of standalone piezoelectric wave energy converter devices | 72 |
| 3.1 | General introduction | 73 |
| 3.2 | Mathematical formulation | 73 |
| 3.3 | Numerical method of solution | 75 |

| | | |
|----------|---|------------|
| 3.4 | Results, discussions and Model validation | 78 |
| 3.5 | Performance of the PWEC device in frequency domain | 79 |
| 3.6 | Time dependent free surface elevation and plate deflection | 83 |
| 3.7 | Optimization of the design parameters of the PWEC device | 84 |
| 3.7.1 | Design of the database | 84 |
| 3.7.2 | Exploratory data analysis | 85 |
| 3.7.3 | Development of the ANN model and optimization | 86 |
| 3.8 | Conclusions | 88 |
| 4 | Optimization of parameters of the OWC wave energy converter device using MLP and XGBoost models | 90 |
| 4.1 | General introduction | 91 |
| 4.2 | Mathematical formulation | 91 |
| 4.3 | Solution methodology based on dual boundary element method | 93 |
| 4.4 | Hydrodynamic performance of the OWC device in the presence of irregular incident waves | 96 |
| 4.5 | Results | 98 |
| 4.5.1 | Validation | 98 |
| 4.5.2 | Results associated with the DBEM methodology | 99 |
| 4.6 | Model building | 100 |
| 4.6.1 | Construction of the database | 101 |
| 4.6.2 | Development of the ANN Model | 102 |
| 4.6.3 | Development of the XGBoost model | 107 |
| 4.7 | Optimization of the parameters of the OWC Device | 110 |
| 4.7.1 | Accumulated local effects(ALE) | 110 |
| 4.7.2 | Results and discussions | 112 |
| 4.8 | Conclusions | 116 |
| 5 | Modeling, Prediction, and Optimization of Hybrid Oscillating Water Column-Piezoelectric WEC Device | 118 |
| 5.1 | General introduction | 119 |
| 5.2 | Mathematical formulation | 119 |
| 5.3 | Solution methodology based on the boundary element method | 122 |
| 5.4 | Parameters corresponding to the wave energy converters | 125 |
| 5.4.1 | Wave power extraction by the OWC device | 125 |
| 5.4.2 | Wave power extraction by the PWEC device | 126 |
| 5.4.3 | Wave power extraction by the hybrid WEC device | 126 |
| 5.5 | Development of the database for machine learning models | 128 |
| 5.6 | Model Selection | 129 |
| 5.6.1 | Extreme gradient boosting (XGBoost) | 129 |
| 5.6.2 | Cross validation and model comparison | 132 |
| 5.7 | Interpretable machine learning approaches | 132 |
| 5.7.1 | Accumulated local effects (ALE) | 132 |
| 5.7.2 | Shapley additive explanation (SHAP) | 133 |
| 5.8 | Results and discussions | 134 |
| 5.9 | Optimization based on response surface methodology (RSM) | 141 |
| 5.10 | Summary and concluding remarks | 144 |

| | |
|--|------------|
| 6 Summary and future work | 146 |
| 6.1 Conclusions | 146 |
| 6.2 Major research developments and findings | 150 |
| 6.3 Applications | 152 |
| 6.4 Scope of possible extensions for the future work | 153 |
| References | 154 |
| | |
| List of Publications | 167 |
| | |
| Biography | 169 |

List of Tables

| | | |
|------|--|-----|
| 2.1 | Reflection coefficient $ R_c $ in presence of PWEC plate when both the edges are fixed in nature. | 61 |
| 2.2 | Resonant period (s) approximated value (s) and corresponding eigenvalues . . . | 64 |
| 3.1 | Descriptive statistics of database for model building | 86 |
| 4.1 | Comparison of annual-averaged efficiency ε_{ann} obtained by the present solution technique and the results provided in De O Falcão and Rodrigues [1]. | 98 |
| 4.2 | Descriptive statistics of database for model building | 101 |
| 4.3 | Activation function definition | 103 |
| 4.4 | Error Matrices | 103 |
| 4.5 | Decision variables of random search algorithm for MLP model. | 104 |
| 4.6 | Error scores and R^2 value of the MLP Model | 104 |
| 4.7 | Decision variables of GA for XGBoost model and the corresponding optimized values | 109 |
| 4.8 | Error scores and R^2 value of the XGBoost Model | 109 |
| 4.9 | Optimum design of the OWC device | 116 |
| 5.1 | Descriptive statistics of database for model building | 128 |
| 5.2 | XGBoost tuning parameters and optimized values. | 131 |
| 5.3 | 10-fold cross-validation of the XGBoost model | 132 |
| 5.4 | Comparison of the average of the 10-fold cross-validation error scores and R^2 value | 132 |
| 5.5 | Spearman's correlation coefficient and corresponding P -values | 134 |
| 5.6 | L_8 orthogonal array | 141 |
| 5.7 | Initial lower and upper sample values of the parameters to construct L_8 orthogonal array | 141 |
| 5.8 | Optimal parameter range, sign of the regression coefficient, T Score and P -Value for R_1 | 142 |
| 5.9 | Optimal parameter range, sign of the regression coefficient, T Score and P -Value for R_2 | 142 |
| 5.10 | Optimal parameter range, sign of the regression coefficient, T Score and P -Value for R_3 | 142 |
| 5.11 | Descriptive statistics of the response variable from the dataset developed in Sec. 5.5. All the units are considered as Wm^{-1} | 143 |
| 5.12 | L_8 orthogonal matrix associated with the optimal parameters for R_1 | 144 |

List of Figures

| | | |
|------|--|----|
| 1.1 | Global annual mean wave power estimation in kWm^{-1} spanning 10 years period (Image is taken from López et al. [2]). | 2 |
| 1.2 | Classification of wave energy converter devices (López et al. [2]). | 6 |
| 1.3 | Illustration of the piezoelectric bimorph (Renzi [3]). | 9 |
| 1.4 | The working principle of OWC caisson device subjected to wave crest and wave trough. | 9 |
| 1.5 | Schematic diagram of water wave propagation problem | 19 |
| 1.6 | Schematic of the vertical cross-section of the piezoelectric device. | 24 |
| 1.7 | Schematic diagram of the vertical cross-section of the OWC device. | 26 |
| 1.8 | Cross-section of the domain Ω bounded by Γ | 30 |
| 1.9 | Discretization of the boundary using constant elements. | 31 |
| 1.10 | Domain consists of non-degenerate boundary Γ_S and degenerate boundary Γ_D | 33 |
| 1.11 | The forward propagation network architecture. | 42 |
| 2.1 | Schematic diagram of the physical problem. | 54 |
| 2.2 | P_{ext} vs. T_0 . Lines represent the solutions obtained by the present boundary element method and symbols represent the solutions provided in Buriani and Renzi [4]. | 60 |
| 2.3 | (a) P_{ext} vs. T_1 , and (b) contour plot of P_{ext} as a function of T_1 and d/h when the PWEC plate edge conditions are fixed. | 61 |
| 2.4 | (a) P_{ext} vs. T_1 , and (b) contour plot of P_{ext} as a function of T_1 and l/h when the PWEC plate edge conditions are fixed.. . . . | 62 |
| 2.5 | P_{ext} vs. T_1 for various values of (a) m , and (b) a_1/h when the PWEC plate edge conditions are fixed. | 62 |
| 2.6 | P_{ext} vs. T_1 , and (b) contour plot of P_{ext} as a function of T_1 and d/h when the PWEC device having fixed rear edge and free front edge. | 65 |
| 2.7 | (a) P_{ext} vs. T_1 , and (b) contour plot of P_{ext} as a function of T_1 and l/h when the PWEC device having fixed rear edge and free front edge. | 65 |
| 2.8 | P_{ext} vs. T_1 for various values of (a) number of ripples m , and (b) ripple amplitude a_1/h of the sinusoidal seabed when the PWEC device having fixed rear edge and free front edge. | 66 |
| 2.9 | (a) P_{ext} as a function of T_1 for various values of mooring stiffness q (Nm^{-1}), and (b) contour plot of P_{ext} as a function of T_1 and q (Nm^{-1}). | 67 |
| 2.10 | P_{ext} vs. T_1 , and (b) contour plot of P_{ext} as a function of T_1 and d/h | 67 |
| 2.11 | (a) P_{ext} vs. T_1 , and (b) contour plot of P_{ext} as a function of T_1 and l/h | 68 |
| 2.12 | Comparison of P_{ext} for fixed and moored lee edges when the front edge is (a) fixed, (b) free, or (c) moored. | 70 |
| 3.1 | Schematic diagram of the physical problem. | 74 |

| | | |
|------|---|-----|
| 3.2 | Validation of P_{ext} vs T_1 . Here $a_1/h = 0$ and $l/h = 2$ | 79 |
| 3.3 | Variation of P_{ext} vs T_1 for different (a) l/h , (b) d/h , (c) a_1/h , and (d) m | 80 |
| 3.4 | Free surface displacement $\zeta_c(x, t)$ at various times (a) $t = 1s$, (b) $t = 10s$, (c) $t = 20s$, and (d) $t = 30s$, (e) $t = 40s$, (f) $t = 50s$ | 81 |
| 3.5 | Free surface displacement and plate deflection $\zeta_p(x, t)$ at various times (a) $t = 1s$, (b) $t = 10s$, (c) $t = 20s$, and (d) $t = 30s$, (e) $t = 40s$, (f) $t = 50s$ | 82 |
| 3.6 | Scatter plot of the input features (a) l/h and (b) d/h for training the ANN model, and the input features (c) l/h and (d) d/h for the optimization of the PWEC device. | 85 |
| 3.7 | Variation of (a) P_{ext} vs. l/h , (b) P_{ext} vs. d/h | 86 |
| 3.8 | (a) ANN model: MSE of training and validation errors w.r.t. Epochs, (b) predicted vs true values for the test set. | 87 |
| 3.9 | (a) Top fifty predicted values of the mean P_{ext} by the PWEC device, (b) plate length of the corresponding sample number as seen in (a), (c) submergence depth of the corresponding sample number as seen in (a). | 87 |
| 4.1 | Schematic of LIMPET OWC wave energy converter device. | 92 |
| 4.2 | σ_p as a function of Λ | 98 |
| 4.3 | Surface plot of P_{ann} (Wm^{-1}) as a function of (a) r/h and y_0/h , and (b) N and D | 100 |
| 4.4 | Scatter plots of the input features (a) submergence depth y_0/h , (b) chamber length r/h , (c) turbine rotor diameter D , and (d) turbine rotational speed N for training, validation and testing the model. | 102 |
| 4.5 | (a) Training and validation loss of the ANN model based on the MAE metric, and (b) comparison between the true values and predicted values using the MLP model. | 104 |
| 4.6 | (a) Training and validation error of the XGBoost model, (b) true values and the predicted values of the test set. | 109 |
| 4.7 | First-order ALE plots of (a) y_0/h , (b) r/h , (c) D , (d) N | 112 |
| 4.8 | Second-order ALE plots of (a) y_0/h and r/h , (b) y_0/h and D | 113 |
| 4.9 | Second-order ALE plots of (a) y_0/h and N , (b) r/h and D | 113 |
| 4.10 | Second-order ALE plots of (a) r/h and N (b) D and N | 114 |
| 5.1 | Schematic diagram of the physical problem. | 120 |
| 5.2 | Latin Hypercube samples of (a) PWEC plate length (l_1/h), (b) submergence depth of the PWEC device (d_1/h), (c) gap between the OWC-PWEC devices (g_p/h), (d) OWC front wall draft (d_2/h), and (e) radius of the OWC device (r/h). | 127 |
| 5.3 | (a) XGBoost model: RMSE of training and validation errors w.r.t. iterations, (b) predicted vs true values for the test set. | 131 |
| 5.4 | Shapely values of (a) train set (b) test set. | 135 |
| 5.5 | ALE plot of (a) l_1/h , (b) d_1/h , (c) d_2/h , (d) g_p/h , and (e) r/h | 137 |
| 5.6 | ALE plot of (a) l_1/h and d_1/h , (b) l_1/h and g_p/h , (c) l_1/h and d_2/h , (d) l_1/h and r/h | 138 |
| 5.7 | Two-dimensional ALE plot of (a) d_1/h and g_p/h , (b) d_1/h and d_2/h , (c) d_1/h and r/h , (d) g_p/h and d_2/h , (e) g_p/h and r/h , (f) d_2/h and r/h | 139 |

List of Symbols

| | |
|-------------------------------|---|
| x, y : | Cartesian coordinates |
| u, v : | Velocity components |
| k_0 : | Wavenumber associated with incident wave |
| ω : | Angular frequency |
| λ : | Wavelength associated with incident wave |
| ∇^2 : | $\left(= \frac{\partial^2}{\partial x^2} + \frac{\partial^2}{\partial z^2} \right)$ Laplacian operator |
| δ_{ij} : | Kronecker delta |
| A : | Amplitude of the incident wave |
| g : | Acceleration due to gravity |
| $G(x, z; x_0, z_0)$: | Fundamental solution |
| (x_0, z_0) : | Source point |
| (x, z) : | Field point |
| H_{ij}, G_{ij} : | Influence coefficients |
| ρ : | Density of the fluid |
| ρ_p : | Density of the plate |
| E : | Young's modulus |
| Φ : | Velocity potential (function of both space and time) |
| ϕ : | Spatial velocity potential |
| ϕ^I : | Incident velocity potential |
| ϕ^S : | Scattered velocity potential |
| ϕ^R : | Radiated velocity potential |
| h : | Water depth |
| ξ : | Plate deflection |
| ζ : | Free surface elevation |
| $\partial/\partial n$: | Normal derivative |
| \tilde{A} and \tilde{B} : | Radiation susceptance and radiation conductance parameters |
| C_g : | Group velocity of wave |

- \wedge : Turbine control parameter
- N : Rotational speed of the Wells turbine
- D : Turbine rotor diameter of the Wells turbine
- H_s : Significant wave height
- T_e : Significant time period
- S_I : Incident wave spectrum
- ω_i^{av} : Average frequency of each regular wave component
- $\mathcal{G}^{[l]}$: Activation function of layer l
- \mathcal{L} : Loss function
- $z_k^{[\ell](i)}$: Cumulative input of the i^{th} sample from k^{th} neuron in the ℓ^{th} hidden layer
- $a_k^{[\ell](i)}$: Cumulative output of the i^{th} sample from k^{th} neuron in the ℓ^{th} hidden layer
- p : True value of the response variable
- \hat{p} : Predicted value of the response variable using ML model
- $p^{(m)}$: True response value of m^{th} sample
- $\overline{p^{(m)}}$: Average of the true response value of m samples
- $\hat{p}^{(m)}$: Predicted response value of m^{th} sample using ML model
- $x_j^{(i)}$: i^{th} input sample of the j^{th} feature in the dataset
- q : Structure of a decision tree
- T : Number of leaves in a decision tree
- α : L_1 regularization weight
- λ : L_2 regularization weight
- $\widehat{f}_{\{j,l\},ALE}(X_j)$: Uncentered ALE of j^{th} feature
- $\hat{f}_{j,ALE}(X_j)$: Centered ALE of j^{th} feature

Abbreviations

ANN: Artificial Neural Network

ALE: Accumulated Local Effect

BEM: Boundary Element Method

BVP: Boundary Value Problem

CatBoost: Categorical Boosting

CV: Cross Validation

DFBC: Dynamic Free Surface Boundary Condition

KFBC: Kinematic Free Surface Boundary Condition

MAE: Mean Absolute Error

MAPE: Mean Absolute Percentage Error

MLP: Multilayer Perceptron

ML: Machine Learning

RF: Random Forest

OWC: Oscillating Water Column

PTO: Power Take-off

PWEC: Piezoelectric Wave Energy Converter

RMSE: Root Mean Square Error

RSM: Response Surface Methodology

SHAP: Shapley Additive exPlanations

WEC: Wave Energy Converter

XGBoost: Extreme Gradient Boosting

Chapter 1

Introduction

1.1 Preamble

In the current scenario, two of the significant challenges that the energy sector is facing are the increasing need for energy and cutting down on greenhouse gas emissions (Li et al. [5], Keleş and Bilgen [6]). In this regard, renewable energy serves as a suitable substitute for conventional energy sources. Renewable energy harvesting is environment friendly, and sources such as solar, wind, and wave energy are abundant and sufficient to ensure energy security. Further, it reduces greenhouse gases and plays a crucial role in environmental protection. Many nations consider renewable energy a vital part of the latest energy technologies. They have set high goals for using more renewable energy in their current and future plans (Sen and Ganguly [7]). He et al. [8] proposed a significant shift in the energy policy to improve renewable energy production in China and also describes how renewable energy research and development and, consequently, renewable energy production will significantly enhance the country's economic growth. Right now, global energy harvesting has drastically changed, moving away from fossil fuels to cleaner energy sources. Ultimately, they aim for a future where most of our energy comes from sustainable renewable sources (Holechek et al. [9]). The use of renewable energy, including bio-fuels and all traded renewable energy except for hydroelectric power, showed continuous growth. This surge constituted over 40% of the total global growth in primary energy during the previous year, which is larger than any other energy source. Consequently, renewable energy expanded its portion within the overall energy composition from 4.5% in 2018 to 5% in 2019 (BP [10]). Out of these renewable energy sources, wave energy is one the most promising ones because of its high energy density, i.e., about 2–3 kW/m². In contrast, solar and wind energy typically ranges from 0.1 – 0.5 kW/m². Moreover, the availability of wave energy is irrespective of any seasonal variation. The exploitable wave energy capacity is estimated at around 1.8 terawatts (TW). However, assessing this potential requires the consideration of multiple factors. These

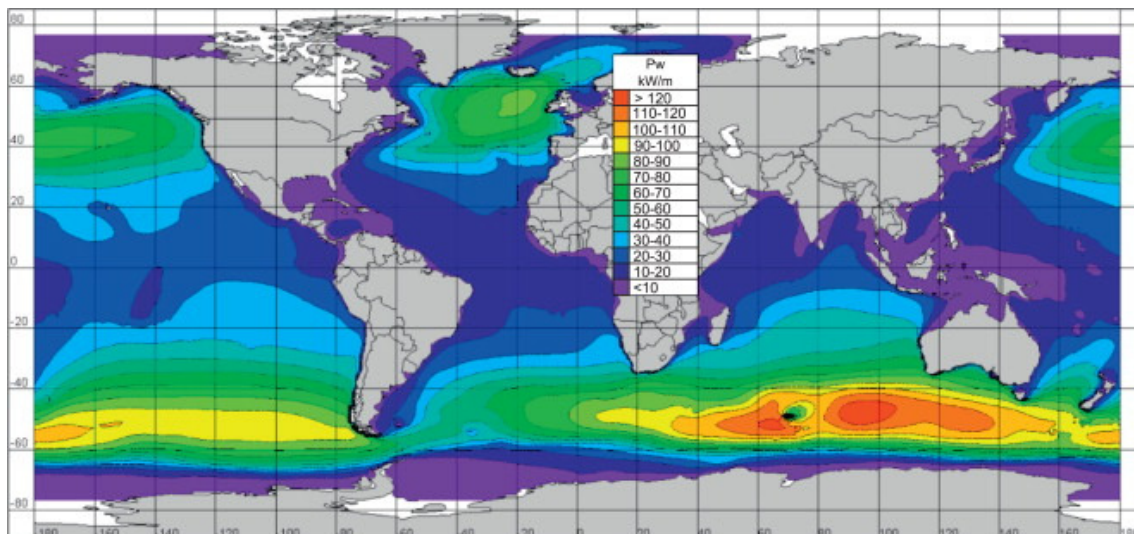


FIGURE 1.1: Global annual mean wave power estimation in kWm^{-1} spanning 10 years period (Image is taken from López et al. [2]).

include distance to the coastline, effects on coastal alignment, and protected zones such as areas occupied by shipping lanes, fishing zones, pipelines, cables, or unsuitable seabed morphology and water depth. Still, with careful evaluation of the suitable regions to produce wave energy, about 500 GW of easily exploitable potential emerges, focusing on areas with high energy density above 30 kW/m . Like exposed west coasts globally, certain regions hold the most promise for wave energy due to long-period swell waves generated by distant weather systems. These areas, including the Atlantic coasts of Europe, North America, Australia, South America, and Africa, possess significant exploitable energy, often independent of local wind conditions. Global annual mean wave power estimation in kWm^{-1} spanning 10 years period is provided in Fig. 1.1 (López et al. [2]). They offer a valuable energy source during periods of limited wind or solar power, highlighting their potential for wave energy utilization (Ocean [11]).

The ocean wave contains kinetic and gravitational potential energy, and the total energy of ocean waves is relevant to two factors, namely, the wave height and wave period. Moreover, the power carried by ocean waves is usually expressed in watts per meter of the incident wavefront, and it is proportional to the square of wave height and period. From an engineering perspective, the wave characteristics are mainly based on four physical quantities: wave height, wave direction, wave period, and phase lag. Further, various physical phenomena related to these parameters are listed as (i) refraction, (ii) diffraction, (iii) reflection, (iv) shoaling and breaking, and (v) friction and large-scale vortex formation and shedding, etc.

The wave structure interaction problems associated with the wave energy converter devices are extensively studied using the eigenfunction expansion method. However, a significant drawback of this method is that it is applicable only if the boundary of the physical problem is in a regular shape, such as circular, rectangular, etc. But in most cases, the boundary of the physical problem

associated with the wave structure interaction may not be regular in nature. One of the realistic examples of the same is the ocean bottom boundary. In reality, the seabed may be undulated in nature. So, one of the best methods to solve such a problem is by making use of the boundary element method (BEM). It is possible to model any irregularly shaped boundaries with respective boundary conditions in BEM. Further, the wave structure interaction problems can be studied using either the finite difference or finite element methods. But in this case, the whole region of the physical domain is to be discretized, and it will significantly increase the computational and time complexity. Hence, the boundary element method is one of the most suitable numerical approaches to solve the physical problems associated with wave structure interactions. It is noteworthy that for problems with degenerate boundaries, the aforementioned BEM has rank deficiency difficulties with influence matrices. Dual BEM is widely used to address this rank deficiency issue.

The focus of this thesis is to mathematically model and optimize the parameters of two of the efficient wave energy converter devices, namely the piezoelectric wave energy converter device and the oscillating water column wave energy converter device. The boundary element method and the dual boundary element method are employed to solve the boundary value problems associated with the power generated by the wave energy converter devices. Moreover, machine learning and deep learning models are carefully chosen based on the complexity of the problem to ensure accurate prediction of the power output by the wave energy converter devices. Further, interpretable machine learning approaches and the response surface methodology are employed to optimize the parameters associated with the wave energy converter devices. The problem associated with the power generation by the PWEC device is studied under the regular incident wave climate. Meanwhile, the problems associated with the power generation of the OWC device are studied under both regular and irregular wave climates. As the seabed need not be regular in nature, the problems associated with the PWEC plate are studied in the presence of the undulated seabed. The time domain analysis of the plate deflection and the free surface displacement are also investigated. It is well known that the samples associated with the machine learning model have great importance in improving the accuracy and generalization ability of the model. So, when the sample does not represent the whole data, the predicted models may lead to wrong conclusions. Hence, to get stratified samples, the Latin hypercube sampling technique is used for data accumulation to train, validate, and test the predictive models. The multilayer perceptron model and the XGBoost models are obtained to be the most suitable predictive models to fit the data associated with the power generation of the wave energy converters. Further, the importance of features and the interaction effects are also studied using interpretable machine-learning approaches. Finally, using these predictive models, along with the interpretable machine learning models, and using the multivariate statistical method, namely the response surface methodology, the design parameters of the wave energy converter devices are optimized

accurately. The findings of various mathematical modeling results are validated with known results available in the literature.

An extensive review of the literature on piezoelectric plates and OWC devices is presented in the following sections. Additionally, a concise description of predictive models and related concepts is provided. Furthermore, a brief overview of the parameter optimization techniques using interpretable machine learning models and the statistical approaches are described. Moreover, detailed descriptions of the governing equation and boundary conditions associated with the linear water wave theory in a homogeneous fluid medium are provided. In addition, comprehensive explanations of the constant and dual boundary element approaches.

1.2 State of the art

In this section, a comprehensive literature review is provided to gain a more profound understanding of the current status of literature associated with the hydrodynamics of wave energy converter devices and the various techniques to optimize the power they generate. Further, a detailed literature review is presented associated with the current improvements in artificial intelligence techniques and the use of machine learning techniques to optimize the power generated by the wave energy converter devices. Moreover, we will go through the literature associated with various multivariate statistical optimization techniques. The challenges that arise to comprehend the wave-structure interaction problems involve the understanding of the wave properties, dynamics that arise on the air-water interface, and behavior of the rigid/impermeable/porous/flexible structures interacting with the fluid. Following Newton's initial contributions, French mathematicians Laplace, Lagrange, Poisson, and Cauchy made significant theoretical developments in the linear theory of water waves during the eighteenth and early nineteenth centuries. Meanwhile, in Germany, Gerstner studied nonlinear waves, while the Weber brothers conducted meticulous experiments on water waves. Between the 1837 and 1847 period, the research works by the British mathematicians Russell, Green, Kelland, Airy, and Earnshaw led to substantial advancements in the field of water waves, which provided the groundwork for the research conducted by Stokes (Craik [12]) at a later stage. Focusing primarily on shallow water waves, Airy conducted pivotal investigations in 1845. Stokes, in 1847, expanded these first-order wave theories to higher-order wave theories, which laid the groundwork for Boussinesq's formulation of long-wave theories in 1872. Following this, Michell and McCowan, in 1893 and 1894, explored the constraints on wave heights concerning the angle of the propagating waves and the wavelength (De [13]). Subsequently, Lamb [14], Mei [15], Dean and Dalrymple [16], Linton and McIver [17], and other related scholars provided profound insights into the propagation of water wave phenomena through their eloquently articulated works (Craik [12]). Presently, a dynamic field of study concerning the interaction of water waves with marine

structures is closely linked to the exploration of untapped ocean wave energy. In this regard, an extensive survey of literature pertaining to different categories of wave energy converter devices is presented. The concept of wave energy harvesting started in the late 1800s. Early inventors, like Pierre-Simon Girard in 1799, had ideas for using waves to pump water for farming. Isidoro Cabanyes, a Spanish engineer in 1895, got a patent for a device that used floating parts to move water and make electricity. Even though these early ideas were mostly written on paper and didn't transform these ideas into real prototypes, they set the base for future wave energy inventions. However, the origin of OWC wave energy converter technology dates back to 1965 when a floating OWC device prototype was developed in Japan (Antonio [18]). Subsequent to this milestone, OWC devices were built across various global sites using different technologies such as "HydroAir" in USA, "SEAREV" in Portugal, "FO3" in Norway, oscillating cascade power system (OCPS) in USA, etc. (López et al. [2])

1.2.1 Classification of wave energy converter devices

The wave energy converter devices can be classified based on (i) the working principle, (ii) device size and directional wave characteristics, and (iii) location. A brief review of these classifications is provided in the following.

1.2.1.1 Working principle

Based on the working principle, the wave energy converter devices are classified into the following four categories (see Fig. 1.2).

- **Pressure differential:** Devices categorized in this class can be segmented into two distinct groups: Archimedes effect converters and oscillating water columns (OWCs). The former is typically located in close proximity to the shoreline, firmly attached to the seabed, and functions by harnessing the pressure fluctuations between the wave crests and troughs. When a wave crest passes over the device, it compresses the internal air, causing a downward motion. Conversely, when a trough is over the device, reduced water pressure leads to the upward motion of the device. An example of this mechanism is demonstrated in the 250 kW Archimedes wave swing (AWS) (Polinder et al. [19]). On the other hand, the OWCs operate on a similar principle and are commonly positioned along the shoreline or in its vicinity. Due to the presence of a semi-submerged chamber, the wave motion alters the water level within the chamber, thereby impacting the volume of the enclosed air. This airflow is subsequently propelled through a turbine, which can work under the bidirectional nature of the airflow. An example of the prototype using this technology is the shore-fixed Limpet 500 kW power plant (Belfast [20]).

- Floating Devices:** These devices rely on a buoyant structure that responds to wave motion. The potential oscillating motion can occur vertically, horizontally, in pitch, or through a combination of these movements. Examples are the searaser WEC (Liu et al. [21]) as single floating structure, and wave star as multiple floating structure (Marquis et al. [22])
- Overtopping devices:** These converters operate on the principle that waves interact with a structure, leading to an enhancement in its potential energy, kinetic energy, or a combination of both. Overtopping systems facilitate the movement of water over the structure, which typically behaves as a reservoir positioned above sea level, followed by the redirection of this water back into the sea through turbines. An example of such a converter is the wave dragon, with power output ranges between 4 MW to 10 MW, contingent upon the energetic characteristics of the wave environment at the specific deployment site (Kofoed et al. [23]).
- Oscillating wave surge/Impact devices:** These converters are flexible constructions strategically situated perpendicular to the wave direction. This arrangement enables the deflector to oscillate in a reciprocating motion, influenced by the impact of the waves. Sarkar et al. [24] studied the power generation of such a system.

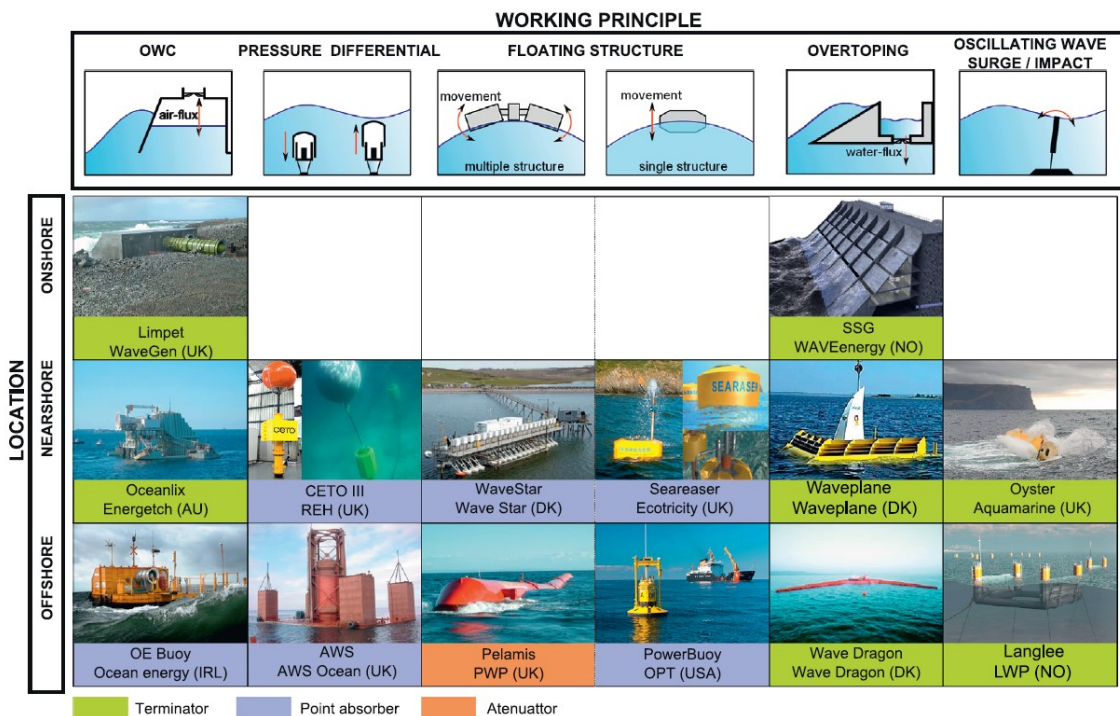


FIGURE 1.2: Classification of wave energy converter devices (López et al. [2]).

1.2.1.2 Size of the device and direction of the incoming wave

The WECs can be classified based on the size of the device and direction of the incoming wave as follows

- **Attenuator:** These particular wave energy converters (WECs) are extended structures, considerably longer than the wavelength, and are positioned in alignment with the wave direction. Their primary function involves reducing the amplitude of the waves they encounter. Attenuators are constructed from a sequence of cylindrical sections interconnected by flexible hinged joints, enabling these sections to pivot independently of each other (López et al. [2]).
- **Point absorber:** Compared to the wavelength, the dimensions of these devices are considerably smaller. Distinguished from other counterparts, the point absorber efficiently gathers energy from all directions through its versatile movements. These mechanisms harness the power generated by the bobbing or pitching motions of the device, converting the vertical oscillations of the waves into either rotary or oscillatory movements, thereby producing electricity (Al Shami et al. [25]).
- **Terminator:** The dimension of these devices are similar to the Attenuators. However, they are positioned perpendicular to the primary wave propagation direction and essentially function to interrupt or cease the wave action.

1.2.1.3 Location

Three distinct types of converters are categorized based on the distance from the coastline to the deployment location of the wave energy converters (WECs).

- **Onshore devices:** These converters are situated along the shoreline and can be installed in various ways, such as above the sea in shallow waters, incorporated into structures like breakwaters, dams, or fixed onto cliffs. Their primary advantage lies in the ease of maintenance and installation due to the accessibility of most shoreline locations. Additionally, they do not necessitate mooring systems or extensive sea cables to link the WEC to the grid. However, shoreline locations typically experience lower wave energy due to interactions of ocean waves with the seabed, and the scarcity of suitable land sites poses deployment challenges (Falcao [26], Drew et al. [27], Czech and Bauer [28]).
- **Nearshore devices:** These converters are typically deployed within a short distance from the shoreline in locations having moderate water depths ranging from 10 to 25 meters. They are commonly placed directly on the seabed, eliminating the need for moorings.

However, the structure must withstand the stress induced when waves pass over it. In certain cases, these converters are also designed as floating structures. (Falcao [26], Drew et al. [27], Czech and Bauer [28]).

- **Offshore devices:** These converters are situated in deep waters, typically beyond 40 meters from the shoreline, and built as floating or submerged structures anchored to the seabed. The advantage behind the deployment of offshore devices is to harness a considerably higher amount of wave energy available in the open sea. However, their location in the open sea poses challenges concerning the reliability and resilience of the device, demanding robust structures capable of withstanding substantial wave loads. Additionally, the complexity and cost associated with the maintenance of these converters pose significant challenges. Also, They require lengthy and expensive sea cables to transmit the generated electricity to the grid (Falcao [26], Drew et al. [27], Czech and Bauer [28]).

1.2.2 Piezoelectric wave energy converter device

The marine energy sector is still untapped mainly because of the significant challenges due to the substantial maintenance costs and the complex deployment procedures associated with wave energy converters (WECs), mainly due to their substantial size. Consequently, the focus has shifted toward developing WECs equipped with flexible structures, aiming to tackle a few of the challenges. In this regard, a promising solution can be to make use of the piezoelectric materials attached to the structures that interact with the water waves. Typically, a piezoelectric WEC device primarily comprises a flexible substrate with piezoelectric material bonded to its sides. If the piezoelectric material coats only one side of the flexible plate, it is termed an unimorph piezoelectric device. Conversely, if both sides of the plate are coated with a piezoelectric material, then it's called a biomorph piezoelectric plate (see Fig. 1.3). These flexible plates are theoretically modeled using the Euler–Bernoulli beam theory (Renzi [3]). Despite generating electricity typically in the range of watts to kilowatts, piezoelectric wave energy converter devices prove adequate to power low-energy electronics such as LEDs, wireless routers, PCs, ocean buoys, and sensors. The merits of these devices extend to their environmentally friendly nature, cost-effectiveness in manufacturing, minimal maintenance requirements, and ease of design. Integrating piezoelectric plates into diverse offshore structures, such as oil platforms, windmills, and sea-crossing bridges, not only facilitates electricity generation but also serves as a means to mitigate ocean wave energy, safeguarding offshore structures from wave-induced loads. The working principle of the PWEC device is the sensor effect. The relatively high kinetic energy of ocean waves can be used to apply external stresses on the piezoelectric material, and consequently, a charge difference occurs in the PWEC material, and useful electric energy will be generated. In conclusion, piezoelectric wave energy converter devices represent one of the simplest and most innovative technologies for harnessing electricity from ocean waves.

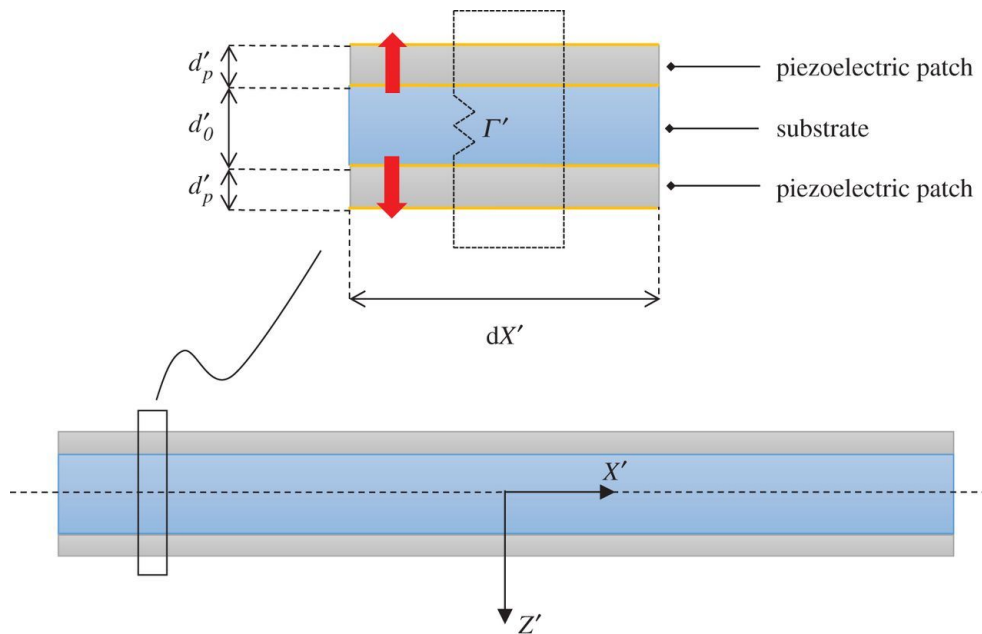


FIGURE 1.3: Illustration of the piezoelectric bimorph (Renzi [3]).

1.2.3 Oscillating water column wave energy converter device

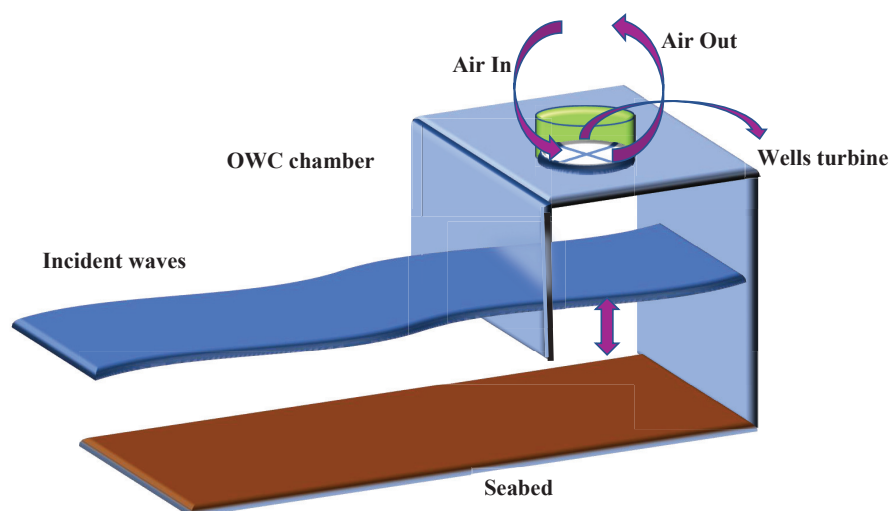


FIGURE 1.4: The working principle of OWC caisson device subjected to wave crest and wave trough.

Among the various technologies available for harnessing ocean wave energy, the OWC device offers distinct advantages over other wave energy converter technologies. The OWC device comprises a partially submerged chamber and a Power Take-Off (PTO) system using a Wells turbine positioned atop the chamber. As waves traverse through the partially submerged collector chamber, the trapped air above the water column experiences oscillations due to the

hydrodynamic pressures associated with the continuous impact of wave crests and troughs (see Fig. 1.4). When a wave crest enters the OWC device, the water level in the chamber rises, compressing the air column and activating the Power take-off (PTO) system, which generates pneumatic power. Conversely, as the wave trough descends, the water level inside the OWC chamber falls, creating a vacuum that draws air into the chamber. The turbine in the PTO system will rotate again in the same direction to generate wave power. OWC devices exhibit exceptional performance as the OWC device can work effectively for a wider range of incident wave frequencies (even low as typically around 0.1 Hz (Evans and Porter [29])). These devices offer multiple advantages, such as no moving parts submerged in the ocean and their adaptability for installation along shorelines or nearshore breakwaters, resulting in reduced construction and maintenance expenses (Heath [30]).

1.2.4 Hydrodynamics of the piezoelectric wave energy converter device

The use of piezoelectric materials to harvest wave energy through vibrations presents an innovative solution to address the limitations of conventional wave energy converters, particularly the challenge of deploying large-sized devices. A few of the essential advantages of using piezoelectric wave energy converter devices are that these are environmentally friendly, have low manufacturing and less maintenance costs involved, and are easy to design (see Safaei et al. [31], and Farrok et al. [32]). The concept of using piezoelectric wave energy converter devices in ocean waves is completely new and started in the last decade. Xie et al. [33] proposed a mathematical model of a piezoelectric energy harvester to convert ocean wave energy into electricity. In this model, a cantilever beam attached to bimorph piezoelectric layers is used, and the transverse wave motion of the water particles is used to vibrate the piezoelectric device. The results demonstrated that the generated electricity significantly depends on the thickness of the cantilever beam, water depth, incident wave height, and the ratio of the incident wavelength to the water depth. Further, Xie and Wu [34] used the aforementioned technique of energy conversion using a vertical piezoelectric device and the longitudinal wave motion of water particles. Wu et al. [35] developed a buoy-type piezoelectric energy harvester by attaching several piezoelectric coupled cantilevers to a buoy, which utilizes the transverse motion of the wave to convert the wave energy into electricity using piezoelectric patches. Renzi [3] developed a fully coupled hydroelectromechanical model for the flexible piezoelectric wave energy converter device. In this study, a submerged flexible plate bonded with piezoelectric layers on both sides is used to generate electricity from the elastic displacement of the flexible plate floating in ocean waves. It was shown that the short-crested flexural gravity waves generated more power than the long-crested flexural gravity waves. Moreover, these short-crested wave components are predominantly responsible for the occurrence of resonant peaks in the power output from the device. Xie and Wang [36] introduced a buoy-type composite PWEC device consisting of a vibrator, slider, and a

heaving buoy and proposed that this system can absorb more wave energy when the size of the composite piezoelectric buoy becomes larger, and the relative speed between the vibrator and slider becomes higher. Zhang et al. [37] studied the performance of a cantilevered piezoelectric wave energy harvester having a variable cross-section in nearshore areas. It is concluded that with appropriate cantilever height and incident wave characteristics, nearly 2.5 times electric power can be generated with a cantilevered piezoelectric harvester having a variable cross-section as compared to the traditional harvester having a uniform cross-section. Mutsuda et al. [38] proposed a flexible piezoelectric wave energy harvester consisting of an elastic substrate and a piezoelectric paint. The study was carried out for both the unimorph and bimorph actuator patterns. Further, the authors studied the influence of key parameters such as the wave steepness, aspect ratio, thickness of the piezoelectric paint, and submergence depth of the harvester on the electricity generation for various incident wave characteristics. Zhou et al. [39] studied the nonlinear mechanism of power generation by PWEC device with different stoppers. To model the problem, a set of coupled nonlinear governing equations was established with the appropriate nonlinear term incorporated to describe the produced impact force by the stoppers. Further, the study demonstrated that the stoppers in the device change the dynamic behavior of the system, which enhances the device's energy-harvesting performance. Chen et al. [40] designed a PWEC device consisting of a buoy that is excited by the ocean waves, and subsequently, this excitation is converted into higher frequency mechanical motion and deforms a piezoelectric film. One major advantage of this PWEC device is that it can work effectively for incident waves having lower frequencies. Zheng et al. [41] studied the performance of a breakwater-integrated submerged flexible PWEC device. The associated physical problem was handled for a solution using the eigenfunction expansion method. The study revealed that the edge conditions, plate width, and submergence depth of the plate are the most significant factors in determining the efficiency of the PWEC device. Moreover, the change in width/draft of the breakwater has limited influence on the wave power absorption by the PWEC device. Ucar [42] investigated the performance of piezoelectric patch-based energy harvesting in which the patches are embedded into marine boats. This study concluded that the patches close to the boat's bow generate higher electricity due to the higher strain. Qi et al. [43] proposed a piezoelectric-electromagnetic wave energy harvester integrated on sea-crossing bridges. By virtue of piezoelectric and electromagnetic effects, the piezoelectric and electromagnetic modules harness energy from vibrations caused by the ocean waves. Recently, Michele et al. [44] proposed a theoretical model to study the working mechanism of a floating flexible circular plate connected to the seabed through multiple power take-off (PTO) mechanisms. It was shown that this proposed WEC device could work efficiently for a wider range of incident wave frequencies.

1.2.5 Hydrodynamics of the oscillating water column wave energy converter device

Among the wave energy converting devices, the oscillating water column (OWC) device is notably recognized as one of the most efficient techniques. The mathematical modeling of wave energy converters started in 1965. Since then, numerous theoretical and technological advances have been achieved in order to create an efficient OWC device. In the modeling of wave energy converters, the wave climate has significant importance. In the real sea, waves typically lack regular single-frequency patterns and instead exhibit irregularities in direction, frequency, phase, and amplitude. The actual ocean surface involves the superposition of regular waves of varying frequencies (Goda [45]). Therefore, it is very important to analyze the performance of the OWC device on regular as well as irregular/random waves.

Evans and Porter [29] adopted the Galerkin method to investigate the performance of a conventional OWC device. This article provided the general expressions for various factors relevant to the device performance, such as radiation susceptance, radiation conductance, and volume flux inside the chamber, and these physical quantities were analyzed for various values of shape parameters associated with the device. De O Falcão and Rodrigues [1] Formulated a stochastic approach to assess the efficiency of an OWC device. The method involved representing random incident waves through an energy spectrum and gauging the wave climate's intensity using sea states. Findings revealed that adjusting the turbine's rotational speed significantly increased energy production compared to employing a control valve system. Josset and Clément [46] used the random phase method to synthesize various sea states from the Pierson–Moskowitz spectrum and performed a time-domain analysis to study the efficiency of the OWC wave power plant for each sea state. It was observed that the productivity of the power plant depends on the turbine characteristics. Gouaud et al. [47] performed the model test to investigate the working mechanism of OWC devices in the presence of underwater mounds under the influence of regular and irregular incident waves. The study revealed that the capture width ratio of the device was significantly influenced by the energy flux at the OWC entrance. He et al. [48] studied the hydrodynamic efficiency of a floating breakwater-integrated OWC device experimentally. In this study, a comparison between the symmetric chamber breakwater and the asymmetric chamber of breakwater shows that the asymmetric chamber significantly enhances the heave response, but it has less influence on the surge and pitch responses. Ning et al. [49] used a higher-order boundary element method to investigate the working mechanism of an OWC device placed over the sloping seabed. In this research, it was noticed that the performance of the device is affected by various parameters such as the structural and bottom configuration of the device, turbine damping coefficient, and nonlinearity of the incident waves. Sheng and Lewis [50] studied the effect of air compressibility on the hydrodynamic performance and power capture factor of floating and fixed-type OWC devices. In this study, the following results are concluded: (i) for fixed OWC

devices, air compressibility significantly reduces the power conversion in the long-wave regime, and a reverse trend is observed in the short-wave regime; (ii) large air compressibility plays a key role in reducing the performance of a floating OWC device. Vyzikas et al. [51] studied the effect of structural configuration on the performance of the OWC device positioned over the undulated seabed employing the model test. It was found that the performance of a U-shaped OWC device is better compared to the other conventional OWC devices. In addition, the U-shaped OWC device placed over the sloping bottom has a higher efficiency than the other suggested models. Within the limits of linear water wave theory, Rezanejad et al. [52] analyzed the performance of an OWC device placed over a step bottom in regular and random sea waves. Further, the results associated with the efficiency of the OWC device are obtained using the model tests. It was reported that the efficiency and performance of the OWC device depend strongly on the incident wave period and damping characteristics of the turbine compared to the incident wave height. Further, the durability of the OWC device depends on the draft of the OWC device. Strati et al. [53], Spanos et al. [54] and Malara and Arena [55] investigated the dynamics of a U-shaped OWC device using a non-linear stochastic and semi-analytical approach, respectively. These studies demonstrated that the shape parameters have a strong impact on the average power delivered by the device. Jalón and Brennan [56] developed a physics-based simulation model to investigate the efficiency and structural durability of a fixed OWC device in random sea waves. Wang and Zhang [57] explored the hydrodynamic efficiency of an OWC device having surging front lip-wall and back lip-wall in the context of potential flow theory. It was concluded that the efficiency of the OWC device having a surging front wall increases with an increase in the submergence depth of the device. It was reported that the moderate chamber width is more desirable to optimize the efficiency, and the surging seaside wall of the device effectively diminishes the sloshing effect inside the device chamber. Mayon et al. [58] analyzed the impact of parabolic reflecting breakwater on the hydrodynamic efficiency of an OWC device having a cylindrical cross-section. The study demonstrated that the cylindrical OWC device placed at the parabolic focal point is able to capture more incoming wave energy than the open sea conditions.

1.2.6 Machine learning models to predict the power generation

In recent years, machine learning algorithms have aided in solving domain-specific problems in various fields including medicine, remote sensing and geographical information systems, various engineering fields such as civil engineering, petroleum engineering, etc. (Butcher et al. [59], Kourou et al. [60], Mohajane et al. [61], Hegde and Rokseth [62], Otchere et al. [63]). The above works clearly demonstrate the machine learning model's remarkable adaptability in learning and predicting data across diverse scientific and industrial domains. Moreover, these models exhibit effectiveness in capturing the complex behavior inherent in highly non-linear data associated with wave interaction problems (Sarkar et al. [64], Zhu et al. [65]). As the wave energy converter

devices show highly non-linear behavior on the power generation, leveraging the machine learning models would be the best choice to study the underlying patterns of the shape parameters to maximize the power generation. Sarkar et al. [64] studied the layout optimization of an array of wave energy converters. A combination of the Gaussian process upper confidence bound with a pure exploration algorithm and a genetic algorithm is used to predict the performance of WECs. The study efficiently explores and concentrates on crucial areas of interest in the optimization problem and ultimately attains the optimal layouts of WECs for improved performance. Li et al. [66] introduced a deep machine learning algorithm, namely the multi-layer artificial neural network for short-term wave force forecasting. The primary application of this model was to enable real-time latching control actions on a heaving point absorber. The study demonstrated a significant increase in average energy absorption when utilizing the controller and studying the future wave force. Zou et al. [67] presented a pioneering method centered on deep reinforcement learning (DRL) control. The efficacy of this approach was assessed through the application of a point absorber WEC. The implemented DRL control exhibited proficiency in optimizing energy production. Nevertheless, it is noteworthy to understand the main limitation of this work is the computational cost associated with the training process. However, among the remarkable ML systems, neural network methods stand out due to their capacity to learn, retain knowledge, establish associations among non-linear data, and accurately predict future data. According to a recent observation by Borisov et al. [68], ensemble models based on decision trees with boosting often exhibit superior performance when compared to deep learning models across diverse supervised machine learning tasks. Wu et al. [69] studied the classification performance of the XGBoost and MLP models on many large-scale public datasets. It is found that in all the data sets, the tree ensemble model XGBoost outperforms the MLP model. Nguyen et al. [70] developed the XGBoost model and ANN model to study the seismic drift response and obtained the important factors associated with the seismic drift. Here in this study, the R^2 value of the XGboost model is 0.987, and for the ANN model, it is only 0.962, showing the outperformance of the XGBoost model over the ANN model. Liu et al. [71] utilized the random forest algorithm to predict and quantify parameter interaction effects and dynamics of the parameters of a battery. All conclusions drawn rely on the use of interpretable ML methodologies. El Bilali et al. [72] used the XGBoost model and the deep neural network model to predict the daily pan evaporation. The interpretable ML approaches, namely the SHAP and LIME, are used to interpret the developed ML models.

1.2.7 Optimization of the parameters of wave energy converter devices

Identifying the proper combination of the input parameters is essential to maximize the power generation by the WECs. Various machine learning-based approaches and pure statistical-based approaches are available in the literature. George et al. [73] employed the eigenfunction expansion

method to model a U-shaped OWC device and optimized the parameters of the WEC device using a complete machine-learning approach by developing an artificial neural network model. Sarkar et al. [64] utilized the Quasi-Newton method employing the Broyden-Fletcher-Goldfarb-Shanno algorithm, a genetic algorithm, and the Monte Carlo method to optimize the WEC layouts within a scalable wave farm. Halder et al. [74] focused on enhancing the torque and efficiency of a Wells turbine rotor, employing a surrogate coupled genetic algorithm and k-means clustering. Trivedi and Koley [75] employed the Taguchi method to optimize the resonance frequency, bandwidth, and shape parameters of the hybrid OWC and PWEC devices. Recently, Li and Wang [76] developed a fully coupled wave-to-wire wave energy converter device that converts the vibration energy from the heave motion to electricity using a marine monitoring buoy. The optimization of the parameters of the buoy is carried out using the Taguchi method. Rezaei et al. [77] proposed a two-dimensional optimization procedure using the design of experiments and the response surface methodology (RSM) to optimize the parameters of a 2B-PA wave energy converter(WEC) in the laboratory scale. Ghaheri et al. [78] proposed a two-step optimization approach combining the Taguchi method and Response Surface Methodology (RSM) to efficiently minimize the number of simulations and computational expenses while ensuring a satisfactory level of accuracy. The initial step employed in the Taguchi method is to identify the important parameters associated with maximum power generation. Subsequently, the response surface methodology (RSM) is employed to achieve highly accurate optimized parameters. It is observed that in most of the literature, the Taguchi method is employed for preliminary screening of the optimization process, and the RSM is used for detailed and accurate parameter optimization.

1.3 Motivation and outline of the thesis

The objectives of the present work are provided as follows:

- Developing a BEM-based numerical model to study the surface gravity waves' interaction with the PWEC and OWC devices.
- To study the performance of the PWEC device in regular water waves placed over the undulated seabed.
- To identify suitable machine learning-based predictive models that can predict the power generation of the WEC devices accurately.
- To optimize the parameters of the stand-alone PWEC device and the PWEC device attached with a breakwater in regular wave climate.
- To optimize the parameters of the standalone OWC device in irregular wave climate and hybrid OWC-PWEC wave energy converter devices under the regular incident wave.

The content of the thesis is divided into six chapters depending on the physical problems and objectives of the study. Chapter 1 is introductory in nature. In Chapter 2, the mathematical modeling associated with the performance of a piezoelectric wave energy converter (PWEC) device integrated with an impermeable breakwater placed over an undulated seabed is studied under the regular incident wave climate. In Chapter 3, the power absorption by a submerged standalone piezoelectric wave energy converter (PWEC) is studied in the frequency domain, and the time-dependent displacements of the free surface and the PWEC plate deflection are discussed. Further, the prediction of the power generation by the device and the optimization of the device parameters are studied using an artificial neural network model, namely the multilayer perceptron model. In Chapters 4 and 5, the mathematical modeling of a standalone OWC device and a hybrid OWC-PWEC device and the optimization of the device parameters to maximize power generation are studied. Chapter 6 summarizes the total work presented in the thesis and also provides the future research scope.

Chapter 1 provides a basic introduction, a detailed literature review, the motivation behind the present work, and the thesis outline. Further, Chapter 1 contains the mathematical preliminaries of the water wave propagation, OWC and PWEC device boundary conditions, the development of the machine learning and deep learning models, the interpretable machine learning approaches, various activation functions, their importance, and the statistical optimization techniques.

In Chapter 2, the mathematical modeling associated with the performance of a piezoelectric wave energy converter (PWEC) device integrated with an impermeable breakwater placed over an undulated seabed is studied under the regular incident wave climate. In real oceans, the seabed is undulated in nature. Hence, the significance of the undulated seabed on the wave scattering and, consequently, on the performance of the PWEC devices is studied extensively. Hence, in this study, the seabed is assumed to be undulated in nature, and the associated seabed profile is taken as the sinusoidal type. The influence of the number of ripples and the ripple amplitude on the performance of the PWEC devices is analyzed. Three different boundary edge conditions of the PWEC plate, such as the fixed, free, and mooring edge conditions, are taken, and a detailed analysis is provided to show the effect of edge conditions on the power generation by the PWEC devices. Major emphasis is given to analyze the effect of submergence depth and length of the PWEC plate on the performance of the PWEC devices.

In Chapter 2, the piezoelectric device is attached to a breakwater; however, it is essential to check the performance of the piezoelectric device when placed standalone in ocean waves. Further, the study in Chapter 2 is restricted to the frequency domain, and it's always preferable to see the free surface elevations and plate deflections in the time domain. With these points under consideration, in Chapter 3, the power absorption by a submerged standalone piezoelectric wave energy converter (PWEC) without attaching the same with an existing breakwater is studied in the frequency domain, and the time-dependent displacement of the free surface and the PWEC

plate deflection is discussed. Further, the prediction of power generation by the device and the optimization of the device parameters are studied using an artificial neural network model, namely the multilayer perceptron model. The problem is studied initially for the case when the PWEC plate is situated over an undulated seabed. However, in the parameters optimization process, the seabed is considered uniform in nature as the effect of bottom undulation is negligible. The boundary element method (BEM) is used to solve the frequency domain problem. Further, the Fourier transform is utilized to convert the frequency domain results into the time domain. In time domain analysis, emphasis is given to analyze the plate deflection and the free surface displacement. The input database for the ANN model building is generated using the Latin hypercube sampling method (LHS), and the corresponding target variable is calculated using the BEM-based numerical tool. After the ANN model building, the optimization of the design parameters of the PWEC device is carried out using a database containing 3000 sample points generated randomly using the LHS method. These generated input samples will be passed through the developed ANN model, and the predicted response variable provides a range for the geometric parameters associated with the PWEC device to optimize the power generation.

The PWEC device discussed in Chapter 3 is capable of generating electricity to run low-energy electronics such as LEDs, wireless routers, PCs, ocean buoys, and sensors. Further, the resonances in power generation occur for certain values of incident wave frequencies. However, ocean waves consist of a wider range of frequencies, and therefore, it's necessary to design a wave energy converter device that will work efficiently for a wider range of incident wave frequencies and also can generate higher power. In this regard, the OWC device can serve the purpose. In the 4th chapter, optimization of various parameters associated with a quarter circular shape OWC-WEC device is provided. An artificial neural network model, namely the MLP model, is developed to precisely predict the power generation and consequently to find the optimized parameters of the OWC device, which maximizes the power generation by leveraging the results obtained by the XGBoost model. The XGBoost model is developed to find the various regions of the input space in which the maximum power generation occurs. These specific high-yield regions are identified by studying the effect of each parameter with respect to the response variable using interpretable machine-learning techniques. Initially, the hydrodynamics problem associated with the power generated by the OWC device is solved using the dual BEM. The training, validation, and testing datasets are constructed using the solution of the numerical technique and Latin hypercube sampling technique. The XGBoost model is only used in this chapter to find the first-order local effect and the interaction effect between the parameters and, consequently, to find the high-yield regions. From each region, a big dataset is generated with 20 levels for each variable and then passed through the MLP model to predict the power generation. Consequently, the samples with maximum prediction are identified and verified the prediction by calculating the true value of the input sample.

In Chapters 2-4, the hydrodynamic performance of the standalone piezoelectric plate and OWC device are studied. However, there is one major shortcoming of standalone wave energy converter devices such as the standalone wave energy converter devices which are unable to absorb a significant amount of incident wave energy. By keeping this in mind, in Chapter 5, the hybrid wave energy converter device consists of a piezoelectric plate, and the OWC device is proposed. This hybrid device can broaden the range of the resonating frequencies in power generation. In the 5th chapter, the prediction, inference, and optimization of the design parameters of the hybrid OWC-PWEC device are studied. Firstly, the hydrodynamic problem associated with the interaction of ocean waves with the hybrid WEC device is carried out using the BEM. The input database for the model building is generated using the Latin hypercube sampling technique, and the response variable is calculated using the developed BEM. The present study identifies a suitable ML model from the five different models, namely: MLP (Rumelhart et al. [79], Nguyen and Widrow [80], Werbos [81], Goodfellow et al. [82]), RF (Breiman [83]), XGBoost (Chen and Guestrin [84]), LightGBM (Ke et al. [85]) and CatBoost (Prokhorenkova et al. [86]) models. The most suitable model is selected based on the smallest variance analyzed using a 10-fold cross-validation and the R^2 value obtained using the test datasets. Optimizing hyperparameters prior to training an ML model can significantly enhance both the model's performance and computational efficiency. This process helps in preventing overfitting or underfitting, thereby further refining the model's capabilities. A random search algorithm is implemented to optimize the hyperparameters of the MLP model, and the tree ensemble model's hyperparameters are optimized using the genetic algorithm. The predictive model with minimum error scores and maximum R^2 values is then used to optimize the parameters of the hybrid OWC-PWEC device with the support of interpretable machine-learning approaches. As a preliminary analysis to understand the relationship between the input attributes and the target variable, the Spearman's correlation coefficient is used. The feature importance of the input parameters is studied using the interpretable ML approach, namely the Shapley values. Further, the direct effect of each of the parameters on the response variable is studied using the 1st-order ALE plot, and similarly, the interaction effect is studied using the second-order ALE plots. Using these ALE plots, the specific regions of the input space that maximize the power generation are identified. Finally, the optimization of the input parameters to maximize the power generation by the hybrid OWC-PWEC device is carried out using the method of design of the experiment and the response surface methodology using the L_8 orthogonal array. Finally, the optimal range of parameters of the OWC-PWEC device and the specific values of the input parameters that maximize the total power generation are provided.

Finally, Chapter 6 summarizes the thesis work and discusses future research directions. This chapter highlights the major contributions of the present works. In the next section, the governing equations and boundary conditions associated with the hydrodynamics of PWEC and OWC devices are provided.

1.4 Mathematical modeling of wave-structure interaction problems

1.4.1 Basic equations for linear water wave theory

This section explores the derivations of mathematical equations associated with the linear water waves theory. A two-dimensional Cartesian coordinate framework (x, z) is considered in which x -axis coincides with the direction of the incident wave propagation the z -axis is positive in the vertically upward direction (see Fig. 1.5). The fluid is considered homogeneous, and the fluid motion is incompressible, inviscid, and irrotational in nature. Under these assumptions, the gradient of the velocity potential $\Phi(x, z, t)$ satisfies

$$\mathbf{q} = \nabla\Phi, \quad (1.1)$$

where $\mathbf{q} = (u, w)$ represents the fluid velocity vector. Under these settings, the equation associated with the conservation of mass principle finally modified into the following form

$$\frac{\partial^2\Phi}{\partial x^2} + \frac{\partial^2\Phi}{\partial z^2} = 0. \quad (1.2)$$

The free surface boundary condition arises by combining the kinematic and dynamic boundary

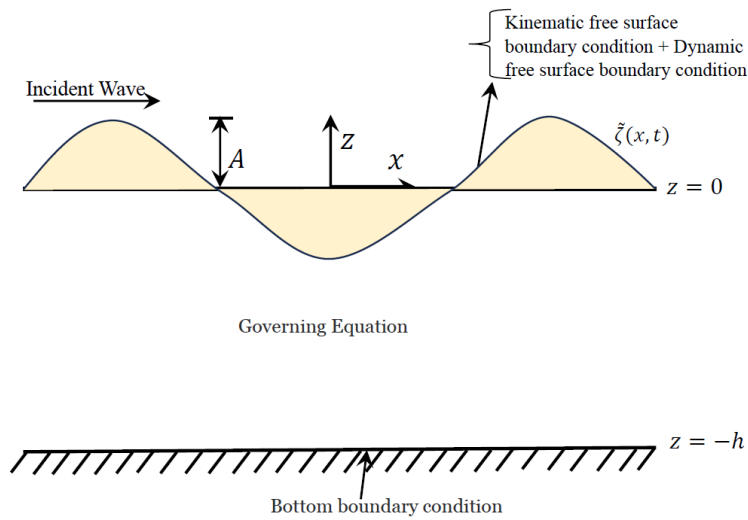


FIGURE 1.5: Schematic diagram of water wave propagation problem

conditions. The kinematic free surface boundary condition (KFBC) is derived under the assumption that there is no gap between the air and water interface along the free surface. On the other hand, the dynamic free surface boundary condition (DFBC) comes from the Bernoulli equation. Let the free surface of the water be represented as $F(x, z, t) = z - \tilde{\zeta}(x, t) = 0$, where $\tilde{\zeta}(x, t)$ represents the free surface about the horizontal line $z = 0$. The KFBC condition implies

that the total derivative of the function F must be zero at the free surface. Therefore we get

$$\frac{DF}{Dt} = 0, \text{ on } z = \tilde{\zeta}(x, t), \quad \frac{D}{Dt} = \frac{\partial}{\partial t} + u \frac{\partial}{\partial x} + w \frac{\partial}{\partial z}. \quad (1.3)$$

Re-arranging Eq. (1.3) in terms of $\Phi(x, z, t)$ and applying the Taylor series to Eq. (1.3) about the mean free surface $z = 0$ yields

$$\begin{aligned} \left(\frac{\partial \Phi}{\partial z} - \frac{\partial \tilde{\zeta}}{\partial t} - \frac{\partial \Phi}{\partial x} \frac{\partial \tilde{\zeta}}{\partial x} \right) \Big|_{z=\tilde{\zeta}} &= \left(\frac{\partial \Phi}{\partial z} - \frac{\partial \tilde{\zeta}}{\partial t} - \frac{\partial \Phi}{\partial x} \frac{\partial \tilde{\zeta}}{\partial x} \right) \Big|_{z=0} \\ &+ \tilde{\zeta} \frac{\partial}{\partial z} \left(\frac{\partial \Phi}{\partial z} - \frac{\partial \tilde{\zeta}}{\partial t} - \frac{\partial \Phi}{\partial x} \frac{\partial \tilde{\zeta}}{\partial x} \right) \Big|_{z=0} + \dots = 0. \end{aligned} \quad (1.4)$$

The amplitude of the incident wave is considered to be significantly smaller as compared to the incident wavelength, i.e., $\tilde{\zeta} \ll 1$. Moreover, within the framework of linearized water wave theory, it is assumed that the fluid particle velocity, surface displacement $\tilde{\zeta}(x, t)$, and their derivatives are all smaller quantities. Consequently, the product and square terms involving $\tilde{\zeta}(x, t)$ and Φ are considerably small. Therefore, neglecting the smaller terms yields the linearized Kinematic Free Surface Boundary Condition (KFBC) at the mean free surface $z = 0$ as the following

$$\frac{\partial \Phi}{\partial z} = \frac{\partial \tilde{\zeta}}{\partial t} \text{ on } z = 0. \quad (1.5)$$

The Bernoulli equation on the free surface $z = \tilde{\zeta}$ is given by

$$\frac{\partial \Phi}{\partial t} + \frac{1}{2}(u^2 + w^2) + \frac{P}{\rho} + gz = 0, \text{ on } z = \tilde{\zeta}(x, t), \quad (1.6)$$

where P is the pressure applied on the free surface $z = \tilde{\zeta}$, ρ is the fluid density, and g is the gravitational acceleration. The pressure P along the interface is considered constant and without the loss of generality it can be taken as zero. Thus, the Bernoulli's equation (1.6) at the interface is rewritten as

$$\frac{\partial \Phi}{\partial t} + \frac{1}{2}(u^2 + w^2) + g\tilde{\zeta} = 0, \text{ on } z = \tilde{\zeta}(x, t). \quad (1.7)$$

Implementing the Taylor series on Eq. (1.7) about $z = 0$ yields

$$\begin{aligned} \left(\frac{\partial \Phi}{\partial t} + \frac{1}{2}(u^2 + w^2) + g\tilde{\zeta} \right) \Big|_{z=\tilde{\zeta}(x, t)} &= \left(\frac{\partial \Phi}{\partial t} + \frac{1}{2}(u^2 + w^2) + g\tilde{\zeta} \right) \Big|_{z=0} \\ &+ \tilde{\zeta} \frac{\partial}{\partial z} \left(\frac{\partial \Phi}{\partial t} + \frac{1}{2}(u^2 + w^2) + g\tilde{\zeta} \right) \Big|_{z=0} + \dots = 0. \end{aligned} \quad (1.8)$$

Retaining the leading order terms as discussed in Eq. (1.4), the DFBC conditions is written as

$$\frac{\partial \Phi}{\partial t} + g\tilde{\zeta} = 0, \text{ on } z = 0. \quad (1.9)$$

On combining Eqs. (1.5) and (1.9), the linearized boundary condition on the mean free surface is written as

$$\frac{\partial^2 \Phi}{\partial t^2} + g \frac{\partial \Phi}{\partial z} = 0, \quad \text{on } z = 0. \quad (1.10)$$

The seabed is considered rigid and impermeable in the present work and therefore, the seabed condition on the uniform seabed profile $z = -h$ is provided as

$$\frac{\partial \Phi}{\partial n} = 0, \quad \text{on } z = -h. \quad (1.11)$$

Here, $\partial/\partial n$ denotes the normal derivative. under the assumption that the fluid motion follows a simple harmonic pattern in time t with angular frequency ω , we get

$$\Phi(x, z, t) = \Re \{ \phi(x, z) e^{-i\omega t} \}, \quad \tilde{\zeta}(x, t) = \Re \{ \tilde{\zeta}(x) e^{-i\omega t} \}, \quad (1.12)$$

Here, $\phi(x, z)$ and $\tilde{\zeta}(x)$ represent the spatial components of the velocity potential and the free surface elevation, respectively. Substituting Eq. (1.12) into Eqs. (1.2), (1.10), and (1.11), we get the following governing equation and boundary conditions

$$\nabla^2 \phi(x, z) = 0, \quad \text{in the fluid regions}, \quad (1.13)$$

$$\frac{\partial \phi}{\partial z} - \frac{\omega^2}{g} \phi = 0, \quad \text{on } z = 0, \quad (1.14)$$

$$\frac{\partial \phi}{\partial n} = 0, \quad \text{at } z = -h. \quad (1.15)$$

The aforementioned boundary value problem (BVP) possess a unique solution if the following Sommerfield radiation conditions or the far-field BCs are implemented (Schot [87])

$$\phi(x, z) \sim \left(A_0 e^{ik_0 x} + B_0 e^{-ik_0 x} \right) \frac{\cosh k_0(z+h)}{\cosh k_0 h}, \quad \text{as } x \rightarrow \pm\infty, \quad (1.16)$$

where the unknown coefficients A_0 and B_0 has to be determined. In Equation (1.16), the wave number k_0 represents the real positive root of the dispersion relation $\omega^2 = gk \tanh kh$. Further, the vertical eigenfunction $\psi_0(z) = \frac{\cosh k_0(z+h)}{\cosh k_0 h}$ satisfies the following property:

$$\int_{-h}^0 \psi_0^2(k_0, z) dz = \frac{2k_0 h + \sinh(2k_0 h)}{4k_0 \cosh^2 k_0 h}, \quad (1.17)$$

The value $k_0 h = 2\pi h/\lambda$ is commonly termed to as the depth-to-wavelength ratio. For long and shallow water waves, the dimensionless wave number follows $k_0 h \ll 1$, while $k_0 h \gg 1$ is considered for short and deep water waves. Accordingly, the corresponding modified dispersion relations are expressed as $\omega^2 = gk^2 h$ (when $k_0 h \ll 1$) and $\omega^2 = gk$ (when $k_0 h \gg 1$). Two important parameters associated with the propagation of water waves are the phase velocity and group velocity. The phase velocity, also known as wave celerity c for a plane progressive wave,

represents the rate at which the waveform propagates and is defined as

$$c = \frac{\lambda}{T} = \frac{\omega}{k_0} = \sqrt{\frac{g}{k_0} \tanh kh}. \quad (1.18)$$

When two progressive waves of identical wave height travel in the same direction with slightly varying wave frequencies and wave numbers, the resulting profile undergoes modulation by a wave envelope. This envelope moves with a velocity denoted as c_g , known as the group velocity. The group velocity c_g is determined as

$$c_g = \frac{d\omega}{dk_0} = \frac{\omega}{2k_0} \left(1 + \frac{2k_0 h}{\sinh(2k_0 h)} \right). \quad (1.19)$$

In the case of potential flow theory, the governing equation for wave-structure interaction problems is typically the Laplace equation. Consequently, investigating fundamental characteristics related to the Laplace equation holds significance. Consider a function ϕ that satisfies the Laplace equation $\nabla^2 \phi = 0$ in a domain Ω bounded by $\partial\Omega$; three types of boundary conditions can be specified on the boundary.

$$\phi|_{\partial\Omega} = f(x), \quad (\text{Dirichlet}), \quad (1.20)$$

$$\left. \frac{\partial\phi}{\partial n} \right|_{\partial\Omega} = g(x), \quad (\text{Neumann}), \quad (1.21)$$

$$a\phi + b \left. \frac{\partial\phi}{\partial n} \right|_{\partial\Omega} = h(x), \quad (\text{Robin BC}). \quad (1.22)$$

The manifestation of ϕ on the surface provides the Cauchy data for the partial differential equation. Solving the PDE under these conditions constitutes a Cauchy problem for the PDE. According to Hadamard, the Cauchy problem is considered well-posed if it satisfies the following conditions: (i) a solution exists, (ii) the solution is unique, and (iii) the solution varies continuously based on the auxiliary data. For a smooth domain Ω , the uniqueness theorem (Folland [88]) is provided as the following

- The Dirichlet problem has at most one solution.
- If u is a solution of the Neumann problem, then any other solution is of the form $v = u + c$, for any $c \in \mathbb{R}$.
- If $a \geq 0$, then the Robin problem has at most one solution.

1.4.2 Basic equations and edge conditions for floating flexible plate type structures

This subsection illustrates the governing equation as well as the associated boundary conditions of a flexible, thin elastic plate by considering the thickness of the plate is very small compared

to the plate length and width. The theories described in the following are solely based on the classical plate theory or the Kirchhoff plate theory. This theory serves as a simplification of the Euler-Bernoulli thin plate theory. The deflection of the flexible elastic plate under the action of ocean waves can be written in the form $\tilde{\xi}(x, z, t) = \Re\{\xi(x, z)e^{-i\omega t}\}$ with $\xi(x, z)$ being a spatial component of the plate deflection. The governing equation of the plate deflection $\xi(x, z, t)$ of an isotropic homogeneous thin elastic plate which deforms slightly in the presence of in-plane compressive forces N_x and N_z along the x and z -directions is given by (see Sahoo [89] for details)

$$EI \left(\frac{\partial^2 \xi}{\partial x^2} + \frac{\partial^2 \xi}{\partial z^2} \right)^2 - \mathcal{N}_x \frac{\partial^2 \xi}{\partial x^2} - \mathcal{N}_z \frac{\partial^2 \xi}{\partial z^2} + m_p \frac{\partial^2 \xi}{\partial t^2} = \mathcal{F}(x, z, t). \quad (1.23)$$

In Eq. (1.23), EI represents the flexural rigidity of the plate, with E being Young's modulus. The plate's inertia I is determined as $I = d_p^3/12(1 - \nu^2)$, wherein d_p signifies the plate's thickness, and ν represents the Poisson ratio. Furthermore, \mathcal{F} denotes the force acting upon the structure. $m_p = \rho_p d_p$ represents the uniform mass per unit area of the plate with ρ_p being the plate's density. For uniform compressive force, we choose $\mathcal{N}_x = \mathcal{N}_z = \mathcal{Q}$. Similarly, in the scenario of a floating membrane structure, $\mathcal{N}_x = \mathcal{N}_z = -\mathcal{T}$ is utilized to depict the uniform tensile force.

Depending on the specific nature of the physical problem, a set of edge conditions must be specified at the two edges of the flexible structures. The fixed edge condition, free edge condition, and mooring edge conditions are used in this thesis to study the variation in the plate characteristics. For the case of fixed edges, the vanishing of plate deflection and the slope of the deflection near both the edges of the plate yield (see Mohapatra et al. [90])

$$\xi = 0, \quad \frac{\partial \xi}{\partial x} = 0. \quad (1.24)$$

For the case of free edges, the vanishing of the bending moment and shear force near the edges of the plate are represented as

$$\frac{\partial^2 \xi}{\partial x^2} + \nu \frac{\partial^2 \xi}{\partial z^2} = 0, \quad EI \left\{ \frac{\partial^3 \xi}{\partial x^3} + (2 - \nu) \frac{\partial^3 \xi}{\partial x \partial z^2} \right\} + \mathcal{Q} \frac{\partial \xi}{\partial x} = 0. \quad (1.25)$$

On the other hand, if the ends of the plate are connected with the mooring chains, the following edge conditions will be considered

$$\frac{\partial^2 \xi}{\partial x^2} + \nu \frac{\partial^2 \xi}{\partial z^2} = 0, \quad EI \left\{ \frac{\partial^3 \xi}{\partial x^3} + (2 - \nu) \frac{\partial^3 \xi}{\partial x \partial z^2} \right\} + \mathcal{Q} \frac{\partial \xi}{\partial x} = q_m \frac{\partial \xi}{\partial x}, \quad (1.26)$$

where q_m is the stiffness constant of the mooring chains (see Sahoo [89]). Here, \mathcal{Q} represents the uniform compressive force.

1.4.3 Basic equations and boundary conditions associated with the piezoelectric wave energy converter device

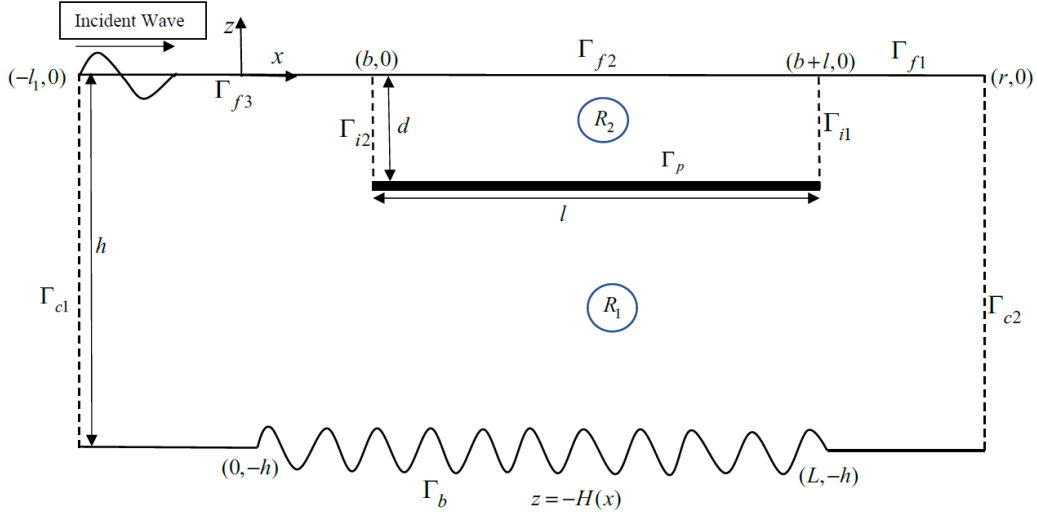


FIGURE 1.6: Schematic of the vertical cross-section of the piezoelectric device.

A flexible floating structure fabricated of bio-compatible soft and flexible piezoelectric materials can generate electricity when mechanical vibrations deform the structure. The piezoelectric wave energy converter device (PWEC) consists of a submerged elastic plate having layers of piezoelectric materials on both sides of the plate, which can extract energy from the ocean waves due to the variations of tension along the plate. Here, the PWEC system is considered to be homogeneous; the stresses, strains, and voltage are continuous along the plate. Hence, the wave energy converter can be modeled as a uniform composite plate based on the Kirchhoff plate theory. The hydroelectromechanical-coupled dynamics associated with the piezoelectric wave energy converter device are considered in the context of linear water wave theory for the sake of mathematical modeling of the piezoelectric plate. In the presence of a submerged floating piezoelectric plate, the fluid domain is divided into two regions R_j ($j = 1, 2$) where $R_2 = \{b < x < b + l, -d < z < 0\}$ and $R_1 = \{-l_1 < x < r, -H(x) < z < 0\} \setminus R_2$ (see Fig. 1.6). The velocity potentials $\Phi_j(x, z, t) = \Re \{\phi_j(x, z)e^{-i\omega t}\}$ associated with regions R_j for $j = 1, 2$ satisfy the Laplace equation (1.13) along with the following boundary conditions. The boundary condition at the mean free surface $z = 0$ is given by

$$\begin{cases} \frac{\partial \phi_1}{\partial n} - K\phi_1 = 0, & \text{on } \Gamma_{f1} \cup \Gamma_{f3}, \\ \frac{\partial \phi_2}{\partial n} - K\phi_2 = 0, & \text{on } \Gamma_{f2}. \end{cases} \quad (1.27)$$

Now, the boundary condition on the rigid and impermeable bottom Γ_2 is given by

$$\frac{\partial \phi_1}{\partial n} = 0, \quad \text{on } \Gamma_b. \quad (1.28)$$

The continuity of pressure and normal velocities along the two fictitious boundaries Γ_{i1} and Γ_{i2} positioned at $x = b + l$ and $x = b$, respectively are given by

$$\phi_1 = \phi_2, \quad \text{and} \quad \frac{\partial \phi_1}{\partial n} = -\frac{\partial \phi_2}{\partial n} \quad \text{on} \quad \Gamma_{i1} \cup \Gamma_{i2}. \quad (1.29)$$

The dynamic boundary condition on the piezoelectric plate $\Gamma_p = \{b < x < b + l, z = -d\}$ is given by

$$g\chi \left[1 + \frac{\beta^2 \varphi \omega}{i + \varphi \omega} \right] \frac{\partial^4 \xi}{\partial x^4} - \omega^2 \gamma \xi = i\omega (\phi_1 - \phi_2), \quad \text{on} \quad \Gamma_p, \quad (1.30)$$

where the expressions for χ , β , φ , and γ are given as

$$\chi = \frac{B}{\rho g}, \quad \beta = \frac{\theta}{\sqrt{BC}}, \quad \varphi = \frac{C}{V}, \quad \gamma = \frac{I_b}{\rho}, \quad (1.31)$$

where B , θ , C and V represent the flexural rigidity of the PWEC plate, piezoelectric coupling factor, electrical surface capacitance, and surface conductance, respectively. Further, I_b represents the surface density of the bimorph. Now, the linearized kinematic boundary condition on the plate Γ_p is given by

$$\frac{\partial \phi_1}{\partial n} = \frac{\partial \phi_2}{\partial n} = -i\omega \xi, \quad \text{on} \quad \Gamma_p. \quad (1.32)$$

For the plate having fixed edges, vanishing of plate displacement and the slope of the displacement near both the edges of the plate yield

$$\xi = 0, \quad \frac{\partial \xi}{\partial x} = 0, \quad \text{at} \quad x = b, b + l, \quad z = -d. \quad (1.33)$$

Similarly, when the plate edges are free, the edge conditions are given by

$$\frac{\partial^2 \xi}{\partial x^2} = 0, \quad \frac{\partial^3 \xi}{\partial x^3} = 0, \quad \text{at} \quad x = b, b + l, \quad z = -d. \quad (1.34)$$

Further, the edge conditions of a plate which is moored to the seabed is given by

$$\frac{\partial^2 \xi}{\partial x^2} = 0, \quad \rho g \chi \left[1 + \frac{\beta^2 \varphi \omega}{i + \varphi \omega} \right] \frac{\partial^3 \xi}{\partial x^3} = q \xi, \quad \text{at} \quad x = b, b + l, \quad (1.35)$$

where q represents mooring stiffness.

1.4.4 Governing equation and boundary conditions associated with the modeling of oscillating water column wave energy converter device

The oscillating water column (OWC) device consists of an open-ended, hollow structure with a downward-facing open end that is partially submerged to trap air above the internal free surface (see Fig. 1.7). The power take-off (PTO) system of the OWC device consists of a Wells turbine positioned at the top wall of the chamber to prevent it from coming into direct contact with

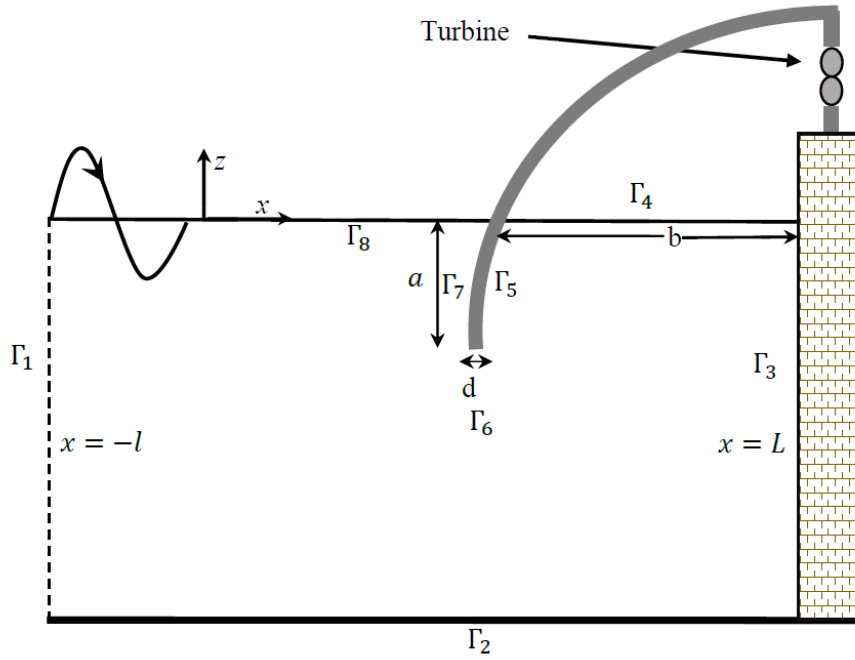


FIGURE 1.7: Schematic diagram of the vertical cross-section of the OWC device.

salt water. In the presence of the ocean waves, the internal free surface oscillates with the same angular frequency ω as the incident wave, and consequently establishing a uniform pressure distribution over the internal free surface Γ_4 . The fluid motion is characterized by the velocity potential $\Phi(x, z, t)$, which satisfies Eq. (1.2). The linearized free surface condition is represented as

$$\frac{\partial \Phi}{\partial t} + g\tilde{\zeta} = \begin{cases} -\frac{P(t)}{\rho}, & \text{on } \Gamma_4 \\ 0, & \text{on } \Gamma_8. \end{cases} \quad (1.36)$$

Here, $P(t)$ is termed as uniformly distributed pressure acting on the internal free surface Γ_4 . Further, the boundary conditions on the rigid and impenetrable boundaries are provided as the following

$$\frac{\partial \Phi}{\partial n} = 0, \quad \text{on } \Gamma_2 \cup \Gamma_3 \cup \Gamma_5 \cup \Gamma_6 \cup \Gamma_7. \quad (1.37)$$

With the assumption that the motion of the fluid is simple harmonic in time t with angular frequency ω , the velocity potential $\Phi(x, z, t)$ and the pressure $P(t)$ are written as

$$\begin{cases} \Phi(x, z, t) = \Re \{ \phi(x, z) e^{-i\omega t} \}, \\ P(t) = \Re \{ p e^{-i\omega t} \}, \end{cases} \quad (1.38)$$

Substituting the expressions (1.38) into Eq. (1.36), and using (1.5) and (1.9), we get

$$\frac{\partial \phi}{\partial z} - K\phi = \begin{cases} \frac{i\omega p}{\rho g}, & \text{on } \Gamma_4, \\ 0, & \text{on } \Gamma_8, \end{cases} \quad (1.39)$$

where $K = \omega^2/g$. In addition, implementing (1.38) into Eq. (1.37), we obtain

$$\frac{\partial \phi}{\partial n} = 0, \quad \text{on } \Gamma_2 \cup \Gamma_3 \cup \Gamma_5 \cup \Gamma_6 \cup \Gamma_7. \quad (1.40)$$

In the presence of the OWC device, the velocity potential ϕ can be decomposed into the scattered and radiated velocity potentials, and therefore, the total velocity potential can be written as

$$\phi = \phi^S + \left(\frac{i\omega p}{\rho g} \right) \phi^R, \quad (1.41)$$

where ϕ^S and ϕ^R represent the scattered and radiated velocity potentials, respectively. Furthermore, the scattered velocity potential ϕ^S is expressed as the sum of incident velocity potential ϕ^I and diffracted velocity potential ϕ^D . During the interaction of water waves with the OWC device, the incoming waves are reflected by the rigid wall boundaries of the OWC device. As a result, the scattered velocity potential appears. Further, the radiated velocity potential appears due to the oscillation of the water column within the OWC device chamber. Here, $\phi^{S,R}$ satisfy the Eqs. (1.13), (1.39) and (1.40). It is to be noted that substituting the expression (1.41) into Eq. (1.39), we get

$$\begin{cases} \frac{\partial \phi^S}{\partial z} - K\phi^S = 0, & \text{on } \Gamma_4 \cup \Gamma_8, \\ \frac{\partial \phi^R}{\partial z} - K\phi^R = \begin{cases} 1, & \text{on } \Gamma_4, \\ 0, & \text{on } \Gamma_8. \end{cases} \end{cases} \quad (1.42)$$

Finally, the far-field boundary conditions on Γ_1 are given by

$$\begin{cases} \phi^S(x, z) = e^{ik_0 x} \psi_0(k_0, z) + A_0^S e^{-ik_0 x} f_0(k_0, z), & \text{as } x \rightarrow -\infty, \\ \phi^R(x, z) = A_0^R e^{-ik_0 x} \psi_0(k_0, z), & \text{as } x \rightarrow -\infty, \end{cases} \quad (1.43)$$

with A_0^S and A_0^R being the coefficients associated with the reflected and radiated wave amplitudes, respectively, as $x \rightarrow -\infty$. In Eq. (1.43), the expression for vertical eigenfunction $\psi_0(k_0, z)$ is given by $\psi_0(k_0, z) = -\left(\frac{igA}{\omega} \right) \frac{\cosh k_0(h+z)}{\cosh(k_0 h)}$ with A represents the incident wave amplitude.

1.5 Fundamentals of integral equations

An integral equation generally involves the unknown function appearing under one or more integral signs. An integral equation can be written in its most general form as

$$\alpha(x)h(x) = f(x) + \lambda \int_a^{\quad} \mathcal{K}(x, t)h(t)dt, \quad (1.44)$$

where the upper limit of the integration is either a fixed number or a variable. The functions $\alpha(x)$, $f(x)$ and $\mathcal{K}(x, t)$ (kernel) are known functions, while $h(x)$ is an unknown function that has to be determined. Here, λ is a non-zero real or complex parameter. The classifications for integral equations are as follows

- **Fredholm integral equations :** The integral equation is known as a Fredholm integral equation if the upper limit of integration in Eq. (1.44) is a constant (say b).

- In Eq. (1.44), if $\alpha(x) = 0$ then the integral equation is termed as the Fredholm integral equation of first kind and the associated form is given as

$$f(x) + \lambda \int_a^b \mathcal{K}(x, t)h(t)dt = 0.$$

- In Eq. (1.44), if $\alpha(x) = 1$ then the integral equation is termed as the Fredholm integral equation of second kind and the associated form is given as

$$h(x) = f(x) + \lambda \int_a^b \mathcal{K}(x, t)h(t)dt.$$

In the aforementioned forms, if $f(x) = 0$, it is called the homogeneous Fredholm integral equation of second kind. Thus, the homogeneous form is written as

$$h(x) = \lambda \int_a^b \mathcal{K}(x, t)h(t)dt.$$

- **Volterra integral equations :** The homogeneous, first, and second types of Volterra integral equations are defined in the same way as Fredholm integral equations with the upper limit b is replaced by x .

- In Eq. (1.44), if $\alpha(x) = 0$ then the integral equation is termed as the Volterra integral equation of first kind and the form is given by

$$f(x) + \lambda \int_a^x \mathcal{K}(x, t)h(t)dt = 0.$$

- In Eq. (1.44), if $\alpha(x) = 1$ then the integral equation is termed as the Volterra integral equation of second kind and the form is given by

$$h(x) = f(x) + \lambda \int_a^x \mathcal{K}(x, t)h(t)dt.$$

In the aforementioned forms of the integral equations, if $f(x) = 0$, it is called as the homogeneous Volterra integral equation of second kind. Thus,

$$h(x) = \lambda \int_a^x \mathcal{K}(x, t)h(t)dt.$$

- **Singular integral equations** : The integral equation is said to be singular when either the upper or lower limit of integration becomes infinite, or when the kernel approaches infinity at one or more points within the range of integration.

1.6 Boundary element method (BEM)

This section provides a brief overview of the boundary element method (BEM) for solving the two-dimensional Laplace equation (see Brebbia et al. [91] for details). The BEM is a widely used numerical tool for solving boundary and initial value problems that appeared in computational mechanics. To transform the boundary value problem into integral equations, the free space Green's function or the fundamental solution of the underlying differential operator is required.

1.6.1 Fundamental solution of the Laplace equation and Green's second identity

The free-space Green's function associated with the two-dimensional Laplace equation is given by (see Ang [92] for details)

$$G(\mathbf{x}, \mathbf{s}) = \frac{1}{2\pi} \ln \tilde{r}, \quad \tilde{r} = |\mathbf{x} - \mathbf{s}|. \quad (1.45)$$

For any two scalar functions f and g which are continuous in the domain Ω having boundary Γ , the Green's second identity is provided as

$$\int_{\Omega} (f\nabla^2 g - g\nabla^2 f) d\Omega = \int_{\Gamma} \left(f \frac{\partial g}{\partial n} - g \frac{\partial f}{\partial n} \right) d\Gamma, \quad (1.46)$$

where ∇^2 is the two-dimensional Laplacian operator.

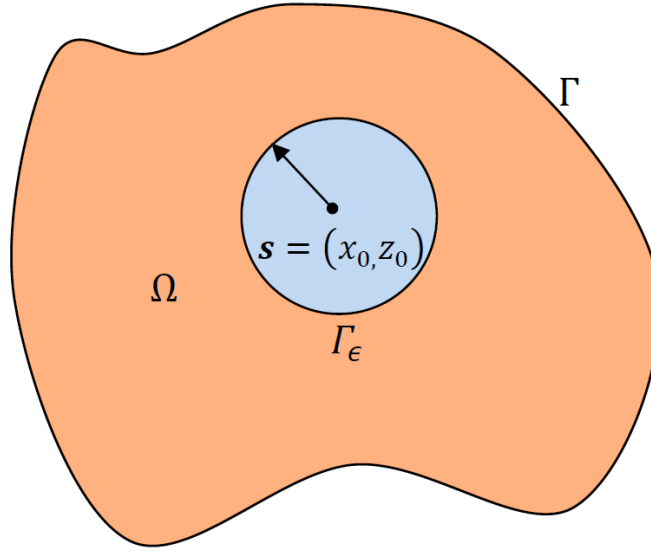


FIGURE 1.8: Cross-section of the domain Ω bounded by Γ

1.6.2 Formulation of the boundary integral equations

Applying the Green's second identity on the velocity potential $\phi(\mathbf{x})$ and the free space Green's function $G(\mathbf{x}, \mathbf{s})$ over the domain Ω bounded by Γ (see Fig. 1.8), we get the following boundary integral equation (see Ang [92], Brebbia et al. [91] for more details)

$$c(\mathbf{s})\phi(\mathbf{s}) = \int_{\Gamma} \left(\phi \frac{\partial G}{\partial n} - G \frac{\partial \phi}{\partial n} \right) d\Gamma, \quad (1.47)$$

where

$$c(\mathbf{s}) = \begin{cases} 0, & \text{if } \mathbf{s} \notin D \cup \Gamma, \\ \frac{1}{2}, & \text{if } \mathbf{s} \in \Gamma, (\Gamma - \text{smooth}), \\ \frac{\alpha}{2\pi}, & \text{if } \mathbf{s} \in \Gamma, (\Gamma - \text{non-smooth}). \end{cases} \quad (1.48)$$

Here, α is the aperture angle. The subsequent section will illustrate briefly the discretization of the aforementioned integral equation to convert the same into a system of linear algebraic equations. It is to be noted that the constant element approach is used in the present work.

1.6.3 Discretization of boundary integral equations using constant element approach

In the first step of BEM, the surface boundary is discretized into a finite number of segments (termed as boundary elements). Thus, we can write the total surface boundary Γ as (see Fig. 1.9)

$$\Gamma = \bigcup_{i=1}^N \Gamma_i, \quad (1.49)$$

In the present approach, the values of ϕ and its normal derivative $\partial\phi/\partial n$ are considered as

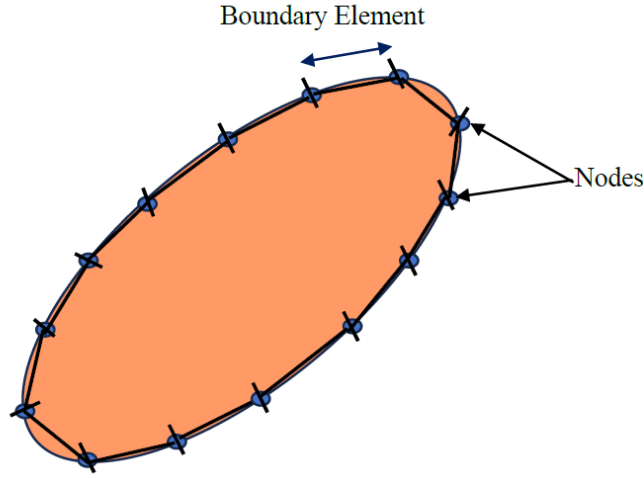


FIGURE 1.9: Discretization of the boundary using constant elements.

constants over each boundary element, and these values are considered at the midpoint (node) on each boundary element (see Ang [93], Brebbia et al. [91], for more details). For smooth boundaries, $c(\mathbf{s}) = 1/2$. Under these assumptions, the discretized form of Eq. (1.47) for i^{th} boundary element is written as

$$-\frac{1}{2}\phi_i + \sum_{j=1}^N \int_{\Gamma_j} \left(\phi \frac{\partial G}{\partial n} \right) d\Gamma = \sum_{j=1}^N \int_{\Gamma_j} \left(G \frac{\partial \phi}{\partial n} \right) d\Gamma. \quad (1.50)$$

Since ϕ and $\partial\phi/\partial n$ are constants over each boundary element, Eq. (1.50) is re-written as

$$-\frac{1}{2}\phi_i + \sum_{j=1}^N \phi_j \left(\int_{\Gamma_j} \frac{\partial G}{\partial n} d\Gamma \right) = \sum_{j=1}^N \frac{\partial \phi_j}{\partial n} \int_{\Gamma_j} G d\Gamma. \quad (1.51)$$

Now, Eq. (1.51) contains the terms that involve the integral over the fundamental solutions and its normal derivative. These terms are known as the influence coefficients and are written as the following

$$H_{ij} = -\frac{1}{2}\delta_{ij} + \int_{\Gamma_j} \frac{\partial G}{\partial n} d\Gamma, \quad G_{ij} = \int_{\Gamma_j} G d\Gamma. \quad (1.52)$$

The evaluation of these influence coefficients are provided in the following section.

1.6.4 Evaluation of influence coefficients

The line integral appears in Eq. (1.52) can be evaluated analytically for $i = j$ as the following (see Brebbia et al. [91] for details)

$$\int_{\Gamma_j} G d\Gamma = \frac{l_j}{2\pi} \left[\ln \left(\frac{l_j}{2} \right) - 1 \right], \quad (1.53)$$

with l_j being the length of j^{th} boundary element, and

$$\int_{\Gamma_j} \frac{\partial G}{\partial n} d\Gamma = 0. \quad (1.54)$$

On the other hand, for $i \neq j$ case, the standard Gauss–Legendre quadrature formula is used to evaluate the influence coefficients (see Brebbia et al. [91] for details). Now, Eq. (1.51) is re-written as

$$\sum_{j=1}^N H_{ij} \phi_j = \sum_{j=1}^N G_{ij} \frac{\partial \phi_j}{\partial n}. \quad (1.55)$$

In order to generate the number of equations equal to the number of unknowns N , the point collocation method is used in which the singular point (\mathbf{s}) runs over each node $i = 1, 2, \dots, N$. In matrix form, Eq. (1.55) can be written as

$$\begin{bmatrix} H_{11} & H_{12} & H_{13} & \dots & H_{1N} \\ H_{21} & H_{22} & H_{23} & \dots & H_{2N} \\ \dots & \dots & \dots & \dots & \dots \\ H_{N1} & H_{N2} & H_{N3} & \dots & H_{NN} \end{bmatrix} \begin{bmatrix} \phi_1 \\ \phi_2 \\ \vdots \\ \phi_N \end{bmatrix} = \begin{bmatrix} G_{11} & G_{12} & G_{13} & \dots & G_{1N} \\ G_{21} & G_{22} & G_{23} & \dots & G_{2N} \\ \vdots & \vdots & \vdots & \ddots & \vdots \\ G_{N1} & G_{N2} & G_{N3} & \dots & G_{NN} \end{bmatrix} \begin{bmatrix} \frac{\partial \phi_1}{\partial n} \\ \frac{\partial \phi_2}{\partial n} \\ \vdots \\ \frac{\partial \phi_N}{\partial n} \end{bmatrix}. \quad (1.56)$$

In order to solve the linear system of equations, it is required to shuffle the columns of the matrix in an appropriate manner. Once all the unknown quantities are shifted to the left-hand side, one can write the system (1.56) as

$$[A]\{X\} = \{Y\}, \quad (1.57)$$

where X is a vector consisting of the unknowns ϕ and $\partial\phi/\partial n$. This system of equations is solved to determine the required unknowns ϕ and $\partial\phi/\partial n$.

The BEM is an efficacious tool to solve the boundary and initial value problems and has the advantage of reducing the unknowns by order one. For problems with degenerate boundaries, the aforementioned BEM has rank deficiency difficulties with influence matrices. Dual BEM is

widely used to address the aforementioned rank deficiency issues. A brief procedure of the dual BEM is provided in the following section.

1.7 Dual boundary element method (DBEM)

In DBEM, the BVP is converted into a system of integral equations using the appropriate Green's function. Applying Green's third identity to the velocity potentials $\phi(\mathbf{x})$ and the free-space Green's function $G(\mathbf{x}, \mathbf{s})$ over the domain Ω bounded by Γ , the following boundary integral equation is derived

$$\phi(\mathbf{x}) = \int_{\Gamma} \left[\phi(\mathbf{s})V(\mathbf{x}, \mathbf{s}) - G(\mathbf{x}, \mathbf{s}) \frac{\partial \phi(\mathbf{s})}{\partial n_{\mathbf{s}}} \right] d\Gamma(\mathbf{s}), \quad \mathbf{x} \in \Omega, \quad (1.58)$$

where

$$V(\mathbf{x}, \mathbf{s}) \equiv \frac{\partial G(\mathbf{x}, \mathbf{s})}{\partial n_{\mathbf{s}}}. \quad (1.59)$$

In Eq. (1.59), the free-space Green's function $G(\mathbf{x}, \mathbf{s})$ remains same as given in Eq. (1.45).

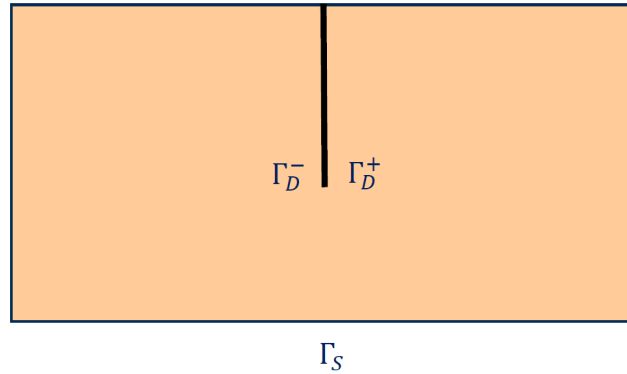


FIGURE 1.10: Domain consists of non-degenerate boundary Γ_S and degenerate boundary Γ_D .

Now, the normal derivative of Eq. (1.58) results into

$$\frac{\partial \phi(\mathbf{x})}{\partial n_{\mathbf{x}}} = \int_{\Gamma} \left[N(\mathbf{x}, \mathbf{s}) \phi(\mathbf{s}) - M(\mathbf{x}, \mathbf{s}) \frac{\partial \phi(\mathbf{s})}{\partial n_{\mathbf{s}}} \right] d\Gamma(\mathbf{s}), \quad \mathbf{x} \in \Omega, \quad (1.60)$$

where

$$M(\mathbf{x}, \mathbf{s}) \equiv \frac{\partial G(\mathbf{x}, \mathbf{s})}{\partial n_{\mathbf{x}}}, \quad N(\mathbf{x}, \mathbf{s}) \equiv \frac{\partial^2 G(\mathbf{x}, \mathbf{s})}{\partial n_{\mathbf{x}} \partial n_{\mathbf{s}}}. \quad (1.61)$$

When the field point $\mathbf{x} \in \Gamma$, Eqs. (1.58) and (1.60) can be written as

$$\frac{1}{2} \phi(\mathbf{x}) = CPV \int_{\Gamma} V(\mathbf{x}, \mathbf{s}) \phi(\mathbf{s}) d\Gamma(\mathbf{s}) - RPV \int_{\Gamma} G(\mathbf{x}, \mathbf{s}) \frac{\partial \phi(\mathbf{s})}{\partial n_{\mathbf{s}}} d\Gamma(\mathbf{s}), \quad \mathbf{x} \in \Gamma, \quad (1.62)$$

$$\frac{1}{2} \frac{\partial \phi(\mathbf{x})}{\partial n_{\mathbf{x}}} = HPV \int_{\Gamma} N(\mathbf{x}, \mathbf{s}) \phi(\mathbf{s}) d\Gamma(\mathbf{s}) - CPV \int_{\Gamma} M(\mathbf{x}, \mathbf{s}) \frac{\partial \phi(\mathbf{s})}{\partial n_{\mathbf{s}}} d\Gamma(\mathbf{s}), \quad \mathbf{x} \in \Gamma. \quad (1.63)$$

Here, *RPV*, *CPV*, and *HPV* are termed as the Riemann principal value, Cauchy principal value, and Hadamard principal value, respectively. In Eqs. (1.62) and (1.63), the total boundary Γ can be written as $\Gamma = \Gamma_S + \Gamma_D^+ + \Gamma_D^-$ with Γ_S represents the non-degenerate boundary, and Γ_D^+ and Γ_D^- are the degenerate boundaries (see Fig. 1.10). Now, for $\mathbf{x} \in \Gamma_S$, Eqs. (1.62) and (1.63) reduced into the following forms (see Trivedi et al. [94] and Chen et al. [95] for details)

$$\begin{aligned} \frac{1}{2}\phi(\mathbf{x}) &= CPV \int_{\Gamma_S} V(\mathbf{x}, \mathbf{s}) \phi(\mathbf{s}) d\Gamma(\mathbf{s}) - RPV \int_{\Gamma_S} G(\mathbf{x}, \mathbf{s}) \frac{\partial\phi(\mathbf{s})}{\partial n_{\mathbf{s}}} d\Gamma(\mathbf{s}) \\ &+ \int_{\Gamma_D^+} V(\mathbf{x}, \mathbf{s}) \Delta\phi(\mathbf{s}) d\Gamma(\mathbf{s}) - \int_{\Gamma_D^+} G(\mathbf{x}, \mathbf{s}) \sum \frac{\partial\phi(\mathbf{s})}{\partial n_{\mathbf{s}}} d\Gamma(\mathbf{s}), \end{aligned} \quad (1.64)$$

$$\begin{aligned} \frac{1}{2} \frac{\partial\phi(\mathbf{x})}{\partial n_{\mathbf{x}}} &= HPV \int_{\Gamma_S} N(\mathbf{x}, \mathbf{s}) \phi(\mathbf{s}) d\Gamma(\mathbf{s}) - CPV \int_{\Gamma_S} M(\mathbf{x}, \mathbf{s}) \frac{\partial\phi(\mathbf{s})}{\partial n_{\mathbf{s}}} d\Gamma(\mathbf{s}) \\ &+ \int_{\Gamma_D^+} N(\mathbf{x}, \mathbf{s}) \Delta\phi(\mathbf{s}) d\Gamma(\mathbf{s}) - \int_{\Gamma_D^+} M(\mathbf{x}, \mathbf{s}) \sum \frac{\partial\phi(\mathbf{s})}{\partial n_{\mathbf{s}}} d\Gamma(\mathbf{s}), \end{aligned} \quad (1.65)$$

where

$$\Delta\phi(\mathbf{s}) \equiv \phi(\mathbf{s}^+) - \phi(\mathbf{s}^-), \quad (1.66)$$

$$\sum \frac{\partial\phi(\mathbf{s})}{\partial n} \equiv \frac{\partial\phi(\mathbf{s}^+)}{\partial n} + \frac{\partial\phi(\mathbf{s}^-)}{\partial n}. \quad (1.67)$$

For $\mathbf{x} \in \Gamma_D^+$, Eqs. (1.62) and (1.63) are reduced into the following forms

$$\begin{aligned} \frac{1}{2} \sum \phi(\mathbf{x}) &= CPV \int_{\Gamma_D^+} V(\mathbf{x}, \mathbf{s}) \Delta\phi(\mathbf{s}) d\Gamma(\mathbf{s}) - RPV \int_{\Gamma_D^+} G(\mathbf{x}, \mathbf{s}) \sum \frac{\partial\phi(\mathbf{s})}{\partial n_{\mathbf{s}}} d\Gamma(\mathbf{s}) \\ &+ \int_{\Gamma_S} V(\mathbf{x}, \mathbf{s}) \phi(\mathbf{s}) d\Gamma(\mathbf{s}) - \int_{\Gamma_S} G(\mathbf{x}, \mathbf{s}) \frac{\partial\phi(\mathbf{s})}{\partial n_{\mathbf{s}}} d\Gamma(\mathbf{s}), \end{aligned} \quad (1.68)$$

$$\begin{aligned} \frac{1}{2} \Delta \frac{\partial\phi(\mathbf{x})}{\partial n_{\mathbf{x}}} &= HPV \int_{\Gamma_D^+} N(\mathbf{x}, \mathbf{s}) \Delta\phi(\mathbf{s}) d\Gamma(\mathbf{s}) - CPV \int_{\Gamma_D^+} M(\mathbf{x}, \mathbf{s}) \sum \frac{\partial\phi(\mathbf{s})}{\partial n_{\mathbf{s}}} d\Gamma(\mathbf{s}) \\ &+ \int_{\Gamma_S} N(\mathbf{x}, \mathbf{s}) \phi(\mathbf{s}) d\Gamma(\mathbf{s}) - \int_{\Gamma_S} M(\mathbf{x}, \mathbf{s}) \frac{\partial\phi(\mathbf{s})}{\partial n_{\mathbf{s}}} d\Gamma(\mathbf{s}), \end{aligned} \quad (1.69)$$

where

$$\sum \phi(\mathbf{s}) \equiv \phi(\mathbf{s}^+) + \phi(\mathbf{s}^-), \quad (1.70)$$

$$\Delta \frac{\partial\phi}{\partial n}(\mathbf{s}) \equiv \frac{\partial\phi}{\partial n}(\mathbf{s}^+) - \frac{\partial\phi}{\partial n}(\mathbf{s}^-). \quad (1.71)$$

It is to be noted that in Eqs. (1.66)-(1.67) and (1.70)-(1.71), the number of unknowns on the degenerate boundaries is double as compared to the unknowns on the non-degenerate boundaries. Therefore, the integral equation (1.60) is necessary to obtain unique solutions. By discretizing

the boundaries Γ of the domain using the constant boundary element method and varying the field point \mathbf{x} over each boundary element, we get the following system of equations (see Chen et al. [96])

$$[\tilde{V}_{ij}] \{\phi_j\} = [G_{ij}] \left\{ \left(\frac{\partial \phi}{\partial n} \right)_j \right\}, \quad (1.72)$$

$$[N_{ij}] \{\phi_j\} = [\tilde{M}_{ij}] \left\{ \left(\frac{\partial \phi}{\partial n} \right)_j \right\}, \quad (1.73)$$

where the influence coefficients G_{ij} , \tilde{V}_{ij} , \tilde{M}_{ij} and N_{ij} are given by

$$G_{ij} = RPV \int_{\Gamma_j} G(\mathbf{x}_i, \mathbf{s}_j) d\Gamma(\mathbf{s}_j), \quad (1.74)$$

$$\tilde{V}_{ij} = -\frac{1}{2}\delta_{ij} + CPV \int_{\Gamma_j} V(\mathbf{x}_i, \mathbf{s}_j) d\Gamma(\mathbf{s}_j), \quad (1.75)$$

$$\tilde{M}_{ij} = \frac{1}{2}\delta_{ij} + CPV \int_{\Gamma_j} M(\mathbf{x}_i, \mathbf{s}_j) d\Gamma(\mathbf{s}_j), \quad (1.76)$$

$$N_{ij} = HPV \int_{\Gamma_j} N(\mathbf{x}_i, \mathbf{s}_j) d\Gamma(\mathbf{s}_j). \quad (1.77)$$

When the field point \mathbf{x}_i and the source point \mathbf{s}_j lies on the different boundary element, the well-known Gauss-Legendre quadrature is used to evaluate the aforementioned influence coefficients. On the other hand, when the field point \mathbf{x}_i and the source point \mathbf{s}_j lies on the same boundary element, singularity occurs, and special treatment is required to evaluate the influence coefficients. Now, two different approaches $GV + MN$ and $MN + GV$ are available to solve the unknowns. In the present work, $GV + MN$ approach is adopted. In this approach, the following system of equations is obtained (Chen et al. [95])

$$\begin{bmatrix} V_{i_{\Gamma_S} j_{\Gamma_S}} & V_{i_{\Gamma_S} j_{\Gamma_D^+}} & V_{i_{\Gamma_S} j_{\Gamma_D^-}} \\ V_{i_{\Gamma_D^+} j_{\Gamma_S}} & V_{i_{\Gamma_D^+} j_{\Gamma_D^+}} & V_{i_{\Gamma_D^+} j_{\Gamma_D^-}} \\ N_{i_{\Gamma_D^+} j_{\Gamma_S}} & N_{i_{\Gamma_D^+} j_{\Gamma_D^+}} & N_{i_{\Gamma_D^+} j_{\Gamma_D^-}} \end{bmatrix} \begin{Bmatrix} \phi_{j_{\Gamma_S}} \\ \phi_{j_{\Gamma_D^+}} \\ \phi_{j_{\Gamma_D^-}} \end{Bmatrix} = \begin{bmatrix} G_{i_{\Gamma_S} j_{\Gamma_S}} & G_{i_{\Gamma_S} j_{\Gamma_D^+}} & G_{i_{\Gamma_S} j_{\Gamma_D^-}} \\ G_{i_{\Gamma_D^+} j_{\Gamma_S}} & G_{i_{\Gamma_D^+} j_{\Gamma_D^+}} & G_{i_{\Gamma_D^+} j_{\Gamma_D^-}} \\ M_{i_{\Gamma_D^+} j_{\Gamma_S}} & M_{i_{\Gamma_D^+} j_{\Gamma_D^+}} & M_{i_{\Gamma_D^+} j_{\Gamma_D^-}} \end{bmatrix} \begin{Bmatrix} \left[\frac{\partial \phi}{\partial n} \right]_{j_{\Gamma_S}} \\ \left[\frac{\partial \phi}{\partial n} \right]_{j_{\Gamma_D^+}} \\ \left[\frac{\partial \phi}{\partial n} \right]_{j_{\Gamma_D^-}} \end{Bmatrix}. \quad (1.78)$$

The system of equations (1.78) is solved using boundary conditions as provided in the given problem to get the unknowns ϕ and $\partial\phi/\partial n$ over each boundary element.

1.8 Artificial neural networks

1.8.1 Background

Artificial Neural Networks (ANNs) are computational modeling tools that have gained widespread recognition across various fields for tackling complex real-world problems. These networks can be characterized as architecture consisting of densely connected adaptive elementary processing units known as artificial neurons. These neurons exhibit the capability to conduct highly parallel computations, facilitating effective data processing and knowledge representation (Basheer and Hajmeer [97]). Extensive research has been conducted on this deep learning paradigm. The historical roots of Artificial Neural Networks (ANNs) trace back to pioneering studies (Hubel and Wiesel [98, 99, 100]) which unveiled that the brain is composed of specialized cells known as neurons interconnected within a network. Every individual brain cell operates through electrical signals. It consists of multiple inputs, referred to as dendrites, a central region known as the soma, and an output termed as the axon, which interacts with the dendrites of the neighboring cells. These connections are commonly referred to as synapses. The strength and nature of these connections, such as stimulating or inhibiting, are regulated by chemical messengers called neurotransmitters. The neuron exhibits activity by producing electrical impulses, often termed as spikes, along its axon when the cumulative impact of its inputs exceeds a specific threshold. The efficacy of synaptic connections is observed to enhance when they receive sustained stimulation from incoming electrical signals originating from other interconnected neurons (Bruner [101], Hebb [102], Rochester et al. [103]). This concept inspired the investigation into the development of artificial networks that replicate the functionalities and learning capabilities of the human brain. The motivation behind developing the ANN model is to leverage the functionalities of biological systems for addressing complex real-world issues. A few of the significant advantages of the ANN models are massively parallel computations, handling nonlinearity, and the ability to handle fuzzy information (Basheer and Hajmeer [97]).

1.8.2 The multilayer perceptron model

The multilayer perceptron is the well-known and most frequently used type of neural network. The multilayer perceptron is characterized by a neuron model, a network architecture, associated objective function, and training algorithms. These four concepts are briefly described in the following.

- **Neuron model:** A neuron serves as the fundamental building block in a neural network model, and a neuron model is a mathematical representation capturing the behavior of an individual neuron within a biological nervous system. In the multilayer perceptron, a

neuron model is known as the perceptron. Within this model, the neuron receives input information as numerical data. Subsequently, this information is combined with a set of model parameters to generate a numerical output value, i.e., each neuron in an MLP model is a function that receives input from the previous layer. It multiplies with the associated weight, and a bias associated with the layer will be added to it.

- **Network architecture:** Like the model of a biological nervous system comprising interconnected biological neurons, an artificial neural network is constructed by arranging artificial neurons in a network architecture. This architectural arrangement contains a specific number of layers, each consisting of a specific number of neurons, their arrangement, and the connections between them. These architectures are commonly represented as directed graphs, where nodes represent neurons and edges illustrate their connections. The label on each edge signifies the neuron's model parameter, specifically the weights. The architecture of the MLP consists of three important layers: an input layer, multiple hidden layers, and an output layer. The input layer receives the inputs from the database, and the output layer will produce the outputs or the prediction values. The number of hidden layers and the number of neurons in each of the hidden layers define the depth of the model.
- **Objective function:** It defines the task that the neural network performs and offers a measure of the output quality the network needs to acquire. The selection of an appropriate objective function depends upon the specific application.
- **Training algorithm:** The training algorithm type defines how the adjustment of model parameters, such as weights and biases in the neural network, is done.

1.8.3 The elements of a perceptron model

Let the input dataset is defined as $X = \{X^{(i)} \mid i = 1, 2, \dots, M\}$. Then the two fundamental components of a perceptron model that convert a single input sample $X^{(i)} = \{x_j^{(i)} \mid j = 1, 2, \dots, n\}$ into a solitary output \hat{p} are the model parameters and the activation function associated with the neuron. Here, n represents the total number of input features, and M denotes the number of samples.

- **Model Parameters:** The model parameters consist of a bias $b \in \mathfrak{R}$ associated with the neuron and a set of weights $W = \{W_j \mid j = 1, 2, \dots, n\}$, $W_j \in \mathfrak{R}$, i.e., there exists a weight associated with each input element and the neuron. These model parameters enable the training of a neuron model for specific tasks.
- **Activation Function:** The activation function, denoted as \mathcal{G} receives the cumulative input function and produce the output \hat{p} . Here, the form of the cumulative input

function, which is the inner product of the weights $\{W_j \mid j = 1, 2, \dots, n\}$ and the input $\{X^{(i)} \mid i = 1, 2, \dots, M\}$ and also consists of the bias term, is given by

$$\sum_{j=1}^n W_j x_j^{(i)} + b, \quad (1.79)$$

where $W_j, x_j^{(i)} \in \mathfrak{R}$ for $j = 1, 2, \dots, n$ and for any $i = 1, 2, \dots, M$.

1.8.4 Activation function

The role of the activation function within a perceptron model is to determine the model's output based on the cumulative input it receives. This cumulative input obtained by the perceptron is a linear combination of the model parameters weights and biases, i.e., it is a polynomial of degree one. Hence, if the activation function is not employed in the cumulative input, in situations where the data is nonlinear in nature, the model will not be able to identify the underlying pattern of the data, so the prediction accuracy will decrease significantly. It is known that most of the real-world problems exhibit nonlinear characteristics. So, applying an external nonlinear function to the cumulative input becomes necessary to enhance the model's performance. This underscores the importance of the activation function. Notably, all activation functions are inherently nonlinear. Consequently, as the linear cumulative input passes through the activation function, the input undergoes a transformation from a linear function to a nonlinear one. This transformation is essential in predictive models to effectively capture nonlinear data relationships. The activation functions used here are described below.

- **Rectified linear unit (ReLU):** The rectified linear unit (ReLU) activation function is defined as

$$\mathcal{G}(x) = \max(0, x). \quad (1.80)$$

The derivative of the function can be written as

$$\mathcal{G}'(x) = \begin{cases} 1, & \text{if } x > 0, \\ 0, & \text{if } x \leq 0. \end{cases} \quad (1.81)$$

ReLU is the activation function used by many neural network practitioners because of its superior training performance, and it reduces the computational complexity of the hyperbolic tangent, logistic sigmoid, etc. (Glorot et al. [104], LeCun et al. [105]). As observed, the derivative of the ReLU function is unity for positive values and becomes zero otherwise. It solves one of the potential issues of vanishing gradients during model training's backpropagation phase for positive values of the cumulative input (Maas et al. [106]). However, a critical drawback associated with the ReLU activation function is the

occurrence of the “Dead State” (Nguyen et al. [107]). This refers to a scenario where multiple neurons receive negative cumulative input, causing all these neurons to become inactive. This can substantially diminish the overall performance of the model. Another concern associated with the ReLU activation function is the potential for the output to explode significantly due to the activation function’s range varying from zero to infinity.

- **Exponential linear unit (ELU):** The exponential linear unit (ELU) (Dubey et al. [108]) activation function is defined as

$$\mathcal{G}(x) = \max(0, x) + \min(0, \alpha(e^x - 1)), \quad \alpha \approx 1.6732. \quad (1.82)$$

The derivative of the function can be written as

$$\mathcal{G}'(x) = \begin{cases} 1 & \text{if } x > 0, \\ \alpha e^x & \text{if } x \leq 0. \end{cases} \quad (1.83)$$

The ELU function is exactly the same as the ReLU function for positive cumulative inputs. However, in instances where the cumulative input to the neuron is negative, the ELU function generates a negative output determined by an exponential operation. This divergence from ReLU, which produces a zero output for negative inputs, prevents the issue of uni-directional weight updates. Introducing an exponential operation for negative inputs creates a gradient on the negative side of ELU. Its existence ensures continuous learning and prevents the neuron from entering an inactive state. Consequently, this approach aids in addressing both the problems associated with vanishing gradients and dead state nodes (Nguyen et al. [107]).

- **Scaled exponential linear Unit (SELU):** The scaled exponential linear Unit (SELU) (Klambauer et al. [109]) activation function is defined as

$$\mathcal{G}(x) = \gamma(\max(0, x) + \min(0, \alpha(e^x - 1))). \quad (1.84)$$

Here, setting $\gamma \approx 1.0507$, $\alpha \approx 1.6732$ helps the output function to follow the normal distribution. The derivative of the function can be written as

$$\mathcal{G}'(x) = \begin{cases} \gamma, & \text{if } x > 0, \\ \gamma\alpha e^x, & \text{if } x \leq 0. \end{cases} \quad (1.85)$$

When both the input and output distributions of each layer within a neural network conform to a standard normal distribution characterized by a mean of 0 and a standard deviation of 1, it presents a notable advantage in accelerating the training process by promoting rapid convergence. Motivated by this concept, the SELU activation function is

developed to transform the output function to follow a normal distribution. Nevertheless, the application of SELU activation necessitates certain prerequisites (Nguyen et al. [107]), such as

- the neural network architecture should solely comprises a series of dense layers.
- all intermediary layers must employ the SELU activation function.
- standardization of input features is essential.
- initialization of the weights in hidden layers must follow the LeCun normal initialization.
- the network structure must adhere to a sequential design.

In summary, SELU avoids the problem of vanishing gradients and dead state nodes. Also, by scaling both the inputs and outputs, this activation function will increase the convergence rate.

- **Gaussian error linear unit (GELU):** The gaussian error linear unit (GELU) (Hendrycks and Gimpel [110]) activation function is defined as

$$\mathcal{G}(x) = \frac{x}{2} \left[1 + \operatorname{erf} \left(\frac{x}{\sqrt{2}} \right) \right]. \quad (1.86)$$

We can approximate the GELU with

$$\mathcal{G}(x) = \frac{x}{2} \left[1 + \tanh \left[\sqrt{2/\pi} (x + 0.044715x^3) \right] \right]. \quad (1.87)$$

The derivative of the function can be written as

$$\begin{aligned} \mathcal{G}'(x) &= \frac{1}{2} \left(1 + \tanh \left(\sqrt{\frac{2}{\pi}} (x + 0.044715x^3) \right) \right) \\ &+ \frac{x}{2} (\cos^{-1})^2 \left(\sqrt{\frac{2}{\pi}} (x + 0.044715x^3) \right) \sqrt{\frac{2}{\pi}} (1 + 0.134145x^2). \end{aligned} \quad (1.88)$$

The GELU activation function is introduced to combine the properties of dropout regularization (Srivastava et al. [111]), zoneout regularization (Krueger et al. [112]), and ReLUs. It takes inspiration from ReLU and dropout to find the neuron's output by multiplying inputs deterministically by zero or one. Additionally, zoneout (a regularization technique in RNNs) stochastically forces some hidden units to maintain their previous values. We combine these functions by multiplying the input by either zero or one. However, the values determining whether it's zero or one are randomly decided and are also based on the input.

Hence, the output of a neuron model with cumulative input as given in Eq. (1.79) is given by

$$\mathcal{G} \left(\sum_{j=1}^n W_j x_j^{(i)} + b \right). \quad (1.89)$$

The single perceptron model demonstrates its ability to handle basic learning tasks, notably tasks like binary classification (McCulloch and Pitts [113], Elizondo [114]). However, addressing more complicated non-linear problems can be handled by a neural network comprising multiple interconnected perceptron models.

1.8.5 Forward propagation algorithm

The feed-forward architecture of an MLP model with dense hidden layers is considered. Here, neurons in the feed-forward neural network are grouped into a sequence of ℓ' number of layers so that neurons in any layer are connected only to neurons in the next layer. The input layer consists of n external inputs representing the number of features in the dataset and is not counted as a layer of neurons. Further, the ℓ^{th} hidden layer comprises $n^{[\ell]}$ neurons, and the output layer is composed of the number of neurons, which is the same as the number of target features. Communication proceeds layer by layer from the input layer via the hidden layers up to the output layer. The output of the MLP model is the output provided by the output layer. Specifically, let the training dataset is denoted as $X = \{X^{(i)} \mid i = 1, 2, \dots, M\}$ with the corresponding target values being denoted by $P = \{p^{(i)} \mid i = 1, 2, \dots, M\}$. In this context, M denotes the number of training samples. Each input sample $X^{(i)}$, consists of n features, represented as $X^{(i)} = \{x_j^{(i)} \mid j = 1, 2, \dots, n\}$. Then, for the i^{th} sample from the k^{th} neuron in the first layer, the cumulative input denoted by $z_k^{[1](i)}$ and the output denoted by $a_k^{[1](i)}$ can be calculated as follows

$$z_k^{[1](i)} = \sum_{j=1}^{n^{[1]}} W_{k,j}^{[1]T} x_j^{(i)} + b_k^{[1]}, \quad (1.90)$$

$$a_k^{[1](i)} = \mathcal{G}^{[1]} \left(z_k^{[1](i)} \right). \quad (1.91)$$

In a similar manner, the cumulative input and the output of the i^{th} sample from k^{th} neuron in the ℓ^{th} hidden layer can be computed as follows

$$z_k^{[\ell](i)} = \sum_{j=1}^{n^{[\ell-1]}} W_{k,j}^{[\ell]T} a_j^{[\ell-1](i)} + b_k^{[\ell]}, \quad (1.92)$$

$$a_k^{[\ell](i)} = \mathcal{G}^{[\ell]} \left(z_k^{[\ell](i)} \right). \quad (1.93)$$

Finally, the cumulative input and the output of the i^{th} sample in the output layer $z_1^{[\ell'](i)}$ and $\hat{p}^{(i)}$ in the output layer can be computed as

$$z_1^{[\ell'](i)} = \sum_{j=1}^{n^{[\ell'-1]}} W_{1,j}^{[\ell']} a_j^{[\ell'-1](i)} + b_1^{[\ell']}, \quad (1.94)$$

$$\hat{p}^{(i)} = \mathcal{G}^{[\ell']} \left(z_1^{[\ell'](i)} \right), \quad (1.95)$$

where $W_{k,j}^{[\ell]}$ signifies the weight associated to the connection between the j^{th} neuron in the $(\ell - 1)^{\text{th}}$ layer and the k^{th} neuron in the ℓ^{th} layer. Additionally, $z_k^{[\ell](i)}$ and $a_k^{[\ell](i)}$ represent the cumulative input and the output of the i^{th} sample from k^{th} neuron in the ℓ^{th} layer. These outputs are determined by applying the activation function $g^{[\ell]}$, which is specifically associated with the ℓ^{th} layer. The predicted output of the model is denoted by $\hat{P} = \{\hat{p}^{(i)} \mid i = 1, 2, \dots, M\}$ obtained from the MLP model involves adjusting the weight and bias factors, denoted as $W = \bigcup_{\ell=1}^{\ell'} W^{[\ell]}$ and

$B = \bigcup_{\ell=1}^{\ell'} \bigcup_{k=1}^{n^{[\ell]}} b_k^{[\ell]}$. Here, $W^{[\ell]}$ represents a matrix of dimension $[n^{[\ell]}, n^{[\ell-1]}]$, where $n^{[\ell]}$ corresponds to the number of neurons in the ℓ^{th} layer, and $n^{[\ell-1]}$ represents the number of neurons in the $(\ell - 1)^{\text{th}}$ layer. Additionally, $b_k^{[\ell]}$ is a constant bias term associated with the k^{th} neuron in the ℓ^{th} layer. The geometric representation of the forward propagation network architecture is shown in Fig. 1.11.

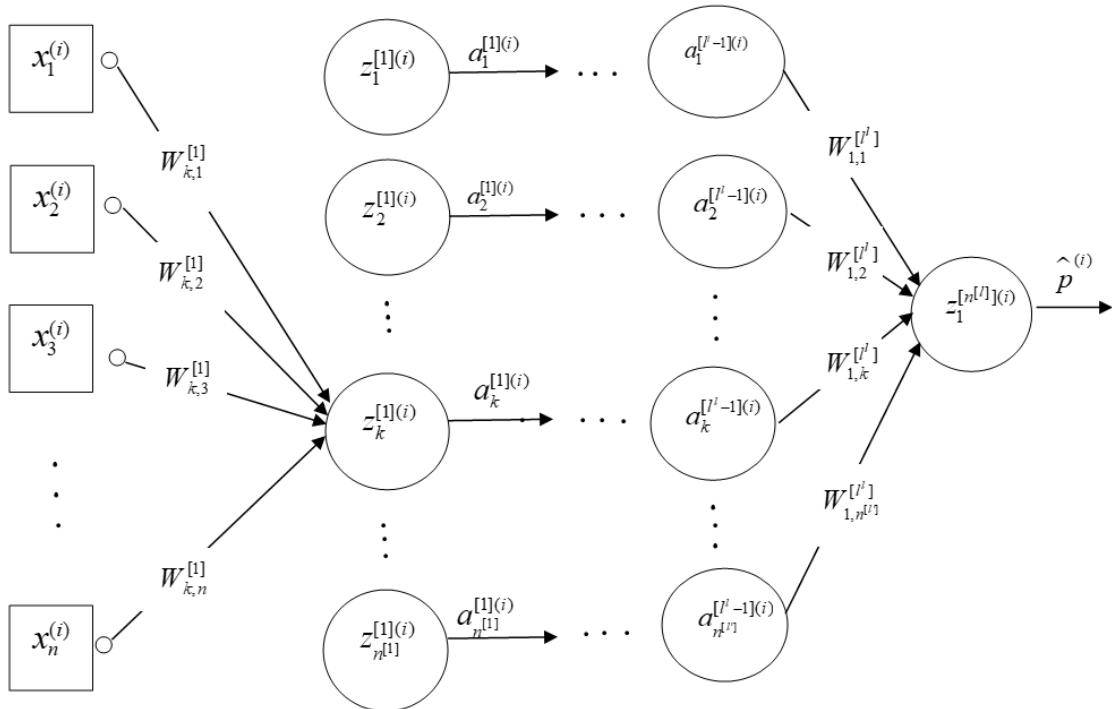


FIGURE 1.11: The forward propagation network architecture.

1.8.6 Back-propagation algorithm

During the training of the neural network model, the forward propagation will proceed up to the determination of the cost function of the model $\mathcal{L}(\cdot)$. In the back-propagation phase, the information will pass from the loss function backward to find the gradients of $\mathcal{L}(\cdot)$ with respect to the weights and the biases. The aim is to find a set of weights and biases that ensure that for each input vector, the output produced by the network \hat{p} is the same as the true output p . If there is a fixed, finite set of input-output samples, the total error in the performance of the network with a particular set of weights and biases can be computed by comparing the actual and predicted output for every sample. Let \mathcal{L} be the loss function, and the weights and biases associated with the prediction of the i^{th} sample using the back-propagation algorithm can be calculated by applying the chain rule as follows.

$$\frac{\partial \mathcal{L}^{(i)}}{\partial z_k^{[\ell']^{(i)}}} = \frac{\partial \mathcal{L}^{(i)}}{\partial \hat{p}^{(i)}} \cdot \frac{\partial \hat{p}^{(i)}}{\partial z_k^{[\ell']^{(i)}}}. \quad (1.96)$$

Similarly, $\frac{\partial \mathcal{L}^{(i)}}{\partial W^{[\ell']^{(i)}}}$ and $\frac{\partial \mathcal{L}^{(i)}}{\partial b^{[\ell']^{(i)}}}$ can be computed using the following chain rule

$$\frac{\partial \mathcal{L}^{(i)}}{\partial W^{[\ell']^{(i)}}} = \frac{\partial \mathcal{L}^{(i)}}{\partial z_k^{[\ell']^{(i)}}} \cdot \frac{\partial z_k^{[\ell']^{(i)}}}{\partial W^{[\ell']^{(i)}}}, \quad (1.97)$$

$$\frac{\partial \mathcal{L}^{(i)}}{\partial b^{[\ell']^{(i)}}} = \frac{\partial \mathcal{L}^{(i)}}{\partial z_k^{[\ell']^{(i)}}} \cdot \frac{\partial z_k^{[\ell']^{(i)}}}{\partial b^{[\ell']^{(i)}}}. \quad (1.98)$$

Similarly, we can compute the gradient of the weights and bias for all the layers. The updated weights and bias to reduce the loss function are given by

$$W^{[\ell']^{(i)}} = W^{[\ell']^{(i)}} - \alpha \frac{\partial \mathcal{L}^{(i)}}{\partial W^{[\ell']^{(i)}}}, \quad (1.99)$$

$$b^{[\ell']^{(i)}} = b^{[\ell']^{(i)}} - \alpha \frac{\partial \mathcal{L}^{(i)}}{\partial b^{[\ell']^{(i)}}}. \quad (1.100)$$

Now, using the updated weights and biases, the next epoch will be carried out, and it will continue till the first layer. Here, α denotes the learning rate.

1.8.7 Optimization algorithms

In this section, two of the widely used neural network model optimizers are discussed briefly.

- **Adam optimizer:** Adam is a stochastic optimization algorithm to optimize the model parameters of the neural network tool. Let α be the step size, β_1 , and $\beta_2 \in [0, 1)$ be the

exponential decay rates for the moment estimates. Let $\mathcal{L}(\theta)$ be the stochastic objective function with parameter θ . Here, θ can be either weight (w) or bias (b) with θ_0 being the initial parameter vector. Initialize the first-moment vectors $m_0 = 0$ and the second-moment vectors $v_0 = 0$. Let $t = 0$ be the initial time step. The algorithm of the Adam optimizer involves the iteration of the following steps with respect to t until θ will converge to the optimal value θ_t (Kingma and Ba [115])

$$\begin{aligned}
t &\leftarrow t + 1 \\
g_t &\leftarrow \frac{\partial \mathcal{L}_t(\theta_{t-1})}{\partial \theta} \\
m_t &\leftarrow \beta_1 m_{t-1} + (1 - \beta_1) g_t \\
v_t &\leftarrow \beta_2 v_{t-1} + (1 - \beta_2) g_t^2 \\
m_t^{\text{Corrected}} &\leftarrow \frac{m_t}{1 - \beta_1^t} \\
v_t^{\text{Corrected}} &\leftarrow \frac{v_t}{1 - \beta_2^t} \\
\theta_t &\leftarrow \theta_{t-1} - \alpha \frac{m_t^{\text{Corrected}}}{\sqrt{v_t^{\text{Corrected}} + \epsilon}}
\end{aligned}$$

Here, g_t represents the gradients w.r.t. the stochastic objective function at timestep t . Further, m_t and v_t are the updated biased first and second-moment estimates, respectively, at timestep t . Moreover, $m_t^{\text{Corrected}}$ and $v_t^{\text{Corrected}}$ are the bias-corrected first and second-moment estimates, respectively.

- **Nadam optimizer:** Nadam is developed by incorporating Nesterov momentum into the Adam optimizer. Let $\alpha_1, \alpha_2, \dots, \alpha_T$, and $\beta_1, \beta_2, \dots, \beta_T$ be the learning rate and decay factor for each time step. Here, γ and ϵ be the hyperparameters with default values 0.999 and $1e^{-8}$ (see Dozat [116] for details). Initialize the first-moment vectors $m_0 = 0$ and the second-moment vectors $v_0 = 0$. Let $t = 0$ be the initial time step. The Nadam optimizer algorithm involves the iteration of the following steps with respect to t until θ will converge to the optimal value θ_t (Dozat [116])

$$\begin{aligned}
t &\leftarrow t + 1 \\
g_t &\leftarrow \frac{\partial \mathcal{L}_t(\theta_{t-1})}{\partial \theta_{t-1}}, \\
m_t &\leftarrow \beta_t m_{t-1} + (1 - \beta_t) g_t \\
v_t &\leftarrow \gamma v_{t-1} + (1 - \gamma) g_t^2 \\
m_t^{\text{Corrected}} &\leftarrow \left(\frac{\beta_{t+1} m_t}{1 - \prod_{i=1}^{t+1} \beta_i} \right) + \left(\frac{(1 - \beta_t) g_t}{1 - \prod_{i=1}^t \beta_i} \right) \\
v_t^{\text{Corrected}} &\leftarrow \frac{\gamma v_t}{1 - \gamma^t} \\
\theta_t &\leftarrow \theta_{t-1} - \alpha_t \frac{m_t^{\text{Corrected}}}{\sqrt{v_t^{\text{Corrected}} + \epsilon}}
\end{aligned}$$

The parameters g_t , m_t , v_t , $m_t^{Corrected}$ and $v_t^{Corrected}$ involved in the Nadam algorithm are same as defined before.

1.9 Extreme gradient boosting and interpretable machine learning approaches

In this section, a widely accepted ML model, namely the extreme gradient boosting (XGBoost), and two of the interpretable machine learning approaches, namely the accumulated local effects (ALE) and Shapley additive explanations (SHAP), are explained briefly. The XGBoost model is implemented in our study to predict the power generated by the WECs, and the ALE values are used to find the specific regions of the input space that maximize power generation. Further, the shapely values are used to analyze the importance of the feature.

1.9.1 Extreme gradient boosting (XGBoost)

As mentioned by Borisov et al. [68], the tree ensemble models consistently outperform the deep learning models across various supervised learning tasks. Consequently, a tree-based ensemble model, specifically extreme gradient boosting (XGBoost), is studied to investigate the complex non-linear data associated with the power generated by the WEC devices. The first gradient-boosting(GB) algorithm based on the decision tree was proposed by Friedman [117]. The XGBoost model is an advanced adaption of the GB algorithm proposed by Chen and Guestrin [84] with several improvements such as parallel and distributed computing, tree pruning, handling missing values, feature importance, handling categorical features, efficient handling of large datasets, etc. The working mechanism behind the better accuracy of the XGBoost model is that a new weak learner/ decision tree will be added to reduce the residual of the previous iteration. Such a greedy approach consistently makes optimal decisions at each step of the learning process (Chen and Guestrin [84]). However, due to the complexity of the XGBoost model, it is more prone to overfitting. The L_1 and L_2 regularization terms are incorporated into the loss function to avoid such overfittings (El Bilali et al. [72]).

Consider the training database $\left\{ \left(X^{(1)}, p^{(1)} \right), \left(X^{(2)}, p^{(2)} \right), \dots, \left(X^{(M)}, p^{(M)} \right) \right\}$ comprising M samples and n features. The XGBoost model develops a predictive function $F(X)$, which predicts \hat{P} for any new input X . Let K denote the number of weak learners sequentially added to the model, representing the number of iterations in the XGBoost model. The final prediction $F(X)$ is derived by aggregating the predictions from all weak learners in the ensemble of trees

through summation as described in the following (see El Bilali et al. [72]).

$$\hat{p}^{(i)} = F\left(X^{(i)}\right) = \sum_{k=1}^K f_k\left(X^{(i)}\right), \quad f_k \in \mathcal{F}, \quad (1.101)$$

where $\mathcal{F} = \{f(X) = w_{q(x)}\}$, ($q: \mathbb{R}^n \rightarrow T, w \in \mathbb{R}^T$) representing the space of regression trees. Here, q denotes the structure of each tree that maps a sample to the corresponding leaf node, with T being the number of leaves in the tree. Further, f corresponds to an independent tree structure q with leaf weights w (Chen and Guestrin [84]). Let $\hat{p}_k^{(i)}$ represent the prediction for the i^{th} example at the k^{th} iteration, and let \mathcal{L} denote a differentiable convex loss function that quantifies the variation between the true response $p^{(i)}$ and the prediction $\hat{p}^{(i)}$. The cost function is defined as $\sum_{i=1}^M \mathcal{L}\left(\hat{p}^{(i)}, p^{(i)}\right)$. After incorporating L_1 and L_2 regularization, the objective function is provided as (Chen and Guestrin [84])

$$\mathcal{L}(F) = \sum_{i=1}^M \mathcal{L}\left(\hat{p}^{(i)}, p^{(i)}\right) + \sum_{k=1}^K R(f_k), \quad \text{where } R(f) = \alpha T + \frac{1}{2} \lambda \|w\|^2. \quad (1.102)$$

In this context, $R(f)$ signifies the L_1 and L_2 regularization term incorporated to reduce overfitting by penalizing the complexity of the XGBoost model. Moreover, α and λ denote the weights associated with the L_1 and L_2 regularizations. After adding f_k to the loss function, the k^{th} iteration of the objective function can be expressed as (employing Taylor's formula Chen and Guestrin [84])

$$\mathcal{L}_k = \sum_{i=1}^M \left[g^{(i)} f_k\left(x^{(i)}\right) + \frac{1}{2} h^{(i)} f_k^2\left(x^{(i)}\right) \right] + R(f_k), \quad (1.103)$$

$$\text{where } g^{(i)} = \frac{\partial \mathcal{L}\left(p^{(i)}, \hat{p}_{k-1}\right)}{\partial \hat{p}_{k-1}}, \quad (1.104)$$

$$h^{(i)} = \frac{\partial^2 \mathcal{L}\left(p^{(i)}, \hat{p}_{k-1}\right)}{\partial \hat{p}_{k-1}^2}. \quad (1.105)$$

Now, the optimized weight of the j^{th} leaf node is calculated as (see Chen and Guestrin [84])

$$w_j = - \frac{\sum_{i \in I_j} g^{(i)}}{\sum_{i \in I_j} h^{(i)} + \lambda}, \quad (1.106)$$

where $I_j = \{i : q(X^{(i)}) = j\}$ signifies the instance set of the j^{th} leaf. The optimal score of the tree structure q is calculated as (see Chen and Guestrin [84])

$$\tilde{\mathcal{L}}_k(q) = -\frac{1}{2} \sum_{j=1}^T \frac{\left(\sum_{i \in I_j} g^{(i)} \right)^2}{\sum_{i \in I_j} h^{(i)} + \lambda} + \alpha T. \quad (1.107)$$

The XGBoost model adopts a greedy algorithm that commences from a solitary leaf and progressively incorporates branches into the tree. The evaluation of the split candidate is carried out using the following formula (see El Bilali et al. [72])

$$L_{split} = \frac{1}{2} \left[\frac{\left(\sum_{i \in I_L} g^{(i)} \right)^2}{\sum_{i \in I_L} h^{(i)} + \lambda} + \frac{\left(\sum_{i \in I_R} g^{(i)} \right)^2}{\sum_{i \in I_R} h^{(i)} + \lambda} - \frac{\left(\sum_{i \in I} g^{(i)} \right)^2}{\sum_{i \in I} h^{(i)} + \lambda} \right] - \alpha, \quad (1.108)$$

where I_L and I_R represent the sets of instances in the left and right nodes after splitting the root node denoted as $I = I_L \cup I_R$.

1.9.2 Accumulated local effects(ALE)

Accumulated Local Effects is an interpretable machine learning approach used to interpret the predictions of complex machine learning models. ALE plots summarize variations in the prediction of an ML model by averaging and aggregating the predicted values across a defined grid. To measure local effects, features are segmented into multiple intervals, and the uncentered effect of a feature is calculated by (see Liu et al. [71])

$$\hat{f}_{j,ALE}(X_j) = \sum_{a=1}^{a_j(X_j)} \frac{1}{M_j(a)} \sum_{v: x_j^{(v)} \in m_j(a)} \left[f(z_{a,j}, X_{\setminus j}^{(v)}) - f(z_{a-1,j}, X_{\setminus j}^{(v)}) \right], \quad (1.109)$$

where $z_{a,j}$ signifies the boundary value of the a^{th} interval for the j^{th} feature. Additionally, $M_j(a)$ represents the count of $m_j(a)$, which contains the sample points in the a^{th} interval. Furthermore, X_j and $X_{\setminus j}$ refer to the j^{th} feature and the features excluding the j^{th} feature, respectively. The centered ALE estimator is derived as (see Liu et al. [71])

$$\hat{f}_{j,ALE}(X_j) = \hat{f}_{j,ALE}(X_j) - \frac{1}{M} \sum_{v=1}^M \hat{f}_{j,ALE}(x_j^{(v)}). \quad (1.110)$$

This centered ALE estimator ensures the mean effect of the response variable is zero. Similarly, the ALE estimator can analyze the interaction effect between two parameters. To compute the second-order ALE involving the j^{th} and l^{th} features, the sample range of the ALE plots will be divided into A^2 rectangular cells. Here, a and b represent indices correspond to the grids for the j^{th} and l^{th} features, respectively. The uncentered interaction effect of the features, considering two features at a time, is determined using the following formula (see Liu et al. [71])

$$\hat{h}_{\{j,l\},ALE}(X_j, X_l) = \sum_{a=1}^{a_j(X_j)} \sum_{b=1}^{b_l(X_l)} \frac{1}{M_{\{j,l\}}(a,b)} \times \sum_{i: x_{\{j,l\}}^{(i)} \in m_{\{j,l\}}(a,b)} \Delta_f^{\{j,l\}} \left(A, a, b; x_{\{j,l\}}^{(i)} \right). \quad (1.111)$$

Here, $\Delta_f^{\{j,l\}} \left(A, a, b; x_{\{j,l\}}^{(i)} \right)$ represents the second-order finite difference of $f \left(X_j, X_l, x_{\{j,l\}}^{(i)} \right)$ for (X_j, X_l) across cell $(\chi_{a-1,j}, \chi_{a,j}] \times (\chi_{b-1,l}, \chi_{b,l}]$. Then the second-order ALE is obtained as (see Liu et al. [71])

$$\begin{aligned} \hat{f}_{\{j,l\},ALE}(X_j, X_l) &= \hat{h}_{\{j,l\},ALE}(X_j, X_l) \\ &- \sum_{a=1}^{a_j(X_j)} \frac{1}{M_j(a)} \sum_{b=1}^a M_{\{j,l\}}(a,b) \left\{ \hat{h}_{\{j,l\},ALE}(\chi_{a,j}, \chi_{b,l}) - \hat{h}_{\{j,l\},ALE}(\chi_{a-1,j}, \chi_{b,l}) \right\} \\ &- \sum_{b=1}^{a_l(X_l)} \frac{1}{M_l(b)} \sum_{a=1}^b M_{\{j,l\}}(a,b) \left\{ \hat{h}_{\{j,l\},ALE}(\chi_{a,j}, \chi_{b,l}) - \hat{h}_{\{j,l\},ALE}(\chi_{a,j}, \chi_{b-1,l}) \right\}. \end{aligned} \quad (1.112)$$

Now, The centered second-order ALE effects are derived as (see Apley and Zhu [118])

$$\hat{f}_{\{j,l\},ALE}(X_j, X_l) = \hat{f}_{\{j,l\},ALE}(X_j, X_l) - \frac{1}{M} \sum_{a=1}^A \sum_{b=1}^A M_{\{j,l\}}(a,b) \hat{f}_{\{j,l\},ALE}(\chi_{a,j}, \chi_{b,l}). \quad (1.113)$$

1.9.3 Shapley additive explanations (SHAP)

In this section, we will provide an overview of the Shapley values associated with an ML model F that can predict the response variable for any input vector $X^{(i)}$, for $i = 1, \dots, M$, where M is the number of samples. The Shapley values will provide the explanation for an individual prediction $F(X^{(i)})$ using the formula (see Heskes et al. [119])

$$F(X^{(i)}) = F_0 + \sum_{k=1}^n \varphi_k, \quad (1.114)$$

where φ_k is the contribution of the feature k to the predictive model F . The baseline F_0 is the expected value of $F(X)$ under the observed data distribution $\mathbf{P}(X)$. Now, the contribution of

the feature k for a given permutation of features π is given by (see Heskes et al. [119])

$$\varphi_k(\pi) = \nu(\{j : j \preceq_\pi k\}) - \nu(\{j : j \prec_\pi k\}), \quad (1.115)$$

where $j \prec_\pi k$ refers to the features j precedes k in the permutation π .

$$\begin{aligned} \nu(S) &= \mathbb{E} \left[F(X) \mid X_S = X_S^{(i)} \right], \\ &= \int f \left(X_{\bar{S}}, X_S^{(i)} \right) \mathbf{P} \left(X_{\bar{S}} \mid \left(X_S = X_S^{(i)} \right) \right) dX_{\bar{S}}, \end{aligned} \quad (1.116)$$

where S is the chosen column to predict the response variable from the set of input variables, and \bar{S} denotes its complement columns. Now, associating uniform distribution for all the permutations, we get

$$\varphi_k = \sum_{S \subseteq N \setminus k} \frac{|S|!(n - |S| - 1)!}{n!} [\nu(S \cup k) - \nu(S)]. \quad (1.117)$$

1.10 k-fold cross-validation

Consider the task of estimating the test error associated with a specific statistical or machine-learning model based on a set of observations. A straightforward method for this purpose is to employ the validation set approach. This technique involves randomly partitioning the available observations into two subsets, a training set and a validation set, also known as a hold-out set. The model is trained using the training set, and the trained model is then utilized to predict the responses for the observations in the validation set. The resulting error rate on the validation set is commonly evaluated using metrics such as MSE, MAE, or MAPE. These metrics provide an estimation of the test error rate. K -fold cross-validation is a highly effective approach for ML model validation. In this method, the set of observations is randomly divided into k number of groups or folds of roughly equal size. One fold is designated as the validation set, and the machine learning model is trained on the remaining $k - 1$ folds. Assuming MSE is the chosen error metric, the mean squared error (MSE_i for $i \leq k$) is computed on the observations in the i^{th} validation fold. This process is iterated k times with each iteration using a different group of observations as the validation set. Consequently, k estimates of the test errors $\text{MSE}_1, \text{MSE}_2, \dots, \text{MSE}_k$ are obtained. The k -fold cross-validation estimate is determined by averaging these values as given by (James et al. [120])

$$CV_{(k)} = \frac{1}{k} \sum_{i=1}^k \text{MSE}_i. \quad (1.118)$$

In practice, typically, k-fold CV is used for $k = 5$ or $k = 10$. The advantages of the k-fold cross-validation are that it requires less computational cost and provides reliable and accurate estimates (Wong and Yeh [121]).

1.11 Response surface methodology (RSM)

Response surface methodology is a multivariate statistical optimization technique consisting of a class of mathematical and statistical tools. This methodology relies on fitting empirical models to the experimental data obtained through experimental design. To achieve this goal, linear or square polynomial functions are utilized to describe the system studied. These functions explore the experimental conditions for optimizing the system (Bezerra et al. [122]). The important stages of implementation of the RSM optimization technique are as follows:

- choosing significant independent variables by conducting screening studies and defining the experimental region in accordance with the objective of the study.
- the selection of the experimental design and the execution of experiments in accordance with the chosen experimental matrix.
- mathematical and statistical analysis of the collected experimental data by fitting a polynomial function.
- the evaluation of the model's fitness.
- confirming the need and feasibility of making a shift in the parameters toward the optimal region.
- obtain the optimum values for each input variable.

In the stage of finding a model that fits the relationship between the predictors and the response using a polynomial function, low-order models such as first or second-order models are often preferred (Bezerra et al. [122]). A first-order model is represented as

$$p = \mathcal{B}_0 + \mathcal{B}_1x_1 + \mathcal{B}_2x_2 + \cdots + \mathcal{B}_nx_n + \epsilon. \quad (1.119)$$

The second-order model can be represented as

$$p = \mathcal{B}_0 + \sum_{j=1}^n \mathcal{B}_jx_j + \sum_{j=1}^n \mathcal{B}_{jj}x_j^2 + \sum_{i<j} \mathcal{B}_{ij}x_ix_j + \epsilon. \quad (1.120)$$

These simplified low-order models serve as an approximation to the actual system. The assumption is that they will exhibit similar behavior to the real system, at least within a small region

in the input space. The RSM proceeds sequentially, where at each step, we move in a direction to improve the objective of maximizing or minimizing the response variable. In this procedure, we try to move as efficiently as possible toward an optimal value of the response variable using a step size and a scale defined by the experimenter (Myers et al. [123]). This procedure is repeated several times, following the path of steepest ascent/steepest descent until no more improvements are found in a local neighborhood.

Chapter 2

Mathematical modeling of a breakwater-integrated piezoelectric wave energy converter device placed over an undulated seabed

* The work, in this chapter, is covered by the following publication:

Vipin, V., Koley, S. (2022). Mathematical modeling of a submerged piezoelectric wave energy converter device installed over an undulated seabed. *Renewable Energy*, 200, 1382-1392.

2.1 General introduction

A piezoelectric wave energy converter (PWEC) device integrated with an impermeable breakwater placed over an undulated seabed is considered. The PWEC device is composed of a single submerged flexible plate with piezoelectric layers attached to both the faces of the flexible plate. Due to the piezoelectric effect, this piezoelectric plate generates electricity when excited by the incident waves. A detailed analysis is done to investigate the effect of PWEC plate submergence depth, plate length, plate edge conditions, incident wave period, bottom ripples amplitude, and ripples number on the power generation by the PWEC device. It is seen that the PWEC device edge conditions, submergence depth, and plate length play a significant role in the resonating pattern associated with the wave power generation curve. The results demonstrate that the PWEC device having moderate plate length and with free and moored type front edges generates a higher amount of wave power for a wider range of incident wave frequencies.

2.2 Mathematical formulation

In the present problem, the performance of a breakwater integrated piezoelectric wave energy converter (PWEC) device is studied. The schematic diagram of the vertical cross-section of the physical problem is provided in Fig. 2.1. To model the hydrodynamics associated with the PWEC device, a two-dimensional Cartesian coordinate system is considered with the direction of wave propagation coinciding with the x -axis and the z -axis pointing vertically upwards from the mean free surface. It is assumed that regular ocean waves of amplitude A and angular frequency ω impinge perpendicularly on the breakwater integrated PWEC device. Here, $A/\lambda \ll 1$ is considered with λ being the incident wavelength so that the small-amplitude wave theory is applicable for the present study. The piezoelectric device consists of three layers in which the middle layer is made up of a flexible substrate, and piezoelectric layers are bonded on both sides of the flexible substrate (see Renzi [3] for details). Due to the piezoelectric effect, the elastic motion of the PWEC device is converted into electricity. The PWEC device of length l is placed at a submergence depth d from the mean free surface $z = 0$ and occupies the region $b \leq x \leq b + l$ along the x -axis. The lee edge of the PWEC device is attached to a rigid and impermeable front wall of the breakwater, and for the same, fixed and moored plate edge conditions are considered at $x = b + l, z = -d$. Further, the front edge of the PWEC device is considered as fixed, free, or moored type. It is to be noted that for the fixed edge of the plate at the seaside, a floating buoy can be used. The bottom topography of the physical problem consists of two parts: an undulated seabed represented by $z = -h(x)$ and occupies the region $0 \leq x \leq L = (b + l)$, and a uniform seabed region $-l_1 < x < 0$ along the x -axis. To solve the associated boundary value problem using the boundary element method, an auxiliary boundary Γ_{c1} is constructed at $x = -l_1$. This auxiliary boundary Γ_{c1} is situated sufficiently far away from the PWEC device and undulated

bottom so that the effect of local wave modes vanishes on the auxiliary boundary Γ_{c1} . For the sake of mathematical modeling, the entire domain of the physical problem is divided into two regions R_1 and R_2 , as shown in Fig. 2.1. The water flow is assumed to be incompressible, inviscid, and irrotational in nature, along with the motion being harmonic in time with the angular frequency ω . These aforementioned assumptions make certain the existence of the velocity potentials of the following form

$$\Phi_j(x, z, t) = \Re \{ \phi_j(x, z) e^{-i\omega t} \}, \quad \text{for } j = 1, 2, \quad (2.1)$$

where Φ_j represent the velocity potentials for the regions R_j for $j = 1, 2$. Further, the spatial velocity potentials ϕ_j for $j = 1, 2$ satisfy

$$\left(\frac{\partial^2}{\partial x^2} + \frac{\partial^2}{\partial z^2} \right) \phi_j = 0. \quad (2.2)$$

Further, the boundary conditions on the mean free surfaces $\Gamma_{f1} = \{b < x < b+l, z=0\}$ and $\Gamma_{f2} = \{-l_1 < x < b, z=0\}$ are given by

$$\frac{\partial \phi_j}{\partial z} = K \phi_j, \quad \text{on } \Gamma_{fj}, \quad \text{for } j = 1, 2, \quad (2.3)$$

where $K = \omega^2/g$ with g represents the acceleration due to gravity. The seabed is considered to

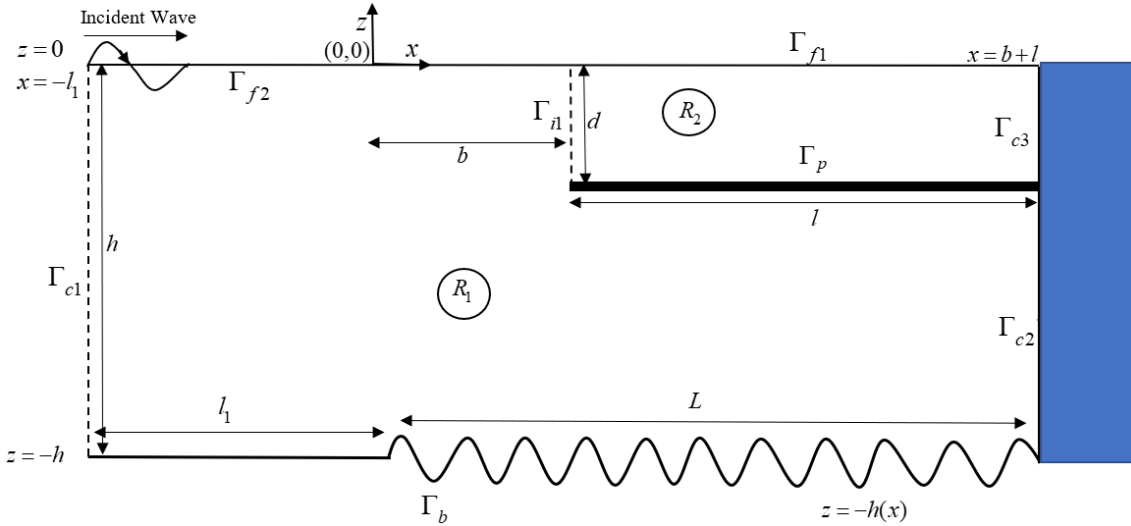


FIGURE 2.1: Schematic diagram of the physical problem.

be rigid and impermeable in nature. Therefore, the bottom boundary condition on Γ_b is given by

$$\frac{\partial \phi_1}{\partial n} = 0, \quad \text{on } z = -H(x), \quad (2.4)$$

where $\partial/\partial n$ represents the normal derivative and $H(x)$ represents the bottom topography

$$H(x) = \begin{cases} h, & x < 0, \\ h(x), & 0 < x < L. \end{cases} \quad (2.5)$$

Here, $h(x)$ represents the undulated seabed as mentioned earlier. The boundary conditions on the rigid and impermeable breakwater wall Γ_{c2} and Γ_{c3} are given by

$$\begin{cases} \frac{\partial\phi_1}{\partial n} = 0, & \text{on } \Gamma_{c2}, \\ \frac{\partial\phi_2}{\partial n} = 0, & \text{on } \Gamma_{c3}. \end{cases} \quad (2.6)$$

The plate deflection $\xi(x, t)$ is assumed to be time harmonic in nature and takes the form $\xi(x, t) = \Re\{\xi(x)e^{-i\omega t}\}$. Now, the kinematic boundary condition on Γ_p (see Zheng et al. [41]) is given by

$$\frac{\partial\phi_1}{\partial n} = -\frac{\partial\phi_2}{\partial n} = -i\omega\xi, \quad \text{on } b < x < b+l, z = -d. \quad (2.7)$$

The dynamic boundary condition on the piezoelectric plate surface Γ_p is given by

$$g\chi \left[1 + \frac{\beta^2\varphi\omega}{i + \varphi\omega} \right] \frac{\partial^4\xi}{\partial x^4} - \omega^2\gamma\xi = i\omega(\phi_1(x, -d^-) - \phi_2(x, -d^+)), \quad \text{on } b < x < b+l, z = -d. \quad (2.8)$$

Here, the parameters used in Eq. (2.8) are given by

$$\chi = \frac{B}{\rho g}, \quad \beta = \frac{\theta}{\sqrt{BC}}, \quad \varphi = \frac{C}{V}, \quad \gamma = \frac{I_b}{\rho}, \quad (2.9)$$

where B, θ, C and V represent the flexural rigidity of the PWEC plate, piezoelectric coupling factor, electrical surface capacitance, and surface conductance, respectively. Further, ρ is the water density, and I_b represents the surface density of the PWEC device. The details of the aforementioned parameters range and physical significance are available in Renzi [3] and Zheng et al. [41]. Now, we need to provide the appropriate plate edge conditions. When the plate edges are fixed, the edge conditions of the plate are given by

$$\xi = 0, \quad \frac{\partial\xi}{\partial x} = 0, \quad \text{at } x = b, b+l. \quad (2.10)$$

Similarly, when the plate edges are free, the edge conditions are given by

$$\frac{\partial^2\xi}{\partial x^2} = 0, \quad \frac{\partial^3\xi}{\partial x^3} = 0, \quad \text{at } x = b, b+l. \quad (2.11)$$

Further, the edge conditions of a plate which is moored to the seabed is given by

$$\frac{\partial^2\xi}{\partial x^2} = 0, \quad \rho g\chi \left[1 + \frac{\beta^2\varphi\omega}{i + \varphi\omega} \right] \frac{\partial^3\xi}{\partial x^3} = q\xi, \quad \text{at } x = b, b+l, \quad (2.12)$$

where q represents mooring stiffness. The continuity of pressure and normal velocity along the auxiliary boundary Γ_{i1} are given by

$$\phi_1 = \phi_2, \quad \frac{\partial \phi_1}{\partial n} = -\frac{\partial \phi_2}{\partial n}, \quad \text{on } \Gamma_{i1}. \quad (2.13)$$

Finally, the far-field boundary condition on Γ_{c1} is given by

$$\frac{\partial(\phi_1 - \phi^I)}{\partial x} + ik_0(\phi_1 - \phi^I) = 0, \quad (2.14)$$

where $\phi^I(x, z) = e^{ik_0x} f_1(k_0, z)$ represents the incident wave potential. Here, $f_1(k_0, z) = \left(\frac{-igA}{\omega}\right) \frac{\cosh(k_0(z+h))}{\cosh(k_0h)}$ with k_0 being the positive root of the dispersion relation $K = k_0 \tanh(k_0h)$.

2.3 Method of solution

In this section, the boundary element method-based solution technique is applied to solve the physical problem formulated in Section 2. Firstly, the boundary value problem formulated in Section 2 is converted into a system of integral equations. These integral equations are derived in terms of the velocity potentials and their normal derivatives using Green's second identity along with the free space Green's function and using the boundary conditions derived in Section 2. The Green's identity is given by

$$\frac{1}{2}\phi(x_0, z_0) = \int_{\Gamma} \left(\phi(x, z) \frac{\partial G(x, z; x_0, z_0)}{\partial n} - G(x, z; x_0, z_0) \frac{\partial \phi(x, z)}{\partial n} \right) d\Gamma(x, z). \quad (2.15)$$

The form of the free space Green's function $G(x, z; x_0, z_0)$ used in Eq. (2.15) is given by

$$G(x, z; x_0, z_0) = \frac{1}{2\pi} \ln(r), \quad \text{where } r = \sqrt{(x - x_0)^2 + (z - z_0)^2}, \quad (2.16)$$

with (x, z) and (x_0, z_0) being the field and source points respectively. For the present problem, $G(x, z; x_0, z_0)$ satisfies

$$\Delta^2 G(x, z; x_0, z_0) = \delta(x - x_0)\delta(z - z_0), \quad \Delta^2 \equiv \left(\frac{\partial^2}{\partial x^2} + \frac{\partial^2}{\partial z^2} \right). \quad (2.17)$$

Furthermore, the normal derivatives of the Green's function is given by

$$\frac{\partial G}{\partial n} = \frac{1}{2\pi r} \frac{\partial r}{\partial n} = \frac{1}{2\pi r} \left(n_x \frac{\partial r}{\partial x} + n_z \frac{\partial r}{\partial z} \right), \quad (2.18)$$

where n_x and n_z are the components of the unit normal vector along the x and z - directions, respectively. Now, applying the boundary conditions as in Eqs. (2.3)-(2.7), (2.13)-(2.14), and

the Green's function $G(x, z; x_0, z_0)$ into Eq. (2.15), we obtain the following integral equations corresponding to each of the regions R_1 and R_2

$$\begin{aligned} & -\frac{1}{2}\phi_1 + \int_{\Gamma_{c1}} \phi_1 \left(\frac{\partial G}{\partial n} - ik_0 G \right) d\Gamma + \int_{\Gamma_b} \phi_1 \frac{\partial G}{\partial n} d\Gamma + \int_{\Gamma_p} \left(\phi_1 \frac{\partial G}{\partial n} + i\omega \xi G \right) d\Gamma \\ & + \int_{\Gamma_{c2}} \phi_1 \frac{\partial G}{\partial n} d\Gamma + \int_{\Gamma_{i1}} \left(\phi_2 \frac{\partial G}{\partial n} + G \frac{\partial \phi_2}{\partial n} \right) d\Gamma + \int_{\Gamma_{f2}} \phi_1 \left(\frac{\partial G}{\partial n} - KG \right) d\Gamma \\ & - \int_{\Gamma_{c1}} G \left(\frac{\partial \phi^I}{\partial n} - ik_0 \phi^I \right) d\Gamma = 0, \end{aligned} \quad (2.19)$$

$$\begin{aligned} & -\frac{1}{2}\phi_2 + \int_{\Gamma_{i1}} \left(\phi_2 \frac{\partial G}{\partial n} - G \frac{\partial \phi_2}{\partial n} \right) d\Gamma + \int_{\Gamma_p} \left(\phi_2 \frac{\partial G}{\partial n} - i\omega \xi G \right) d\Gamma + \int_{\Gamma_{c3}} \phi_2 \frac{\partial G}{\partial n} d\Gamma \\ & + \int_{\Gamma_{f1}} \phi_2 \left(\frac{\partial G}{\partial n} - KG \right) d\Gamma = 0. \end{aligned} \quad (2.20)$$

Now, the boundary element method is applied to convert the integral equations as in Eqs. (2.19) - (2.20) into a system of linear algebraic equations under the assumption that ϕ and $\partial\phi/\partial n$ are constants over each of the boundary elements (see Koley et al. [124] for details). The discretized forms of the integral equations Eqs. (2.19) and (2.20) are given by

$$\begin{aligned} & \sum_{j=1}^{N_{c1}} \phi_{1j} (H_{ij} - ik_0 G_{ij}) \Big|_{\Gamma_{c1}} + \sum_{j=1}^{N_b} \phi_{1j} H_{ij} \Big|_{\Gamma_b} + \sum_{j=1}^{N_{c2}} \phi_{1j} H_{ij} \Big|_{\Gamma_{c2}} + \sum_{j=1}^{N_p} (\phi_{1j} H_{ij} + i\omega \xi_j G_{ij}) \Big|_{\Gamma_p} \\ & + \sum_{j=1}^{N_{i1}} \left(\phi_{2j} H_{ij} + G_{ij} \frac{\partial \phi_{2j}}{\partial n} \right) \Big|_{\Gamma_{i1}} + \sum_{j=1}^{N_{f2}} \phi_{1j} (H_{ij} - KG_{ij}) \Big|_{\Gamma_{f2}} - \sum_{j=1}^{N_{c1}} G_{ij} \left(\frac{\partial \phi_j^I}{\partial n} - ik_0 \phi_j^I \right) \Big|_{\Gamma_{c1}} = 0, \end{aligned} \quad (2.21)$$

$$\begin{aligned} & \sum_{j=1}^{N_{i1}} \left(\phi_{2j} H_{ij} - G_{ij} \frac{\partial \phi_{2j}}{\partial n} \right) \Big|_{\Gamma_{i1}} + \sum_{j=1}^{N_p} (\phi_{2j} H_{ij} - i\omega \xi_j G_{ij}) \Big|_{\Gamma_p} + \sum_{j=1}^{N_{c3}} (\phi_{2j} H_{ij}) \Big|_{\Gamma_{c3}} \\ & + \sum_{j=1}^{N_{f1}} \phi_{2j} (H_{ij} - KG_{ij}) \Big|_{\Gamma_{f1}} = 0, \end{aligned} \quad (2.22)$$

where

$$H_{ij} = \frac{1}{2} \delta_{ij} + \int_{\Gamma_j} \frac{\partial G}{\partial n} d\Gamma, \quad G_{ij} = \int_{\Gamma_j} G d\Gamma \quad (2.23)$$

are the influence coefficients and can be evaluated numerically using the Gauss-Legendre quadrature formulae when the field point (x, z) and the source point (x_0, z_0) lies in different boundary element. Whereas in the case of the field point (x, z) and the source point (x_0, z_0) lies in the same boundary element, the singularity occurs. In this case, the influence coefficients need to be solved analytically (see Koley and Sahoo [125], Brebbia and Dominguez [126]) for details). The method of point collocation is used to make the number of equations equal to the number of unknowns. The system of equations (2.21)-(2.22) are rewritten in the matrix form as

the following

$$\begin{aligned} & [\phi_1]([H] - ik_0[G]) \Big|_{\Gamma_{c1}} + [\phi_1][H] \Big|_{\Gamma_b} + [\phi_1][H] \Big|_{\Gamma_{c2}} + ([\phi_1][H] + i\omega[\xi][G]) \Big|_{\Gamma_p} \\ & + [\phi_1]([H] - K[G]) \Big|_{\Gamma_{f2}} + \left([\phi_2][H] + [G] \left[\frac{\partial \phi_2}{\partial n} \right] \right) \Big|_{\Gamma_{i1}} - [G] \left(\left[\frac{\partial \phi_I}{\partial n} \right] - ik_0[\phi_I] \right) \Big|_{\Gamma_{c1}} = 0, \end{aligned} \quad (2.24)$$

$$\begin{aligned} & \left([\phi_2][H] - [G] \left[\frac{\partial \phi_2}{\partial n} \right] \right) \Big|_{\Gamma_{i1}} + ([\phi_2][H] - i\omega[\xi][G]) \Big|_{\Gamma_p} + ([\phi_2][H]) \Big|_{\Gamma_{c3}} \\ & + [\phi_2]([H] - K[G]) \Big|_{\Gamma_{f1}} = 0. \end{aligned} \quad (2.25)$$

Since, the plate deflection ξ is an unknown parameter in Eqs. (2.24) and (2.25), the system of equations (2.24) and (2.25) are not possible to solve at this point. For the same, using the central-difference formula, the plate dynamic boundary condition Eq. (2.8) is discretized and written in the following form

$$\left(\frac{\xi_{j+2} - 4\xi_{j+1} + 6\xi_j - 4\xi_{j-1} + \xi_{j-2}}{\Delta^4} \right) + \mathcal{A}\xi_j = \mathcal{B}(\phi_1^j - \phi_2^j), \quad (2.26)$$

where $\mathcal{A} = -\gamma\omega^2/\Pi$ and $\mathcal{B} = i\omega/\Pi$ with $\Pi = g\chi \left[1 + \frac{\beta^2\varphi\omega}{i + \varphi\omega} \right]$. Now, Eqs. (2.24)-(2.26) are solved together to get the unknowns ϕ , $\partial\phi/\partial n$ and ξ over the corresponding boundaries of the domain.

2.4 Results and discussions

In this section, the computational results associated with the power generated by the PWEC device P_{ext} are plotted and discussed for various values of wave and structural parameters. Coding is performed in MATLAB software for numerical computations and the generation of graphs. Further, the sensitivity analysis is carried out to optimize the performance of the PWEC device for various edge conditions of the piezoelectric plate, including the fixed edge, free edge, and mooring edge conditions. In addition, the performance of the PWEC device is analyzed for variation in the length and submergence depth of the PWEC device, the number of ripples, and the amplitude of ripples of the undulated seabed. The shape of the undulated seabed is taken as the following

$$h(x) = h - a_1 \sin\left(\frac{2m\pi x}{L}\right), \quad 0 < x < L. \quad (2.27)$$

The parameter values associated with the PWEC device, incident wave and the undulated seabed are taken as follows: $h = 10$ m, $l/h = 2.0$, $d/h = 0.1$, $\chi/h^4 = 4.78 \times 10^{-7}$, $\beta = 0.24$, $\varphi = \sqrt{h/g}$, $\gamma/h = 1.258 \times 10^{-3}$, $m = 5$, $a_1/h = 0.32$, $q = 10^3$ N/m and $T_1 = T_0\sqrt{g/h}$ unless

otherwise mentioned. In all the subsequent figures, power generated by the PWEC device is plotted as a function of non-dimensional incident wave period T_1 . For free surface gravity waves, the range of the typical wave period is 1 – 25sec (Mei et al. [127]). While considering the real sea spectrum, for example, in the case of Bretschneider Spectrum (Koley [128]), sea states 3 and 4 are moderate in nature and occur mostly in the marine environment (see Goda [45]) for details). For sea states 3 and 4, most probable wave periods lie within the range 7.5 – 8.75sec. Therefore, we have considered the incident wave periods in the range of 4 – 9sec approximately to cover a wide range of incident wave frequencies under moderate wave climate in the nearshore regions. The wave power generated by the PWEC device is obtained as (see Zheng et al. [41] for details)

$$P_{ext} = \frac{\omega^2 \rho g}{2} \frac{\beta^2 \chi \varphi}{1 + \omega^2 \varphi^2} \int_b^{b+l} |\partial_x^2 \xi|^2 dx. \quad (2.28)$$

Another form of the power generated by the PWEC device is provided in the following. The power generated by the PWEC device can be derived based on the Green's theorem (see Zheng et al. [41] for details)

$$P_{ext} = \frac{i\rho\omega}{4} \int_{-h}^0 \left(\phi \frac{\partial \phi^*}{\partial x} - \phi^* \frac{\partial \phi}{\partial x} \right) \Big|_{x=-l_1} dz. \quad (2.29)$$

To derive the expression of P_{ext} using Eq. (2.29), the far-field boundary condition as in Eq. (2.14) is rewritten as the following

$$\phi_1(x, z) = \phi^I(x, z) + R_c \phi^I(-x, z), \quad (2.30)$$

where R_c is the complex coefficient associated with the reflected waves. Now, by substituting the expression of $\phi_1(x, z)$ as in Eq. (2.30) into Eq. (2.29), the power generated by the PWEC device P_{ext} (Wm^{-1}) is expressed as the following

$$P_{ext} = \frac{\rho g^2 A^2 [\sinh(k_0 h) \cosh(k_0 h) + k_0 h]}{4\omega \cosh^2(k_0 h)} (1 - |R_c|^2). \quad (2.31)$$

2.4.1 Model validation

Before proceeding with various results and discussions, the present computational results need to be validated with standard results available in the literature. In Fig. 2.2, the power generated by the PWEC device P_{ext} (Wm^{-1}) is plotted as a function of incident wave period T_0 for the case when the PWEC is moored on the breakwater. The remaining parameters are same as provided in Buriani and Renzi [4] (see Fig. 4 of Buriani and Renzi [4]). From Fig. 2.2, it is seen that the present computed results are matched well with the results provided by Buriani and Renzi [4].

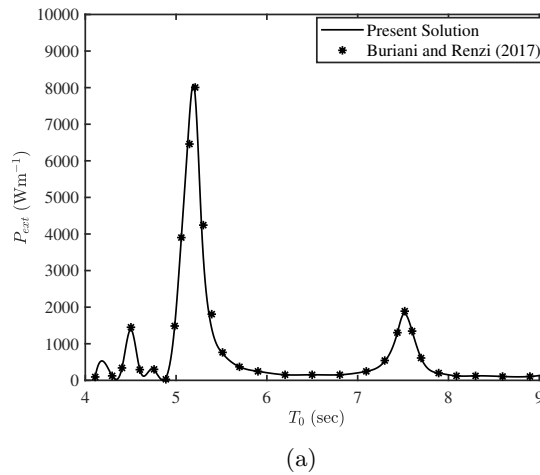


FIGURE 2.2: P_{ext} vs. T_0 . Lines represent the solutions obtained by the present boundary element method and symbols represent the solutions provided in Buriani and Renzi [4].

2.4.2 Numerical convergence

In this subsection, the numerical convergence of the boundary element method-based results is discussed with respect to the variation in submergence depth of the PWEC plate. The convergence of the boundary element method depends on the panel size (see Wang and Meylan [129] for details). The panel size is proportional to the wavelength of the incident wave, and therefore, the panel size is inversely proportional to the wavenumber k_0 . So, the panel size P_s can be expressed in the form

$$P_s = \frac{1}{\kappa k_0}, \quad (2.32)$$

where the proportionality constant κ is determined from the numerical convergence study. In Table 2.1, the variation of the reflection coefficient $|R_c|$ is plotted for various non-dimensional incident wave period T_1 and submergence depth d/h of the PWEC plate. From Table 2.1, it is concluded that the numerical results obtained using BEM converges well for $\kappa \geq 50$. In the following results, the graphs are plotted by taking the panel size $\kappa = 50$.

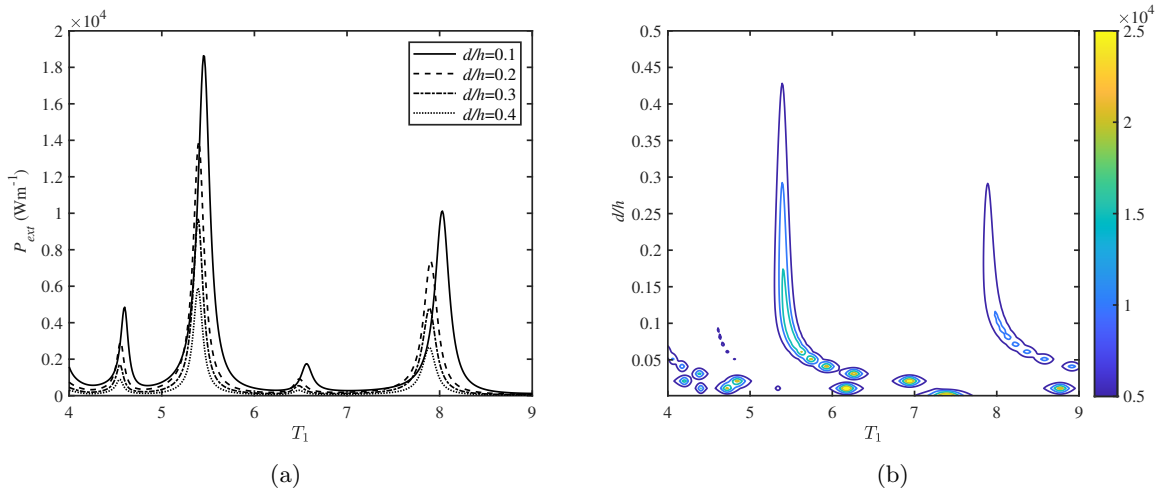
2.4.3 PWEC device with fixed edges

In this subsection, the performance of the PWEC device is analyzed for various wave, structural and seabed parameters when the front edge of the plate is attached to a floating buoy and the lee edge of the plate is attached to the rigid and impermeable front wall of the breakwater such that the fixed edge conditions are valid on both edges (see Eq. (2.10)).

In Fig. 2.3(a), the variation of the wave power generated by the PWEC device P_{ext} is plotted as a function of incident wave period T_1 for various values of submergence depth d/h of the PWEC plate. It is clearly seen from Fig. 2.3(a) that a number of distinct peaks occur in the

TABLE 2.1: Reflection coefficient $|R_c|$ in presence of PWEC plate when both the edges are fixed in nature.

| T_1 | κ | $d/h = 0.1$ | $d/h = 0.2$ | $d/h = 0.3$ | $d/h = 0.4$ |
|-------|----------|-------------|-------------|-------------|-------------|
| 5 | 30 | 0.98425 | 0.98364 | 0.98728 | 0.98845 |
| | 40 | 0.98429 | 0.98369 | 0.98610 | 0.98850 |
| | 50 | 0.98435 | 0.98371 | 0.98604 | 0.98859 |
| | 60 | 0.98438 | 0.98372 | 0.98602 | 0.98858 |
| 6 | 30 | 0.99668 | 0.98002 | 0.99882 | 0.99929 |
| | 40 | 0.99670 | 0.99815 | 0.99884 | 0.99931 |
| | 50 | 0.99671 | 0.99816 | 0.99885 | 0.99932 |
| | 60 | 0.99671 | 0.99816 | 0.99885 | 0.99932 |
| 7 | 30 | 0.98019 | 0.98035 | 0.98083 | 0.99847 |
| | 40 | 0.98023 | 0.98039 | 0.98087 | 0.98132 |
| | 50 | 0.98027 | 0.98042 | 0.98091 | 0.98136 |
| | 60 | 0.98028 | 0.98043 | 0.98092 | 0.98138 |

FIGURE 2.3: (a) P_{ext} vs. T_1 , and (b) contour plot of P_{ext} as a function of T_1 and d/h when the PWEC plate edge conditions are fixed.

P_{ext} curve irrespective of the variation in the submergence depth d/h . This can be explained from Eq. (2.28). See, the mean extracted power P_{ext} depends on the square of the plate curvature. Consequently, the short-crested component of the hydroelastic wave significantly affects the power generation P_{ext} of the PWEC device (see Renzi [3] for details). Therefore, the above-mentioned resonating peaks in power generated by the PWEC device P_{ext} occur due to the matching between the wavelengths of the natural plate vibration and the wavelength of the short-crested component of the hydroelastic wave. Moreover, it is seen that the height of the resonating peaks in the power generation P_{ext} curve increases as the submergence depth d/h of

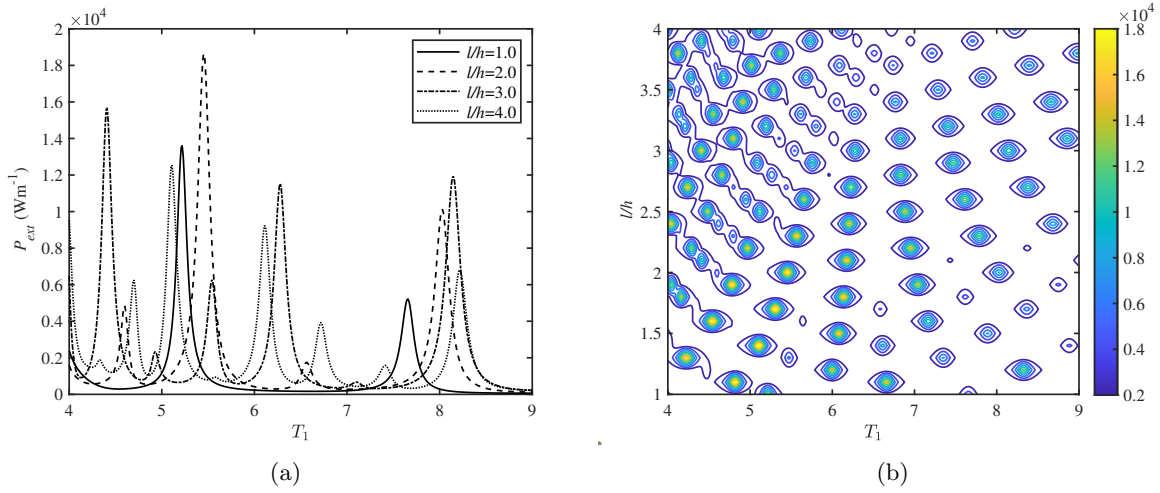


FIGURE 2.4: (a) P_{ext} vs. T_1 , and (b) contour plot of P_{ext} as a function of T_1 and l/h when the PWEC plate edge conditions are fixed..

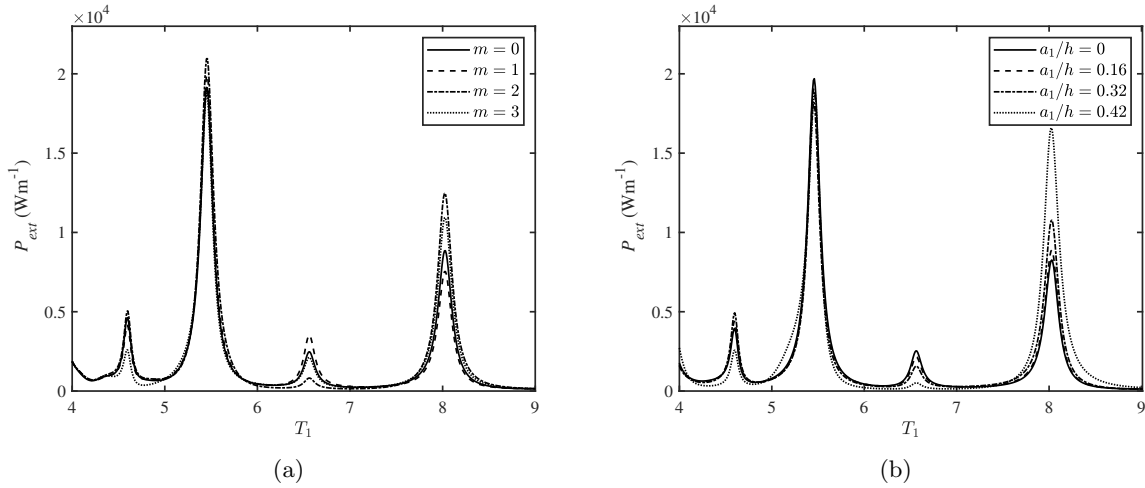


FIGURE 2.5: P_{ext} vs. T_1 for various values of (a) m , and (b) a_1/h when the PWEC plate edge conditions are fixed.

the PWEC decreases. A similar observation is found in Zheng et al. [41]. The reason behind this phenomenon is that the wave energy concentration is more near to the free surface. Further, it is observed that certain shifts in the positions of the resonating peaks in the power generation P_{ext} curve occur due to the change in submergence depth d/h of the plate. This phase shift occurs due to the complex coefficient in the fourth-order equation of the plate (see Eq. (2.8)). To demonstrate the effect of incident wave period T_1 and plate submergence depth d/h on the power generation P_{ext} , a contour plot of P_{ext} as functions of T_1 and d/h is provided in Fig. 2.3(b). It is seen that the resonances in the power generation P_{ext} occur for moderate values of incident wave period T_1 when the PWEC is situated near to the mean free surface $z = 0$.

Fig. 2.4(a) depicts the variation in the power generation by the PWEC device P_{ext} as a function of incident wave period T_1 for various values of the PWEC plate length l/h . It is clearly seen

that the number of peaks associated with the resonances of the power generation P_{ext} curve increases with an increase in plate length l/h of the PWEC device. The reason behind these resonating peaks is that the frequencies associated with the natural vibration of the PWEC plate (having fixed edges) becomes lower as the PWEC plate length increases. Consequently, the possibility of matching between the natural frequency of the PWEC plate and the frequency of the hydroelastic wave. The short-crested component of the flexural waves travelling on the plate is responsible for the resonant behaviour of the PWEC device. It is to be noted that the resonant periods are directly proportional to the density ratio and the length of the PWEC plate, and inversely proportional to its stiffness. Therefore, such parameters could be optimized to make the device resonate with the most energetic sea states in a given ocean waves. As mentioned in Renzi (2016), for $\varphi = 0$, the approximated expression for the resonant periods of the system is given by

$$T_p \approx 16 \sqrt{\frac{r l}{(p + 0.5)^5 \pi^3 \chi \rho g^2}}, \quad p = 1, 2, \dots \quad (2.33)$$

where $r = \frac{\rho l}{\rho_0 d_0 + 2\rho_p d_p}$ with ρ_0 , ρ_p and ρ being the densities of the substrate, piezoelectric layers, and fluid, respectively. Further, d_0 and d_p represent the thicknesses of the substrate and the piezoelectric layers, respectively. The bimorph piezoelectric plate is characterised by $d_0 = 0.01\text{m}$, $d_p = 1.1 \times 10^{-4} \text{ m}$, $\rho_0 = 1250 \text{ Kg/m}^3$, $\rho_p = 1780 \text{ Kg/m}^3$. Because of the presence of dissipation owing to both radiation damping and wave energy extraction, the resonant period in the present scenario will slightly change than the obtained value as mentioned in the earlier equation. The resonant period (s), approximated value (s) and the corresponding eigen value associated with the resonating peaks are provided in the following Table. 2.2. The eigen values responsible for the resonating periods are obtained from the Sturm-Liouville problem associated with the plate equation when the external force and the short circuit conditions are zero. The eigenvalues are

$$\mu = \mu_p \approx \left(p + \frac{1}{2}\right) \frac{\pi}{2}, \quad p = 1, 2, 3, \dots$$

To demonstrate the effect of incident wave period T_1 and PWEC plate length l/h on the power generation P_{ext} , a contour plot of P_{ext} as functions of T_1 and l/h is provided in Fig. 2.4(b). It is observed that for certain combinations of plate length l/h and incident wave period T_1 , the power generation by the PWEC device P_{ext} becomes higher. To obtain the appropriate combinations of T_1 and l/h which can generate more wave power P_{ext} , a quadratic polynomial regression model is used to fit the set of points where the power generation is more than 13000Wm^{-1} . In the present case, the following relation is obtained

$$l/h = 0.0985 T_1^2 - 0.9669 T_1 + 4.0787. \quad (2.34)$$

Eq. (2.34) depicts that the PWEC device having length $2.0 \leq l/h \leq 2.5$ is capable of generating

TABLE 2.2: Resonant period (s) approximated value (s) and corresponding eigenvalues

| l/h | Resonant period (s) | Approximated value (s) | Eigen values |
|-----------|---------------------|------------------------|--------------|
| $l/h = 2$ | 8 | 7.61 | p=12 |
| | 6.5 | 6.28 | p=13 |
| | 5.4 | 5.25 | p=14 |
| | 4.6 | 4.44 | p=15 |
| $l/h = 3$ | 8.1 | 7.69 | p=13 |
| | 6.6 | 6.43 | p=14 |
| | 5.6 | 5.44 | p=15 |
| | 4.9 | 4.65 | p=16 |
| | 4.5 | 4.02 | p=17 |
| $l/h = 4$ | 8.3 | 8.8 | p=13 |
| | 6.8 | 7.43 | p=14 |
| | 6.2 | 6.3 | p=15 |
| | 5.2 | 5.37 | p=16 |
| | 4.7 | 4.64 | p=17 |
| | 4 | 4.04 | p=18 |

maximum power P_{ext} for a wide range of incident wave periods T_1 . This observation is also seen in Fig 2.4(b).

The effects of the parameters associated with the undulated seabed, i.e., the number of ripples m and the ripple amplitude a_1/h of the sinusoidally varying seabed (as in Eq. (2.27)) on the power generation P_{ext} by the PWEC device is shown in Figs. 2.5(a) and 2.5(b). It is seen from both the figures that the resonances in the power generation P_{ext} curve occur for the same incident wave period T_1 irrespective of variation in the number of ripples m and the ripple amplitude a_1/h . This is due to the fact that the natural frequency for the PWEC plate vibration does not change due to the variations of the undulated bed. Further, due to the presence of the plate near the free surface, a major amount of wave energy is absorbed by the plate, and so the bottom impact on the wave propagation is reduced significantly.

2.4.4 PWEC device having fixed rear edge and free front edge

In this subsection, the performance of the PWEC device is analyzed for various wave, structural, and seabed parameters when the front edge is free, and the rear edge is fixed on the breakwater (see Eqs. (2.10) - (2.11)).

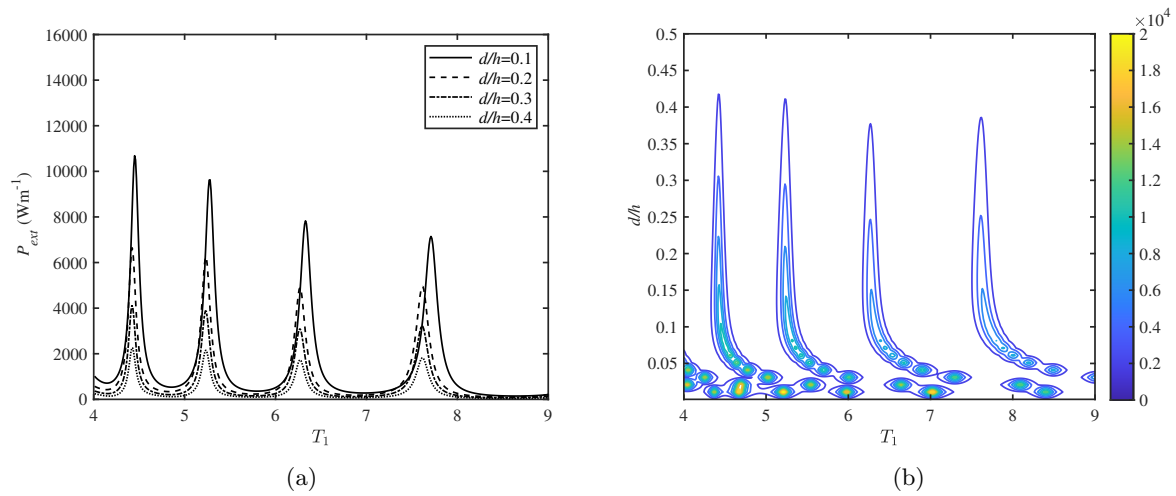


FIGURE 2.6: P_{ext} vs. T_1 , and (b) contour plot of P_{ext} as a function of T_1 and d/h when the PWEC device having fixed rear edge and free front edge.

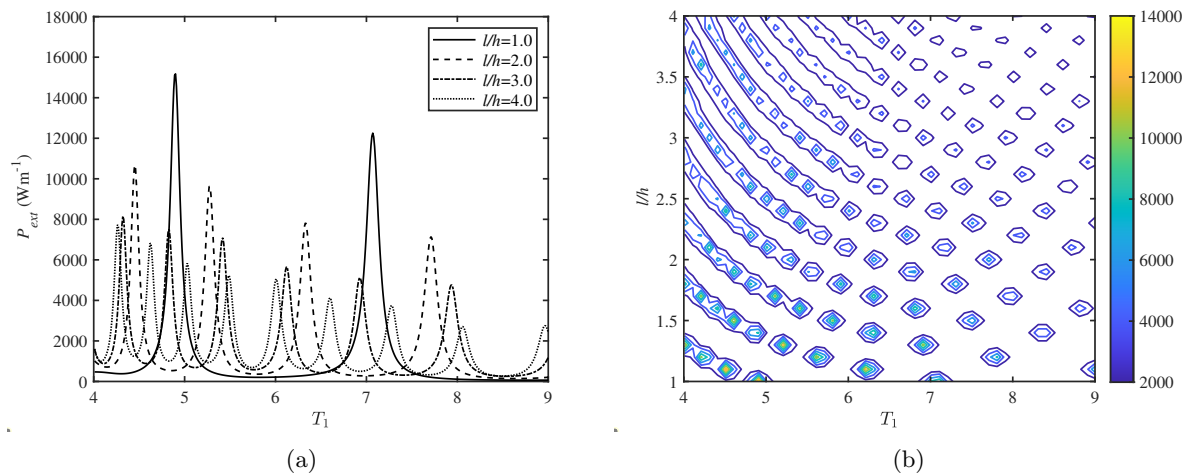


FIGURE 2.7: (a) P_{ext} vs. T_1 , and (b) contour plot of P_{ext} as a function of T_1 and l/h when the PWEC device having fixed rear edge and free front edge.

In Fig. 2.6(a), the variation of the wave power generated by the PWEC device P_{ext} is plotted as a function of incident wave period T_1 for various values of submergence depth d/h of the PWEC plate. It is clearly seen from Fig. 2.6(a) that a number of resonating peaks occur for different values of incident wave periods T_1 . Moreover, it is also seen that for each of the depth parameter values d/h , all the resonating peaks occur within a small neighborhood of the same wave period T_1 . In addition, Fig. 2.6(a) demonstrates that the amplitude of the resonating peaks is more when the submergence depth d/h of the PWEC plate is less, i.e., when the PWEC plate is placed near to the free surface. The reason for the same is already mentioned in Fig. 2.3(a). A comparison between Figs. 2.6(a) and 2.3(a) reveals that the wave power generated by the PWEC device P_{ext} is more when the front edge of the PWEC plate is free as compared to the case when the front edge is fixed for a wider range of incident wave period T_1 and submergence

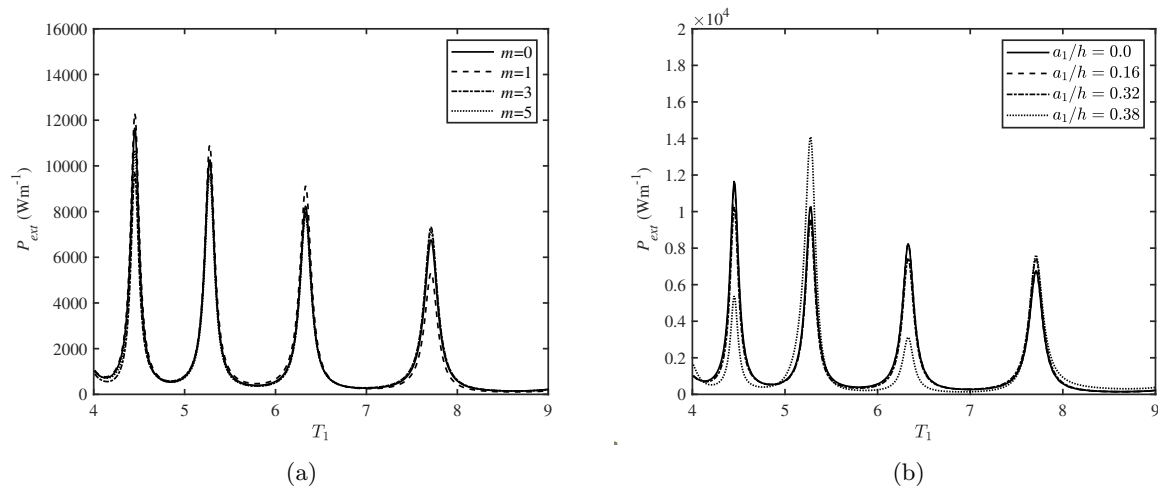


FIGURE 2.8: P_{ext} vs. T_1 for various values of (a) number of ripples m , and (b) ripple amplitude a_1/h of the sinusoidal seabed when the PWEC device having fixed rear edge and free front edge.

depth d/h . This particular result is clearly visible while comparing Figs. 2.6(b) with 2.3(b). Further, it is seen that the number of resonances is more when the PWEC plate is positioned near to the free surface in the case when the front edge of the plate is free as compared to the fixed edge.

Fig. 2.7(a) depicts the variation in the power generation by the PWEC device P_{ext} as a function of incident wave period T_1 for various values of the PWEC plate length l/h . It is observed that the number of resonating peaks increases, whereas the amplitude of the resonating peaks reduces gradually as the PWEC plate length l/h increases. The reason for this phenomenon is already mentioned in the discussion of Fig. 2.4(a). A comparison between Figs. 2.7 and 2.4 reveals that the resonating peaks occur more for smaller plate length when the front edge of the PWEC is free. Whereas, for a plate having a fixed front edge, the resonance in power generation P_{ext} occurs for moderate and smaller values of PWEC plate length l/h . To analyze the effect of PWEC plate length l/h and incident wave period T_1 on the resonances in power generation P_{ext} , a quadratic polynomial regression model is adopted, and the same is obtained as the following

$$l/h = -0.0859 T_1^2 + 0.6855 T_1 + 0.4572. \quad (2.35)$$

Eq. (2.35) depicts that the PWEC device having a length in the range of $1.2 \leq l/h \leq 2.0$ is suitable to generate maximum power P_{ext} by the PWEC device having a free front edge and fixed rear edge.

The effect of the sinusoidally varying bottom undulation (as in Eq. (2.27)) on the power generation by the PWEC device P_{ext} is demonstrated in Figs. 2.8(a) and 2.8(b). Fig. 2.8(a) shows that the power generation by the PWEC device P_{ext} doesn't vary much due to the variation in the number of ripples m of the seabed except at positions where resonances occur. The reason

behind the same is that a major amount of incoming wave energy is absorbed by the PWEC plate, which is placed above the undulated bottom and nearer to the free surface. On the other hand, in Fig. 2.8(b), it is seen that the amplitude of the undulated seabed has a significant effect on the power generation P_{ext} by the PWEC device.

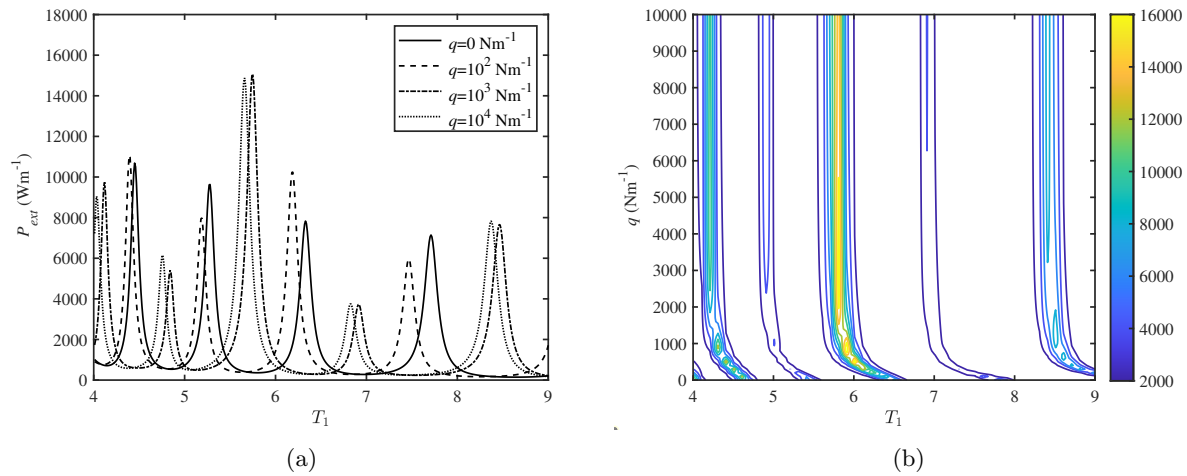


FIGURE 2.9: (a) P_{ext} as a function of T_1 for various values of mooring stiffness q (Nm^{-1}), and (b) contour plot of P_{ext} as a function of T_1 and q (Nm^{-1}).

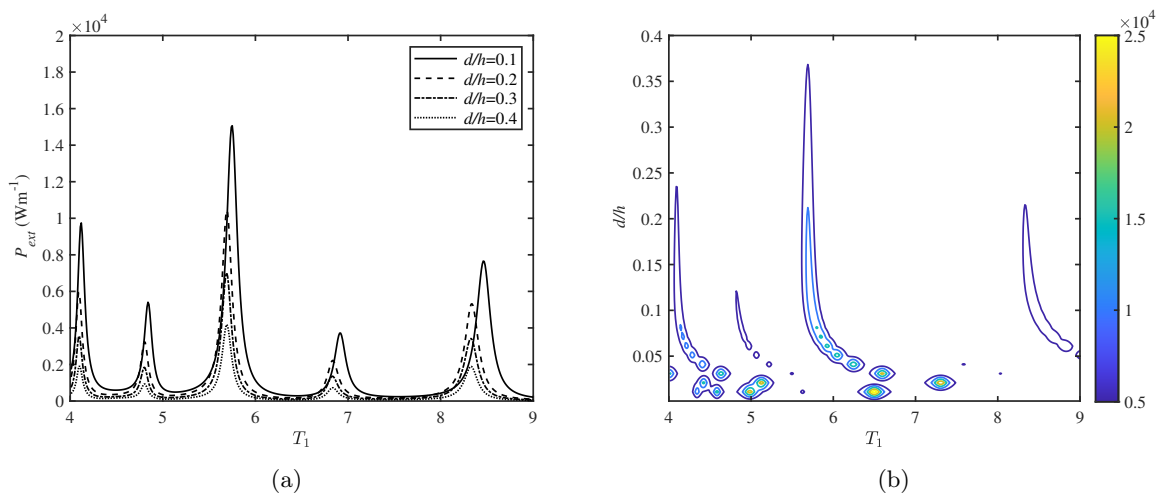


FIGURE 2.10: P_{ext} vs. T_1 , and (b) contour plot of P_{ext} as a function of T_1 and d/h .

2.4.5 PWEC device having fixed rear edge and moored front edge

In Fig. 2.9(a), the variation of the wave power generated by the PWEC device P_{ext} is plotted as a function of incident wave period T_1 for various values of the stiffness parameter q of the mooring line attached to the front edge of the PWEC device. It is to be noted that the stiffness parameter $q = 0$ corresponds to the free edge boundary conditions of the PWEC plate. It is observed that certain shifts in the resonating peaks occur due to the variation in mooring

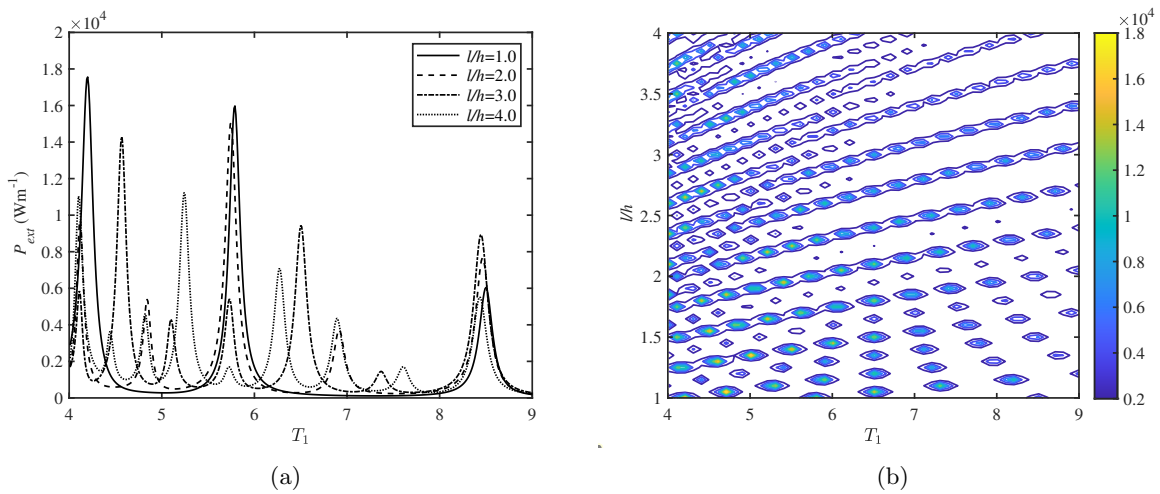


FIGURE 2.11: (a) P_{ext} vs. T_1 , and (b) contour plot of P_{ext} as a function of T_1 and l/h .

stiffness parameter q . This happens as the natural vibration of the PWEC plate will change due to the variation in the mooring stiffness, and consequently, resonating peaks in the power generation P_{ext} curve occur for different values of incident wave period T_1 . These shifts in the resonating peaks are clearly seen in Fig. 2.9(b). It is also seen that for $5.5 < T_1 < 6.5$, the wave power generated by the PWEC device P_{ext} initially increases as the mooring stiffness q takes higher values, and then after a threshold value of the mooring stiffness q , the variation on the power generation by the PWEC device P_{ext} is significantly less.

In Fig. 2.10(a), the variation of the wave power generated by the PWEC device P_{ext} is plotted as a function of incident wave period T_1 for various values of submergence depth d/h of the PWEC plate. The overall pattern of the power generation curve P_{ext} as seen in Fig. 2.10(a) is similar in nature to that of Figs. 2.3(a) and 2.6(a). A comparison among Figs. 2.10(a), 2.3(a) and 2.6(a) reveals that the amplitude of resonating peaks P_{ext} is higher for PWEC plate having fixed front edge as compared to free and moored front edges of the PWEC plate. In Fig. 2.10(b), the contour plot of power generation P_{ext} by the PWEC device is plotted as functions of incident wave period T_1 and submergence depth d/h of the PWEC plate. A comparison among Figs. 2.10(b), 2.3(b) and 2.6(b) depicts that the PWEC plate having free front edge generates higher amount of wave power P_{ext} for a wider range of incident wave periods T_1 and submergence depth d/h as compared to PWEC plate having fixed and moored edges.

In Fig. 2.11(a), the variation of the wave power generated by the PWEC device P_{ext} is plotted as a function of incident wave period T_1 for various values of PWEC plate length l/h . It is observed that the overall pattern of the resonances associated with the power generation P_{ext} by the PWEC device is similar in nature to that of Figs. 2.4(a) and 2.7(a). It is clearly seen that the number of resonating peaks for the PWEC plate having moored and fixed front edges is more as compared to the PWEC plate having free front edges. This happens due to the

reason that for the PWEC plate having free and moored front edges (having moderate mooring stiffness), the natural vibration frequency is less as compared to the PWEC plate having fixed edges. To analyze the effect of the PWEC plate length l/h and incident wave period T_1 on the resonances of power generation P_{ext} by the PWEC device, a quadratic polynomial regression model is adopted, and the same is obtained as the following

$$l/h = 0.0252 T_1^2 - 0.4735 T_1 + 3.7201. \quad (2.36)$$

Eq. (2.36) depicts that the PWEC device having a smaller length is suitable to generate more wave power P_{ext} on those locations having smaller incident wave periods T_1 . Further, Eq. (2.34) shows that PWEC device having length l/h in range $1.5 \leq l/h \leq 2.3$ is suitable to generate maximum power P_{ext} for a wider range of incident wave period.

It is to be noted that the effect of the sinusoidally varying bottom undulation on the power generation by the PWEC device P_{ext} when the front edge is moored is similar in nature to that of Figs. 2.5 and 2.8. For this reason, the details are deferred here.

2.4.6 Effect of plate lee edge conditions on the power generation

Figs. 2.12(a)-2.12(c) show the variation of the wave power generated by the PWEC device P_{ext} for the fixed and moored lee edge conditions when the front edge of the plate is fixed, free, or moored type. From these figures, it is clearly observed that the overall wave power generated by the PWEC device P_{ext} is significantly higher when the lee side of the PWEC plate is fixed in nature as compared to the mooring edge condition. Further, it is seen that the number of resonating peaks as well as the associated amplitudes of the peaks is higher for PWEC plate having fixed lee edge as compared to moored lee edge. A comparison among Figs. 2.12(a)-2.12(c) reveals that the PWEC plate having a free front edge can generate a higher amount of wave power P_{ext} for a wider range of incident wave period T_1 as compared to PWEC plate having fixed and moored front edges.

It is to be noted that the proposed PWEC device can be used in sea crossing bridges, oil platforms, windmills, etc. to power electricity to run low-power electronic devices such as LED lights, wind velocity and direction sensors, stress-strain sensors, vibration sensors, and temperature sensor, etc. (Qi et al. [43]). The traditional way to power these devices were either to use a long-distance electric line or to use batteries. These long-distance electric lines cause huge electric power loss and are far costlier than the proposed PWEC device. The battery power method causes environmental problems due to electromechanical pollution. The study in this work depicts that the power generated by the PWEC device is maximum if the edges are fixed in nature. Hence, in practice, it is possible to install the PWEC device integrated with the

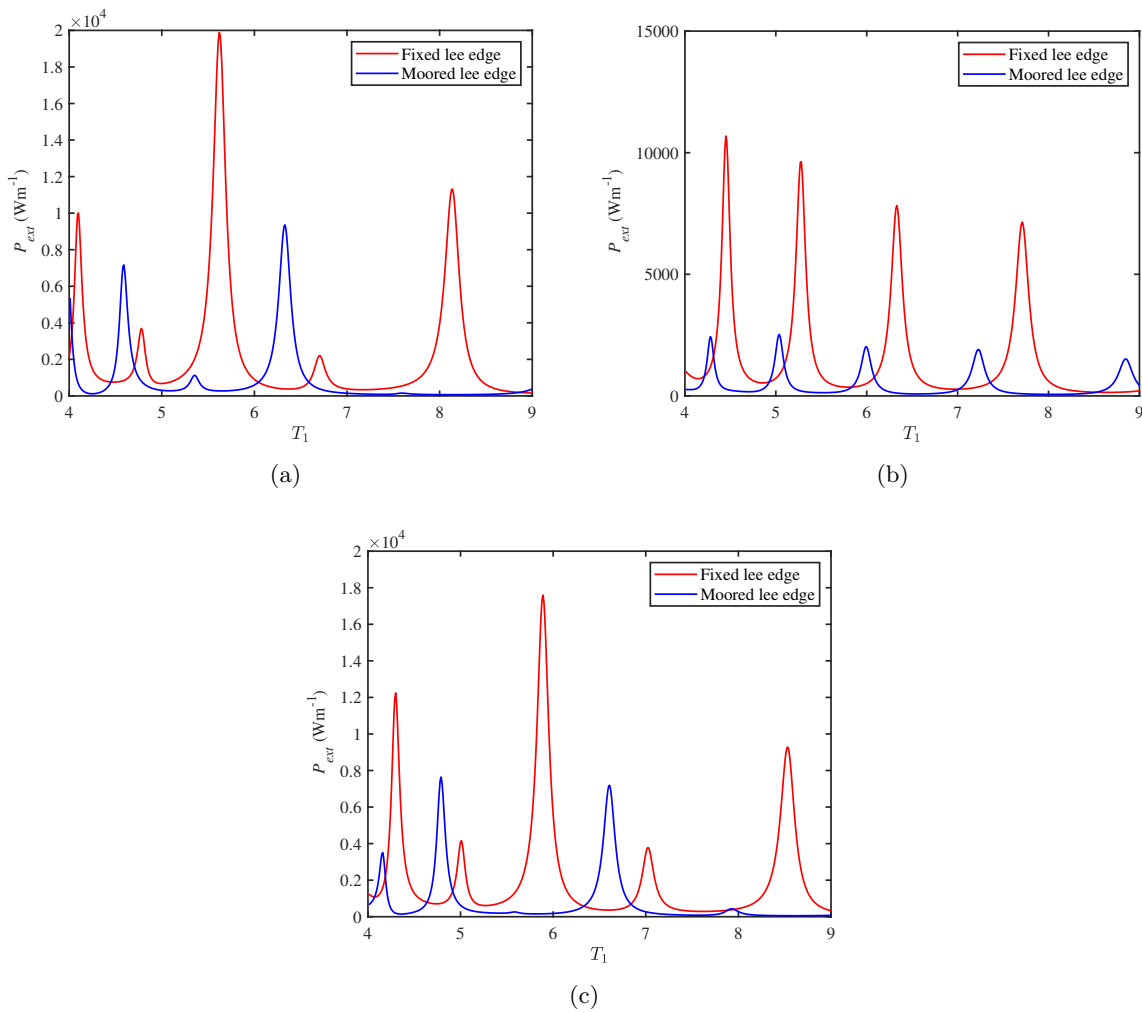


FIGURE 2.12: Comparison of P_{ext} for fixed and moored lee edges when the front edge is (a) fixed, (b) free, or (c) moored.

pillars of the offshore structures using fixed edge boundary conditions. Further, the engineers can also integrate multiple PWEC devices at the same pillars of the offshore structures without hitting each other. It is to be noted that the electric power generated by the PWEC device is irregular, and therefore, it must be regulated and stabilized. The rectifying circuit can be made of diodes with low power and high precision, and a capacitor can be used for voltage regulation (see Qi et al. [43] for details). Finally, the rectified and stabilized electric power generated by the PWEC device can be used to power low-power electronic devices as mentioned earlier.

The drawbacks of using PWEC devices to generate electricity are the following. The narrow bandwidth of the highest resonating peaks for the power generated by the PWEC device depicts that the energy generation is irregular. Hence, the power generated by the PWEC device should be stabilized by an external rectifying circuit before putting the energy on the grid. Further, the PWEC device can convert only around 10% of the available ocean energy into useful electric energy (see Wang [130]). While comparing the power generated by the PWEC device with other

wave energy converter devices, the PWEC device generated less electric power than other wave energy converter devices because of the energy transduction principle (see Ahamed et al. [131]).

2.5 Conclusions

In this study, the performance of a submerged PWEC device attached to an impermeable vertical breakwater placed over an undulated seabed is analyzed for various parameters associated with the incident waves, PWEC plate, and undulated seabed. Major emphasis is given to analyze the effect of PWEC plate submergence depth, plate length, plate edge conditions, incident wave period, bottom ripple amplitude, and ripple number on the power generation by the PWEC device. Major conclusions obtained from the present study are summarized in the following:

- The results demonstrated that the overall wave power generated by the PWEC device is significantly higher when the lee side of the PWEC plate is fixed in nature as compared to moored edge condition. Further, the number of resonating peaks and associated amplitudes are also higher for the PWEC device with a fixed type lee edge.
- The maximum peak in the wave power generation curve is observed for PWEC devices with fixed-type front edges. In contrast, it is seen that the PWEC device with free and moored type front edges generates moderate wave power for a wider range of incident wave periods.
- As the length of the PWEC device increases, the number of resonating peaks in the wave power generation curve increases gradually. Further, it is also observed that the PWEC device having moderate length can generate maximum wave power for a wider range of incident wave periods.
- As the submergence depth of the PWEC device increases, the wave power generated by the PWEC device decreases gradually, irrespective of the PWEC device edge conditions.
- The power generated by the PWEC device doesn't vary much due to the variation in the number of ripples and ripple amplitude of the seabed except at positions where resonances occur.

In summary, it is concluded that the plate edge conditions and various parameters associated with the PWEC device can be optimized to generate maximum wave power for a wider range of incident wave frequencies. The present study will be extended for irregular and multi-directional incident waves in the near future.

Chapter 3

Performance and optimization of design parameters of standalone piezoelectric wave energy converter devices

* The work, in this chapter, is covered by the following publications:

1. Vipin, V., Trivedi, K., Koley, S. (2022). Performance of a submerged piezoelectric wave energy converter device floating over an undulated seabed. *Energy Reports*, 8, 182-188.
2. Vipin, V., Trivedi, K., Koley, S. (2022). Performance of a submerged piezoelectric wave energy converter device in time domain. *Energy Reports*, 8, 309-314.
3. Vipin, V., Koley, S. (2023). Design optimization of a submerged piezoelectric wave energy converter device using an artificial neural network model. *Energy Reports*, 9, 322-326.

3.1 General introduction

In this chapter, the power absorption by a submerged piezoelectric wave energy converter (PWEC) in the frequency domain and the time-dependent displacement of the free surface and the PWEC plate deflection are discussed. Further, the prediction of power generation by the device and the optimization of the device parameters using an artificial neural network model, namely the multilayer perceptron model, are discussed. The problem is studied initially for the case when PWEC plate is situated over an undulated seabed. However, in the parameters optimization process, the seabed is considered uniform in nature as the effect of bottom undulation is negligible. Here, the PWEC plate is considered standalone without attaching the same with an existing breakwater. The boundary element method (BEM) is used to solve the frequency domain problem. Further, the Fourier transform is utilized to convert the frequency domain results into time domain. In time domain analysis, emphasis is given to analyze the the plate deflection and the free surface displacement. The input database for the ANN model building is generated using the latin hypercube sampling method (LHS), and the corresponding target variable is calculated using the BEM-based numerical tool. After the ANN model building, the optimization of the design parameters of the PWEC device is carried out using a database containing 3000 sample points generated randomly using the LHS method. These generated input samples will be passed through the developed ANN model, and the predicted response variable provides a range for the geometric parameters associated with the PWEC device to optimize the power generation.

3.2 Mathematical formulation

In the present problem, the performance of a piezoelectric wave energy converter (PWEC) device placed over an undulated seabed with fixed edge conditions on both the edges of the PWEC plate is studied in both the frequency domain as well as in the time domain. The schematic diagram depicting the vertical cross-section of the physical problem is given in Fig. 3.1. To model the hydrodynamics associated with the PWEC device, a two-dimensional Cartesian coordinate system is considered with the direction of wave propagation coinciding with the x -axis and the z -axis pointing vertically upwards from the mean free surface. It is assumed that the regular ocean waves of amplitude A and angular frequency ω impinge on the PWEC plate. Here, $A/\lambda \ll 1$ is considered with λ being the incident wavelength so that the small-amplitude wave theory is applicable for the present study. The PWEC device of length l is placed at a submergence depth d from the mean free surface $z = 0$ and occupies the region $b \leq x \leq b+l$ along the x -axis. The PWEC plate is floating over an undulated finitely extended seabed represented by $z = -H(x)$. To solve the associated boundary value problem using the boundary element method, two auxiliary boundaries Γ_{c1} and Γ_{c2} are considered at $x = -l_1$ and $x = r$, respectively. These auxiliary boundaries Γ_{c1} and Γ_{c2} are situated sufficiently far away from the PWEC device

and the undulated bottom so that the effect of local wave modes vanishes on the auxiliary boundaries. Moreover, another two auxiliary boundaries Γ_{i1} and Γ_{i2} are considered at $x = b + l$ and $x = b$, respectively. Consequently, the physical domain is divided into two regions R_j for $j = 1, 2$ with $R_2 = \{b < x < b + l, -d < z < 0\}$ and $R_1 = \{-l_1 < x < r, -H(x) < z < 0\} \setminus R_2$ as shown in Fig. 3.1. The water flow is assumed to be incompressible, inviscid, and irrotational in nature, along with the motion being harmonic in time with the angular frequency ω . These aforementioned assumptions provide certainty about the existence of the velocity potentials of the following form

$$\Phi_j(x, z, t) = \Re \{ \phi_j(x, z) e^{-i\omega t} \}, \quad \text{for } j = 1, 2, \quad (3.1)$$

where Φ_j represent the velocity potentials for the regions R_j for $j = 1, 2$. Further, the spatial velocity potentials ϕ_j for $j = 1, 2$ satisfy

$$\left(\frac{\partial^2}{\partial x^2} + \frac{\partial^2}{\partial z^2} \right) \phi_j = 0. \quad (3.2)$$

The boundary conditions on the mean free surfaces $\Gamma_{f1} = \{b + l < x < r, z = 0\}$, $\Gamma_{f2} = \{b < x < b + l, z = 0\}$ and $\Gamma_{f3} = \{-l_1 < x < b, z = 0\}$ are given by

$$\frac{\partial \phi_j}{\partial z} = K \phi_j, \quad \text{on } \Gamma_{fj}, \quad \text{for } j = 1, 2, 3, \quad (3.3)$$

where $K = \omega^2/g$ with g represents the acceleration due to gravity. The seabed is considered to

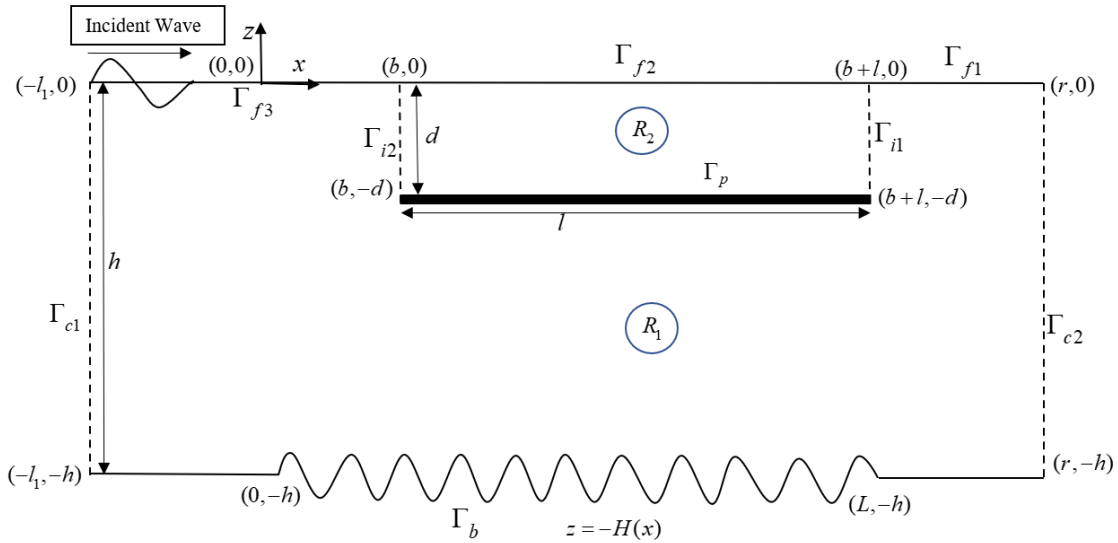


FIGURE 3.1: Schematic diagram of the physical problem.

be rigid and impermeable in nature. Therefore, the bottom boundary condition on Γ_b is given by

$$\frac{\partial \phi_1}{\partial n} = 0, \quad \text{on } z = -H(x), \quad (3.4)$$

where $\partial/\partial n$ represents the normal derivative and $H(x)$ represents the bottom topography

$$H(x) = \begin{cases} h, & x < 0 \cup x > L, \\ h(x), & 0 < x < L. \end{cases} \quad (3.5)$$

Here, $h(x)$ represents the undulated sinusoidal seabed. A uniform seabed is considered for the optimization of the design parameters of the PWEC device. The bottom topography in this case can be defined as

$$H(x) = h, \quad -l_1 < x < r. \quad (3.6)$$

The plate deflection $\xi(x, t)$ is assumed to be time harmonic in nature and takes the form $\xi(x, t) = \Re \{ \xi(x) e^{-i\omega t} \}$. Now, the kinematic boundary condition on Γ_p is same as given in Eq. (2.7). The dynamic boundary condition on the piezoelectric plate surface Γ_p is given by Eqs. (2.8) and Eq. (2.9). Now, we need to provide the appropriate plate edge conditions. As the plate edges are assumed to be fixed, the edge conditions of the plate are given by

$$\xi = 0, \quad \frac{\partial \xi}{\partial x} = 0, \quad \text{at } x = b, b + l. \quad (3.7)$$

The continuity of pressure and normal velocity along the auxiliary boundary Γ_{i1} and Γ_{i2} are given by

$$\phi_1 = \phi_2, \quad \frac{\partial \phi_1}{\partial n} = -\frac{\partial \phi_2}{\partial n}, \quad \text{on } \Gamma_{i1} \cup \Gamma_{i2}. \quad (3.8)$$

Finally, the far-field boundary conditions on Γ_{c1} and Γ_{c2} are given by

$$\begin{cases} \frac{\partial(\phi_1 - \phi^I)}{\partial x} + ik_0(\phi_1 - \phi^I) = 0, & \text{on } \Gamma_{c1}, \\ \frac{\partial \phi_1}{\partial x} - ik_0 \phi_1 = 0, & \text{on } \Gamma_{c2}, \end{cases} \quad (3.9)$$

where $\phi^I(x, z) = e^{ik_0 x} f_1(k_0, z)$ represents the incident wave potential. Here, $f_1(k_0, z) = \left(\frac{-igA}{\omega} \right) \frac{\cosh(k_0(z+h))}{\cosh(k_0 h)}$ with k_0 being the positive root of the dispersion relation $K = gk_0 \tanh(k_0 h)$.

3.3 Numerical method of solution

In this section, the boundary element method-based solution technique is applied to solve the physical problem formulated in Section 2. Firstly, the boundary value problem formulated in Section 2 is converted into a system of integral equations. These integral equations are derived in terms of the velocity potentials and their normal derivatives using the Green's second identity along with the free space Green's function and using the boundary conditions derived in Section

2. The Green's identity is given by

$$\frac{1}{2}\phi(x_0, z_0) = \int_{\Gamma} \left(\phi(x, z) \frac{\partial G(x, z; x_0, z_0)}{\partial n} - G(x, z; x_0, z_0) \frac{\partial \phi(x, z)}{\partial n} \right) d\Gamma(x, z). \quad (3.10)$$

The form of the free space Green's function $G(x, z; x_0, z_0)$ used in Eq. (3.10) is given by

$$G(x, z; x_0, z_0) = \frac{1}{2\pi} \ln(r), \quad \text{where } r = \sqrt{(x - x_0)^2 + (z - z_0)^2}, \quad (3.11)$$

with (x, z) and (x_0, z_0) being the field and source points respectively. For the present problem, $G(x, z; x_0, z_0)$ satisfies

$$\Delta^2 G(x, z; x_0, z_0) = \delta(x - x_0)\delta(z - z_0), \quad \Delta^2 \equiv \left(\frac{\partial^2}{\partial x^2} + \frac{\partial^2}{\partial z^2} \right). \quad (3.12)$$

Furthermore, the normal derivatives of the Green's function is given by

$$\frac{\partial G}{\partial n} = \frac{1}{2\pi r} \frac{\partial r}{\partial n} = \frac{1}{2\pi r} \left(n_x \frac{\partial r}{\partial x} + n_z \frac{\partial r}{\partial z} \right), \quad (3.13)$$

where n_x and n_z are the components of the unit normal vector along the x and z - directions, respectively. Now, applying the boundary conditions as in Eqs. (3.3)-(3.9), and the Green's function $G(x, z; x_0, z_0)$ defined in Eq. (3.11) into (3.10), we obtain the following integral equations corresponding to each of the regions R_1 and R_2

$$\begin{aligned} & -\frac{1}{2}\phi_1 + \int_{\Gamma_{c1}} \phi_1 \left(\frac{\partial G}{\partial n} - ik_0 G \right) d\Gamma + \int_{\Gamma_b} \phi_1 \frac{\partial G}{\partial n} d\Gamma + \int_{\Gamma_{c2}} \phi_1 \left(\frac{\partial G}{\partial n} - ik_0 G \right) d\Gamma \\ & + \int_{\Gamma_{f1}} \phi_1 \left(\frac{\partial G}{\partial n} - KG \right) d\Gamma + \int_{\Gamma_{i1}} \left(\phi_1 \frac{\partial G}{\partial n} - G \frac{\partial \phi_1}{\partial n} \right) d\Gamma + \int_{\Gamma_p} \left(\phi_1 \frac{\partial G}{\partial n} + i\omega \xi G \right) d\Gamma \\ & + \int_{\Gamma_{i2}} \left(\phi_1 \frac{\partial G}{\partial n} - G \frac{\partial \phi_1}{\partial n} \right) d\Gamma + \int_{\Gamma_{f3}} \phi_1 \left(\frac{\partial G}{\partial n} - KG \right) d\Gamma - \int_{\Gamma_{c1}} G \left(\frac{\partial \phi^I}{\partial n} - ik_0 \phi^I \right) d\Gamma = 0, \end{aligned} \quad (3.14)$$

$$\begin{aligned} & -\frac{1}{2}\phi_2 + \int_{\Gamma_{i2}} \left(\phi_1 \frac{\partial G}{\partial n} + G \frac{\partial \phi_1}{\partial n} \right) d\Gamma + \int_{\Gamma_p} \left(\phi_2 \frac{\partial G}{\partial n} - i\omega \xi G \right) d\Gamma \\ & + \int_{\Gamma_{i1}} \left(\phi_1 \frac{\partial G}{\partial n} + G \frac{\partial \phi_1}{\partial n} \right) d\Gamma + \int_{\Gamma_{f2}} \phi_2 \left(\frac{\partial G}{\partial n} - KG \right) d\Gamma = 0. \end{aligned} \quad (3.15)$$

Now, the boundary element method is used to solve the integral equations as in Eqs. (3.14) - (3.15) into a system of linear algebraic equations under the assumption that ϕ and $\partial\phi/\partial n$ are constants over each of the boundary elements (see Koley et al. [124] for details). The discretized

forms of the integral equations Eqs. (3.14) and (3.15) are given by

$$\begin{aligned}
& \sum_{j=1}^{N_{c1}} \phi_{1j} (H_{ij} - ik_0 G_{ij}) \Big|_{\Gamma_{c1}} + \sum_{j=1}^{N_b} \phi_{1j} H_{ij} \Big|_{\Gamma_b} + \sum_{j=1}^{N_{c2}} \phi_{1j} (H_{ij} - ik_0 G_{ij}) \Big|_{\Gamma_{c2}} \\
& + \sum_{j=1}^{N_{f1}} \phi_{1j} (H_{ij} - KG_{ij}) \Big|_{\Gamma_{f1}} + \sum_{j=1}^{N_{i1}} \left(\phi_{1j} H_{ij} - G_{ij} \frac{\partial \phi_{1j}}{\partial n} \right) \Big|_{\Gamma_{i1}} + \sum_{j=1}^{N_p} (\phi_{1j} H_{ij} + i\omega \xi_j G_{ij}) \Big|_{\Gamma_p} \\
& + \sum_{j=1}^{N_{i2}} \left(\phi_{1j} H_{ij} - G_{ij} \frac{\partial \phi_{1j}}{\partial n} \right) \Big|_{\Gamma_{i2}} + \sum_{j=1}^{N_{f3}} \phi_{1j} (H_{ij} - KG_{ij}) \Big|_{\Gamma_{f3}} - \sum_{j=1}^{N_{c1}} G_{ij} \left(\frac{\partial \phi_j^I}{\partial n} - ik_0 \phi_j^I \right) \Big|_{\Gamma_{c1}} = 0,
\end{aligned} \tag{3.16}$$

$$\begin{aligned}
& \sum_{j=1}^{N_{i2}} \left(\phi_{1j} H_{ij} + G_{ij} \frac{\partial \phi_{1j}}{\partial n} \right) \Big|_{\Gamma_{i2}} + \sum_{j=1}^{N_p} (\phi_{2j} H_{ij} + i\omega \xi_j G_{ij}) \Big|_{\Gamma_p} + \sum_{j=1}^{N_{i1}} \left(\phi_{1j} H_{ij} + G_{ij} \frac{\partial \phi_{1j}}{\partial n} \right) \Big|_{\Gamma_{i1}} \\
& + \sum_{j=1}^{N_{f2}} \phi_{2j} (H_{ij} - KG_{ij}) \Big|_{\Gamma_{f2}} = 0,
\end{aligned} \tag{3.17}$$

where

$$H_{ij} = \frac{1}{2} \delta_{ij} + \int_{\Gamma_j} \frac{\partial G}{\partial n} d\Gamma, \quad G_{ij} = \int_{\Gamma_j} G d\Gamma, \tag{3.18}$$

are the influence coefficients and can be evaluated numerically using the Gauss-Legendre quadrature formulae when the field point (x, z) and the source point (x_0, z_0) lies in different boundary elements. When the field point (x, z) and the source point (x_0, z_0) lies on the same boundary element, the influence coefficients need to be solved analytically (see (Koley and Sahoo [125] for details). The system of equations (3.16)-(3.17) are converted into the matrix form using the point collocation method and the matrix form is given as

$$\begin{aligned}
& [\phi_1] ([H] - ik_0 [G]) \Big|_{\Gamma_{c1}} + [\phi_1] [H] \Big|_{\Gamma_b} + [\phi_1] ([H] - ik_0 [G]) \Big|_{\Gamma_{c2}} + [\phi_1] ([H] - K[G]) \Big|_{\Gamma_{f1}} \\
& + \left([\phi_1] [H] - [G] \left[\frac{\partial \phi_1}{\partial n} \right] \right) \Big|_{\Gamma_{i1}} + ([\phi_1] [H] + i\omega [\xi] [G]) \Big|_{\Gamma_p} + \left([\phi_1] [H] - [G] \left[\frac{\partial \phi_1}{\partial n} \right] \right) \Big|_{\Gamma_{i2}} \\
& + [\phi_1] ([H] - K[G]) \Big|_{\Gamma_{f3}} - [G] \left(\left[\frac{\partial \phi^I}{\partial n} \right] - ik_0 [\phi^I] \right) \Big|_{\Gamma_{c1}} = 0,
\end{aligned} \tag{3.19}$$

$$\begin{aligned}
& \left([\phi_1] [H] + [G] \left[\frac{\partial \phi_1}{\partial n} \right] \right) \Big|_{\Gamma_{i2}} + ([\phi_2] [H] - i\omega [\xi] [G]) \Big|_{\Gamma_p} + \left([\phi_1] [H] + [G] \left[\frac{\partial \phi_1}{\partial n} \right] \right) \Big|_{\Gamma_{i1}} \\
& + [\phi_2] ([H] - K[G]) \Big|_{\Gamma_{f2}} = 0.
\end{aligned} \tag{3.20}$$

Since, the plate deflection ξ is an unknown quantity to be determined in Eqs. (3.19) and (3.20), the system of equations (3.19) and (3.20) can not be solved at this point. To solve the same, the central-difference formula is applied over the plate dynamic boundary condition and written in the form provided in (2.26). Now, Eqs. (3.19) and (3.20) are solved simultaneously to determine

the unknowns ϕ , $\partial\phi/\partial n$ and ξ over the corresponding boundaries of the domain.

3.4 Results, discussions and Model validation

In this section, the numerical results associated with the power generated by the PWEC device P_{ext} are plotted and discussed for various values of wave and structural parameters. The performance of the PWEC device is analyzed for variation in the length and submergence depth of the PWEC device, the amplitude and number of ripples of the sinusoidal seabed. The undulated seabed take the following shape

$$h(x) = h - a_1 \sin\left(\frac{2m\pi x}{L}\right), \quad 0 < x < L. \quad (3.21)$$

The parameter associated with the PWEC device, incident wave and the sinusoidal seabed are taken as follows: $h = 10\text{m}$, $l/h = 3.0$, $g = 9.81\text{m/s}^2$, $d/h = 0.2$, $\chi/h^4 = 4.78 \times 10^{-7}$, $\beta = 0.21$, $\varphi = \sqrt{h/g}$, $\gamma/h = 1.258 \times 10^{-3}$, $m = 5$, $a_1/h = 0.32$ unless otherwise mentioned. The wave power generated by the PWEC device is obtained as (see Zheng et al. [41] for details)

$$P_{ext} = \frac{\omega^2 \rho g}{2} \frac{\beta^2 \chi \varphi}{1 + \omega^2 \varphi^2} \int_b^{b+l} |\partial_x^2 \xi|^2 dx. \quad (3.22)$$

The power generated by the PWEC device can be calculated in another way which is stated in the following. Using the Green's second identity on the velocity potential and its derivative, we get (see Zheng et al. [41] for details)

$$P_{ext} = \frac{i\rho\omega}{4} \int_{-h}^0 \left[\left(\phi \frac{\partial \phi^*}{\partial x} - \phi^* \frac{\partial \phi}{\partial x} \right) \Big|_{x=-l_1} - \left(\phi \frac{\partial \phi^*}{\partial x} - \phi^* \frac{\partial \phi}{\partial x} \right) \Big|_{x=r} \right] dz. \quad (3.23)$$

To derive the expression of P_{ext} using Eq. (3.23), the far-field boundary condition as in Eq. (3.9) is rewritten as the following

$$\phi_1(x, z) = \begin{cases} \phi^I(x, z) + R_c \phi^I(-x, z), & \Gamma_{c1}, \\ T_c \phi^I(x, z), & \Gamma_{c2}, \end{cases} \quad (3.24)$$

where R_c and T_c are the complex coefficients associated with the reflected and transmitted waves. Now, by substituting the expression of $\phi_1(x, z)$ as in Eq. (3.24) into Eq. (3.23), the power generated by the PWEC device P_{ext} (Wm^{-1}) is expressed as the following

$$P_{ext} = \frac{\rho g^2 A^2}{8\omega} \left(\frac{2k_0 h + \sinh(2k_0 h)}{\cosh^2(k_0 h)} \right) [1 - |R_c|^2 - |T_c|^2]. \quad (3.25)$$

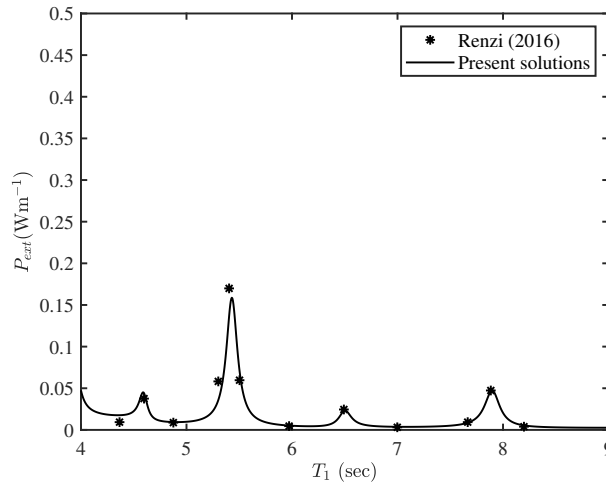


FIGURE 3.2: Validation of P_{ext} vs T_1 . Here $a_1/h = 0$ and $l/h = 2$

Before proceeding with various results, the present computational results need to be validated with standard results available in the literature. In Fig. 3.2, the power generation P_{ext} is plotted as a function of the non-dimensional incident wave period T_1 for the case when there is no breakwater placed at the lee side of the PWEC plate which is floating over the uniform seabed, and both the edges of the PWEC plate are fixed in nature. Under the aforementioned conditions, the present results are compared with the analytical results provided in Renzi [3] (see Fig. 7 of Renzi [3]). From Fig. 3.2, it is seen that the present computed results are matched well with the results provided by Renzi [3].

3.5 Performance of the PWEC device in frequency domain

Figs. 3.3(a)- 3.3(d) depict the variation of the power generated by the PWEC device P_{ext} as a function of incident wave period T_1 for different (a) plate length (l/h), (b) submergence depth (d/h), (c) amplitude of the bottom undulation (a_1/h), and (d) number of ripples in the undulated seabed (m). Fig. 3.3(a) illustrates that as the plate length increases, the number of resonating peaks also increases. This occurs due to the inherent low-frequency vibrations of long plates, enhancing the alignment of frequencies with the hydroelastic wave and the PWEC plate. It is important to highlight that the amplitude of the peaks is more pronounced for moderate plate lengths. Additionally, in the shortwave regime, there is a greater number of peaks and higher associated amplitudes compared to the intermediate and long-wave regimes. Consequently, it can be observed that plates with moderate lengths in the shortwave regime exhibit the highest power generation. Fig. 3.3(b) depicts that the amplitude of the resonating peaks increases as the submergence depth of the plate decreases. This might be due to an accumulation of wave energy at the free surface. It is also noticed that the resonance occurs around the same values of the incident wave period irrespective of the variations in submergence depth. Fig. 3.3(c) illustrates

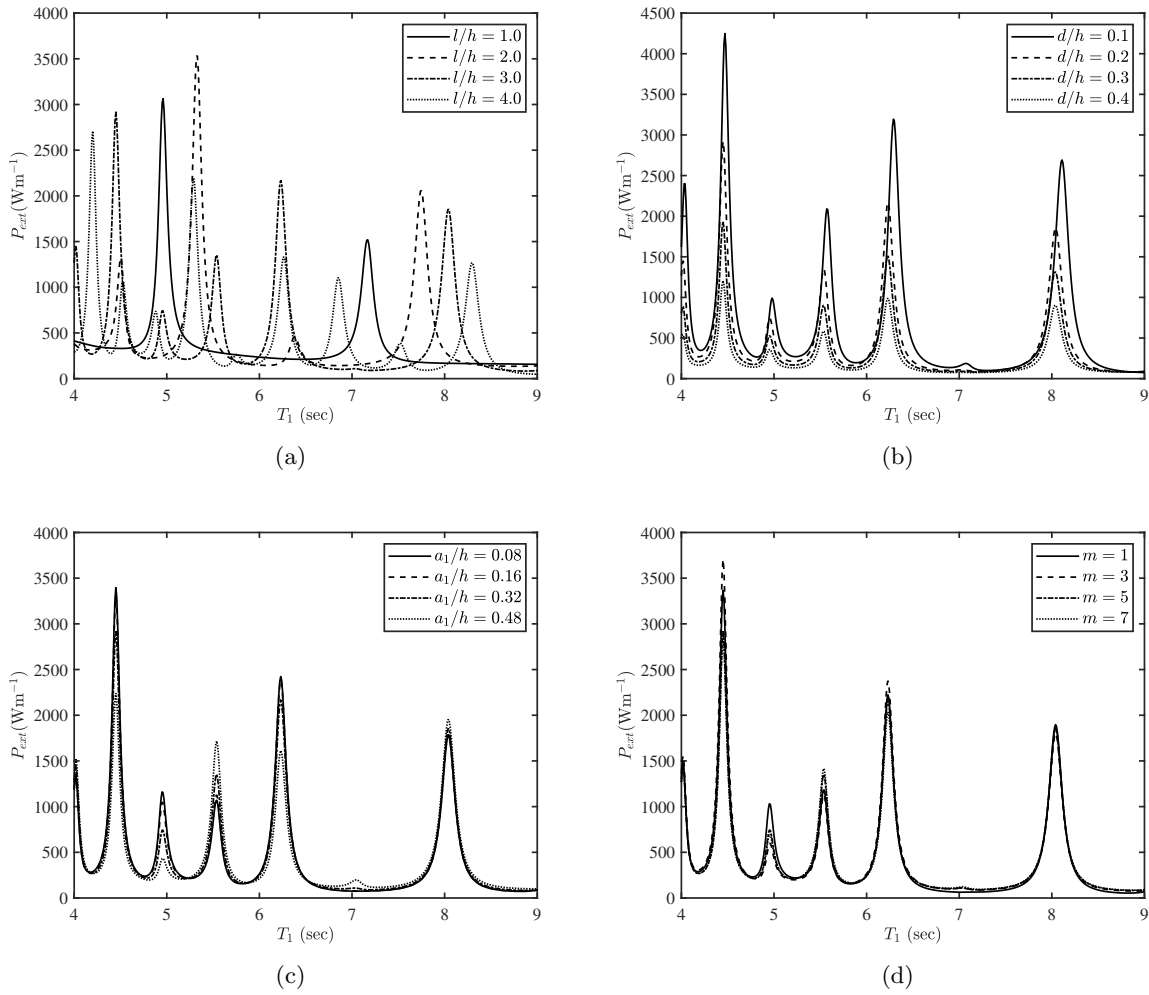


FIGURE 3.3: Variation of P_{ext} vs T_1 for different (a) l/h , (b) d/h , (c) a_1/h , and (d) m .

the increase in amplitude of the peaks as the ripple amplitude decreases within the shortwave regime. Conversely, in the long and intermediate-wave regimes, an opposite trend is evident for certain values of incident wave period. Additionally, it is observed that resonance takes place at a same wave period, regardless of variations in ripple amplitude. From Fig. 3.3(d), it is observed that the amplitude of the resonating peak is higher with a moderate number of ripples in both the shortwave and intermediate wave regimes. Moreover, there is minimal change in power absorption within the long-wave regime. Additionally, it is noteworthy that, irrespective of the changes in the number of seabed ripples, resonances consistently occur around the same wave period.

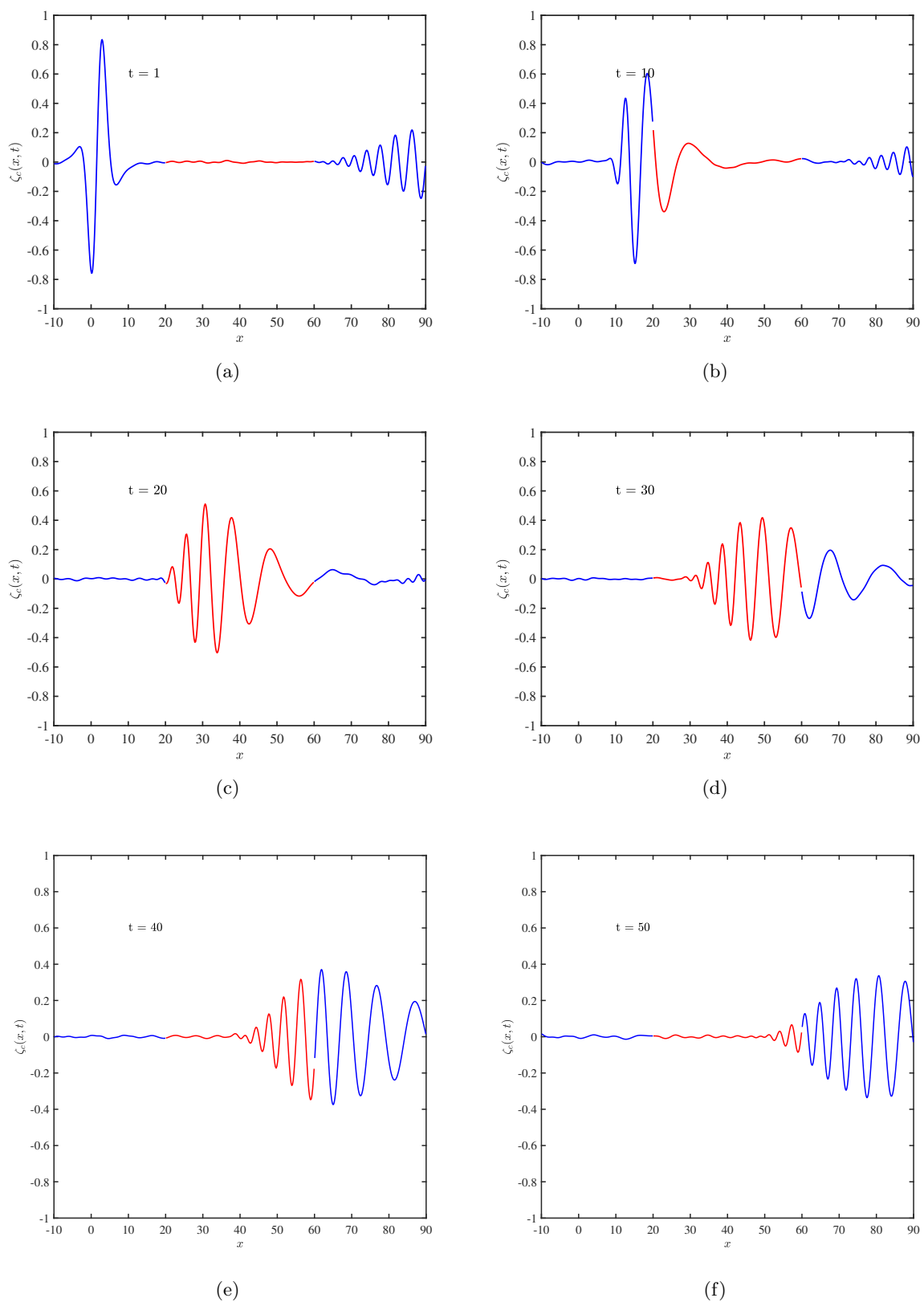


FIGURE 3.4: Free surface displacement $\zeta_c(x, t)$ at various times (a) $t = 1$ s, (b) $t = 10$ s, (c) $t = 20$ s, and (d) $t = 30$ s, (e) $t = 40$ s, (f) $t = 50$ s.

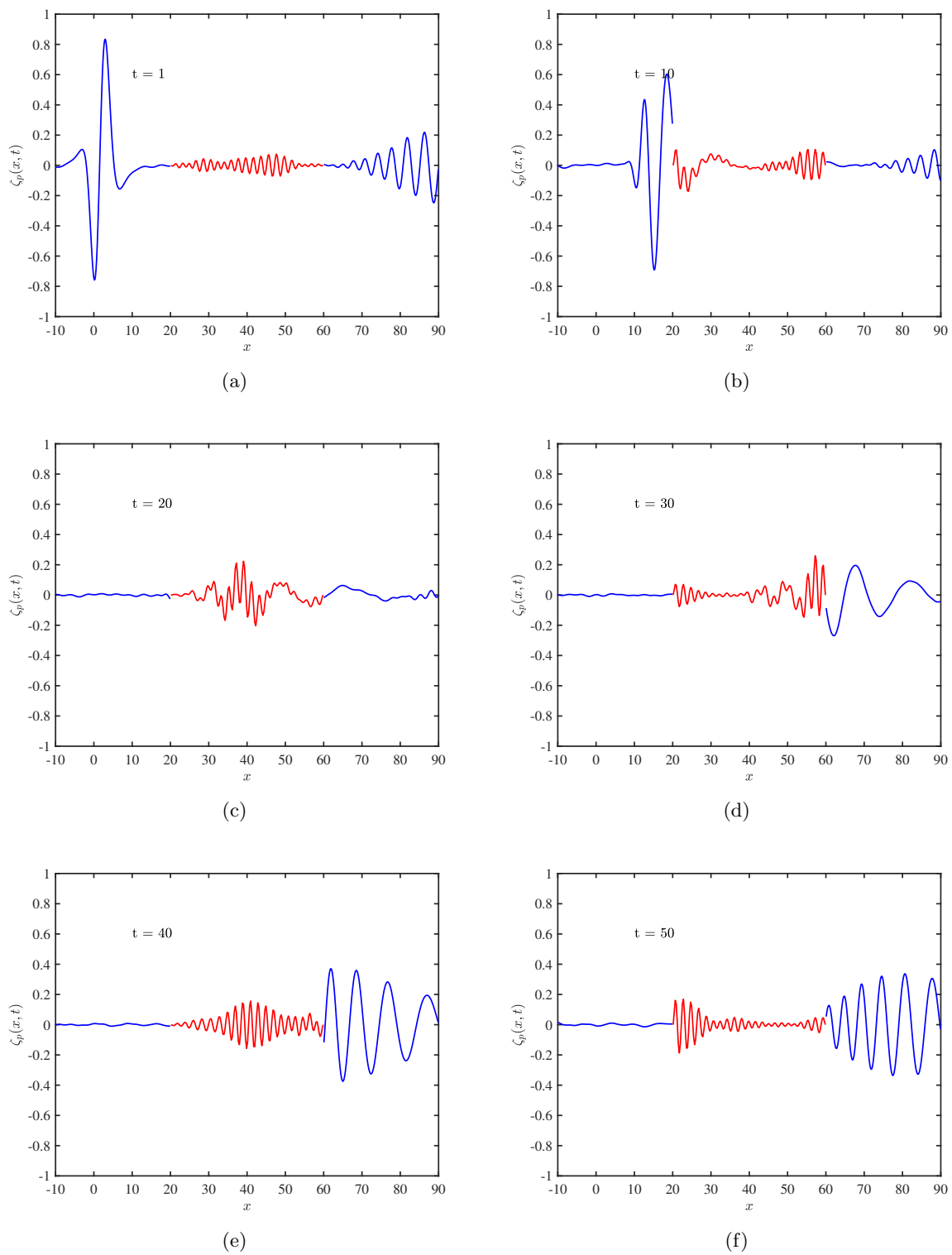


FIGURE 3.5: Free surface displacement and plate deflection $\zeta_p(x, t)$ at various times (a) $t = 1$ s, (b) $t = 10$ s, (c) $t = 20$ s, (d) $t = 30$ s, (e) $t = 40$ s, (f) $t = 50$ s

3.6 Time dependent free surface elevation and plate deflection

The study of the free surface displacement in the time domain provides more realistic results than in the frequency domain. This study illustrates the deflection of the PWEC plate and the free surface displacement of the incident and transmitted waves, which demonstrate the capability of power generation by the PWEC device. The free surface displacement in time domain $\zeta_c(x, t)$ and the plate deflection $\xi(x, t)$ are obtained as

$$\zeta_c(x, t) = \zeta(x, t), \quad \text{for } \{-l_1 < x < b, z = 0\} \cup \{b < x < b + l, z = 0\} \cup \{b + l < x < r, z = 0\}, \quad (3.26)$$

$$\zeta_p(x, t) = \begin{cases} \zeta(x, t), & \text{for } \{-l_1 < x < b, z = 0\} \cup \{b + l < x < r, z = 0\}, \\ \xi(x, t), & \text{for } \{b < x < b + l, z = -d\}, \end{cases} \quad (3.27)$$

where

$$\zeta(x, t) = \Re \left\{ \int_{-\infty}^{\infty} \tilde{f}(\omega) \zeta(x, \omega) e^{-i\omega t} d\omega \right\}, \quad (3.28)$$

$$\xi(x, t) = \Re \left\{ \int_{-\infty}^{\infty} \tilde{f}(\omega) \xi(x, \omega) e^{-i\omega t} d\omega \right\}. \quad (3.29)$$

Here $\tilde{f}(\omega)$ represents the Fourier transform corresponding to the incident wave pulse. Moreover, $\xi(x, \omega)$ and $\zeta(x, \omega)$ denote the plate deflection and free surface elevation in the frequency domain. It is to be noted that in Eq. (3.27), $\zeta_p(x, t)$ consists of the free surface elevation $\zeta(x, t)$ on both the left and right sides of the plate region to compare the free surface elevation of the incoming and transmitted waves with the PWEC plate deflection $\xi(x, t)$. It is assumed that the incoming wave packets follows Gaussian distribution whose Fourier transform is of the form $\tilde{f}(\omega) = \sqrt{\frac{b}{\pi}} e^{-b(\omega - \omega_0)^2}$, with b being the standard deviation and ω_0 being the mean frequency of the incident wave. Using the boundary condition (3.3), the free surface elevation ζ and the plate deflection ξ used in Eq. (3.29) can be expressed as (Zheng et al. [41])

$$\zeta = \frac{i\omega}{g} \phi \Big|_{z=0}, \quad (3.30)$$

$$\xi = \frac{i}{\omega} \partial_z \phi \Big|_{z=-d}. \quad (3.31)$$

Fig. 3.4 demonstrates the free surface elevation for the open water regions (blue lines) and for the region above the PWEC plate (red lines). The free surface displacement is given for different instants of time (a) $t = 1$ s, (b) $t = 10$ s, (c) $t = 20$ s, and (d) $t = 30$ s, (e) $t = 40$ s, and (f) $t = 50$ s. Here, all figures demonstrate the scattering of waves around the plate. In a similar way, Fig. 3.5 demonstrates the free surface elevation for the open water regions (blue lines) and the plate

deflection (red lines). It is clear from in Figs. 3.4 and 3.5 that the plate deflection is governed by short crested waves which are generated due to weakly damped waves created by the interface between the incoming wave and the PWEC plate. These short crested weakly damped waves play a major role in power generation by the PWEC device. Since the wave energy is linearly varies with the square of the wave amplitude, this reduction of the wave amplitude in the plate's occupied regime and in the transmitted regions clearly depicts the power absorption by the PWEC plate. A comparison between Figs. 3.4 and 3.5 explains that the PWEC plate can collect and retain the wave energy for a longer duration. A similar observation was reported by Renzi [3], Zheng et al. [41].

3.7 Optimization of the design parameters of the PWEC device

The design of the PWEC device is optimized by choosing the appropriate values of the physical parameters associated with the PWEC plate. The creation of the database for the input features and the values of the target variable, namely the power generation, exploratory data analysis, construction of the ANN model, and training and testing of the models, are explained in the following subsections.

3.7.1 Design of the database

The database for the model building is created using the boundary element method, mentioned in the previous section. The input features of the model are PWEC plate length l/h and submergence depth d/h . The output feature is the power generated by the PWEC device P_{ext} . The parameters such as the water depth and wave height are considered to be fixed, and the power generation is calculated as the average P_{ext} for the wave period varies from 4-9 sec. A good sampling method always gives a more generalized sample distribution and it will enhance the accuracy of the model. In this study, the Latin Hypercube Sampling (LHS) methodology is used for sampling to generate random sample points. The sampling range for the device parameters is $0 \leq l/h \leq 5$ and $0 \leq d/h \leq 0.4$. The important property of LHS methodology is that it will increase the stratification of the input features, which will improve the uniformity of the samples. For the training purpose, we randomly selected 40 data points for l/h and 10 data points selected for d/h . The scatter plot for the same is given in Figs. 3.6(a) and 3.6(b). The training dataset is generated by finding the power generated by the PWEC device for different combinations of l/h and d/h for wave periods varying from 4s to 9s. The average of the power generation with respect to the wave periods is considered the power generated by the PWEC device for the associated design parameters. The training dataset contains 400 different combinations of the input values, and the corresponding average power generated for the wave periods varies from 4s to 9s. After training the model to optimize the design of the PWEC device, we again

generate a dataset with 100 random samples for the PWEC plate length and 30 random samples for submergence depth. Hence, we get 3000 random input values and the corresponding power generated by the PWEC device. The scatter plot of the input dataset for optimization is shown in the Figs. 3.6(c) and 3.6(d).

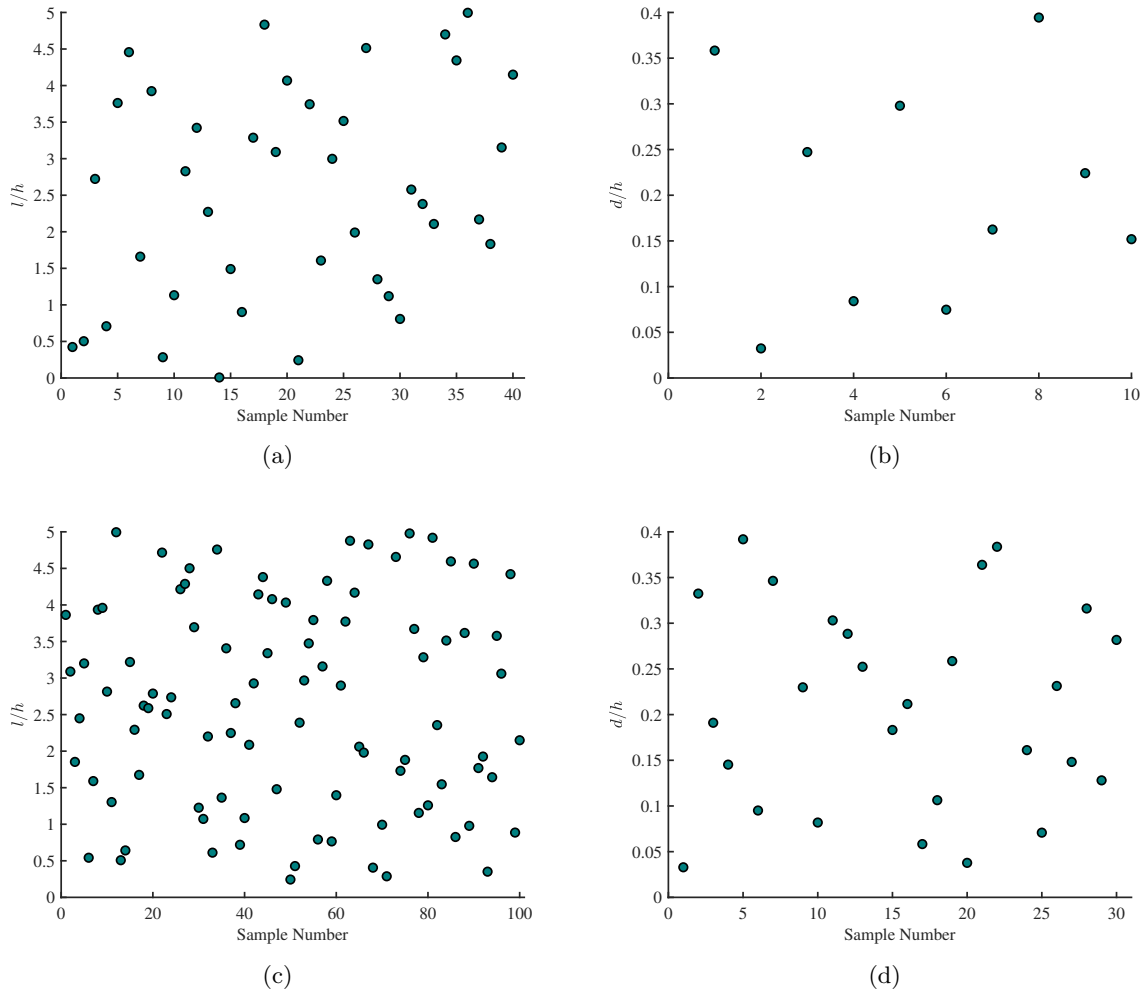


FIGURE 3.6: Scatter plot of the input features (a) l/h and (b) d/h for training the ANN model, and the input features (c) l/h and (d) d/h for the optimization of the PWEC device.

3.7.2 Exploratory data analysis

In this section, the correlation between the input features and the target variable will be investigated. The descriptive statistics of the database for model building is provided in Tab. 3.1. It is clearly seen from Fig. 3.7(a) that the power generated by the PWEC device (P_{ext}) is quadratically related to the length of the PWEC device (l/h), i.e., the power generated by the PWEC device is less for a PWEC plate of smaller length and the power generated by the PWEC device (P_{ext}) increases according to an increase in the PWEC plate length and then started decreasing after a stage. Whereas, a linear relationship is observed between the power

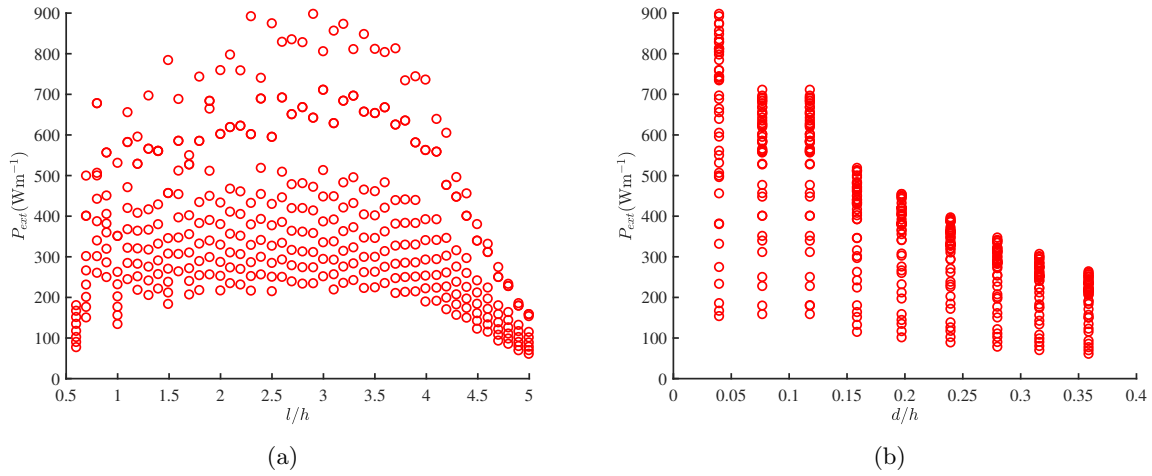
FIGURE 3.7: Variation of (a) P_{ext} vs. l/h , (b) P_{ext} vs. d/h .

TABLE 3.1: Descriptive statistics of database for model building

| | l/h | d/h | P_{ext} (Wm^{-1}) |
|-------|-------|-------|--------------------------------|
| count | 400 | 400 | 400 |
| mean | 2.78 | 0.19 | 383.84 |
| std | 1.30 | 0.10 | 192.47 |
| min | 0.29 | 0.03 | 61.23 |
| 25% | 1.69 | 0.11 | 240.83 |
| 50% | 2.79 | 0.19 | 340.20 |
| 75% | 3.89 | 0.27 | 512.16 |
| 90% | 4.59 | 0.35 | 668.49 |
| 95% | 4.79 | 0.35 | 735.91 |
| 99% | 4.99 | 0.35 | 856.46 |
| max | 4.99 | 0.35 | 878.22 |

generated by the PWEC device and the submergence depth of the PWEC device as shown in Fig. 3.7(b). i.e., the power generated by the PWEC device (P_{ext}) decreases gradually as the submergence depth of the PWEC device (d/h) increases.

3.7.3 Development of the ANN model and optimization

A supervised machine learning model, namely the ANN model, is developed to predict the best suitable values of the parameters to maximize P_{ext} by the PWEC device. The input layer of the ANN model contains two neurons representing two input features, and similarly, the output layer contains a single neuron representing the output feature. The hidden layers contain four layers containing 128, 64, 64, and 32 neurons, respectively. The accuracy of the model is verified by the mean absolute error matrix and by the R^2 value (for further details, see George et al. [73]). Fig. 3.8(a) shows a good agreement between the training accuracy and the validation accuracy. Fig. 3.8(b) shows the true value and the predicted values of the power generated by

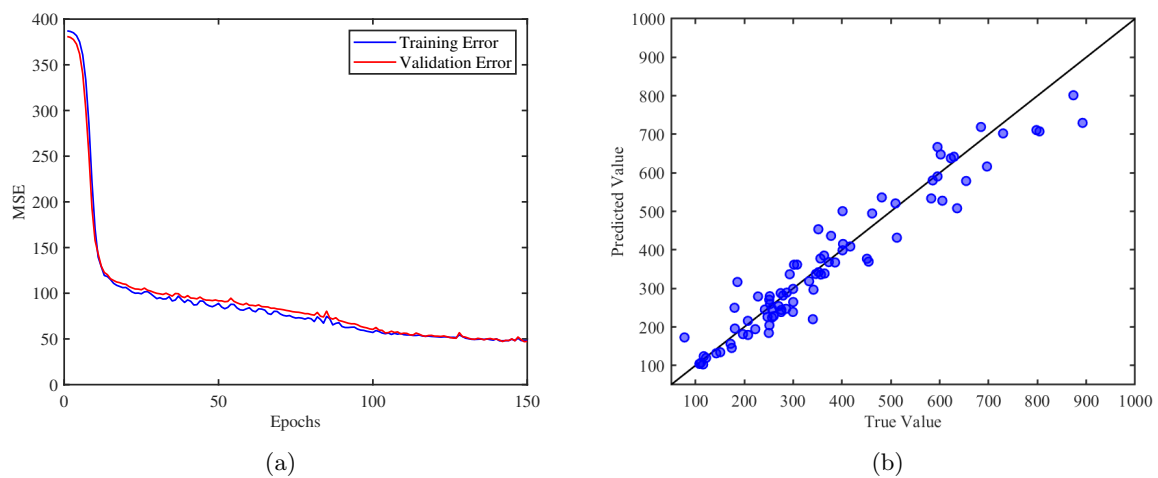


FIGURE 3.8: (a) ANN model: MSE of training and validation errors w.r.t. Epochs, (b) predicted vs true values for the test set.

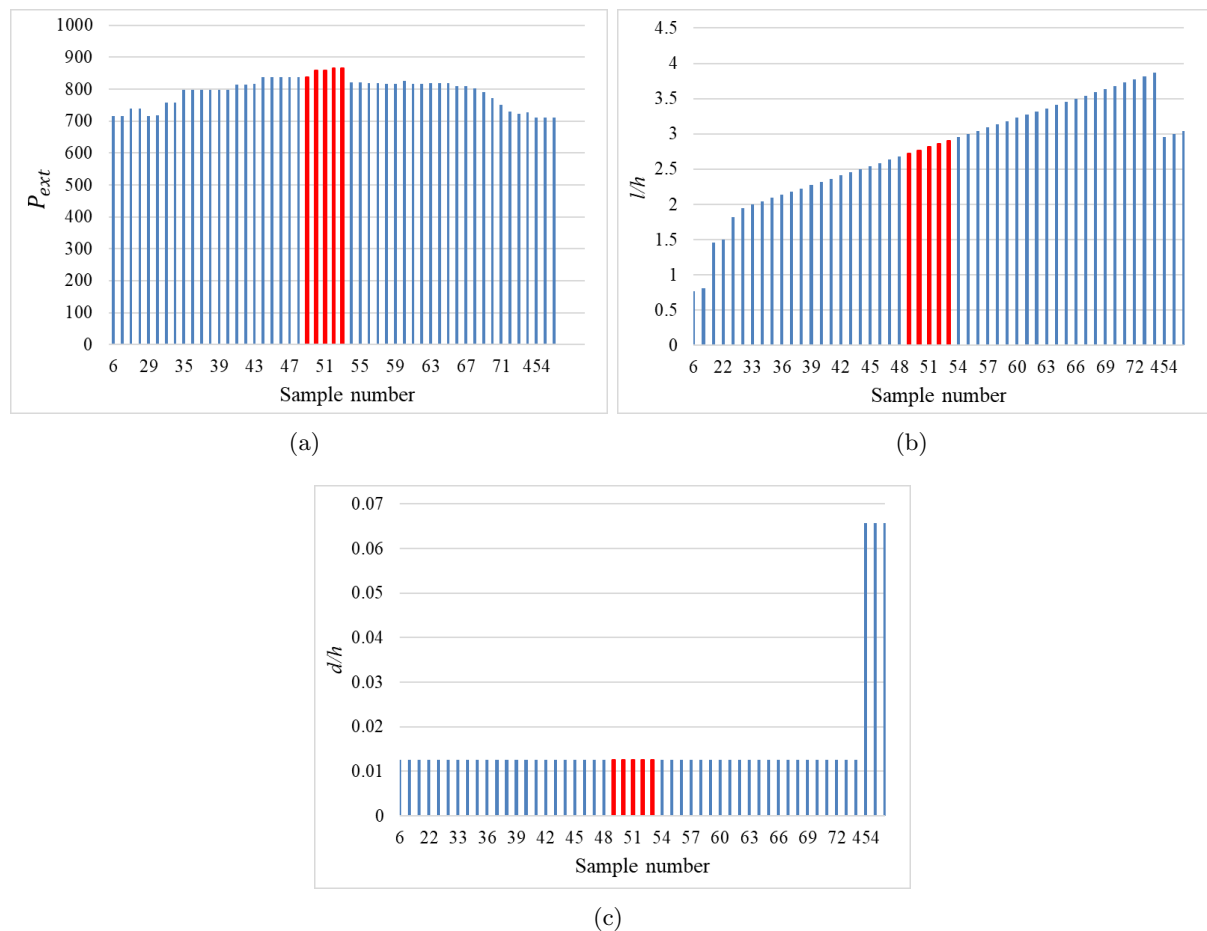


FIGURE 3.9: (a) Top fifty predicted values of the mean P_{ext} by the PWEC device, (b) plate length of the corresponding sample number as seen in (a), (c) submergence depth of the corresponding sample number as seen in (a).

the PWEC device. The R^2 value for the model is obtained to be 0.94, which means that the model is able to predict the output feature with an accuracy of 94%. Using the developed ANN model, the prediction of the power generated by the PWEC device for the large dataset having 3000 samples can be made with less computational cost and also not time-consuming. Fig. 3.9(a) shows bar plots for the top 50 predicted values of the power generated by the PWEC device with respect to the sample number for the large dataset. Out of these 50 samples, the highest five values are represented by the red bars. The mean power generated by the PWEC is highest for the sample numbers 49, 50, 51, 52, and 53. The power generation for these samples lies in the interval $[840\text{Wm}^{-1}, 866\text{Wm}^{-1}]$, the corresponding PWEC plate length, and the submergence depth with respect to the sample number are shown in Figs. 3.9(b) and 3.9(c). From Fig. 3.9(b), it is clearly seen that the highest five predicted values for the mean power generated by the PWEC device occur when the plate length varies in the range $2.7 \leq l/h \leq 2.9$. From Fig. 3.9(c), it is observed that all the 47 out of the 50 highest values are obtained for the least submerged depth considered for the modeling. It clearly indicates that the optimum power generated by the PWEC device P_{ext} is obtained for the PWEC plate placed with minimum submergence depth (d/h), and the length of the PWEC plate l/h should be in between 2.7 and 2.9.

3.8 Conclusions

The present work investigates the power generation, the time-dependent free surface displacement and the PWEC plate deflection, and the optimization of the parameters of a submerged PWEC device floating over a sinusoidal seabed, under the linear wave-structure interaction theory. The BEM-based numerical method is used to solve the BVP associated with the hydrodynamics of the PWEC device. Various parameters related to the performance of the PWEC device are analyzed. Prediction of the power generated by the PWEC device and optimization of the parameters of the submerged PWEC device to maximize the P_{ext} by the PWEC device are studied using a supervised machine learning algorithm, namely the ANN model. From the current investigation, the following findings are obtained

- The number of resonating peaks increases with an increase in plate length (l/h), and the amplitude of the resonating peak is higher for the moderate values of the plate length (l/h).
- The amplitude of the resonating peak increases as the submergence depth of the plate decreases. Furthermore, regardless of differences in submergence depth, ripple amplitude, or number of ripples in the seabed, the resonance occurs around the same values of the incident wave period.

- The amplitude of the resonating peaks increases as the ripple amplitude decreases in the shortwave regime. On the other hand, an opposite trend is observed for the intermediate and longwave regimes for certain values of the incident wave period.
- The decrease in the amplitude of the free surface displacement in the transmitted wave from the incident wave pack is due to the power generation by the PWEC device via the interaction of the incident wave pack. Further, the results represent the power-holding behavior of the PWEC device for a longer duration.
- It is also observed that the power extraction curve attains its maximum when the amplitude of the bottom undulation is negligible. Hence, in the parameter optimization phase, we considered a uniform seabed.
- For maximum power generation by the PWEC plate, the optimum geometric value for l/h is $2.7 \leq l/h \leq 2.9$ and minimum submergence depth is considered for d/h (the value of d/h is 0.012 chosen in the present study). The mean power generation for this range lies in the interval $[840\text{Wm}^{-1}, 866\text{Wm}^{-1}]$.

Chapter 4

Optimization of parameters of the OWC wave energy converter device using MLP and XGBoost models

* The work, in this chapter, is covered by the following publication:

Vipin, V., Trivedi, K., Koley, S. (2023). Optimization of parameters of the OWC wave energy converter device using MLP and XGBoost models. *Results in Physics*, 55, 107163.

4.1 General introduction

In the present work, we have studied the performance of a breakwater-integrated quarter-circle-shaped front wall OWC device under the influence of irregular incident waves. Firstly, the boundary value problem associated with the hydrodynamics of OWC device is handled for a solution using the dual boundary element method (DBEM). To examine the complex relationships between all input features and the target variable in a time-efficient manner, supervised machine learning models are developed. Here, two different models: (i) multilayer perceptron (MLP) model based on an artificial neural network, and (ii) a tree ensemble model, namely the XGBoost model are developed. The submergence depth of the front wall of the OWC device, chamber length, rotational speed, and diameter of the turbine blade are considered as input attributes, and the average annual power generated by the OWC device is considered as the output attribute. The MLP model is employed to optimize these input parameters, leveraging the insights provided by the XGBoost model to maximize the annual average power generation. From the dual BEM based numerical results, and using the Latin hypercube sampling technique, 3750 samples were generated to train, validate, and test the machine learning models. Using the XGBoost model with the support of accumulated local effect plots, we find four specific regions of the input space in which the annual average power extraction will be maximum. Hereafter, an extended input database is generated with twenty equally spaced levels for each parameter and the dataset is passed through the developed MLP model to find the optimized values of the parameters of the OWC device which maximizes the power generation. It is obtained that the maximum power generation is attained for $y_0/h = -0.65$, $r/h = 3$, $2.8 \leq D \leq 3$ and $\{70 \leq N \leq 80 \cup 105 \leq N \leq 116\}$.

4.2 Mathematical formulation

This section deals with the mathematical modeling of the quarter circle-shaped front wall of the OWC device in the Cartesian coordinate system in two-dimensions. In this specific instance, the x -axis is taken along the horizontal direction, whilst the z -axis extends vertically upward direction. The schematic representation of the present problem is illustrated in Fig. 4.1. The quarter circle-shaped front wall of the device intersects the mean free surface level $z = 0$ at $x = L - b$. The OWC device is integrated with the trapezoidal breakwater. The trapezoidal-shaped breakwater is situated over the bottom foundation with bottom height b_h . Further, the front wall of the OWC device is considered to be thin, and the submergence depth of the tip of the front wall is symbolized as a . Γ_2 is a representation of the bottom boundary and the front wall of the breakwater within the OWC device chamber. Further, due to the presence of the OWC device, the mean free surface is divided into two parts, namely internal free surface Γ_3 (i.e., free surface within the OWC chamber) and external free surface Γ_5 (i.e., free surface

outside of the OWC chamber). In addition, Γ_4 is termed as an impenetrable fixed front wall of the OWC device, which is submerged in the water. To close the domain, an auxiliary boundary Γ_1 is taken at $x = -l$. For the modeling purpose, the water and the related motion are assumed to be inviscid, incompressible, and irrotational in nature. Further, the water waves are assumed to be time-harmonic in nature with the circular frequency ω . These assumptions ensure the existence of the velocity potential of the form $\Phi(x, y, z, t) = \text{Re}\{\phi(x, z)e^{-i\omega t}\}$. Therefore, $\phi(x, z)$ satisfies the Laplace equation (see Vipin et al. [132, 133])

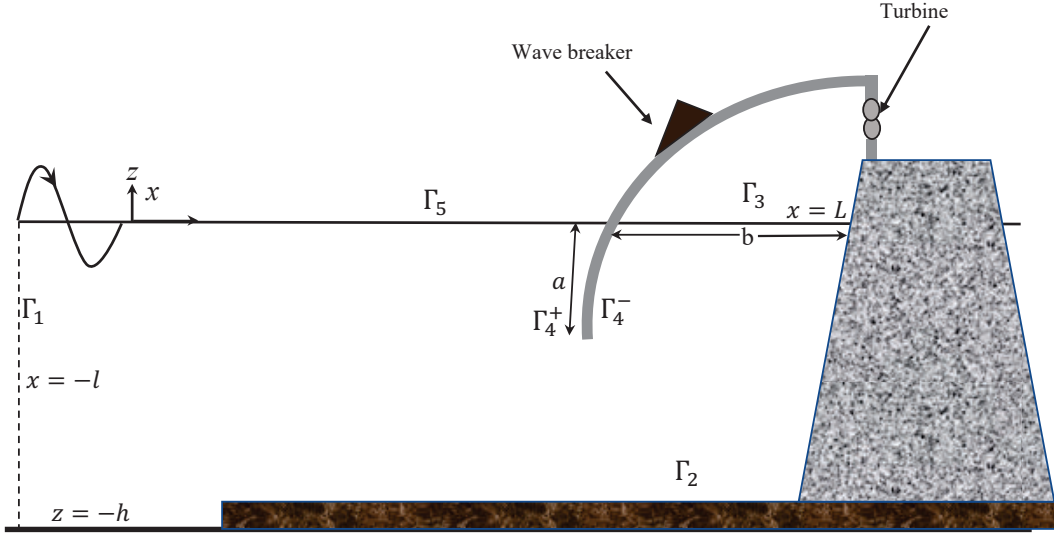


FIGURE 4.1: Schematic of LIMPET OWC wave energy converter device.

$$\left(\frac{\partial^2}{\partial x^2} + \frac{\partial^2}{\partial z^2} \right) \phi(x, z) = 0. \quad (4.1)$$

The boundary condition at the mean free surface $z = 0$ is given by Trivedi and Koley [75]

$$\frac{\partial \phi}{\partial n} - K\phi = \begin{cases} \frac{i\omega p}{\rho g}, & \text{on } \Gamma_3, \\ 0, & \text{on } \Gamma_5, \end{cases} \quad (4.2)$$

where $K = \omega^2/g$ with g being the gravitational acceleration and $\partial/\partial n$ represents the normal derivative. Now, the boundary condition on the rigid and impervious boundaries $\Gamma_2 \cup \Gamma_4$ is given by (Trivedi and Koley [134], Vipin and Koley [135])

$$\frac{\partial \phi}{\partial n} = 0, \quad \text{on } \Gamma_2 \cup \Gamma_4. \quad (4.3)$$

In the presence of the OWC device, the total velocity potential ϕ is decomposed into two parts as follows (Trivedi and Koley [136])

$$\phi = \phi^S + \left(\frac{i\omega p}{\rho g} \right) \phi^R, \quad (4.4)$$

where ϕ^S and ϕ^R represent the scattered and radiated velocity potentials, respectively. Further, the scattered velocity potential ϕ^S can be decomposed into incident potential ϕ^I and diffracted potential ϕ^D . Now, ϕ^S and ϕ^R satisfy Eqs. (4.1)-(4.3) and the modified form of Eq. (4.2) can be written as

$$\frac{\partial \phi^{S,R}}{\partial n} - K\phi^{S,R} = \begin{cases} \delta, & \text{on } \Gamma_3, \\ 0, & \text{on } \Gamma_5, \end{cases} \quad (4.5)$$

where $\delta = 1$ for the radiation potential ϕ^R , and $\delta = 0$ for the scattered potential ϕ^S . Finally, the far-field boundary conditions are given by (Rodríguez et al. [137], Trivedi and Koley [138])

$$\begin{cases} \phi^S(x, z) = e^{ik_0x} f_0(k_0, z) + A_0^S e^{-ik_0x} f_0(k_0, z), & \text{as } x \rightarrow -\infty, \\ \phi^R(x, z) = A_0^R e^{-ik_0x} f_0(k_0, z), & \text{as } x \rightarrow -\infty, \end{cases} \quad (4.6)$$

where $f_0(k_0, z) = \left(-\frac{igA}{\omega}\right) \frac{\cosh k_0(h+z)}{\cosh(k_0h)}$ with k_0 satisfies the dispersion relation $\omega^2 = gk \tanh(kh)$. To handle the boundary value problem, the boundary element method is used. In boundary element method, the computational domain should be closed. To close the computational domain, an auxiliary boundary Γ_1 is located sufficiently far away from the OWC device at $x = -l$. As a result, the far-field boundary conditions (4.6) hold on Γ_1 . The modified form of the far-field boundary conditions (4.6) are expressed as

$$\begin{cases} \frac{\partial(\phi^S - \phi^I)}{\partial n} - ik_0(\phi^S - \phi^I) = 0, & \text{on } \Gamma_1, \\ \frac{\partial \phi^R}{\partial n} - ik_0\phi^R = 0, & \text{on } \Gamma_1, \end{cases} \quad (4.7)$$

with $\phi^I(x, z) = e^{ik_0x} f_0(k_0, z)$ being the incident wave velocity potential.

4.3 Solution methodology based on dual boundary element method

In the present section, the dual boundary element method (DBEM) is used to handle the BVP (boundary value problem) provided in Section 4.2. In this solution methodology, the BVP is converted into a system of integral equations using the appropriate Green's function. Applying Green's third identity on the velocity potentials $\phi^{S,R}(\mathbf{x})$ and the free-space Green's function $G(\mathbf{x}, \mathbf{s})$ over the domain Ω bounded by Γ , the following integral equation is obtained as (Trivedi et al. [94])

$$\phi^{S,R}(\mathbf{x}) = \int_{\Gamma} \left[\phi^{S,R}(\mathbf{s}) V(\mathbf{x}, \mathbf{s}) - G(\mathbf{x}, \mathbf{s}) \frac{\partial \phi^{S,R}(\mathbf{s})}{\partial n_{\mathbf{s}}} \right] d\Gamma(\mathbf{s}), \quad \mathbf{x} \in \Omega, \quad (4.8)$$

where

$$V(\mathbf{x}, \mathbf{s}) \equiv \frac{\partial G(\mathbf{x}, \mathbf{s})}{\partial n_{\mathbf{s}}}, \quad \mathbf{x} = (x, z), \quad \mathbf{s} = (x_0, z_0). \quad (4.9)$$

It is to be mentioned that the free-space Green's function as in (4.8) satisfies the governing equation

$$\left(\frac{\partial^2}{\partial x^2} + \frac{\partial^2}{\partial z^2} \right) G(\mathbf{x}, \mathbf{s}) = \delta(\mathbf{x} - \mathbf{s}), \quad (4.10)$$

and takes the form (Koley [128], Koley and Sahoo [139])

$$G(\mathbf{x}, \mathbf{s}) = \frac{1}{2\pi} \ln r, \quad (4.11)$$

where $\delta(\mathbf{x} - \mathbf{s})$ is the Dirac-delta function, and r is defined as the distance between the field point $\mathbf{x} = (x, z)$ and the source point $\mathbf{s} = (x_0, z_0)$. Further, the normal derivative of Eq. (4.8) results into

$$\frac{\partial \phi^{S,R}(\mathbf{x})}{\partial n_{\mathbf{x}}} = \int_{\Gamma} \left[N(\mathbf{x}, \mathbf{s}) \phi^{S,R}(\mathbf{s}) - M(\mathbf{x}, \mathbf{s}) \frac{\partial \phi^{S,R}(\mathbf{s})}{\partial n_{\mathbf{s}}} \right] d\Gamma(\mathbf{s}), \quad \mathbf{x} \in \Omega, \quad (4.12)$$

where

$$M(\mathbf{x}, \mathbf{s}) \equiv \frac{\partial G(\mathbf{x}, \mathbf{s})}{\partial n_{\mathbf{x}}}, \quad N(\mathbf{x}, \mathbf{s}) \equiv \frac{\partial^2 G(\mathbf{x}, \mathbf{s})}{\partial n_{\mathbf{x}} \partial n_{\mathbf{s}}}. \quad (4.13)$$

When the field point $\mathbf{x} \in \Gamma$, Eqs. (4.8) and (4.12) can be written as

$$\frac{1}{2} \phi^{S,R}(\mathbf{x}) = CPV \int_{\Gamma} V(\mathbf{x}, \mathbf{s}) \phi^{S,R}(\mathbf{s}) d\Gamma(\mathbf{s}) - RPV \int_{\Gamma} G(\mathbf{x}, \mathbf{s}) \frac{\partial \phi^{S,R}(\mathbf{s})}{\partial n_{\mathbf{s}}} d\Gamma(\mathbf{s}), \quad \mathbf{x} \in \Gamma, \quad (4.14)$$

$$\frac{1}{2} \frac{\partial \phi^{S,R}(\mathbf{x})}{\partial n_{\mathbf{x}}} = HPV \int_{\Gamma} N(\mathbf{x}, \mathbf{s}) \phi^{S,R}(\mathbf{s}) d\Gamma(\mathbf{s}) - CPV \int_{\Gamma} M(\mathbf{x}, \mathbf{s}) \frac{\partial \phi^{S,R}(\mathbf{s})}{\partial n_{\mathbf{s}}} d\Gamma(\mathbf{s}), \quad \mathbf{x} \in \Gamma. \quad (4.15)$$

Here, RPV , CPV and HPV are termed as the Riemann principal value, Cauchy principal value and Hadamard principal value, respectively. In Eqs. (4.14) and (4.15), the total boundary Γ can be written as $\Gamma = \Gamma_s + \Gamma_4^+ + \Gamma_4^-$ with Γ_s represent the non-degenerate boundary, and Γ_4^+ and Γ_4^- are the degenerate boundaries. Further, the non-degenerate boundary Γ_s is composed of $\Gamma_s = \Gamma_1 + \Gamma_2 + \Gamma_3 + \Gamma_5$. Now, for $\mathbf{x} \in \Gamma_s$, Eqs. (4.14) and (4.15) reduced into the following forms Trivedi et al. [94], Chen et al. [95]

$$\begin{aligned} \frac{1}{2} \phi^{S,R}(\mathbf{x}) &= CPV \int_{\Gamma_s} V(\mathbf{x}, \mathbf{s}) \phi^{S,R}(\mathbf{s}) d\Gamma(\mathbf{s}) - RPV \int_{\Gamma_s} G(\mathbf{x}, \mathbf{s}) \frac{\partial \phi^{S,R}(\mathbf{s})}{\partial n_{\mathbf{s}}} d\Gamma(\mathbf{s}) \\ &+ \int_{\Gamma_4^+} V(\mathbf{x}, \mathbf{s}) \Delta \phi^{S,R}(\mathbf{s}) d\Gamma(\mathbf{s}) - \int_{\Gamma_4^+} G(\mathbf{x}, \mathbf{s}) \sum \frac{\partial \phi^{S,R}(\mathbf{s})}{\partial n_{\mathbf{s}}} d\Gamma(\mathbf{s}), \end{aligned} \quad (4.16)$$

$$\begin{aligned} \frac{1}{2} \frac{\partial \phi^{S,R}(\mathbf{x})}{\partial n_{\mathbf{x}}} &= HPV \int_{\Gamma_s} N(\mathbf{x}, \mathbf{s}) \phi^{S,R}(\mathbf{s}) d\Gamma(\mathbf{s}) - CPV \int_{\Gamma_s} M(\mathbf{x}, \mathbf{s}) \frac{\partial \phi^{S,R}(\mathbf{s})}{\partial n_{\mathbf{s}}} d\Gamma(\mathbf{s}) \\ &+ \int_{\Gamma_4^+} N(\mathbf{x}, \mathbf{s}) \Delta \phi^{S,R}(\mathbf{s}) d\Gamma(\mathbf{s}) - \int_{\Gamma_4^+} M(\mathbf{x}, \mathbf{s}) \sum \frac{\partial \phi^{S,R}(\mathbf{s})}{\partial n_{\mathbf{s}}} d\Gamma(\mathbf{s}), \end{aligned} \quad (4.17)$$

where

$$\Delta\phi^{S,R}(\mathbf{s}) \equiv \phi^{S,R}(\mathbf{s}^+) - \phi^{S,R}(\mathbf{s}^-), \quad (4.18)$$

$$\sum \frac{\partial\phi^{S,R}(\mathbf{s})}{\partial n} \equiv \frac{\partial\phi^{S,R}(\mathbf{s}^+)}{\partial n} + \frac{\partial\phi^{S,R}(\mathbf{s}^-)}{\partial n}. \quad (4.19)$$

For $\mathbf{x} \in \Gamma_4^+$, Eqs. (4.14) and (4.15) are reduced into the following forms

$$\begin{aligned} \frac{1}{2} \sum \phi^{S,R}(\mathbf{x}) = & CPV \int_{\Gamma_4^+} V(\mathbf{x}, \mathbf{s}) \Delta\phi^{S,R}(\mathbf{s}) d\Gamma(\mathbf{s}) - RPV \int_{\Gamma_4^+} G(\mathbf{x}, \mathbf{s}) \sum \frac{\partial\phi^{S,R}(\mathbf{s})}{\partial n_{\mathbf{s}}} d\Gamma(\mathbf{s}) \\ & + \int_{\Gamma_s} V(\mathbf{x}, \mathbf{s}) \phi^{S,R}(\mathbf{s}) d\Gamma(\mathbf{s}) - \int_{\Gamma_s} G(\mathbf{x}, \mathbf{s}) \frac{\partial\phi^{S,R}(\mathbf{s})}{\partial n_{\mathbf{s}}} d\Gamma(\mathbf{s}), \end{aligned} \quad (4.20)$$

$$\begin{aligned} \frac{1}{2} \Delta \frac{\partial\phi^{S,R}(\mathbf{x})}{\partial n_{\mathbf{x}}} = & HPV \int_{\Gamma_4^+} N(\mathbf{x}, \mathbf{s}) \Delta\phi^{S,R}(\mathbf{s}) d\Gamma(\mathbf{s}) - CPV \int_{\Gamma_4^+} M(\mathbf{x}, \mathbf{s}) \sum \frac{\partial\phi^{S,R}(\mathbf{s})}{\partial n_{\mathbf{s}}} d\Gamma(\mathbf{s}) \\ & + \int_{\Gamma_s} N(\mathbf{x}, \mathbf{s}) \phi^{S,R}(\mathbf{s}) d\Gamma(\mathbf{s}) - \int_{\Gamma_s} M(\mathbf{x}, \mathbf{s}) \frac{\partial\phi^{S,R}(\mathbf{s})}{\partial n_{\mathbf{s}}} d\Gamma(\mathbf{s}), \end{aligned} \quad (4.21)$$

where

$$\sum \phi^{S,R}(\mathbf{s}) \equiv \phi^{S,R}(\mathbf{s}^+) + \phi^{S,R}(\mathbf{s}^-), \quad (4.22)$$

$$\Delta \frac{\partial\phi^{S,R}}{\partial n}(\mathbf{s}) \equiv \frac{\partial\phi^{S,R}}{\partial n}(\mathbf{s}^+) - \frac{\partial\phi^{S,R}}{\partial n}(\mathbf{s}^-). \quad (4.23)$$

It is to be noted that in Eqs. (4.18)-(4.19) and (4.22)-(4.23), the number of unknowns on the degenerate boundaries is double as compared to the unknowns on the non-degenerate boundaries. Therefore, the integral equation (4.12) is necessary to obtain unique solutions. By discretizing the boundaries Γ of the domain using the constant boundary element method and varying the field point \mathbf{x} over each boundary element, we get the following system of equations (see Trivedi et al. [94], Chen et al. [96])

$$[\tilde{V}_{ij}] \left\{ \phi_j^{S,R} \right\} = [G_{ij}] \left\{ \left(\frac{\partial\phi^{S,R}}{\partial n} \right)_j \right\}, \quad (4.24)$$

$$[N_{ij}] \left\{ \phi_j^{S,R} \right\} = [\tilde{M}_{ij}] \left\{ \left(\frac{\partial\phi^{S,R}}{\partial n} \right)_j \right\}, \quad (4.25)$$

where the influence coefficients G_{ij} , \tilde{V}_{ij} , \tilde{M}_{ij} and N_{ij} are given by

$$G_{ij} = RPV \int_{\Gamma_j} G(\mathbf{x}_i, \mathbf{s}_j) d\Gamma(\mathbf{s}_j), \quad (4.26)$$

$$\tilde{V}_{ij} = -\frac{1}{2}\delta_{ij} + CPV \int_{\Gamma_j} V(\mathbf{x}_i, \mathbf{s}_j) d\Gamma(\mathbf{s}_j), \quad (4.27)$$

$$\tilde{M}_{ij} = \frac{1}{2}\delta_{ij} + CPV \int_{\Gamma_j} M(\mathbf{x}_i, \mathbf{s}_j) d\Gamma(\mathbf{s}_j), \quad (4.28)$$

$$N_{ij} = HPV \int_{\Gamma_j} N(\mathbf{x}_i, \mathbf{s}_j) d\Gamma(\mathbf{s}_j). \quad (4.29)$$

When the field point \mathbf{x}_i and the source point \mathbf{s}_j lies on the different boundary element, the well-known Gauss-Legendre quadrature is used to evaluate the aforementioned influence coefficients. On the other hand, when the field point \mathbf{x}_i and the source point \mathbf{s}_j lies on the same boundary element, singularity occurs, and special treatment is required to evaluate the influence coefficients. Now, two different approaches $GV + MN$ and $MN + GV$ are available to solve the unknowns. In the present study, $GV + MN$ approach is adopted. In this approach, the following system of equations is obtained (Chen et al. [95])

$$\begin{bmatrix} V_{i_{\Gamma_s} j_{\Gamma_s}} & V_{i_{\Gamma_s} j_{\Gamma_4^+}} & V_{i_{\Gamma_s} j_{\Gamma_4^-}} \\ V_{i_{\Gamma_4^+} j_{\Gamma_s}} & V_{i_{\Gamma_4^+} j_{\Gamma_4^+}} & V_{i_{\Gamma_4^+} j_{\Gamma_4^-}} \\ N_{i_{\Gamma_4^+} j_{\Gamma_s}} & N_{i_{\Gamma_4^+} j_{\Gamma_4^+}} & N_{i_{\Gamma_4^+} j_{\Gamma_4^-}} \end{bmatrix} \begin{Bmatrix} \phi_{j_{\Gamma_s}}^{S,R} \\ \phi_{j_{\Gamma_4^+}}^{S,R} \\ \phi_{j_{\Gamma_4^-}}^{S,R} \end{Bmatrix} = \begin{bmatrix} G_{i_{\Gamma_s} j_{\Gamma_s}} & G_{i_{\Gamma_s} j_{\Gamma_4^+}} & G_{i_{\Gamma_s} j_{\Gamma_4^-}} \\ G_{i_{\Gamma_4^+} j_{\Gamma_s}} & G_{i_{\Gamma_4^+} j_{\Gamma_4^+}} & G_{i_{\Gamma_4^+} j_{\Gamma_4^-}} \\ M_{i_{\Gamma_4^+} j_{\Gamma_s}} & M_{i_{\Gamma_4^+} j_{\Gamma_4^+}} & M_{i_{\Gamma_4^+} j_{\Gamma_4^-}} \end{bmatrix} \begin{Bmatrix} \left[\frac{\partial \phi^{S,R}}{\partial n} \right]_{j_{\Gamma_s}} \\ \left[\frac{\partial \phi^{S,R}}{\partial n} \right]_{j_{\Gamma_4^+}} \\ \left[\frac{\partial \phi^{S,R}}{\partial n} \right]_{j_{\Gamma_4^-}} \end{Bmatrix}. \quad (4.30)$$

Using boundary conditions (4.2)-(4.7), the system of equations (4.30) is solved to get the unknowns $\phi^{S,R}$ and $\partial \phi^{S,R} / \partial n$ over each boundary elements.

4.4 Hydrodynamic performance of the OWC device in the presence of irregular incident waves

This section yields the expressions corresponding to the hydrodynamic performance of the OWC device in the presence of irregular incident waves. Since the mathematical model is based on the linear water wave theory and the free surface elevation is assumed to be a Gaussian random process, the scattered volume flow rate $Q^s(t) = \Re\{q^s e^{-i\omega t}\}$ and instantaneous pressure across the turbine $P(t) = \Re\{p e^{-i\omega t}\}$ are also Gaussian processes. Therefore, the probability density function of instantaneous pressure is given by

$$f(p) = \frac{1}{\sqrt{2\pi}\sigma_p} \exp\left(\frac{-P^2}{2\sigma_p^2}\right) \quad (4.31)$$

where the expression for σ_p is

$$\sigma_p^2 = \int_0^\infty S_I(\omega) \left| \frac{p(\omega)}{A_i(\omega)} \right|^2 d\omega, \quad A_i(\omega) = \sqrt{2S_I(\omega_i^{av})\Delta\omega_i}, \quad (4.32)$$

Now, the power available to the wave energy converter is

$$P_{avg} = \frac{\dot{m}P}{\rho_a} = \wedge\sigma_P^2 \quad (4.33)$$

where $\wedge = \frac{K_a D}{\rho_a N}$, ρ_a and \dot{m} are termed as air density and mass flow rate of air across the Wells turbine. Here, N and D represent the rotational speed and turbine rotor diameter of the Wells turbine, respectively, and $K_a = 0.375$. Therefore, The average power output by the OWC device can be expressed as

$$P_{avg} = \wedge \int_0^\infty S_I(\omega) \left| \frac{p(\omega)}{A_i(\omega)} \right|^2 d\omega, \quad A_i(\omega) = \sqrt{2S_I(\omega_i^{av})\Delta\omega_i}, \quad (4.34)$$

where p is the instantaneous pressure across the turbine and \wedge is the turbine damping coefficient. Furthermore, A_i is the incident wave amplitude for each regular wave component and the form of incident wave spectrum is provided as

$$S_I(\omega) = 131.5H_s^2T_e^{-4}\omega^{-5} \exp(T_e^{-4}\omega^{-4}). \quad (4.35)$$

Here, H_s and T_e are symbolized as significant wave height and significant time period, respectively. Further, the average incident wave energy flux for the irregular waves is written as (De O Falcão and Rodrigues [1], Trivedi and Koley [140])

$$P_{inc} = \rho g L_w \int_0^\infty S_I(\omega) C_g d\omega. \quad (4.36)$$

Here, L_w is the chamber width of the OWC device. Subsequently, the annual-averaged power output by the OWC device is provided as (Trivedi and Koley [140])

$$P_{ann} = \wedge \int_0^\infty S_{I,ann}(\omega) \left| \frac{p(\omega)}{A_i(\omega)} \right|^2 d\omega, \quad (4.37)$$

where $S_{I,ann}$ is symbolized as annual spectral density, and its expression is provided as

$$S_{I,ann} = \sum_{j=1}^9 S_{I_j} \psi_j. \quad (4.38)$$

Here, ψ_j is termed as frequency of occurrence related to the set of nine sea states represent the local wave climate at the OWC plant site Pico, Azores, Portugal. The details for the same are provided in De O Falcão and Rodrigues [1].

4.5 Results

The present section yields the various results associated with the hydrodynamic performances of quarter circle-shaped OWC devices in a detailed manner. The parameters corresponding to the incident wave and the OWC device are considered as follows: $h = 8\text{m}$, $L_w = 12\text{m}$, $\rho = 1025\text{ kg/m}^3$, $g = 9.81\text{m/s}^2$, $L/h = 2.0$, $l/h = 3.0$, $r/h = 2.5$, $y_0/h = -0.72$, $b_h/h = 0.1$, $\theta = 45^\circ$, $V_0 = 1050\text{ m}^3$, $\gamma = 1.4$, $\rho_a = 1.25\text{ kg/m}^3$ and $p_a = 1.013 \times 10^5\text{Pa}$ unless otherwise mentioned.

4.5.1 Validation

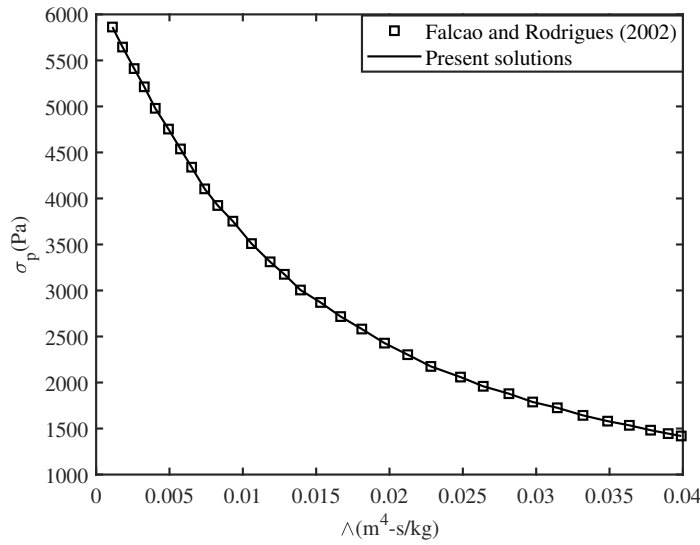


FIGURE 4.2: σ_p as a function of Λ .

TABLE 4.1: Comparison of annual-averaged efficiency ε_{ann} obtained by the present solution technique and the results provided in De O Falcão and Rodrigues [1].

| Λ | ε_{ann} (De O Falcão and Rodrigues [1]) | ε_{ann} (present solutions) | Percentage errors |
|-----------|---|---|-------------------|
| 0.005 | 0.57065 | 0.57017 | 0.084% |
| 0.01 | 0.68611 | 0.68623 | 0.017% |
| 0.015 | 0.66253 | 0.66201 | 0.078% |
| 0.02 | 0.60781 | 0.60793 | 0.019% |
| 0.025 | 0.55287 | 0.55264 | 0.041% |
| 0.03 | 0.50144 | 0.50134 | 0.019% |

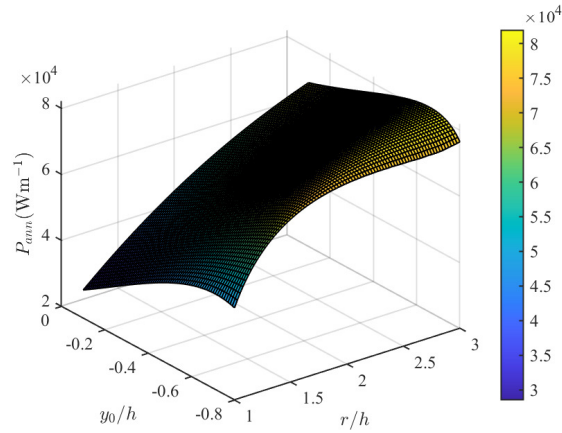
Fig. 4.2 demonstrates the comparison between the present solutions and the results provided in De O Falcão and Rodrigues [1] for the variation of chamber pressure standard deviation σ_p as a function of turbine damping coefficient Λ for a rectangular shape OWC device. The input parameters are taken the same as provided in De O Falcão and Rodrigues [1]. This comparison

demonstrates that the present computational results match well with the results provided by De O Falcão and Rodrigues [1]. For further validation in tabulated form, Tab. 4.1 compares the annual-averaged efficiency ε_{ann} obtained by the present solutions and the results provided in De O Falcão and Rodrigues [1] for different values of turbine damping coefficient Λ . It's observed from Tab. 4.1 that the percentage errors are less than 0.1%, and this demonstrates the accuracy of the present solutions.

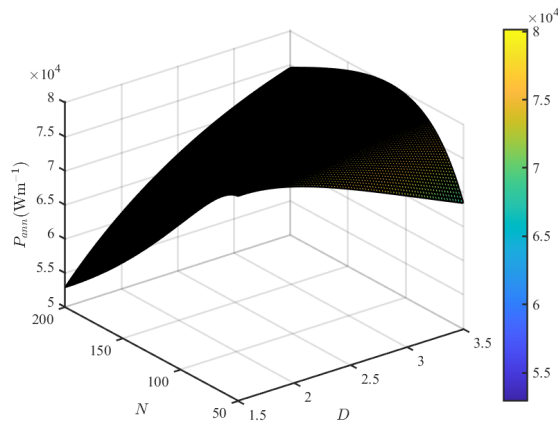
4.5.2 Results associated with the DBEM methodology

Various results associated with the quarter circle-shaped front wall OWC device are already available in Trivedi and Koley [140], and therefore, the same are excluded here just to avoid mere repetitions. Since in the subsequent MLP model and XGBoost model, the optimization of annual averaged power generated by the OWC device as a function of submergence depth of the front wall of the OWC device, chamber length, rotational speed, and diameter of the turbine blade will be demonstrated, the surface plot for the same are provided in the following.

To get combined effects of r/h and y_0/h on the annual average power extraction P_{ann} by the OWC device, a surface plot for P_{ann} as a function of r/h and y_0/h is demonstrated in Fig. 4.3(a). It is found that for fixed values of y_0/h , the annual average power extraction P_{ann} by the OWC device increases with an increase in r/h . However, there is no change noticed for higher values of r/h . Further, for fixed values of r/h , the annual average power extraction P_{ann} by the OWC device increases with an increase in y_0/h except for very higher values of y_0/h . It is due to the fact that less amount of water can actually enter into the OWC chamber for very higher values of submergence depth y_0/h . In summary, it can be concluded that the annual average power extraction P_{ann} by the OWC device is achieved for the OWC device with $2.5 < r/h < 3.0$ and $-0.7 < y_0/h < -0.5$. On the other hand, to analyze the combined effects of turbine rotor diameter D and rotational speed N on the annual average power extraction P_{ann} by the OWC device, a surface plot of P_{ann} as a function of N and D is illustrated in Fig. 4.3(b). It is observed that for lower values of rotational speed N , annual average power extraction P_{ann} by the OWC device decreases as the rotor diameter D increases. However, for higher values of rotational speed N , the annual average power extraction P_{ann} by the OWC device increases as the rotor diameter D increases. Similarly, for lower values of D , annual average power extraction P_{ann} by the OWC device decreases with an increase in N . Further, for higher values of D , the annual average power extraction P_{ann} by the OWC device initially increases with an increase in N and attains a maximum. Hereafter, the annual average power extraction P_{ann} by the OWC device decreases for further increase in N . These results indicate that the annual average power extraction P_{ann} by the OWC device can be enhanced with the suitable combinations of turbine rotor diameter $2 \leq D \leq 3.5$ and rotational speed $70 \leq N \leq 135$.



(a)



(b)

FIGURE 4.3: Surface plot of P_{ann} (Wm^{-1}) as a function of (a) r/h and y_0/h , and (b) N and D .

Utilizing MLP model and XGBoost model for device parameters optimization offers several advantages over traditional optimization methods. Unlike surface plots as provided in Fig. 4.3, which restricts the study of only two independent parameters at a time. The XGBoost model allows for the examination of complex relationships between all input features and the target variable in a time-efficient manner and MLP can be used for accurate prediction. The MLP models and XGBoost models effectively handling non-linear functions, making them well-suited for intricate optimization problems. They possess the ability to generalize learned knowledge, adapt to new data, and efficiently explore large design spaces.

4.6 Model building

In this section, we focus on optimizing the design attributes of the OWC device to maximize its annual average power extraction, denoted as P_{ann} . To accomplish this, we utilize a sequential ANN model known as the multi-layer perceptron model with the support of the XGBoost model.

The MLP model will effectively predict the annual average power generated by the oscillating water column wave energy converter device, and the XGBoost model will explain the dynamic effect as well as the interaction effect between various parameters of the device. The subsequent subsections provide detailed explanations of how the dataset is constructed for the architecture of the multi-layer perceptron model and the XGBoost model used for the optimization process.

4.6.1 Construction of the database

The training, validation, and testing database for the model are built using the dual boundary element method, as explained in Section 3. The model takes four input features into account: the submergence depth of the front wall of the device (y_0/h), chamber length (r/h), turbine rotor diameter (D), and turbine rotational speed (N). On the other hand, the output feature of the model is the annual average power extraction (P_{ann}) achieved by the OWC device. The power generation of the OWC device is calculated based on the average annual power generation, as mentioned earlier.

TABLE 4.2: Descriptive statistics of database for model building

| | y_0/h | r/h | $N(\text{rad/s})$ | $D(\text{m})$ | $P_{ann}(\text{Wm}^{-1})$ |
|-------|---------|---------|-------------------|---------------|---------------------------|
| count | 3750.00 | 3750.00 | 3750.00 | 3750.00 | 3750.00 |
| mean | -0.41 | 2.00 | 124.98 | 2.50 | 56102.52 |
| std | 0.23 | 0.58 | 43.04 | 0.57 | 13263.71 |
| min | -0.78 | 1.03 | 54.89 | 1.56 | 20478.18 |
| 25% | -0.61 | 1.48 | 89.65 | 2.03 | 46089.84 |
| 50% | -0.41 | 2.02 | 124.96 | 2.52 | 56421.47 |
| 75% | -0.22 | 2.49 | 160.38 | 3.01 | 66583.05 |
| 90% | -0.11 | 2.76 | 182.20 | 3.25 | 74301.41 |
| 95% | -0.05 | 2.89 | 193.31 | 3.42 | 77662.63 |
| 99% | -0.02 | 2.95 | 197.19 | 3.44 | 81363.70 |
| max | -0.02 | 2.95 | 197.19 | 3.44 | 82602.98 |

The accuracy of a machine learning model is widely recognized to be closely linked to the sampling technique employed. When a sampling technique generates a well-stratified sample, it significantly enhances the model's accuracy. In this study, we employ the Latin Hypercube Sampling (LHS) methodology to construct the most stratified input database possible. The database is designed by selecting 30 random samples from each input feature, considering specific ranges: $-0.8 \leq y_0/h \leq -0.01$, $1 \leq r/h \leq 3$, $50 \leq N \leq 200$, and $1.5 \leq D \leq 3.5$ as seen in Fig. 4.4. The significance of these ranges for the input features is explained in Trivedi and Koley [140]. The descriptive statistics of the database for model building is given in Tab. 4.2. As we are considering 30 random samples for each parameter, we theoretically have the potential to generate a total of 30^4 different input examples. However, due to the high computational cost of handling such an extensive dataset, the focus is only on a well-stratified subset consisting

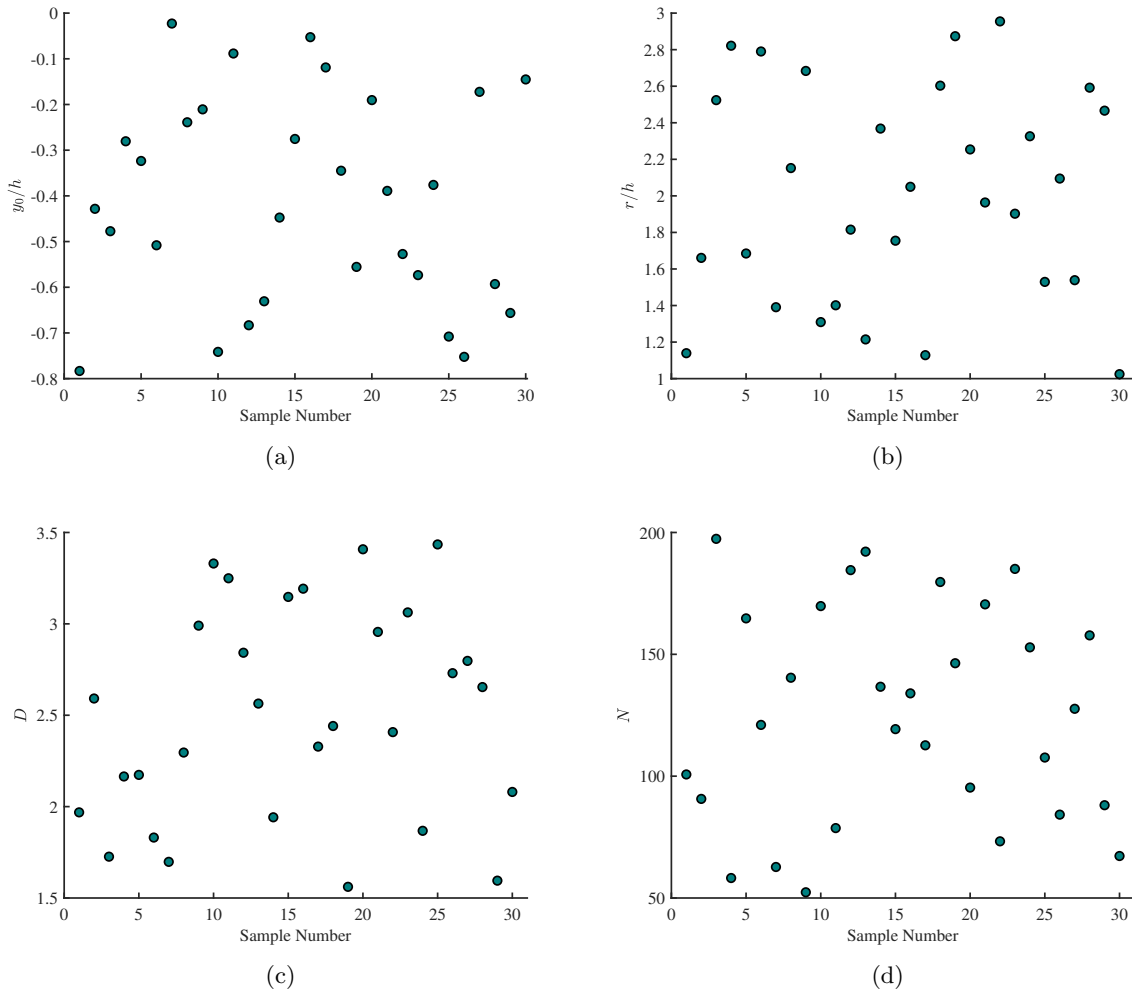


FIGURE 4.4: Scatter plots of the input features (a) submergence depth y_0/h , (b) chamber length r/h , (c) turbine rotor diameter D , and (d) turbine rotational speed N for training, validation and testing the model.

of precisely 3750 samples. To create this set of input data combinations, the 30 samples for each variable are partitioned into sets of five, with a six-value interval within a specific feature. Consequently, we will have a total of six sets, each containing five unique samples for every parameter value. Subsequently, the database is formed by generating 5^4 distinct samples from each of these six sets. Hence, the training, validation, and test datasets are derived from the pool of 3750 unique input combinations and their corresponding response variable, i.e., annual average power extraction (P_{ann}) obtained from the OWC device.

4.6.2 Development of the ANN Model

A multi-layer perceptron (MLP) is a type of artificial neural network (ANN) that consists of multiple layers of interconnected nodes, known as artificial neurons or perceptrons. The architecture of the MLP consists of three important layers: an input layer, multiple hidden layers,

and an output layer. The input layer receives the inputs from the database, and the output layer will produce the outputs or the prediction values. The number of hidden layers and the number of neurons in each of the hidden layer defines the depth of the model. Each neuron in a MLP model is a function that receives input from the previous layer, and it multiplies with the associated weight, and a bias associated with the layer will be added to it. The cumulative input of the neuron will pass through an activation function to introduce non-linearity in the model and will produce the output. To get better prediction performance, four different activation functions are tested in the present study, and the same is provided in Tab. 4.3 (see Kim et al. [141]). The error matrices used in this study is provided in Tab. 4.4. Here, the measured value

TABLE 4.3: Activation function definition

| Function | Definition |
|---------------------------------------|--|
| Rectified linear unit (ReLU) | $g(x) = \max(0, x)$ |
| Exponential linear Unit (ELU) | $g(x) = \max(0, x) + \min(0, \alpha(e^x - 1))$, $\alpha \approx 1.6732$ |
| Scaled exponential linear Unit (SELU) | $g(x) = \gamma(\max(0, x) + \min(0, \alpha(e^x - 1)))$, $\gamma \approx 1.0507$ |
| Gaussian Error Linear Unit (GELU) | $g(x) = \frac{x}{2} \left[1 + \operatorname{erf} \left(\frac{x}{\sqrt{2}} \right) \right]$ |

and the estimated value are denoted by $p^{(m)}$ and $\hat{p}^{(m)}$, respectively. Further, M denotes the number of observations. Further, the performance of the model is calculated using the coefficient

TABLE 4.4: Error Matrices

| Function | Definition |
|---------------------------------------|---|
| Mean absolute error (MAE) | $\frac{1}{M} \sum_{m=1}^M \hat{p}^{(m)} - p^{(m)} $ |
| Mean absolute percentage error (MAPE) | $\frac{1}{M} \sum_{m=1}^M \frac{ \hat{p}^{(m)} - p^{(m)} }{p^{(m)}} \times 100\%$ |
| Root mean square error (RMSE) | $\sqrt{\frac{\sum_{m=1}^M (\hat{p}^{(m)} - p^{(m)})^2}{M}}$ |

of determination (Rahman et al. [142]) as provided in the following expression

$$R^2 = 1 - \frac{\sum_{m=1}^M (\hat{p}^{(m)} - p^{(m)})^2}{\sum_{m=1}^M (\hat{p}^{(m)} - \overline{p^{(m)}})^2}. \quad (4.39)$$

Here, $\overline{p^{(m)}}$ represents the average value of $p^{(m)}$. Now, to construct the training database, we employ the Latin Hypercube Sampling (LHS) technique. Using this LHS technique, the generated

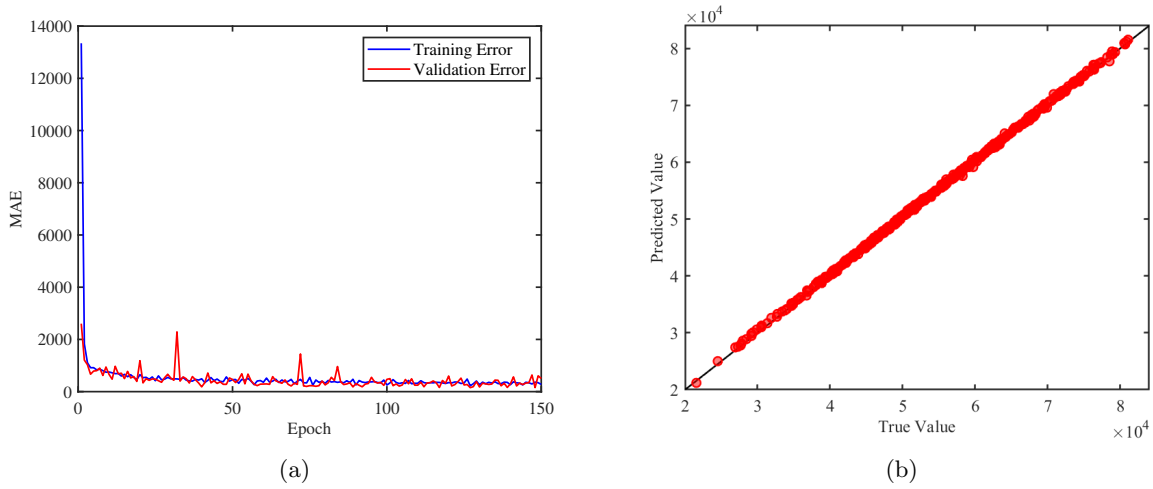


FIGURE 4.5: (a) Training and validation loss of the ANN model based on the MAE metric, and (b) comparison between the true values and predicted values using the MLP model.

TABLE 4.5: Decision variables of random search algorithm for MLP model.

| | |
|---|--|
| Number of hidden layer | { 5, 6, 7, 8, 9, 10 } |
| Number neurons in each hidden layer | { 16, 32, 64, 128, 256, 512, 1024 } |
| Activation function in each of the hidden layer | { ReLU, GELU, ELU, SELU } |
| Optimization function of the MLP model | { SGD, RMSPROP, ADAGRAD, ADADELTA, ADAM, ADAMAX, NADAM } |

TABLE 4.6: Error scores and R^2 value of the MLP Model

| Train MAPE | Test MAPE | Train MAE | Test MAE | Train RMSE | Test RMSE | R^2 - Test set |
|------------|-----------|-----------|----------|------------|-----------|------------------|
| 0.41% | 0.44% | 216.35 | 224.98 | 280.95 | 309.81 | 0.9995 |

input dataset is denoted as $X = \{X^{(i)} \mid i = 1, 2, \dots, M\}$. The corresponding output $P = \{p^{(i)} \mid i = 1, 2, \dots, M\}$ for the training database is then obtained by applying the input dataset to the model developed in Section 3. In this context, M denotes the number of training samples. Each input sample $X^{(i)}$, consists of n features, represented as $X^{(i)} = \{x_j^{(i)} \mid j = 1, 2, \dots, n\}$. Here, n represents the total number of input features. Moreover, the MLP model architecture includes ℓ' number of hidden layers with the ℓ^{th} layer comprises of $n^{[\ell]}$ neurons. The output of the i^{th} sample from the k^{th} neuron in the first layer, denoted by $a_k^{[1](i)}$, can be calculated as follows

$$a_k^{[1](i)} = g^{[1]} \left(\sum_{j=1}^n W_{k,j}^{[1]T} x_j^{(i)} + b_k^{[1]} \right). \quad (4.40)$$

In a similar manner, the output of the i^{th} sample from k^{th} neuron in the ℓ^{th} hidden layer can be computed as follows:

$$a_k^{[\ell](i)} = g^{[\ell]} \left(\sum_{j=1}^{n^{[\ell-1]}} W_{k,j}^{[\ell]T} a_j^{[\ell-1](i)} + b_k^{[\ell]} \right). \quad (4.41)$$

Finally, the output of the i^{th} sample $\hat{p}^{(i)}$ in the output layer can be computed as:

$$\hat{p}^{(i)} = g^{[\ell']} \left(\sum_{j=1}^{n^{[\ell'-1]}} W_{k,j}^{[\ell']T} a_j^{[\ell'-1](i)} + b_k^{[\ell']} \right), \quad (4.42)$$

where $W_{k,j}^{[\ell]}$ signifies the weight associated to the connection between the j^{th} neuron in the $(\ell - 1)^{th}$ layer and the k^{th} neuron in the ℓ^{th} layer. Additionally, $a_k^{[\ell](i)}$ represents the output of the i^{th} sample from k^{th} neuron in the ℓ^{th} layer. These outputs are determined by applying the activation function $g^{[\ell]}$, which is specifically associated with the ℓ^{th} layer. The minimization of the MAE between the actual output P obtained by applying the dual boundary element method developed in Section 3 and the predicted output $\hat{P} = \{\hat{p}^{(i)} \mid i = 1, 2, \dots, M\}$ obtained from the MLP model involves adjusting the weight and bias factors, denoted as $W = \bigcup_{\ell=1}^{\ell'} W^{[\ell]}$ and $B = \bigcup_{\ell=1}^{\ell'} \bigcup_{k=1}^{n^{[\ell]}} b_k^{[\ell]}$. Here, $W^{[\ell]}$ represents a matrix of dimension $[n^{[\ell]}, n^{[\ell-1]}]$, where $n^{[\ell]}$ corresponds to the number of neurons in the ℓ^{th} layer, and $n^{[\ell-1]}$ represents the number of neurons in the $(\ell - 1)^{th}$ layer. Additionally, $b_k^{[\ell]}$ is a constant bias term associated with the k^{th} neuron in the ℓ^{th} layer.

The primary objective of the MLP model is to minimize the discrepancy between the actual output P and the predicted output \hat{P} . To improve the accuracy and generalization ability of the MLP model, the parameters of the neural network model are optimized using a random search algorithm (Bergstra and Bengio [143]), and the chosen parameter values for the optimization process are provided in Tab. 4.5 (see Kingma and Ba [144], Zeiler [145]).

The input layer of the ANN model comprises four neurons representing the four input features. On the other hand, the output layer of the ANN model consists of a single neuron, which effectively captures the output feature, i.e., the annual average power extraction (P_{ann}) achieved by the OWC device. After the optimization of the parameters of the ANN model, the number of hidden layers is obtained to be five, which consists of the number of neurons as 256, 128, 128, 64, and 32, respectively. Moreover, the ‘‘NADAM’’ optimizer is found to be the best optimizer for the training datasets associated with the annual average power extraction (P_{ann}) achieved by the OWC device. To introduce non-linearity in the model, the GELU activation function is found to be the most suitable for each of the hidden layers. In the pre-processing stage, the total dataset

comprising 3750 data points is partitioned into a training, validating, and testing set. Using this dataset comprising of 3750 samples, the ANN model undergoes training with 60% of the data and validation using 20%. Post-training, the ANN model is tested on the remaining 20% of the dataset. Due to the diverse scales of the input features, the numerical values are standardized in the pre-processing stage. The standardization process involves transforming the input features using the formula $(x - \bar{x})/\sigma(x)$, where \bar{x} represents the mean and $\sigma(x)$ signifies the standard deviation of the respective input feature. By adhering to this standardized approach, the model will proficiently capture the unique characteristics of the input data, leading to more precise predictions.

To evaluate the performance of the developed ANN model, the MAE metric is chosen from the set of error matrices considered in Tab. 4.4. Fig. 4.5(a) shows the training error and the validation error of the ANN model over the course of 150 epochs. Notably, as the number of epochs increases, the training error steadily decreases until it reaches a threshold value, beyond which its variation becomes minimal. Further, the gap between the training and validation errors remains insignificantly small. This observation demonstrates that the model exhibits an optimal fit to the training data. The quantified values of the training and the testing errors for MAPE, MAE, and RMSE are provided in Tab. 4.6. The results demonstrated that the MAE and RMSE values are significantly smaller as compared to the response variable, which varies from about 20,000 to 80,000. This can be easily verified from the MAPE value, which is less than 0.5% for both the training and testing sets. Here, the R^2 value for the test set is found to be 0.9995, which signifies that the present model effectively captures 99.95% of the variation in the target variable based on the input variables. This can be clearly observed from Fig. 4.5(b), which represents the actual value and the predicted value of the test set. The aforementioned results demonstrate that this model can be used for the prediction of the annual average power extraction (P_{ann}) for a new set of input parameter values and can be achieved with minimal computational effort.

In the domain of supervised machine learning models, tree ensemble models are widely recognized for their inherent explainability. Among these, XGBoost models are assumed to be self-interpretable machine learning models, and this XGBoost model can be used for both regression and classification problems (El Bilali et al. [72]). The XGBoost model can be used to find particular regions consisting of different combinations of input features, which can result in maximum power generation by the device. This can be achieved by employing interpretable machine-learning techniques such as ALE (Accumulated Local Effect) plots (Apley and Zhu [118]), Shapley values (Lundberg and Lee [146]), etc. Hereafter, an extended input dataset will be generated associated with each of the selected regions, and by using the developed MLP model, the corresponding response variable will be obtained. Consequently, the optimal values of the parameters will be obtained, which maximize the annual average power extraction (P_{ann}). The framework of the above-mentioned XGBoost model will be discussed in the next section.

4.6.3 Development of the XGBoost model

Extreme Gradient Boosting (XGBoost) is an efficient and scalable implementation of a gradient boosting framework (see Chen et al. [147]). XGBoost models have several advantages, such as sparsity awareness and support parallel processing. Further, to avoid overfitting due to the model complexity, the L_1 and L_2 regularization terms are incorporated into the loss function (El Bilali et al. [72]). Additionally, the XGBoost algorithm employs an exact greedy approach, consistently making optimal decisions at each step of the learning process (Chen and Guestrin [84]).

For a given training set with M samples $\left\{ \left(X^{(1)}, p^{(1)} \right), \left(X^{(2)}, p^{(2)} \right), \dots, \left(X^{(M)}, p^{(M)} \right) \right\}$ with n number of features, the aim of the XGBoost model is to construct a predictive function $F(X)$ that estimate \hat{P} for a new input X . Let K be the number of iterations or the number of ensemble trees in the model. The final prediction $F(X)$ is achieved through summing the predictions made by all weak learners in the ensemble and is given by (see El Bilali et al. [72])

$$\hat{p}^{(i)} = F \left(X^{(i)} \right) = \sum_{k=1}^K f_k \left(X^{(i)} \right), \quad f_k \in \mathcal{F}, \quad (4.43)$$

where $\mathcal{F} = \{ f(X) = w_{q(x)} \}$, $(q : \mathbb{R}^n \rightarrow T, w \in \mathbb{R}^T)$ is the space of regression trees and q is the structure of each tree that maps a sample to the corresponding leaf node. Here, T is the number of leaves in the tree, and f corresponds to an independent tree structure q and leaf weights w (Chen and Guestrin [84]).

Let $\hat{p}_k^{(i)}$ be the prediction of the i^{th} example at the k^{th} iteration, and let L be a differentiable convex loss function that measures the difference between the target $p^{(i)}$ and the prediction $\hat{p}^{(i)}$, the cost function is considered to be $\sum_{i=1}^M L \left(\hat{p}^{(i)}, p^{(i)} \right)$. Then, the regularized objective function is provided as (Chen and Guestrin [84])

$$\mathcal{L}(F) = \sum_{i=1}^M L \left(\hat{p}^{(i)}, p^{(i)} \right) + \sum_{k=1}^K R(f_k), \quad \text{where } R(f) = \alpha T + \frac{1}{2} \lambda \|w\|^2. \quad (4.44)$$

Here, $R(f)$ is the regularization term, which penalizes the model complexity. Moreover, α and λ are the L_1 and L_2 regularization weights, respectively. Using the Taylor's formula, the k^{th} iteration of the objective function after adding f_k to the loss function is given by (Chen and

Guestrin [84])

$$\mathcal{L}_k = \sum_{i=1}^M \left[g^{(i)} f_k(x^{(i)}) + \frac{1}{2} h^{(i)} f_k^2(x^{(i)}) \right] + R(f_k), \quad (4.45)$$

$$\text{where } g^{(i)} = \frac{\partial L(p^{(i)}, \hat{p}_{k-1})}{\partial \hat{p}_{k-1}}, \quad (4.46)$$

$$h^{(i)} = \frac{\partial^2 L(p^{(i)}, \hat{p}_{k-1})}{\partial \hat{p}_{k-1}^2}. \quad (4.47)$$

Now, optimal weights of the j^{th} leaf node is computed as (see Chen and Guestrin [84])

$$w_j = - \frac{\sum_{i \in I_j} g^{(i)}}{\sum_{i \in I_j} h^{(i)} + \lambda}, \quad (4.48)$$

where $I_j = \{i : q(X^{(i)}) = j\}$ signifies the instance set of j^{th} leaf. The optimal score of the tree structure q is calculated by (see Chen and Guestrin [84])

$$\tilde{\mathcal{L}}_k(q) = -\frac{1}{2} \sum_{j=1}^T \frac{\left(\sum_{i \in I_j} g^{(i)} \right)^2}{\sum_{i \in I_j} h^{(i)} + \lambda} + \alpha T \quad (4.49)$$

The XGBoost model follows a greedy algorithm that starts from a single leaf and iteratively adds branches to the tree. The splitting of the leaf node is carried out using the formula (see El Bilali et al. [72]).

$$L_{split} = \frac{1}{2} \left[\frac{\left(\sum_{i \in I_L} g^{(i)} \right)^2}{\sum_{i \in I_L} h^{(i)} + \lambda} + \frac{\left(\sum_{i \in I_R} g^{(i)} \right)^2}{\sum_{i \in I_R} h^{(i)} + \lambda} - \frac{\left(\sum_{i \in I} g^{(i)} \right)^2}{\sum_{i \in I} h^{(i)} + \lambda} \right] - \alpha, \quad (4.50)$$

where I_L and I_R are the instance sets of left and right nodes after the split with $I = I_L \cup I_R$.

Prior to the model training, it is essential to optimize the hyperparameters of the XGBoost model based on the dataset's complexity. A genetic algorithm(GA) based optimization technique is used with the support of the TPOTRegressor library. The decision variables, their range of values for the optimization, and the corresponding optimized values are provided in Tab. 4.7. Fig. 4.6(a) shows the reduction in the training and validation errors of the XGBoost model with an increase number of iterations. A good agreement between the training set and the validation set shows that the model is able to capture the variation of the response variable from the input

features. Fig. 4.6(b) shows the scattering of the observed and the predicted values of the XGB model for the test set. Here it is seen that the observed and the predicted values lie on the $X = Y$ line, showing the accuracy of the predicted model.

TABLE 4.7: Decision variables of GA for XGBoost model and the corresponding optimized values

| Hyperparameters | Range of Values | Optimized value |
|----------------------|--------------------------------|-----------------|
| Max depth | {3, 4, \dots , 20} | 5 |
| Learning rate | {0.001, 0.0061, \dots , 0.2} | 0.19 |
| Max bin | {10, 30, \dots , 190} | 110 |
| Number of leaves | {2,3,4, \dots , 50} | 27 |
| Bagging fraction | {0.6, 0.7, 0.8, 0.9} | 0.9 |
| Bagging freq | {1, 2, \dots , 10} | 1 |
| α | {0.0, 0.1, 0.5, 1.0} | 0.5 |
| λ | {0.0, 0.1, 0.5, 1.0} | 1 |
| Min samples leaf | {1, 2, \dots , 20} | 12 |
| Min samples split | {1, 2, \dots , 20} | 8 |
| Number of estimators | {10, 30, \dots , 230} | 190 |

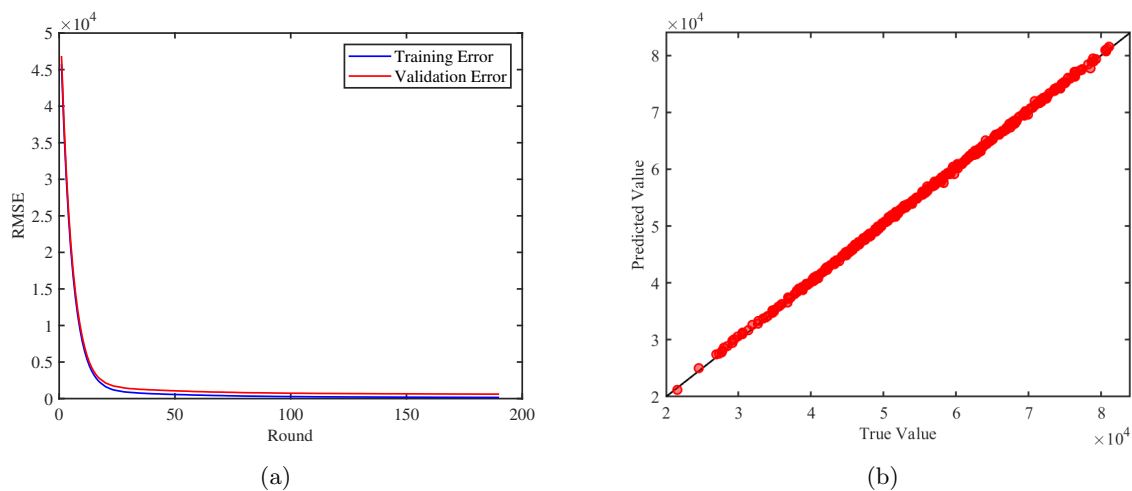


FIGURE 4.6: (a) Training and validation error of the XGBoost model, (b) true values and the predicted values of the test set.

TABLE 4.8: Error scores and R^2 value of the XGBoost Model

| Train MAPE | Test MAPE | Train MAE | Test MAE | Train RMSE | Test RMSE | R^2 - Test set |
|------------|-----------|-----------|----------|------------|-----------|------------------|
| 0.24% | 0.86% | 131.50 | 435.62 | 179.32 | 592.90 | 0.9978 |

The Train MAPE, Test MAPE, Train MAE, Test MAE, Train RMSE, Test RMSE, and R^2 values of the XGBoost model are given in Table 4.8. A comparative analysis of error scores between the XGBoost and the proposed MLP model indicates a slight tendency of the XGBoost model to overfit the training data. This is evident as the training error of the XGBoost model across all error metrics is notably lower than that of the MLP model, while the testing error is

comparatively higher. In light of these observations, it becomes evident that the MLP model stands to be the more suitable choice for accurate predictions regarding the annual-averaged power output of the OWC device. However, it's worth noting that despite the slight overfitting exhibited by the XGBoost model over the MLP model, it still demonstrates an ability to capture the underlying patterns associated with the variation in the annual averaged power output. This is evident from the model's training and testing errors, which are less than 1% and a substantial R^2 value of 0.9978. So, in the next section, the XGBoost model will be employed to identify the regions where the power generation has the potential to reach its peak. Within each of these high-yield regions, an expanded dataset will be generated. Subsequently, this augmented dataset will be applied to the developed ANN model to get the predicted annual average power generation. Subsequently, the optimized input values will be obtained, which maximize the response variable.

4.7 Optimization of the parameters of the OWC Device

4.7.1 Accumulated local effects(ALE)

In the present work, MLP and XGBoost models are developed to predict the annual average power extraction (P_{ann}) achieved by the OWC device. On many occasions, understanding the prediction mechanism of the developed model is very informative to the application of the model. Besides, it could also benefit the engineers who design and deploy the device in the ocean to analyze how each of the parameters specifically affects the performance of the device and how much is the interaction effect between any pairs of parameters of the device. The results illustrated in the above section show that both the MLP model and XGBoost model predict the annual average power generation precisely, with a slight superiority in the case of the MLP model over the XGBoost model. But, as a black box model, explaining the prediction mechanisms, such as how the features would dynamically affect the prediction using the MLP model, is difficult (Masís [148]). However, the importance of tree ensemble models is that their prediction mechanisms can be explained with the support of human-interpretable machine learning techniques such as the accumulated local effect (ALE). In this subsection, the accumulated local effect (ALE) will be explored based on the developed XGBoost model to obtain information regarding how the variation of the input parameters would dynamically affect the annual average power (P_{ann}) generated by the OWC device.

The key of ALE is to simplify a complicated prediction function f to a function with only a few factors. ALE plots have the capacity to average prediction variations and aggregate them across a specified grid. To quantify local effects, the features are partitioned into multiple intervals,

and the uncentered effect of a feature will be obtained by (see Liu et al. [71]).

$$\widehat{f}_{j,ALE}(X_j) = \sum_{a=1}^{a_j(X_j)} \frac{1}{M_j(a)} \sum_{i: x_j^{(i)} \in m_j(a)} \left[f(z_{a,j}, X_{\setminus j}^{(i)}) - f(z_{a-1,j}, X_{\setminus j}^{(i)}) \right], \quad (4.51)$$

where $z_{a,j}$ represents the boundary value of the a^{th} interval for the j^{th} feature. Further, $M_j(a)$ denotes the cardinality of $m_j(a)$ which consists of the sample points in the a^{th} interval. Moreover, X_j and $X_{\setminus j}$ stand for j^{th} feature and features other than the j^{th} feature. The centered ALE estimator is obtained by (see Liu et al. [71])

$$\widehat{f}_{j,ALE}(X_j) = \widehat{f}_{j,ALE}(X_j) - \frac{1}{M} \sum_{i=1}^M \widehat{f}_{j,ALE}(x_j^{(i)}) \quad (4.52)$$

This centered ALE estimator will make the mean effect of the response variable zero. Similarly, the ALE estimator can be used to study the interaction effect of two parameters. To calculate the second-order ALE of the j^{th} and l^{th} feature, the sample range of the ALE plots will be divided into A^2 rectangular cells with a and b denotes the indices into grids corresponding to the j^{th} and l^{th} features, respectively. The uncentered interaction effect of the features by considering two features at a time will be obtained using the following formula (see Liu et al. [71])

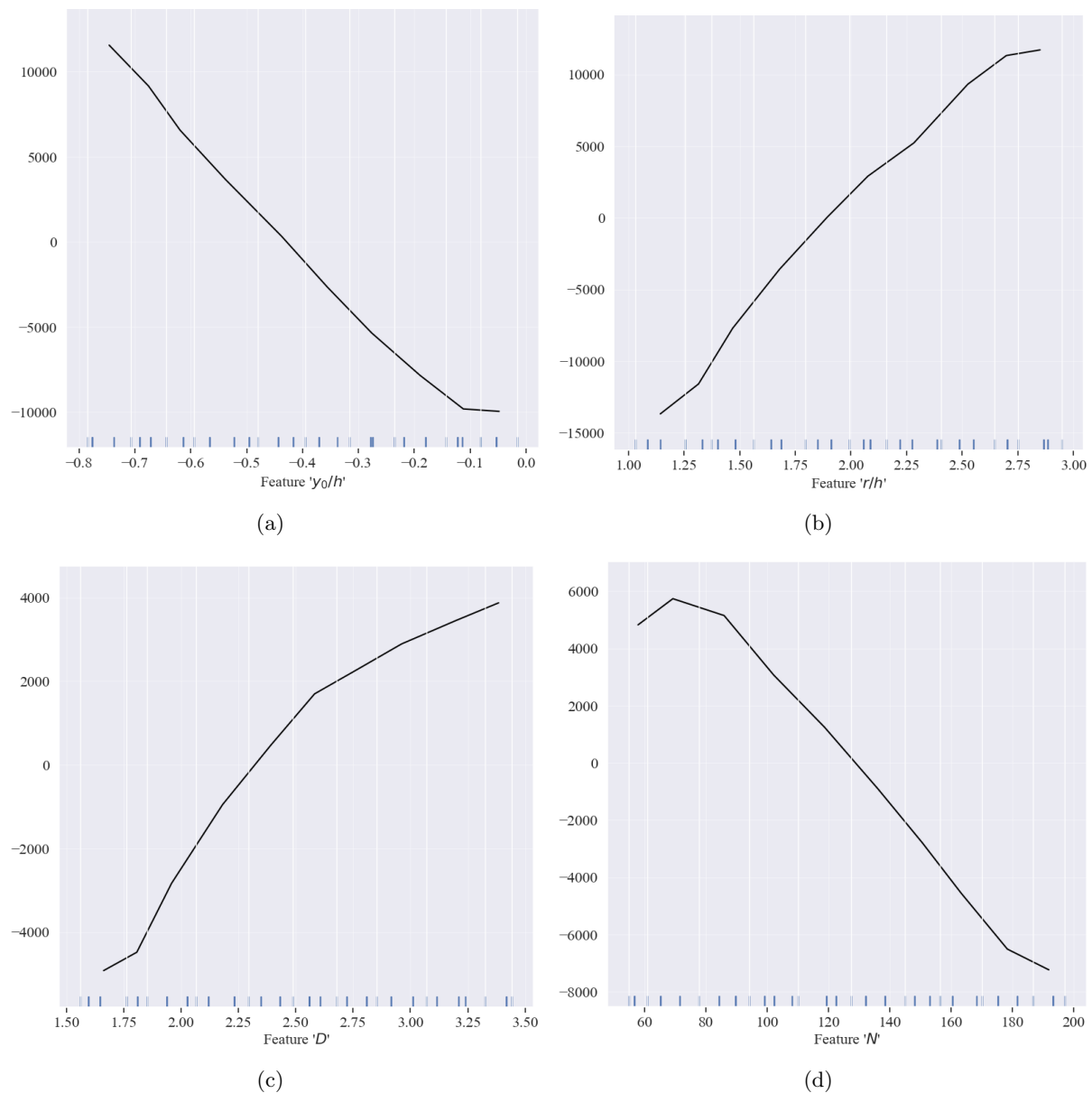
$$\widehat{h}_{\{j,l\},ALE}(X_j, X_l) = \sum_{a=1}^{a_j(X_j)} \sum_{b=1}^{b_l(X_l)} \frac{1}{M_{\{j,l\}}(a,b)} \times \sum_{i: x_{\{j,l\}}^{(i)} \in m_{\{j,l\}}(a,b)} \Delta_f^{\{j,l\}}(A, a, b; x_{\{j,l\}}^{(i)}). \quad (4.53)$$

Here, $\Delta_f^{\{j,l\}}(A, a, b; x_{\{j,l\}}^{(i)})$ represents the second-order finite difference of $f(X_j, X_l, x_{\{j,l\}}^{(i)})$ for (X_j, X_l) across cell $(\chi_{a-1,j}, \chi_{a,j}] \times (\chi_{b-1,l}, \chi_{b,l}]$. Then the second-order ALE is obtained as (see Liu et al. [71])

$$\begin{aligned} \widehat{f}_{\{j,l\},ALE}(X_j, X_l) &= \widehat{h}_{\{j,l\},ALE}(X_j, X_l) \\ &- \sum_{a=1}^{a_j(X_j)} \frac{1}{M_j(a)} \sum_{b=1}^a M_{\{j,l\}}(a,b) \left\{ \widehat{h}_{\{j,l\},ALE}(\chi_{a,j}, \chi_{b,l}) - \widehat{h}_{\{j,l\},ALE}(\chi_{a-1,j}, \chi_{b,l}) \right\} \\ &- \sum_{b=1}^{a_l(X_j)} \frac{1}{M_l(b)} \sum_{a=1}^b M_{\{j,l\}}(a,b) \left\{ \widehat{h}_{\{j,l\},ALE}(\chi_{a,j}, \chi_{b,l}) - \widehat{h}_{\{j,l\},ALE}(\chi_{a,j}, \chi_{b-1,l}) \right\} \end{aligned} \quad (4.54)$$

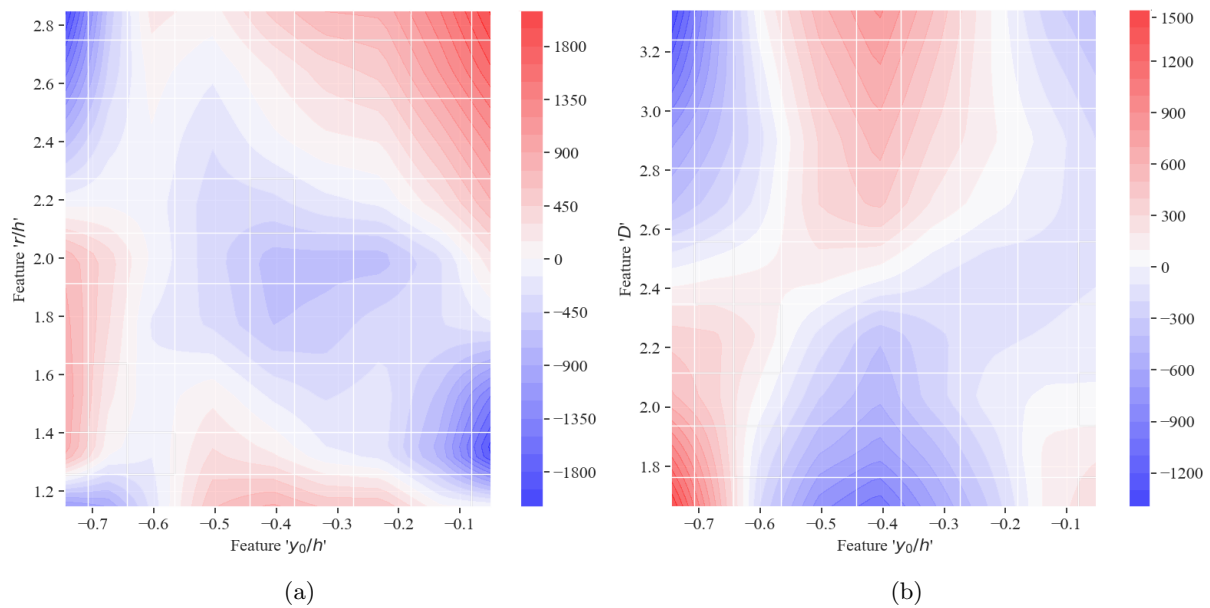
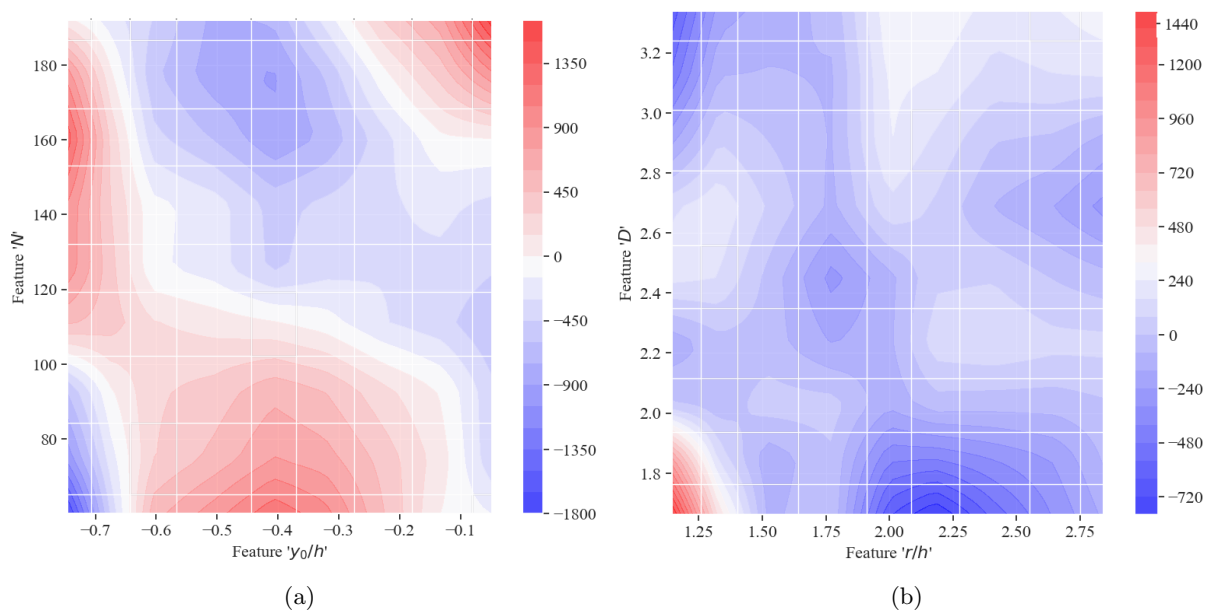
Now, the centered second-order ALE effects is obtained by (see Apley and Zhu [118])

$$\widehat{f}_{\{j,l\},ALE}(X_j, X_l) = \widehat{f}_{\{j,l\},ALE}(X_j, X_l) - \frac{1}{M} \sum_{a=1}^A \sum_{b=1}^A M_{\{j,l\}}(a,b) \widehat{f}_{\{j,l\},ALE}(\chi_{a,j}, \chi_{b,l}). \quad (4.55)$$

FIGURE 4.7: First-order ALE plots of (a) y_0/h , (b) r/h , (c) D , (d) N

4.7.2 Results and discussions

In the present section, we will optimize the structural parameters associated with the OWC device and turbine. This optimization process involves identifying specific regions of the input space where annual average power extraction (P_{ann}) will attain its maximum. These regions will be identified using the XGBoost model and the interpretable machine-learning approaches namely the Accumulated Local Effect (ALE) Plots, discussed in the previous subsection. After finding the regions for which maximum annual average power generation occurs, twenty samples are selected from each parameter from the selected regions and input into the pre-trained MLP model. This allows us to predict the maximum power generation within each identified region.

FIGURE 4.8: Second-order ALE plots of (a) y_0/h and r/h , (b) y_0/h and D .FIGURE 4.9: Second-order ALE plots of (a) y_0/h and N , (b) r/h and D .

Subsequently, we obtain the optimized parameter values for the OWC device, along with the corresponding maximum annual average power extraction (P_{ann}) achieved by the OWC device.

Fig. 4.7 shows the first-order Accumulated Local Effect (ALE) plots, which illustrate how the annual average power extraction (P_{ann}) varies with respect to individual parameters of the OWC device. In the ALE plot, the $y = 0$ line indicates that the corresponding parameter values

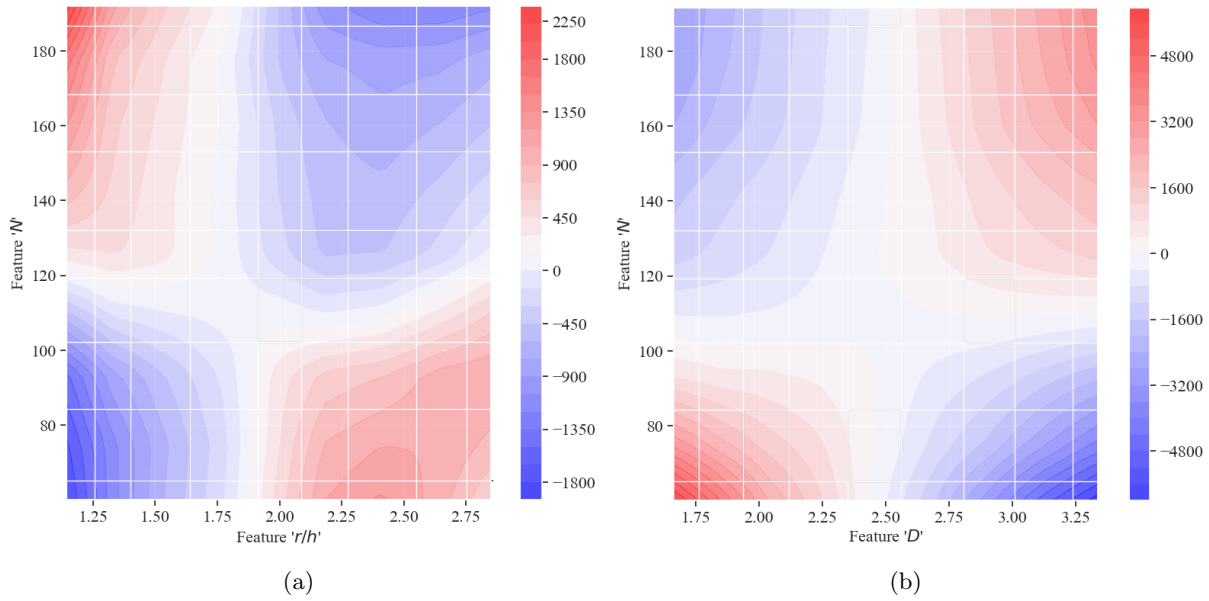


FIGURE 4.10: Second-order ALE plots of (a) r/h and N (b) D and N .

maintain the expected value of the response variable, i.e., the annual average power extraction (P_{ann}). For $y > 0$, the corresponding parameter values increase the response variable from its expected value, and similarly, for $y < 0$, the response variable decreases from its expected value. Figs. 4.7(a)- 4.7(d) show the impact of the parameters y_0/h , r/h , D , and N , respectively on the annual average power extraction (P_{ann}).

Fig. 4.7(a) illustrates the influence of the parameter y_0/h on the annual average power extraction (P_{ann}) by the OWC device. The graph clearly shows that the highest ALE (Accumulated Local Effect) value is achieved when y_0/h is at its maximum. As y_0/h decreases to -0.45 , the ALE score gradually increases and attains the expected value of P_{ann} . Notably, the power output (P_{ann}) never surpasses the baseline score again, and P_{ann} increases as y_0/h decreases gradually. A similar trend can also be seen in Fig. 4.7(d), which illustrates the influence of the parameter N on the annual average power extraction (P_{ann}) by the OWC device. The results demonstrated that higher ALE values are attained for $60 < N < 100$, and P_{ann} reduces as well as reaches its baseline as $N \approx 130$. Hereafter, the ALE value reduces gradually. Figs. 4.7(b) and 4.7(c) illustrate the influence of the parameters r/h and D , respectively on the annual average power extraction (P_{ann}) by the OWC device. An opposite trend is seen in the ALE values for both the parameters r/h and D . The ALE values are minimal as r/h and D are minimal, and then, the ALE value increases as r/h and D increase gradually.

Figs. 4.8 - 4.10 represents the second-order Accumulated Local Effect (ALE) plots, which visually demonstrate the interaction between two individual parameters on the annual average power extracted by the OWC device (P_{ann}). It is to be noted that the second-order ALE will illustrate

only the interaction effect but not the main effect (Liu et al. [71]). In Figs. 4.8(a), 4.8(b) and 4.9(a) depicts the interaction between y_0/h with r/h , D and N , respectively. Fig. 4.8(a) depicts that the ALE score is above the baseline value of the response variable in three of the regions $y_0/h < -0.65$ with $1.2 < r/h < 2.2$, $y_0/h > -0.45$ with $r/h > 2.4$ and $-0.6 < y_0/h < -0.2$ with $r/h < 1.3$. Now, by observing the interaction effect between y_0/h and D as shown in 4.8(b), the ALE score is above the baseline in two of the regions $-0.55 < y_0/h < -0.25$ with $D > 2.6$ and $y_0/h < -0.65$ with $1.5 < D < 2.25$. Fig. 4.9(a) demonstrates the interaction between y_0/h and N . It is seen from Fig. 4.9(a) that the ALE score is above the baseline of the response variable in three regions, $-0.65 < y_0/h < -0.15$ with $N < 100$, $y_0/h < -0.65$ with $N > 100$ and in the region $y_0/h > -0.3$ with $N > 160$. From these three figures, it is also observed that the variation in the interaction effect between y_0/h and r/h is comparatively higher than the interaction effect between y_0/h and D , and y_0/h and N as the range of ALE values is higher.

Figs. 4.9(b) and 4.10(a) depict the interaction between r/h with D and N , respectively, on the annual average power extracted by the OWC device (P_{ann}). From Fig. 4.9(b), it is seen that the ALE score for the interaction effect is above the expected value of the response variable only for the region $r/h < 1.4$ with $D < 2.0$. Whereas, from Fig. 4.10(a), it is seen that the interaction effect of r/h and N is significant in two of the regions, $r/h < 2$ with $N > 120$ and on the region $r/h > 2$ with $N < 100$. Fig.4.10(b) depicts the interaction effect of D and N , and it is seen that the ALE score is maximum if both the parameter values are minimal or if both the parameters are higher.

Now, for the optimization of the parameters of the OWC device, four regions were found by identifying the regions with the highest first-order and second-order ALE scores of the parameters. The four regions are listed below.

$$R_1 = \{-0.65 \leq y_0/h \leq -0.2 \cup 2 \leq r/h \leq 3 \cup 50 \leq N \leq 100 \cup 2.5 \leq D \leq 3.5\} \quad (4.56)$$

$$R_2 = \{-0.65 \leq y_0/h \leq -0.2 \cup 2 \leq r/h \leq 3 \cup 100 \leq N \leq 200 \cup 2.5 \leq D \leq 3.5\} \quad (4.57)$$

$$R_3 = \{-0.8 \leq y_0/h \leq -0.6 \cup 1 \leq r/h \leq 2.2 \cup 100 \leq N \leq 200 \cup 1.5 \leq D \leq 2.5\} \quad (4.58)$$

$$R_4 = \{-0.8 \leq y_0/h \leq -0.6 \cup 1 \leq r/h \leq 2.2 \cup 50 \leq N \leq 100 \cup 1.5 \leq D \leq 2.5\} \quad (4.59)$$

Now, from each region, we select twenty equally spaced points for all the parameters and then pass them through the developed MLP model. Then, the top three combinations of the parameters for which the highest predicted response by the MLP model is chosen from all four regions R_j , $j = 1, 2, 3, 4$. Also the actual values of the response variable associated with these three combinations are also calculated from the numerical model developed in Section 3. All the results are listed in Tab. 4.9. From Tab. 4.9, it can be seen that the maximum annual average power extraction by the OWC device occurs when $y_0/h = -0.65$ and $r/h = 3$. Also, from the first and second regions, it is seen that the optimized range of values of the turbine rotor diameter is $2.8 \leq D \leq 3$. Further, the results reveal that the two particular ranges of values

of the turbine rotational speed N , which maximizes the power extraction, are $70 \leq N \leq 80$ and $105 \leq N \leq 116$. Hence, the optimized turbine rotational speed of the OWC device that maximizes the power generation is $\{70 \leq N \leq 80 \cup 105 \leq N \leq 116\}$. These ranges of optimized parameter values are significantly shorter than the ranges provided in Trivedi and Koley [140].

TABLE 4.9: Optimum design of the OWC device

| | $(y_0/h, r/h, N, D)$ | \hat{p} (Wm^{-1}) | p (Wm^{-1}) |
|-------|------------------------------|--------------------------------|--------------------------|
| R_1 | $(-0.65, 3, 77.34, 3.00)$ | 82580 | 82662 |
| | $(-0.65, 3, 71.05, 2.85)$ | 82549 | 82637 |
| | $(-0.65, 3, 72.54, 2.96)$ | 82522 | 82655 |
| R_2 | $(-0.65, 3, 105.26, 3.00)$ | 82549 | 82634 |
| | $(-0.65, 3, 115.78, 2.96)$ | 82532 | 82658 |
| | $(-0.65, 3, 110.52, 2.80)$ | 82529 | 82650 |
| R_3 | $(-0.75, 2.2, 105.26, 1.71)$ | 79906 | 79198 |
| | $(-0.8, 2.2, 115.78, 1.86)$ | 79595 | 79070 |
| | $(-0.75, 2.2, 110.52, 1.76)$ | 79583 | 79858 |
| R_4 | $(-0.75, 2.2, 55.26, 1.76)$ | 78024 | 77766 |
| | $(-0.75, 2.2, 57.89, 1.86)$ | 77994 | 77739 |
| | $(-0.75, 2.2, 52.63, 1.71)$ | 77925 | 77257 |

4.8 Conclusions

In this study, we have analyzed the performance of a breakwater-integrated quarter-circle-shaped front wall OWC device under the influence of irregular incident waves. By employing the dual BEM, we effectively addressed the associated boundary value problem. We also provided detailed derivations of the physical parameters relevant to the power extraction by the OWC device. To shorten the ranges of parameters for maximum power extraction obtained from the numerical results, we employed a supervised machine learning approach based on the ANN model called the MLP model with the support of the tree ensemble model XGBoost. Both the MLP model and the XGBoost model were trained, validated, and tested using 3750 input data points in a 60 : 20 : 20 ratio. The optimized MLP architecture consists of five hidden layers comprising of 256, 128, 128, 64, and 32 neurons, respectively, with the ‘‘GELU’’ activation function on each of the hidden layers and the best optimization function is obtained to be ‘‘nadam’’. On the other hand, the architecture of the XGBoost model is also optimized using the genetic algorithm. By utilizing the XGBoost model, we have identified four distinct regions of the input space where the maximum annual average power extraction occurs. These high-yield areas have been determined by studying the highest first-order and second-order ALE scores of the input parameters. Further, in each of the regions, twenty equally spaced samples are selected for all the parameters and then passed through the developed MLP model. Then, the top three combinations of the parameters

for which the highest predicted annual average power extraction are chosen for all four regions. Further, the true values of the response variable are also calculated from the dual BEM-based numerical model. The current investigation results in the subsequent findings:

- The annual average power extraction by the OWC device can be accurately predicted using both the MLP and XGBoost models with R^2 values are obtained to be 0.9995 and 0.9978, respectively.
- The numerical results obtained using the dual BEM demonstrate that the annual average power extraction (P_{ann}) by the OWC device achieves maximum for the following ranges of OWC device and turbine parameters: $2.5 < r/h < 3.0$, $-0.7 < y_0/h < -0.5$, $2 \leq D \leq 3.5$ and $70 \leq N \leq 135$.
- From the developed optimization approach employing XGBoost model, interpretable ML approaches and MLP model, it is found that the maximum annual average power extraction by the OWC device occurs when $y_0/h = -0.65$, $r/h = 3$, $2.8 \leq D \leq 3$ and $\{70 \leq N \leq 80 \cup 105 \leq N \leq 116\}$. Clearly, the results obtained from the optimization approach by employing ML significantly shortens the optimal range of input parameters obtained from the numerical technique.

These present methodologies for the parameter optimization associated with the OWC devices can be broadened to other wave energy converter devices such as the piezoelectric wave energy converter devices and oyster wave energy converters, etc. Further improvement of the present study can be achieved by employing additional interpretable machine-learning approaches such as Shapely additive explanations (SHAP), Sobol-based sensitivity analysis, and local interpretable Model-agnostic explanations. These approaches can be used to interpret the models including deep neural network, and support Vector Regression.

Chapter 5

Modeling, Prediction, and Optimization of Hybrid Oscillating Water Column-Piezoelectric WEC Device

* The work, in this chapter, is covered by the following communicated article:

1. Vipin, V., Trivedi, K., Koley, S. Mathematical Modeling, Prediction, and Optimization of Hybrid Oscillating Water Column-Piezoelectric Wave Energy Converter Device using Machine Learning Models.(Communicated in Engineering Applications of Artificial Intelligence)

5.1 General introduction

The current study focuses on the optimization of the geometric parameters of a hybrid WEC device, comprising of a piezoelectric plate and an oscillating water column WEC. Firstly, the BEM-based numerical technique is used to solve the hydrodynamic problem associated with the total power generated by the hybrid WEC device. To generate the database for the ML-based model building, the input samples are generated using the Latin hypercube sampling technique, and the corresponding values of the target variable are calculated from the solution of the BEM. To optimize the device parameters, an appropriate ML model is identified from four tree ensemble models and a deep learning model, namely random forest(RF), extreme gradient boosting(XGBoost), light gradient boosting machine(LightGBM), categorical boosting(CatBoost), and multilayer perceptron(MLP). Spearman's correlation coefficient is employed to assess the correlation strength between the input attributes and the target variable, and subsequently, we leverage an interpretable ML approach, specifically SHAP values, to analyze the importance of features in the database. Further, using the extreme gradient boosting model along with the interpretable ML approaches, we find the specific regions of the input space that yield maximum power generation. Further, the response surface methodology is used to find the exact parameters of the hybrid WEC device, which maximizes the total power generated by the hybrid WEC device. It is found that the maximum power generation is attained for $l_1/h = 0.21$, $d_1/h = -0.08$, $g_p/h = 0.06$, $d_2/h = -0.19$, and $r/h = 0.63$, respectively.

5.2 Mathematical formulation

This section addresses the mathematical formulation associated with a hybrid WEC device, comprising a PWEC plate and a quarter-circle-shaped OWC device, within the framework of potential flow theory. The schematic representation of the physical problem is provided in Fig. 5.1. The analysis is conducted in the two-dimensional cartesian coordinate system (x, z) , with the x -axis extending along the mean free surface and the positive z -axis oriented vertically upward. The thin piezoelectric plate, with a length of l_1 , is immersed in water at $z = -d_1$. The OWC device is situated near the lee side of the piezoelectric plate, with a gap length denoted as g_p . The immersion depth of the draft of the OWC device is symbolized as d_2 , and the thickness of the front wall is denoted as d . Additionally, b denotes the distance from the origin to the PWEC plate along the x -axis, the length of the OWC chamber is labeled as c , and the OWC device's back wall is situated at $x = R$. According to the geometric shape of the devices, the total free surface is divided into four regions, (i) $\Gamma_4 = \{(x, z) : R - c < x < R; z = 0\}$, (ii) $\Gamma_8 = \{(x, z) : b + l_1 < x < R - c - d; z = 0\}$, (iii) $\Gamma_{13} = \{(x, z) : -L < x < b; z = 0\}$, (iv) $\Gamma_{12} = \{(x, z) : b < x < b + l_1; z = 0\}$. Here, Γ_4 represents the internal free surface, Γ_{12} represents the surface above the PWEC plate, and $\Gamma_8 \cup \Gamma_{13}$ represents the open free surface area. Furthermore,

the OWC device is positioned over the uniform seabed at $z = -h$, and the bottom bed is rigid and impenetrable. The submerged boundaries of the OWC device's front wall are represented by $\Gamma_5 \cup \Gamma_6 \cup \Gamma_7$. The existence of PWEC and OWC devices leads to the subdivision of the domain of physical problem into two distinct regions R_j ($j = 1, 2$) with $R_2 = \{b < x < b + l_1, -d_1 < z < 0\}$ and $R_1 = \{-L < x < R, -h < z < 0\} \setminus R_2$. To numerically solve the BVP, the BEM is employed. The computational domain of the physical problem must be closed to apply the BEM method. Thus, an additional fictitious boundary denoted as Γ_1 is considered at $x = -L$. Moreover, another two fictitious boundaries Γ_{11} and Γ_9 are located at $x = b$ and $x = b + l_1$, respectively. In the context of modeling, the fluid is presumed to adhere to potential flow theory (Babarit [149]) and the motion is assumed to be simple harmonic in time with angular frequency denoted as ω . Consequently, the total velocity potentials are of the form $\Phi_j(x, z, t) = \Re\{\phi_j(x, z)e^{-i\omega t}\}$ and satisfy the Laplace equation

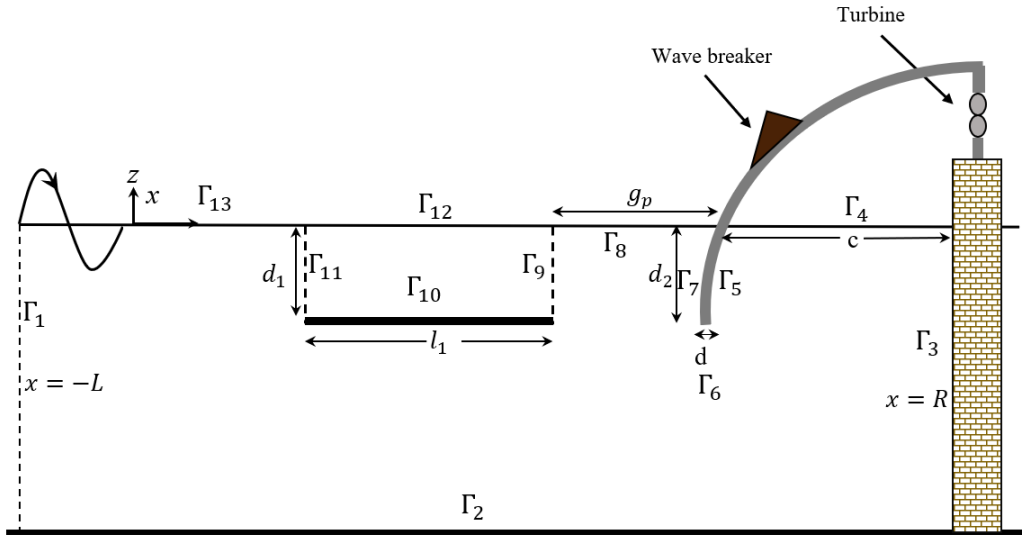


FIGURE 5.1: Schematic diagram of the physical problem.

$$\nabla^2 \phi_j(x, z) = 0, \quad \text{for } j = 1, 2, \quad \nabla^2 \equiv \left(\frac{\partial^2}{\partial x^2} + \frac{\partial^2}{\partial z^2} \right). \quad (5.1)$$

The free surface boundary condition in the linearized form at $z = 0$ is given by

$$\begin{cases} \frac{\partial \phi_1}{\partial n} - K \phi_1 = \begin{cases} \frac{i\omega p}{\rho g}, & \text{on } \Gamma_4, \\ 0, & \text{on } \Gamma_8 \cup \Gamma_{13}, \end{cases} \\ \frac{\partial \phi_2}{\partial n} - K \phi_2 = 0, & \text{on } \Gamma_{12}, \end{cases} \quad (5.2)$$

where $K = \omega^2/g$. The vanishing of the normal velocity on the rigid and impervious bottom $z = -h$ yields

$$\frac{\partial \phi_1}{\partial n} = 0, \quad \text{on } \Gamma_2. \quad (5.3)$$

The back wall as well as the front wall of the OWC device are considered impenetrable, and so the boundary conditions are defined as follows

$$\frac{\partial \phi_1}{\partial n} = 0, \quad \text{on } \Gamma_3 \cup \Gamma_5 \cup \Gamma_6 \cup \Gamma_7. \quad (5.4)$$

Since the boundaries at $x = b$ and $x = b + l_1$ from $z = 0$ to $z = -d$ are auxiliary in nature, we can define the continuity of pressure as well as normal velocities throughout $\Gamma_9 \cup \Gamma_{11}$. So, the boundary conditions are given by

$$\phi_1 = \phi_2, \quad \text{and} \quad \frac{\partial \phi_1}{\partial n} = -\frac{\partial \phi_2}{\partial n} \quad \text{on } \Gamma_9 \cup \Gamma_{11}. \quad (5.5)$$

It is assumed that the PWEC plate undergoes uniform motion along the longitudinal direction. Hence, the displacement of the PWEC device is represented as $\tilde{\xi}(x, t) = \Re\{\xi(x)e^{-i\omega t}\}$, where $\xi(x)$ denotes the complex amplitude of deflection. The dynamic boundary condition on the PWEC plate on Γ_{10} is given by

$$g\chi \left[1 + \frac{\beta^2 \varphi \omega}{i + \varphi \omega} \right] \frac{\partial^4 \xi}{\partial x^4} - \omega^2 \gamma \xi = i\omega(\phi_1(x, -d^-) - \phi_2(x, -d^+)), \quad \text{on } b < x < b + l_1, z = -d. \quad (5.6)$$

Here, the parameters used in Eq. (2.8) are given by

$$\chi = \frac{B}{\rho g}, \quad \beta = \frac{\theta}{\sqrt{BC}}, \quad \varphi = \frac{C}{V}, \quad \gamma = \frac{I_b}{\rho}, \quad (5.7)$$

In this context, the electric surface capacitance, flexural rigidity of the PWEC device, the surface conductance, surface density of the PWEC plate bimorph, and the piezoelectric coupling factor are represented by C , B , G , I_b , and θ . The kinematic boundary condition on the PWEC device on Γ_{10} is given by

$$\frac{\partial \phi_1}{\partial n} = -\frac{\partial \phi_2}{\partial n} = -i\omega \xi, \quad \text{on } z = -d_1, b < x < b + l_1. \quad (5.8)$$

For the fixed boundary edge condition of the PWEC plate, the slope of the deflection as well as the deflection of the PWEC plate will vanish. The same boundary conditions are given below

$$\xi = 0, \quad \frac{\partial \xi}{\partial n} = 0, \quad \text{at } x = b, b + l_1, z = -d_1. \quad (5.9)$$

It is worth noting that the plate deflection ξ and the total velocity potentials ϕ_j ($j = 1, 2$) involve the radiated and scattered potentials. As a result, the plate deflection and the total velocity potentials can be expressed as (Evans and Porter [29])

$$\phi_j = \phi_j^S + \left(\frac{i\omega p}{\rho g} \right) \phi_j^R, \quad (j = 1, 2), \quad \xi = \xi^S + \left(\frac{i\omega p}{\rho g} \right) \xi^R. \quad (5.10)$$

Here, ϕ_j^S and ϕ_j^R are referred to as the velocity potentials associated with the scattering and radiation phenomena, respectively for regions R_j ($j = 1, 2$) (Koley and Trivedi [150] and Evans and Porter [29]). Further, ξ^S and ξ^R are symbolized as the plate deflection corresponds to the scattered and radiated waves, respectively. Now, $\phi_1^{S,R}$ satisfies the Eqs. (5.1)-(5.8), and $\phi_2^{S,R}$ satisfies Eqs. (5.1)-(5.2), (5.5)-(5.8). In contrast, $\xi^{S,R}$ satisfies the Eqs. (5.6)-(5.9). It is to be stated that in regions R_1 and R_2 , all the boundary conditions remain unchanged as expressed above except Eq. (5.2) in the region R_1 . Here, Eq. (5.2) is modified as

$$\frac{\partial \phi_1^S}{\partial n} - K\phi_1^S = 0, \quad \text{on } \Gamma_4 \cup \Gamma_8 \cup \Gamma_{13}, \quad \frac{\partial \phi_1^R}{\partial n} - K\phi_1^R = \begin{cases} 1, & \text{on } \Gamma_4, \\ 0, & \text{on } \Gamma_8 \cup \Gamma_{13}. \end{cases} \quad (5.11)$$

The radiation boundary conditions on Γ_1 are provided as

$$\begin{cases} \frac{\partial(\phi_1^S - \phi^I)}{\partial n} - ik_0(\phi_1^S - \phi^I) = 0, & \text{on } \Gamma_1, \\ \frac{\partial \phi_1^R}{\partial n} - ik_0\phi_1^R = 0, & \text{on } \Gamma_1. \end{cases} \quad (5.12)$$

Here, ϕ^I is the incident wave potential and takes the form $\phi^I = e^{ik_0x} f_0(k_0, z)$ with $f_0(k_0, z) = \left(\frac{-igA}{\omega} \right) \frac{\cosh k_0(z+h)}{\cosh(k_0h)}$. It is to be noted that k_0 satisfies the dispersion relation $\omega^2 = gk_0 \tanh(k_0h)$.

5.3 Solution methodology based on the boundary element method

In this section, the detailed boundary integral equation formulation, the discretization of the integral equations, and the associated numerical solution technique are provided.

Employing ‘‘Green’s second identity’’ to the $\phi_j^{S,R}(x, z)$ ($j = 1, 2$), and the ‘‘free space Green’s function’’ $G(x, z; x_0, z_0)$ over the domain Ω bounded by Γ (Katsikadelis [151]), we obtain

$$\epsilon(x_0, z_0) \phi_j^{S,R}(x_0, z_0) = \int_{\Gamma} \left[\phi_j^{S,R}(x, z) \frac{\partial G}{\partial n}(x, z; x_0, z_0) - G(x, z; x_0, z_0) \frac{\partial \phi_j^{S,R}}{\partial n}(x, z) \right] d\Gamma(x, z), \quad \text{for } j = 1, 2. \quad (5.13)$$

The free-term coefficient is given as

$$\epsilon(x_0, z_0) = \begin{cases} 1, & (x_0, z_0) \in \Omega, \\ \frac{1}{2}, & (x_0, z_0) \in \Gamma(\text{smooth}), \\ 0, & (x_0, z_0) \notin \Omega \cup \Gamma. \end{cases} \quad (5.14)$$

It is to be noted that the free space Green's function $G(x, z; x_0, z_0)$ satisfies the governing equation (Katsikadelis [151] and Behera et al. [152])

$$\left(\frac{\partial^2}{\partial x^2} + \frac{\partial^2}{\partial z^2} \right) G(x, z; x_0, z_0) = \delta(x - \varsigma)\delta(z - \eta), \quad (5.15)$$

and takes the form

$$G(x, z, x_0, z_0) = \frac{1}{2\pi} \ln(r), \quad r = \sqrt{(x - x_0)^2 + (z - z_0)^2}. \quad (5.16)$$

Employing the boundary conditions (5.3)-(5.5), (5.8), (5.11)-(5.12) into Eq. (5.13), the integral equation related to the ϕ_1^S in R_1 can be expressed as

$$\begin{aligned} & -\frac{1}{2}\phi_1^S + \int_{\Gamma_1} \left(\frac{\partial G}{\partial n} - ik_0 G \right) \phi_1^S d\Gamma + \int_{\Gamma_2 \cup \Gamma_3 \cup \Gamma_5 \cup \Gamma_6 \cup \Gamma_7} \frac{\partial G}{\partial n} \phi_1^S d\Gamma + \int_{\Gamma_4} \left(\frac{\partial G}{\partial n} - KG \right) \phi_1^S d\Gamma \\ & + \int_{\Gamma_8 \cup \Gamma_{13}} \left(\frac{\partial G}{\partial n} - KG \right) \phi_1^S d\Gamma + \int_{\Gamma_9 \cup \Gamma_{11}} \left(\phi_1^S \frac{\partial G}{\partial n} - G \frac{\partial \phi_1^S}{\partial n} \right) d\Gamma \\ & + \int_{\Gamma_{10}} \phi_1^S \frac{\partial G}{\partial n} d\Gamma + i\omega \int_{\Gamma_{10}} G \xi^S d\Gamma = \int_{\Gamma_1} \left(\frac{\partial \phi^I}{\partial n} - ik_0 \phi^I \right) G d\Gamma. \end{aligned} \quad (5.17)$$

In a similar manner, implementing the boundary conditions (5.2), (5.5), and (5.8) into Eq. (5.13), the integral equation corresponding to the ϕ_2^S in R_2 takes the form as

$$\begin{aligned} & -\frac{1}{2}\phi_2^S + \int_{\Gamma_{11} \cup \Gamma_9} \left(\phi_1^S \frac{\partial G}{\partial n} + G \frac{\partial \phi_1^S}{\partial n} \right) d\Gamma + \int_{\Gamma_{10}} \phi_2^S \frac{\partial G}{\partial n} d\Gamma - i\omega \int_{\Gamma_{10}} G \xi^S d\Gamma \\ & + \int_{\Gamma_{12}} \left(\frac{\partial G}{\partial n} - KG \right) \phi_2^S d\Gamma = 0. \end{aligned} \quad (5.18)$$

In addition, utilizing the boundary conditions (5.3)-(5.5), (5.8), (5.11)-(5.12) into Eq. (5.13), the subsequent integral equation is obtained for the ϕ_1^R in R_1 as

$$\begin{aligned} & -\frac{1}{2}\phi_1^R + \int_{\Gamma_1} \left(\frac{\partial G}{\partial n} - ik_0 G \right) \phi_1^R d\Gamma + \int_{\Gamma_2 \cup \Gamma_3 \cup \Gamma_5 \cup \Gamma_6 \cup \Gamma_7} \frac{\partial G}{\partial n} \phi_1^R d\Gamma + \int_{\Gamma_4} \left(\frac{\partial G}{\partial n} - KG \right) \phi_1^R d\Gamma \\ & + \int_{\Gamma_8 \cup \Gamma_{13}} \left(\frac{\partial G}{\partial n} - KG \right) \phi_1^R d\Gamma + \int_{\Gamma_9 \cup \Gamma_{11}} \left(\phi_1^R \frac{\partial G}{\partial n} - G \frac{\partial \phi_1^R}{\partial n} \right) d\Gamma \\ & + \int_{\Gamma_{10}} \phi_1^R \frac{\partial G}{\partial n} d\Gamma + i\omega \int_{\Gamma_{10}} G \xi^S d\Gamma = \int_{\Gamma_4} G d\Gamma. \end{aligned} \quad (5.19)$$

Similarly, implementing the boundary conditions (5.2), (5.5), and (5.8) into Eq. (5.13), the integral equation related to the ϕ_2^R in R_2 is provided as

$$\begin{aligned} & -\frac{1}{2}\phi_2^R + \int_{\Gamma_{11}\cup\Gamma_9} \left(\phi_1^R \frac{\partial G}{\partial n} + G \frac{\partial \phi_1^R}{\partial n} \right) d\Gamma + \int_{\Gamma_{10}} \phi_2^R \frac{\partial G}{\partial n} d\Gamma - i\omega \int_{\Gamma_{10}} G \xi^R d\Gamma \\ & + \int_{\Gamma_{12}} \left(\frac{\partial G}{\partial n} - KG \right) \phi_2^R d\Gamma = 0. \end{aligned} \quad (5.20)$$

The BEM-based numerical approach is used to solve Eqs. (5.17)-(5.20). For the same, the boundaries of R_j for $j = 1, 2$ are discretized and assumed that the values of $\phi_j^{S,R}$ and $\partial\phi_j^{S,R}/\partial n$ are constants over each boundary element of the discretization (see Katsikadelis [151]). In this context, the system of integral Eqs. (5.17)-(5.20) can be represented as

$$\begin{aligned} & \sum_{j=1}^{N_1} (H_{ij} - ik_0 G_{ij}) \phi_{1j}^S |_{\Gamma_1} + \sum_{j=1}^{N_2+N_3+N_5+N_6+N_7} H_{ij} \phi_{1j}^S |_{\Gamma_2\cup\Gamma_3\cup\Gamma_5\cup\Gamma_6\cup\Gamma_7} \\ & + \sum_{j=1}^{N_4+N_8+N_{13}} (H_{ij} - KG_{ij}) \phi_{1j}^S |_{\Gamma_4\cup\Gamma_8\cup\Gamma_{13}} + \sum_{j=1}^{N_9+N_{11}} \left(\phi_{1j}^S H_{ij} - G_{ij} \frac{\partial \phi_{1j}^S}{\partial n} \right) \Big|_{\Gamma_9\cup\Gamma_{11}} \\ & + \sum_{j=1}^{N_{10}} \phi_{1j}^S H_{ij} |_{\Gamma_{10}} + i\omega \sum_{j=1}^{N_{10}} G_{ij} \xi_j^S |_{\Gamma_{10}} + \sum_{j=1}^{N_{11}} \left(\phi_{1j}^S H_{ij} - G_{ij} \frac{\partial \phi_{1j}^S}{\partial n} \right) \Big|_{\Gamma_{11}} \\ & + \sum_{j=1}^{N_{13}} (H_{ij} - KG_{ij}) \phi_{1j}^S |_{\Gamma_{13}} = \sum_{j=1}^{N_1} \left(\frac{\partial \phi_j^I}{\partial n} - ik_0 \phi_j^I \right) G_{ij} \Big|_{\Gamma_1}, \end{aligned} \quad (5.21)$$

$$\begin{aligned} & \sum_{j=1}^{N_{11}+N_9} \left(H_{ij} \phi_{1j}^S + G_{ij} \frac{\partial \phi_{1j}^S}{\partial n} \right) \Big|_{\Gamma_{11}\cup\Gamma_9} + \sum_{j=1}^{N_{10}} \phi_{2j}^S H_{ij} |_{\Gamma_{10}} - i\omega \sum_{j=1}^{N_{10}} G_{ij} \xi_j^S |_{\Gamma_{10}} \\ & + \sum_{j=1}^{N_9} \left(H_{ij} \phi_{1j}^S + G_{ij} \frac{\partial \phi_{1j}^S}{\partial n} \right) \Big|_{\Gamma_9} + \sum_{j=1}^{N_{12}} (H_{ij} - KG_{ij}) \phi_{2j}^S |_{\Gamma_{12}} = 0, \end{aligned} \quad (5.22)$$

$$\begin{aligned} & \sum_{j=1}^{N_1} (H_{ij} - ik_0 G_{ij}) \phi_{1j}^R |_{\Gamma_1} + \sum_{j=1}^{N_2+N_3+N_5+N_6+N_7} H_{ij} \phi_{1j}^R |_{\Gamma_2\cup\Gamma_3\cup\Gamma_5\cup\Gamma_6\cup\Gamma_7} \\ & + \sum_{j=1}^{N_4+N_8+N_{13}} (H_{ij} - KG_{ij}) \phi_{1j}^R |_{\Gamma_4\cup\Gamma_8\cup\Gamma_{13}} + \sum_{j=1}^{N_9+N_{11}} \left(\phi_{1j}^R H_{ij} - G_{ij} \frac{\partial \phi_{1j}^R}{\partial n} \right) \Big|_{\Gamma_9\cup\Gamma_{11}} \\ & + \sum_{j=1}^{N_{10}} \phi_{1j}^R H_{ij} |_{\Gamma_{10}} + i\omega \sum_{j=1}^{N_{10}} G_{ij} \xi_j^R |_{\Gamma_{10}} = \sum_{j=1}^{N_4} G_{ij} |_{\Gamma_4}, \end{aligned} \quad (5.23)$$

$$\begin{aligned} & \sum_{j=1}^{N_{11}+N_9} \left(H_{ij} \phi_{1j}^R + G_{ij} \frac{\partial \phi_{1j}^R}{\partial n} \right) \Big|_{\Gamma_{11}\cup\Gamma_9} + \sum_{j=1}^{N_{10}} \phi_{2j}^R H_{ij} |_{\Gamma_{10}} - i\omega \sum_{j=1}^{N_{10}} G_{ij} \xi_j^R |_{\Gamma_{10}} \\ & + \sum_{j=1}^{N_{12}} (H_{ij} - KG_{ij}) \phi_{2j}^R |_{\Gamma_{12}} = 0, \end{aligned} \quad (5.24)$$

where

$$H_{ij} = -\frac{1}{2}\delta_{ij} + \int_{\Gamma_j} \frac{\partial G}{\partial n} d\Gamma, \quad G_{ij} = \int_{\Gamma_j} G d\Gamma, \quad (5.25)$$

are denoted as influence coefficients. The calculations to obtain the influence coefficients are explained in Vipin and Koley [135]. It is to be noted that Eqs. (5.21)-(5.24) contain the unknowns $\xi_j^{S,R}$. To handle this, the central difference formula is utilized to discretize the plate dynamic boundary condition (5.6) as mentioned below

$$\left(\frac{\xi_{j+2}^{S,R} - 4\xi_{j+1}^{S,R} + 6\xi_j^{S,R} - 4\xi_{j-1}^{S,R} + \xi_{j-2}^{S,R}}{\Delta_j^4} \right) + P\xi_j^{S,R} = Q \left(\phi_{1j}^{S,R} - \phi_{2j}^{S,R} \right). \quad (5.26)$$

Here, $P = \frac{-\omega^2\gamma}{g\chi \left(1 + \frac{\beta^2\varphi\omega}{i + \varphi\omega} \right)}$, and $Q = \frac{i\omega}{g\chi \left(1 + \frac{\beta^2\varphi\omega}{i + \varphi\omega} \right)}$. Similarly, the plate edge conditions given in Eq. (5.9) are represented as

$$\xi_j^{S,R} = 0, \quad \xi_{j-1}^{S,R} = \xi_{j+1}^{S,R}. \quad (5.27)$$

Now, Eqs. (5.21)-(5.24), and (5.26)-(5.27) are handled simultaneously to determine the unknown velocity potentials, their normal derivatives, and plate deflections over the boundary elements of the respective boundaries (Koley [153]).

5.4 Parameters corresponding to the wave energy converters

5.4.1 Wave power extraction by the OWC device

The mean power generated, denoted as P_{OWC} , by the OWC device per unit length of the pressure distribution is calculated as follows

$$P_{OWC} = \frac{1}{2} \Re \{ \bar{p}q \}. \quad (5.28)$$

Here, pressure across the turbine and the volume flux are denoted as p and q , respectively. Considering a linear relationship between the volume flux and the pressure across the turbine, we derive the subsequent relation as

$$q = \wedge p, \quad (5.29)$$

where \wedge is a parameter related to the turbine characteristics. Consequently, the P_{OWC} per unit length of the pressure distribution is expressed as follows

$$P_{OWC} = \frac{1}{2} \frac{\wedge |q^S|^2}{\left(\wedge + \tilde{B} \right)^2 + \tilde{A}^2}. \quad (5.30)$$

Here, q^S is symbolized as the volume flux related to the scattered potential. The descriptive derivations are given in Koley and Trivedi [150] and Trivedi and Koley [140].

5.4.2 Wave power extraction by the PWEC device

Wave power extraction by the PWEC device is provided as (Zheng et al. [41] for details)

$$P_{Plate} = \frac{\omega^2 \rho g}{2} \frac{\beta^2 \chi \varphi}{1 + \omega^2 \varphi^2} \int_b^{b+l_1} \left| \frac{\partial^2 \xi}{\partial x^2} \right|^2 dx. \quad (5.31)$$

Further, ξ can be written in terms of the ξ^S and ξ^R . Now, utilizing Eq. (5.10) in Eq. (5.31), we obtain

$$P_{Plate} = \frac{\omega^2 \rho g}{2} \frac{\beta^2 \chi \varphi}{1 + \omega^2 \varphi^2} \int_b^{b+l_1} \left| \frac{\partial^2}{\partial x^2} \left(\xi^S + \left(\frac{i\omega p}{\rho g} \right) \xi^R \right) \right|^2 dx, \quad (5.32)$$

where $\frac{\partial^2 \xi^S}{\partial x^2}$ and $\frac{\partial^2 \xi^R}{\partial x^2}$ are calculated using the ‘‘central difference formulae’’.

5.4.3 Wave power extraction by the hybrid WEC device

The total wave power extracted P_{Total} by the hybrid WEC device is the addition of power extracted by the OWC device P_{OWC} and the power generated by the PWEC plate P_{Plate} and so can be calculated as

$$P_{Total} = P_{OWC} + P_{Plate}. \quad (5.33)$$

The run time for the aforementioned BEM-based computations is higher due to the presence of a number of boundaries in the domain where appropriate discretization needs to be done. Also, computations of influence coefficients are time-consuming in nature. Consequently, for multi-parameter optimization, the aforementioned computations are not suitable due to the requirement of very long computational time. Further, as the P_{Total} by the hybrid OWC-PWEC device exhibits a highly non-linear pattern w.r.t. the input parameters, conventional optimization techniques alone cannot predict the response variables accurately for the optimization of the parameters. To get rid of this problem, often ML tools are used, which provide a substantial reduction in the computational time and also maintain the accuracy of the computation (Li et al. [154]). In view of these computational advantages, one of the most suitable ML models is chosen for the further study associated with the optimization of the WEC device’s parameters from a set of five different ML models, namely, the MLP, XGBoost, RF, LightGBM, and CatBoost models. The details for the same are provided in the following sections.

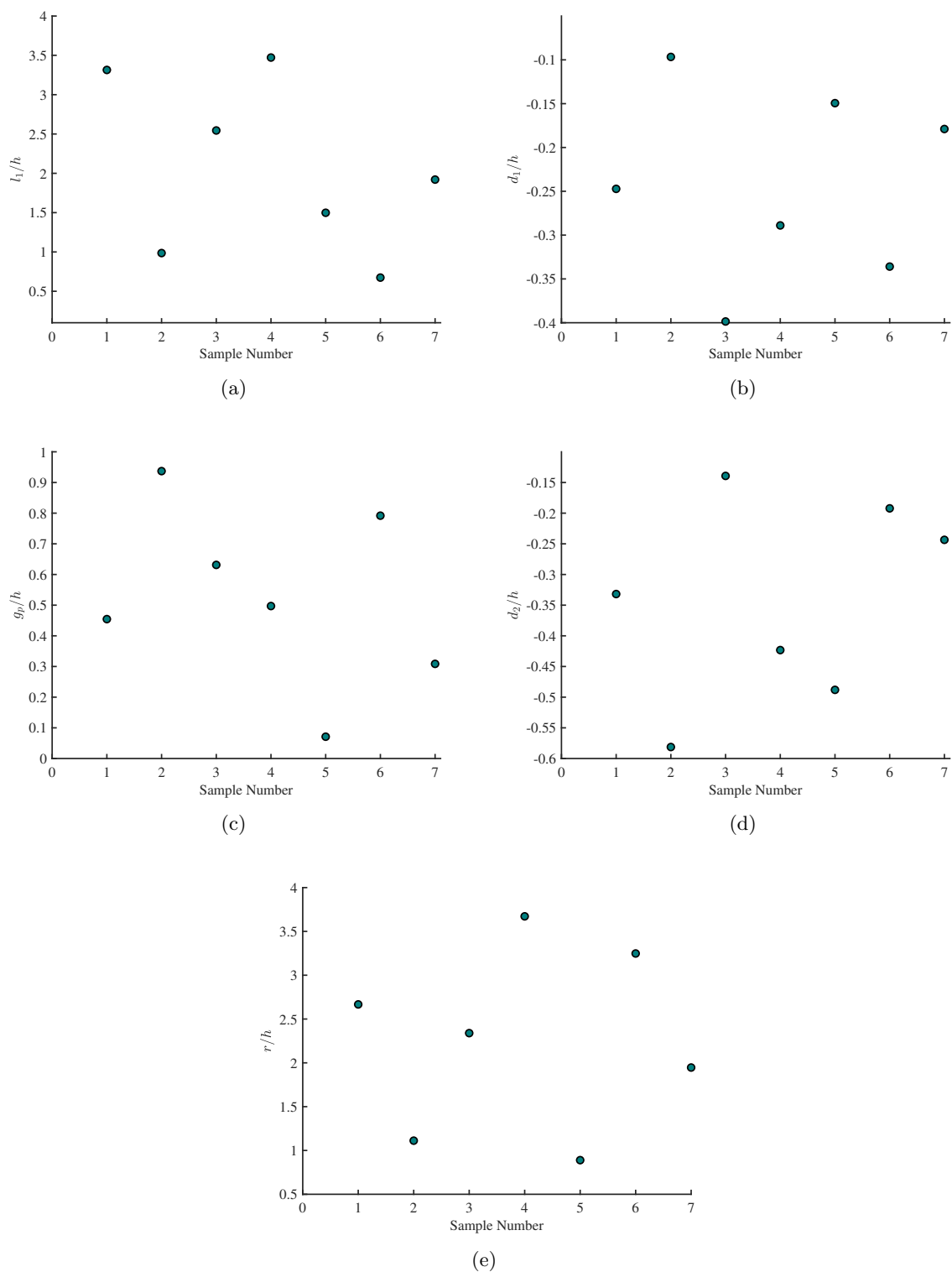


FIGURE 5.2: Latin Hypercube samples of (a) PWEC plate length (l_1/h), (b) submergence depth of the PWEC device (d_1/h), (c) gap between the OWC-PWEC devices (g_p/h), (d) OWC front wall draft (d_2/h), and (e) radius of the OWC device (r/h).

5.5 Development of the database for machine learning models

In this section, the dataset for the ML model building is developed using the LHS technique and the BEM-based numerical solution derived in Sections 5.3 and 5.4. The model takes into account five input features: PWEC plate length (l_1/h), submergence depth of the PWEC device (d_1/h), OWC front wall draft (d_2/h), the radius of the OWC device (r/h), and the gap between the OWC and PWEC devices (g_p/h). The target attribute of the model is the P_{Total} by the hybrid OWC-PWEC device. It is to be noted that for the OWC device, the center of the quarter circle lies within the breakwater. The radius of the circle is taken as r/h and the center of the circle is taken as $(0, d_2/h)$. It is clear from the Fig. 5.1 that the chamber length c/h increases when r/h takes higher values and vice versa. Further, the constant parameter values used for the numerical computation are $h = 8\text{m}$, $\rho = 1025\text{ kg/m}^3$, $g = 9.81\text{ m/s}^2$, $\chi/h^4 = 4.78 \times 10^{-7}$, $\beta = 0.24$, $\varphi = \sqrt{h/g}$, $\gamma/h = 1.258 \times 10^{-3}$.

It is crucial to train and validate the model using a sample that thoroughly represents the domain of the problem being studied to achieve accurate predictions of the response variable on test datasets through ML models. The choice of sampling technique employed in data collection for the study holds significant importance in this regard. In this work, we utilize the LHS technique to construct a highly representative input dataset. For training purposes, seven samples are chosen at random for each input feature within defined intervals: $0.1 \leq l_1/h \leq 4$, $-0.4 \leq d_1/h \leq -0.05$, $0.05 \leq g_p/h \leq 1$, $-0.6 \leq d_2/h \leq -0.1$, and $0.5 \leq r/h \leq 4$, as illustrated in Fig. 5.2. Consequently, the database consists of 16807 input samples and their corresponding power generated by the hybrid OWC-PWEC device. The explanation for the chosen intervals of the input features is detailed in Trivedi and Koley [75]. The descriptive statistics of the database for model building is provided in Tab. 5.1.

TABLE 5.1: Descriptive statistics of database for model building

| | l_1/h | d_1/h | g_p/h | d_2/h | r/h | $P_{Total}(\text{Wm}^{-1})$ |
|-------|---------|---------|---------|---------|-------|-----------------------------|
| count | 16807 | 16807 | 16807 | 16807 | 16807 | 16807 |
| mean | 2.24 | -0.21 | 0.55 | -0.39 | 2.30 | 1794.75 |
| std | 0.98 | 0.10 | 0.27 | 0.12 | 1.09 | 974.43 |
| min | 0.63 | -0.36 | 0.16 | -0.56 | 0.63 | 151.57 |
| 25% | 1.40 | -0.31 | 0.29 | -0.52 | 1.17 | 1131.71 |
| 50% | 2.38 | -0.21 | 0.53 | -0.40 | 2.44 | 1507.01 |
| 75% | 3.17 | -0.10 | 0.85 | -0.29 | 3.30 | 2112.53 |
| 90% | 3.73 | -0.07 | 0.97 | -0.20 | 3.94 | 3232.30 |
| 95% | 3.73 | -0.07 | 0.97 | -0.20 | 3.94 | 3952.20 |
| 99% | 3.73 | -0.07 | 0.97 | -0.20 | 3.94 | 5063.75 |
| max | 3.73 | -0.07 | 0.97 | -0.20 | 3.94 | 6440.21 |

5.6 Model Selection

In this study, we utilize tree ensemble models such as random forest (RF) (Breiman [83]), extreme gradient boosting (Chen and Guestrin [84]), light gradient boosting machine (LightGBM) (Ke et al. [85]), categorical boosting (CatBoost) (Prokhorenkova et al. [86]), and a deep learning model namely the multilayer perceptron (Rumelhart et al. [79], Nguyen and Widrow [80], Werbos [81], Goodfellow et al. [82]) to predict the P_{Total} by the Hybrid OWC-PWEC device. We then determine the model that accurately predicts the target variable from the input variables of the hybrid OWC-PWEC device. The motivation behind the power generation prediction is to eventually optimize the device input parameters to maximize the total power generation P_{Total} .

5.6.1 Extreme gradient boosting (XGBoost)

As mentioned by Borisov et al. [68], the tree ensemble models outperform deep learning models in many supervised learning tasks. Therefore, an ensemble model based on trees, specifically XGBoost, is developed to analyze the highly non-linear data of P_{Total} by the hybrid OWC-PWEC device. The first gradient-boosting (GB) algorithm based on the decision tree was proposed by Breiman [83]. The XGBoost model is an advanced implementation of the GB algorithm proposed by Chen and Guestrin [84] with several improvements such as parallel and distributed computing, tree pruning, handling missing values, feature importance, handling categorical features, efficient handling of large datasets, etc. The working mechanism behind the better accuracy of the XGBoost model is that a new weak learner/ decision tree will be added to reduce the residual of the previous iteration. Adopting such a greedy strategy enables the consistent making of optimal decisions throughout each stage of the learning process (Chen and Guestrin [84]). Yet, the complexity inherent in the XGBoost model increases its susceptibility to overfitting. To counteract this, the loss function integrates L_1 and L_2 regularization terms (El Bilali et al. [72]) to mitigate overfitting concerns.

It is to be noted that the detailed procedure associated with the XGBoost model is available in Vipin et al. [155]. However, the same is provided here for better readability. Let $\left\{ \left(X^{(1)}, p^{(1)} \right), \left(X^{(2)}, p^{(2)} \right), \dots, \left(X^{(M)}, p^{(M)} \right) \right\}$ be the training database with M samples and each $X^{(i)}$ contain n number of features. The XGBoost model develops a predictive function $F(X)$ that estimates \hat{P} for any new input X . Let K be the number of weak learners added sequentially into the model, i.e., K represents the number of iterations in the XGBoost model. The final prediction $F(X)$ is obtained by combining the predictions generated by all weak learners in the ensemble of trees through summation and is given by (El Bilali et al. [72])

$$\hat{p}^{(i)} = F \left(X^{(i)} \right) = \sum_{k=1}^K f_k \left(X^{(i)} \right), f_k \in \mathcal{F}. \quad (5.34)$$

Here, the space of regression trees, denoted as $\mathcal{F} = \{f(X) = w_{q(x)}\}$, where $(q : \mathbb{R}^n \rightarrow T, w \in \mathbb{R}^T)$, represents the structure of each tree mapping a sample to the corresponding leaf node. Here, T stands for the number of leaves in the tree, and f represents an independent tree structure q along with leaf weights w (Chen and Guestrin [84]). Suppose, $\hat{p}_k^{(i)}$ represents the prediction for the i^{th} instance during the k^{th} iteration. Let L be a differentiable convex loss function that measures the dissimilarity between the actual response $p^{(i)}$ and the predicted response $\hat{p}^{(i)}$. The cost function is defined as $\sum_{i=1}^M L(\hat{p}^{(i)}, p^{(i)})$. After incorporating L_1 and L_2 regularization into the loss function, the objective function takes the form (Chen and Guestrin [84])

$$\mathcal{L}(F) = \sum_{i=1}^M L(\hat{p}^{(i)}, p^{(i)}) + \sum_{k=1}^K R(f_k), \quad \text{where } R(f) = \alpha T + \frac{1}{2} \lambda \|w\|^2. \quad (5.35)$$

In this context, $R(f)$ represents the L_1 and L_2 regularization terms designed to reduce the overfitting by penalizing the complexity of the XGBoost model. Additionally, α and λ denote the weights associated with the L_1 and L_2 regularizations. The k^{th} iteration of the objective function, after adding the k^{th} week learner f_k to the loss function and employing Taylor's formula, we will get

$$\mathcal{L}_k = \sum_{i=1}^M \left[g^{(i)} f_k(x^{(i)}) + \frac{1}{2} h^{(i)} f_k^2(x^{(i)}) \right] + R(f_k), \quad (5.36)$$

$$\text{where } g^{(i)} = \frac{\partial L(p^{(i)}, \hat{p}_{k-1})}{\partial \hat{p}_{k-1}}, \quad (5.37)$$

$$h^{(i)} = \frac{\partial^2 L(p^{(i)}, \hat{p}_{k-1})}{\partial \hat{p}_{k-1}^2}. \quad (5.38)$$

Now, optimized weight of the j^{th} leaf node is calculated as (see Chen and Guestrin [84])

$$w_j = - \frac{\sum_{i \in I_j} g^{(i)}}{\sum_{i \in I_j} h^{(i)} + \lambda}, \quad (5.39)$$

where $I_j = \{i : q(X^{(i)}) = j\}$ signifies the instance set of j^{th} leaf. The formula for calculating the optimal score of the tree structure q and the evaluation of the split candidate are given in Vipin et al. [155].

During the development of a ML model, optimizing the tuning parameters of the model is crucial for maximizing accuracy and enhancing overall performance before commencing the model training. To achieve this, the GA is employed using the TPOTRegressor library. Tab. 5.2 presents the tuning parameters, their respective ranges for optimization, and the resulting optimized values. Fig. 5.3(a) visually depicts the training and validation errors observed in the

XGBoost model with respect to the number of iterations. The convergence of the training and validation sets indicates the model's ability to capture the variance in the target variable within an independent set (James et al. [120]). Also, this agreement shows the correct level of flexibility of the model (James et al. [120]). Additionally, Fig. 5.3(b) demonstrates the distribution of observed versus predicted values generated by the XGBoost model for the test set. Notably, the observed and predicted values align closely along the straight line as seen in Fig. 5.3(b), highlighting the accuracy of the predictive model. Additionally, the error matrices utilized in this work is provided in Tab. 4.4. The model's performance is calculated using the R^2 score given by (Rahman et al. [142]).

$$R^2 = 1 - \frac{\sum_{m=1}^M \left(\hat{p}^{(m)} - p^{(m)} \right)^2}{\sum_{m=1}^M \left(\hat{p}^{(m)} - \overline{p^{(m)}} \right)^2}. \quad (5.40)$$

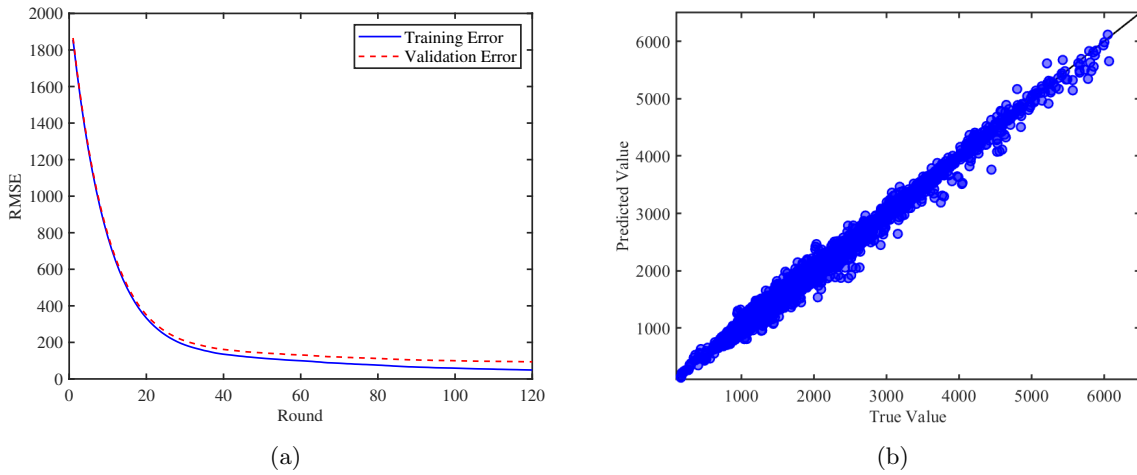


FIGURE 5.3: (a) XGBoost model: RMSE of training and validation errors w.r.t. iterations, (b) predicted vs true values for the test set.

TABLE 5.2: XGBoost tuning parameters and optimized values.

| Hyperparameters | Range of values | Optimized value |
|----------------------|---------------------------|-----------------|
| Max depth | {3, 4, ..., 15} | 8 |
| Learning rate | {0.001, 0.0061, ..., 0.2} | 0.2 |
| α | {0.0, 0.1, ..., 1.0} | 0.2 |
| λ | {0.0, 0.1, ..., 1.0} | 0.2 |
| Min child weight | {1, 2, ..., 10} | 2 |
| Number of estimators | {10, 30, ..., 150} | 120 |
| Subsample | {0.0, 0.1, ..., 1.0} | 1.0 |

5.6.2 Cross validation and model comparison

The 10-fold cross-validation score of the XGBoost model for the error matrices and the R-squared (R^2) score of the test set are provided in Tab. 5.3. The error scores in Tabs. 5.3- 5.4 shows that the XGBoost model outperforms all other four models. Further, the R^2 value of the XGBoost model is 0.9959 and all other models giving lower R^2 values. Hence, it can be concluded that the XGBoost model is the most accurate ML model to study the P_{Total} by the hybrid OWC-PWEC device. After choosing the appropriate ML model to predict the power generated by the hybrid OWC-PWEC device, our task is now to optimize the parameters of the WEC devices, i.e., we need to find specific regions of the input parameters space that optimize P_{Total} by the hybrid OWC-PWEC device. The advantage of the interpretable ML approaches can be utilized effectively in this scenario. Hence, two of the interpretable machine-learning approaches are used and discussed in the next subsection.

TABLE 5.3: 10-fold cross-validation of the XGBoost model

| Fold | Train MAPE | Test MAPE | Train MAE | Test MAE | Train RMSE | Test RMSE | R^2 |
|---------|------------|-----------|-----------|----------|------------|-----------|--------|
| 1 | 0.0175 | 0.027 | 25.77 | 42.02 | 36.91 | 60.79 | 0.9959 |
| 2 | 0.0172 | 0.029 | 25.53 | 43.27 | 36.59 | 60.37 | 0.9960 |
| 3 | 0.0167 | 0.026 | 24.60 | 42.05 | 35.18 | 61.66 | 0.9957 |
| 4 | 0.0177 | 0.028 | 26.12 | 44.64 | 37.62 | 65.08 | 0.9955 |
| 5 | 0.0172 | 0.027 | 25.70 | 42.98 | 36.67 | 62.04 | 0.9958 |
| 6 | 0.0170 | 0.026 | 25.38 | 41.75 | 36.21 | 57.74 | 0.9968 |
| 7 | 0.0172 | 0.028 | 25.45 | 44.19 | 36.14 | 63.42 | 0.9959 |
| 8 | 0.0175 | 0.028 | 26.00 | 45.63 | 37.43 | 67.99 | 0.9951 |
| 9 | 0.0176 | 0.027 | 25.99 | 42.65 | 36.69 | 59.74 | 0.9961 |
| 10 | 0.0175 | 0.026 | 26.03 | 41.34 | 36.98 | 59.75 | 0.9961 |
| Average | 0.017 | 0.027 | 25.66 | 43.05 | 36.64 | 61.86 | 0.9959 |

TABLE 5.4: Comparison of the average of the 10-fold cross-validation error scores and R^2 value

| Model | Train MAPE | Test MAPE | Train MAE | Test MAE | Train RMSE | Test RMSE | R^2 |
|----------|------------|-----------|-----------|----------|------------|-----------|--------|
| MLP | 0.129 | 0.134 | 369.08 | 370.17 | 136.17 | 147.56 | 0.9759 |
| RF | 0.050 | 0.060 | 80.64 | 96.17 | 118.72 | 140.92 | 0.9789 |
| LightGBM | 0.059 | 0.068 | 93.14 | 95.14 | 127.73 | 137.36 | 0.9827 |
| CatBoost | 0.031 | 0.035 | 45.45 | 58.48 | 60.64 | 79.17 | 0.9933 |

5.7 Interpretable machine learning approaches

5.7.1 Accumulated local effects (ALE)

In this subsection, a brief overview of the accumulated local effect (ALE) using the ML model is provided to understand how changes in input parameters influence the P_{Total} by the hybrid OWC-PWEC device. The objective of ALE is to simplify a complicated prediction function f and provides the variations in the prediction by averaging and accumulating it across defined

intervals of the input space. To assess the local impacts, attributes are divided into a defined number of intervals, and the uncentered impact of a particular attribute is computed according to the following methodology (Liu et al. [71])

$$\widehat{f}_{j,ALE}(X_j) = \sum_{a=1}^{a_j(X_j)} \frac{1}{M_j(a)} \sum_{i: x_j^{(i)} \in m_j(a)} \left[f(z_{a,j}, X_{\setminus j}^{(i)}) - f(z_{a-1,j}, X_{\setminus j}^{(i)}) \right]. \quad (5.41)$$

In this context, $z_{a,j}$ signifies the boundary value corresponding to the a^{th} interval associated with the j^{th} attribute. Additionally, $M_j(a)$ represents the count of $m_j(a)$, which contains the sample points within the a^{th} interval. Furthermore, X_j and $X_{\setminus j}$ refer to the j^{th} feature and the features excluding the j^{th} feature, respectively. The centered ALE estimator is derived as (see Liu et al. [71])

$$\widehat{f}_{j,ALE}(X_j) = \widehat{f}_{j,ALE}(X_j) - \frac{1}{M} \sum_{i=1}^M \widehat{f}_{j,ALE}(x_j^{(i)}). \quad (5.42)$$

The centered ALE estimator guarantees a response variable with a zero mean effect. Furthermore, it has the capability to analyze the interaction effect between two attributes of the model. A detailed explanation to calculate the two-dimensional ALE is given in Vipin et al. [155].

5.7.2 Shapley additive explanation (SHAP)

In this section, we will provide an overview of the shapley values associated with a ML model F that can predict the response variable for any input vector $X^{(i)}$, for $i = 1, \dots, M$, where M is the number of samples. The goal of Shapley values is to give the explanation for an individual prediction $F(X^{(i)})$ using the formula (see Heskes et al. [119])

$$F(X^{(i)}) = F_0 + \sum_{k=1}^n \varphi_k, \quad (5.43)$$

where φ_k is the contribution of the feature k to the predictive model F . The baseline F_0 is the expected value $\mathbb{E}[F(X)]$ under the observed data distribution $\mathbf{P}(X)$. Now, the contribution of the feature k for a given permutation of features π is given by (see Heskes et al. [119])

$$\varphi_k(\pi) = \nu(\{j : j \preceq_{\pi} k\}) - \nu(\{j : j \prec_{\pi} k\}), \quad (5.44)$$

where $j \prec_{\pi} k$ refers to the features j precedes k in the permutation π .

$$\begin{aligned} \nu(S) &= \mathbb{E} \left[F(X) \mid X_S = X_S^{(i)} \right] \\ &= \int f(X_{\bar{S}}, X_S^{(i)}) \mathbf{P}(X_{\bar{S}} \mid (X_S = X_S^{(i)})) dX_{\bar{S}}, \end{aligned} \quad (5.45)$$

where S is the chosen column to predict the response variable from the set of input variables, and \bar{S} denotes its complement columns. Now, by considering a uniform distribution for all the permutations, we get

$$\varphi_k = \sum_{S \subseteq N \setminus k} \frac{|S|!(n - |S| - 1)!}{n!} [\nu(S \cup k) - \nu(S)]. \quad (5.46)$$

5.8 Results and discussions

It is a common culture in a data analytic study to explore the strength of the association between the input attributes and the target variable as a preliminary investigation (Puth et al. [156]). Pearson's product-moment correlation coefficient will provide only the linear relationship between the attributes (Puth et al. [156]), and the attributes are assumed to follow normal distribution (Whitlock and Schluter [157]). Specifically, it is developed to work with continuous data attributes but not nominal or ordinal-type attributes. In such a scenario, two non-parametric measures of association in common use are 'Spearman's rank order correlation coefficient' r_S and 'Kendall's rank correlation coefficient' τ (Puth et al. [156]). A higher absolute value of Spearman's or Kendall's correlation coefficient indicates a monotonic relation between the attributes. Further, we have considered only seven levels for each attribute, and the input samples are the combination of these seven levels of data. In such a scenario, Spearman's rank correlation coefficient will return the accurate correlation (Puth et al. [156]). The 'Spearman's correlation coefficient' can be calculated by

$$r_S = 1 - \frac{6 \sum d_i^2}{n(n^2 - 1)}, \quad (5.47)$$

where d_i denotes the difference between the two ranks of each sample and n denotes the number of samples. The Spearman's correlation coefficient and the significance of the correlation coefficient in terms of the P -values are provided in Tab. 5.5. It shows that Spearman's correlation coefficient is significant for l_1/h , d_1/h , d_2/h , and r/h . Further, l_1/h and r/h exhibit the largest negative monotonic correlation with the response variable P_{Total} , while the d_1/h and d_2/h demonstrate weaker positive monotonic correlation.

TABLE 5.5: Spearman's correlation coefficient and corresponding P -values

| Parameter | Spearman's correlation | P -value |
|-----------|------------------------|-----------------|
| l_1/h | -0.325 | < 0.001 |
| d_1/h | 0.101 | < 0.001 |
| g_p/h | -0.005 | ≈ 0.636 |
| d_2/h | 0.105 | < 0.001 |
| r/h | -0.327 | < 0.001 |

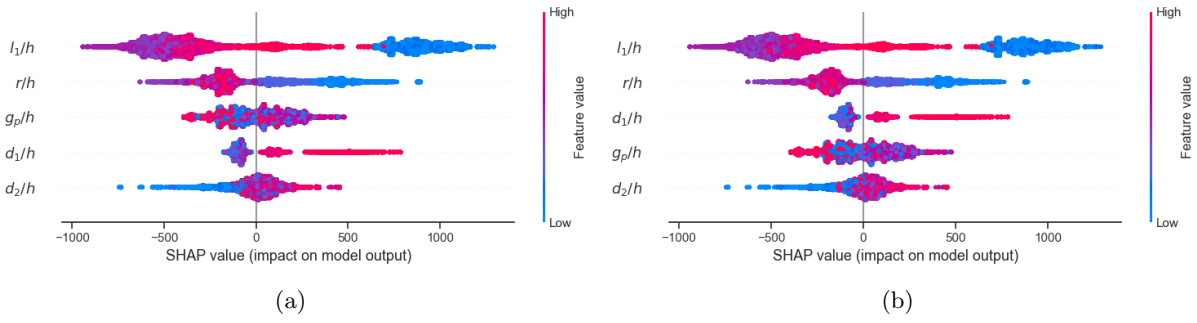


FIGURE 5.4: Shapely values of (a) train set (b) test set.

Fig. 5.4 depicts the feature importance calculated using the Shapely values, which assigns a value to every single entry in the input database using Eq. (5.46) and can be accumulated to a feature in a predictive model, indicating its contribution to the final prediction (Ferraro et al. [158]). The bars are sorted based on the feature importance, with the most important feature is placed at the top. Figs. 5.4(a) and 5.4(b) depict the Shapely values for both the training and test datasets. The SHAP interpretation approach will assign a Shapely value for each data point in the dataset that represents the dots in Figs. 5.4(a) and 5.4(b) (Ferraro et al. [158]). Each horizontal line corresponds to the variation in the Shapely values for a particular feature. The blue points in the figure represent the lower values of the feature, and the higher values are represented in red color. The first horizontal line in Fig. 5.4 represents the feature l_1/h , which depicts that l_1/h is the most significant input parameter in the study. The Shapely values are notably higher when l_1/h is small, indicating that its contribution to the response variable P_{Total} is significant in the lower range of l_1/h . For moderate values of l_1/h , the Shapely values are negative and minimal in nature, suggesting that P_{Total} for inputs in this range of l_1/h is below the expected values of P_{Total} . Further, for higher values of l_1/h , the Shapely values again increase, but it's clearly less than the Shapely values associated with the lower values of l_1/h . The next horizontal line corresponding to r/h in Fig. 5.4 shows a similar trend, indicating that higher r/h values are associated with lower P_{Total} values. However, there seems to be a contradiction as maximum power generation occurs when both l_1/h and r/h are small. This calls for a further study of the trade-off between the values of these parameters l_1/h and r/h . The fourth horizontal line in Fig. 5.4(b) represents g_p/h , showing a considerable impact on the model output for moderate values of g_p/h . As g_p/h values are moderate in nature, P_{Total} hovers above its baseline. Further investigation is needed to better understand the relationship between g_p/h and P_{Total} because the Shapely values associated with the lower values and higher values of g_p/h are highly scattered in nature. The following two horizontal lines in Fig. 5.4(a) represent d_1/h and d_2/h , both showing a gradual increase in P_{Total} as the parameter values increase. However, Spearman's correlation coefficient in Tab. 5.5 is not significantly higher for these parameters, indicating that the underlying nature of their effect on P_{Total} is not entirely clear and have to be studied further. Overall, the SHAP summary plot provides valuable insights

into the impact of different parameters on the total power generation (P_{Total}), revealing trends and areas that require deeper examination for a comprehensive understanding of the feature impact. One important observation to be noted is that the Shapely value distribution for the training set and the test set are identical in nature. The Shapely value for a feature is calculated as the mean of the absolute values of the individual Shapely values associated with each value within the feature. Here, the Shapely values for the features l_1/h , r/h , g_p/h , d_1/h , and d_2/h associated with the training set are 560.67, 239.38, 135.77, 135.12, and 87.76, respectively. For test set, it is 563.93, 238.60, 135.18, 136.72 and 87.38, respectively. This implies that the model's interpretability of feature importance and the influence of input samples on predictions remain consistent across both datasets. Such consistency suggests that the ML model has the ability to generalize well to an independent dataset within the same domain. It is to be noted that the Shapely value of the features g_p/h and d_2/h are very close to each others in both the training set and test set. This is the reason behind the interchange of orders in g_p/h and d_2/h that can be seen in Fig. 5.4.

So far, we have studied the importance of the input features and its impact on the target variable. Next, we aim to identify particular regions within the input space where the P_{Total} reaches its peak. This identification process will be facilitated using the XGBoost model and an interpretable ML technique, specifically through the utilization of ALE plots. Fig. 5.5 shows the ALE plots, providing visual insights into the variations in P_{Total} by the hybrid OWC-PWEC device concerning each individual attributes. In the ALE plot, the Y -coordinate represents the ALE value of the corresponding value associated with the feature on the X -coordinate. The line $y = 0$ signifies the expected value of the P_{Total} by the hybrid OWC-PWEC device. Figs. 5.5(a) - 5.5(e) illustrate the individual effects of the parameters l_1/h , d_1/h , d_2/h , g_p/h , and r/h on the P_{Total} by the hybrid OWC-PWEC device. In Fig. 5.5(a), the graph depicts the impact of the parameter l_1/h on the P_{Total} by the hybrid OWC-PWEC device in terms of ALE value. It is evident from the plot that the maximum ALE value is attained when l_1/h is at its minimum. Additionally, it reveals that the effect of l_1/h is maximum and stable in the range $0.5 \leq l_1/h \leq 1.2$. As l_1/h increases to ≈ 1.7 , the ALE value gradually decreases and approaches towards the baseline of the total power output P_{Total} . Notably, P_{Total} never surpasses the baseline again. However, once the ALE value reaches its minimum within the range $2.0 < l_1/h < 2.5$, P_{Total} starts to rise slowly and approaches the baseline level again when l_1/h exceeds 3.5. This trend of P_{Total} with respect to l_1/h can also be seen in Tab. 5.5 that Spearman's correlation coefficient is most negative for l_1/h . Fig. 5.5(b) shows the impact of the parameter d_1/h on the P_{Total} by the OWC-PWEC device. As d_1/h is at its minimum, the ALE value is at its lowest and gradually rises and reaching the baseline score of the target variable P_{Total} at approximately $d_1/h \approx -0.18$. The graph clearly demonstrates a sudden increase in P_{Total} as d_1/h increases from -0.2 . The sharp elevation in P_{Total} as d_1/h reaches its maximum is attributed to the heightened concentration of wave power near the free surface. Fig. 5.5(c) demonstrates the

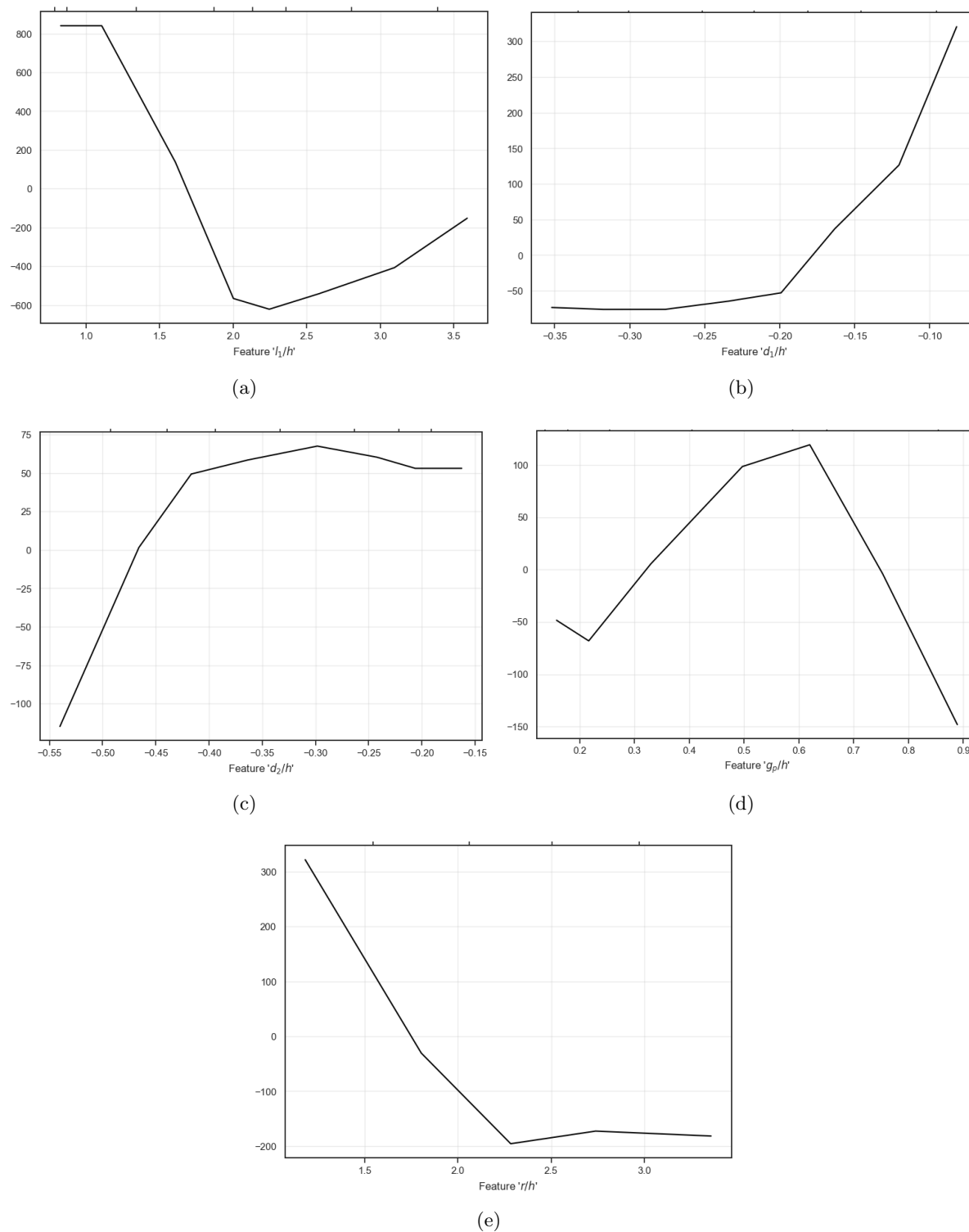


FIGURE 5.5: ALE plot of (a) l_1/h , (b) d_1/h , (c) d_2/h , (d) g_p/h , and (e) r/h .

impact of the parameter d_2/h on P_{Total} which is similar to Fig. 5.5(b), specifically an increase in the value of d_2/h corresponds to a simultaneous rise in the ALE value. However, a notable difference is observed that the ALE values are started increase from the minimal values of d_2/h and reaches the baseline of P_{Total} at approximately $d_2/h \approx -0.47$. As the P_{Total} increases and

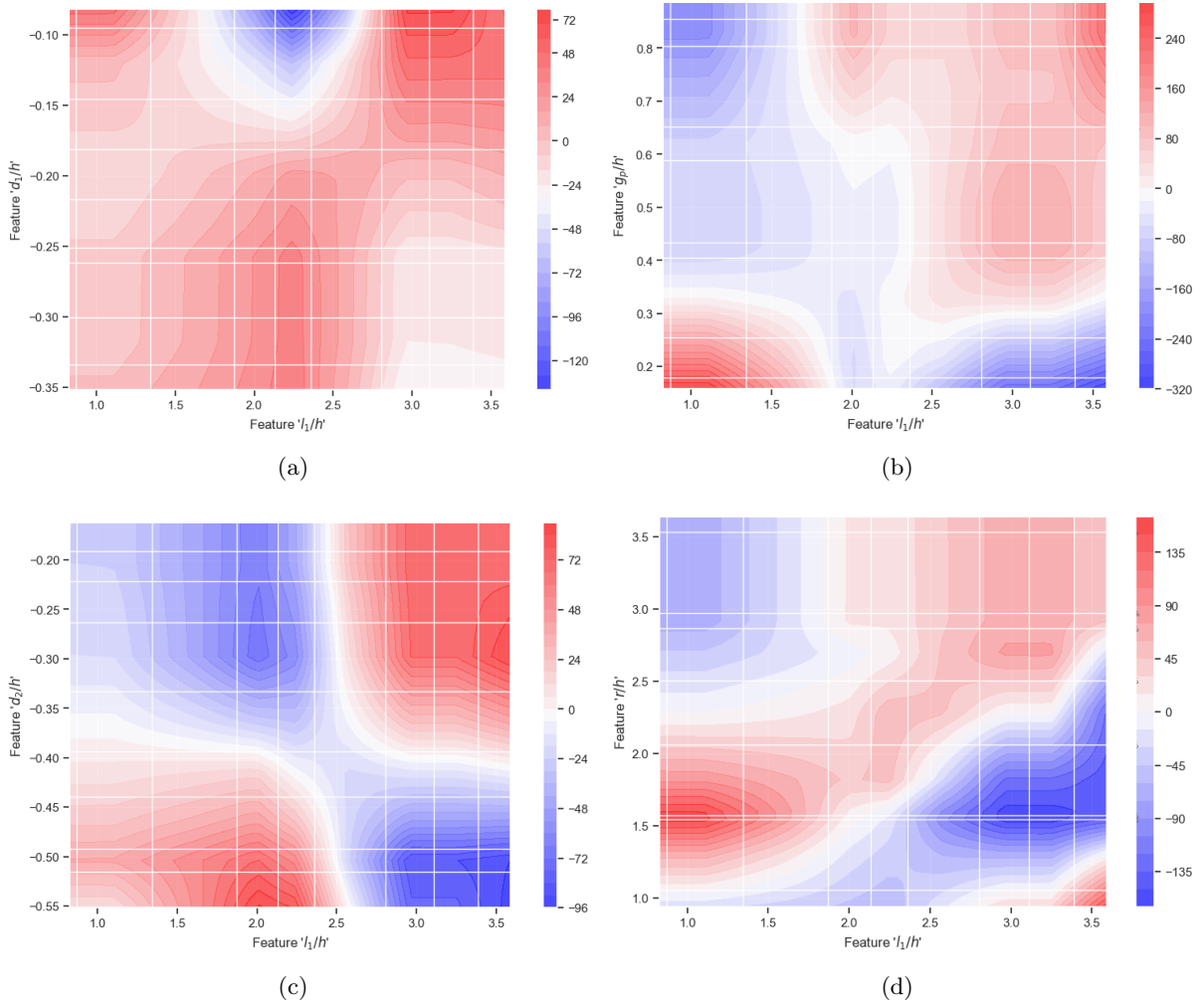


FIGURE 5.6: ALE plot of (a) l_1/h and d_1/h , (b) l_1/h and g_p/h , (c) l_1/h and d_2/h , (d) l_1/h and r/h .

reaches to a threshold range at approximately $d_1/h \approx -0.42$, the variation in P_{Total} saturates hereafter. It is to be noted that the maximum value of the ALE value does not align with the maximum value of d_2/h . Instead, it occurs at approximately $d_2/h \approx -3.0$ and thereafter, a slight reduction in P_{Total} is observed. Furthermore, it is noteworthy that the variation in the ALE value is much higher for d_1/h compared to d_2/h which clearly indicates that d_1/h is the more influential parameter on the variation of P_{Total} than d_2/h . In Fig. 5.5(d), the graph illustrates how the parameter g_p/h affects the P_{Total} by the hybrid OWC-PWEC device. The plot demonstrates that within the interval $0.32 < g_p/h < 0.75$, P_{Total} consistently exceeds the baseline. Furthermore, it is noteworthy that the ALE value reaches its optimum within the range $0.6 < g_p/h < 0.65$. Hence, careful consideration should be made to the relative positioning of the PWEC and OWC devices to ensure the maximum total power generation P_{Total} . Fig. 5.5(e) demonstrates the impact of r/h on the P_{Total} the hybrid OWC-PWEC device. Similar to Fig. 5.5(a), we observe a comparable trend where the ALE value attains its maximum when r/h is minimal. As r/h increases and reaches 1.75, P_{Total} reduces to its baseline value. Furthermore,

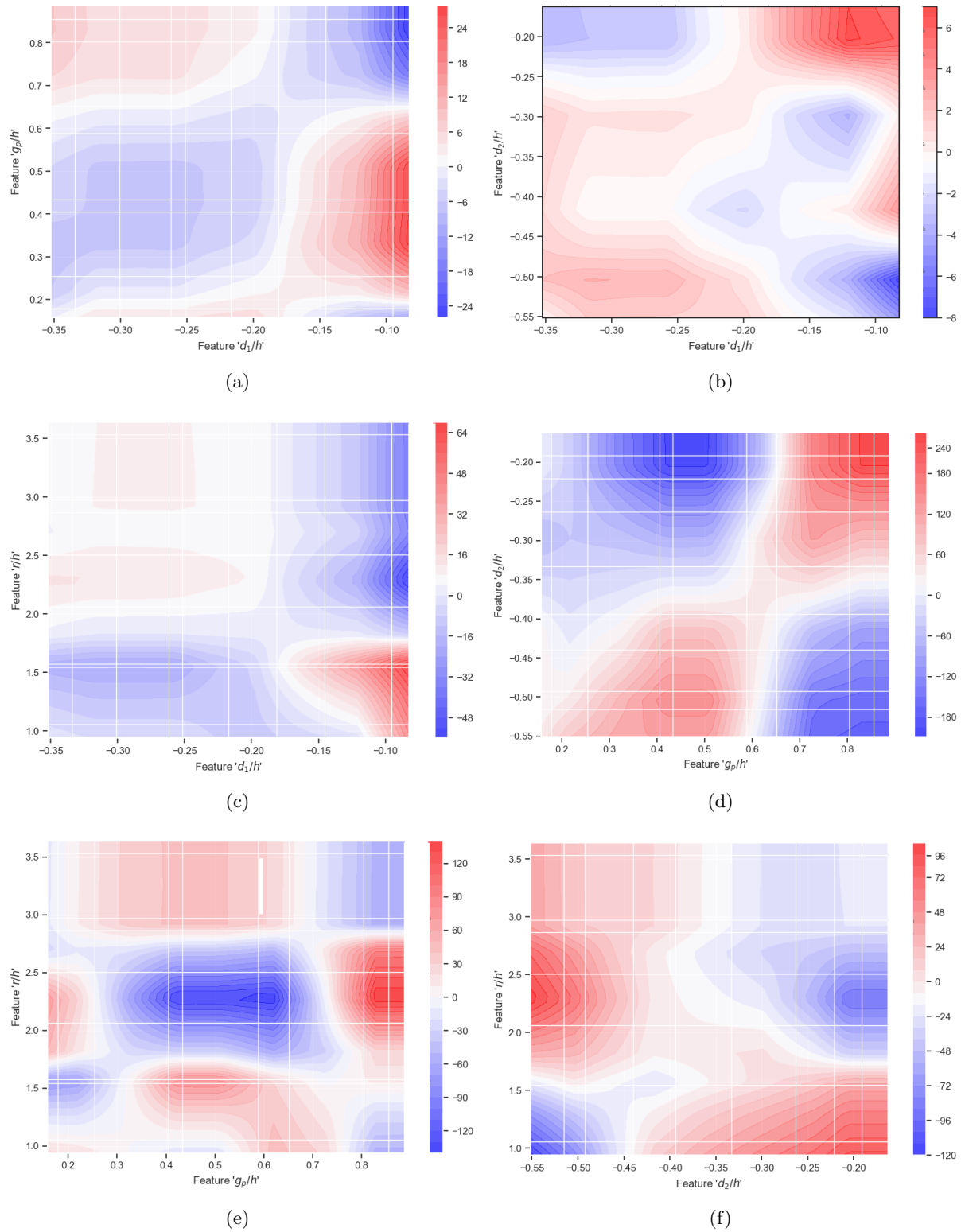


FIGURE 5.7: Two-dimensional ALE plot of (a) d_1/h and g_p/h , (b) d_1/h and d_2/h , (c) d_1/h and r/h , (d) g_p/h and d_2/h , (e) g_p/h and r/h , (f) d_2/h and r/h .

with a further increase in r/h , the ALE value decreases as well, reaching to a threshold value at $r/h \approx 2.25$, and then maintaining the ALE value. Upon observing both Fig. 5.5(a) and Fig. 5.5(e), it becomes apparent that the maximum power generation occurs when both l_1/h and r/h are minimal, leading to some confusion. Further investigation and analysis of the trade-off between l_1/h and r/h will be conducted to gain deeper insights into their combined effects on P_{Total} by the hybrid OWC-PWEC device.

Figs. 5.6(a)-(d) and 5.7(a)-(f) depict the two-dimensional ALE plots, providing a visual representation of the interplay between pairs of individual attributes on the P_{Total} by the hybrid OWC-PWEC WEC device. Figs. 5.6(a)-5.6(d) show the interaction effect of l_1/h with d_1/h , g_p/h , d_2/h and r/h , respectively. In Fig. 5.6(a), it is evident that the ALE value surpasses a significant threshold for the response variable within three distinct regions: $l_1/h < 1.5$ with $d_1/h > -0.15$, $1.5 < l_1/h < 2.7$ with $d_1/h < -0.2$, and $l_1/h > 3$ with $d_1/h > -0.15$. Turning to the interaction between l_1/h and g_p/h , as illustrated in Fig. 5.6(b), the ALE value exceeds the baseline value within two regions: $l_1/h < 1.7$ with $g_p/h < 0.3$, and $l_1/h > 2.7$ with $g_p/h > 0.3$. Fig. 5.6(c) demonstrates that the maximum power output is obtained when both the input parameters are either minimum or both the input parameters are maximum. Here, the high yield regions are $l_1/h < 2.5$ with $d_2/h < -0.4$, and $l_1/h > 2.5$ with $d_2/h > -0.4$. From Fig. 5.6(d), a positive linear correlation between the attributes l_1/h and r/h is observed as the interaction effect is maximum along the principal diagonal points in the figure. A significant interaction effect is observed in the regions $l_1/h < 2$ with $1 < r/h < 2$ and $l_1/h > 3.3$ with $r/h < 1.2$. Figs. 5.7(a)-5.7(c) show the interaction between d_1/h with g_p/h , d_2/h and r/h , respectively. Fig. 5.7(a) shows that the only region with significant interaction is $d_1/h > -0.15$ with $0.2 < g_p/h < 0.6$. Since the variation in the ALE value in Fig. 5.7(b) is very less, it suggests that the interaction between the parameters d_1/h and d_2/h is insignificant. Turning attention to the interaction effect between d_1/h and r/h in Fig. 5.7(c), it is observed that P_{Total} surpasses its average solely in the region where $r/h < 1.7$ and $d_1/h > -0.15$. Figs. 5.7(d) and 5.7(e) illustrate the interaction involving g_p/h with d_2/h and r/h . Specifically, Fig. 5.7(d) indicates positive ALE values in two regions: firstly, for $g_p/h < 0.6$ and $d_2/h < -0.4$, and secondly, for $g_p/h > 0.65$ and $d_2/h > -0.35$. Whereas in Fig. 5.7(e), there is only one region $g_p/h > 0.7$ with $2.0 < r/h < 2.7$ in which the ALE value is significant. Finally, Fig. 5.7(f) depicts the interaction between d_2/h and r/h . It is seen that there are two significant regions in which the power generation is above its expected value, which are $d_2/h > -0.4$ with $r/h < 1.5$ and $d_2/h < -0.45$ with $2.0 < r/h < 2.8$.

Now, to optimize the parameters associated with the hybrid WEC device, three distinct regions within the input space are determined by identifying those areas exhibiting the optimal ALE

values. All the three regions are given below

$$\begin{aligned}
R_1 &= \{0.1 \leq l_1/h \leq 1.5 \cup -0.15 \leq d_1/h \leq -0.05 \cup 0.05 \leq g_p/h \leq 0.3\} \\
&\quad \cup \{-0.4 \leq d_2/h \leq -0.1 \cup 0.5 \leq r/h \leq 1.75\}, \\
R_2 &= \{0.1 \leq l_1/h \leq 1.5 \cup -0.15 \leq d_1/h \leq -0.05 \cup 0.35 \leq g_p/h \leq 0.7\} \\
&\quad \cup \{-0.55 \leq d_2/h \leq -0.4 \cup 0.5 \leq r/h \leq 1.75\}, \\
R_3 &= \{0.1 \leq l_1/h \leq 1.5 \cup -0.15 \leq d_1/h \leq -0.05 \cup 0.65 \leq g_p/h \leq 1\} \\
&\quad \cup \{-0.4 \leq d_2/h \leq -0.1 \cup 0.5 \leq r/h \leq 1.75\}.
\end{aligned} \tag{5.48}$$

We will now use the RSM to find the exact input parameters that maximize P_{Total} by the Hybrid WEC device.

5.9 Optimization based on response surface methodology (RSM)

TABLE 5.6: L_8 orthogonal array

| Experiment | Attributes | | | | |
|------------|------------|---------|---------|---------|-------|
| | l_1/h | d_1/h | g_p/h | d_2/h | r/h |
| 1 | - | - | - | - | - |
| 2 | - | - | - | + | + |
| 3 | - | + | + | - | - |
| 4 | - | + | + | + | + |
| 5 | + | - | + | - | + |
| 6 | + | - | + | + | - |
| 7 | + | + | - | - | + |
| 8 | + | + | - | + | - |

TABLE 5.7: Initial lower and upper sample values of the parameters to construct L_8 orthogonal array

| R_1 | | R_2 | | R_3 | |
|-------|-------|-------|-------|-------|-------|
| Lower | Upper | Lower | Upper | Lower | Upper |
| 0.5 | 1 | 0.5 | 1 | 0.5 | 1 |
| -0.12 | -0.08 | -0.12 | -0.08 | -0.12 | -0.08 |
| 0.1 | 0.2 | 0.4 | 0.6 | 0.75 | 0.9 |
| -0.3 | -0.2 | -0.5 | -0.45 | -0.3 | -0.2 |
| 0.8 | 1.5 | 0.8 | 1.5 | 0.8 | 1.5 |

This section outlines a comprehensive optimization process to maximize P_{Total} by analyzing the impact of input attributes associated with the hybrid OWC-PWEC device. The statistical procedure, namely the response surface methodology (RSM) (Myers et al. [123]) and the method

TABLE 5.8: Optimal parameter range, sign of the regression coefficient, T Score and P -Value for R_1 .

| Term | Lower | Upper | Sign of the Coefficient | T Score | P -Value |
|-----------------|-------|-------|-------------------------|-----------|------------|
| Intercept | | | +ve | 4.24 | 0.05 |
| l_1/h | 0.21 | 0.23 | +ve | 3.13 | 0.09 |
| d_1/h | -0.08 | -0.05 | -ve | -1.71 | 0.23 |
| g_p/h | 0.06 | 0.09 | -ve | -1.67 | 0.18 |
| d_2/h | -0.19 | -0.11 | -ve | -5.26 | 0.10 |
| r/h | 0.63 | 1.05 | -ve | -3.83 | 0.07 |
| Max P_{Total} | 7912 | | | | |

TABLE 5.9: Optimal parameter range, sign of the regression coefficient, T Score and P -Value for R_2 .

| Term | Lower | Upper | Sign of the Coefficient | T Score | P -Value |
|-----------------|-------|-------|-------------------------|-----------|------------|
| Intercept | | | +ve | 3.38 | 0.07 |
| l_1/h | 0.45 | 0.55 | -ve | -1.15 | 0.36 |
| d_1/h | -0.09 | -0.07 | -ve | -0.73 | 0.54 |
| g_p/h | 0.36 | 0.44 | +ve | 0.28 | 0.80 |
| d_2/h | -0.50 | -0.41 | +ve | 3.54 | 0.07 |
| r/h | 0.72 | 0.88 | +ve | 0.14 | 0.90 |
| Max P_{Total} | 6013 | | | | |

TABLE 5.10: Optimal parameter range, sign of the regression coefficient, T Score and P -Value for R_3 .

| Term | Lower | Upper | Sign of the Coefficient | T Score | P -Value |
|-----------------|-------|-------|-------------------------|-----------|------------|
| Intercept | | | +ve | 2.15 | 0.16 |
| l_1/h | 0.45 | 0.55 | -ve | -1.32 | 0.31 |
| d_1/h | -0.12 | -0.08 | -ve | -0.70 | 0.55 |
| g_p/h | 0.75 | 0.09 | -ve | -0.32 | 0.77 |
| d_2/h | -0.3 | -0.2 | -ve | -1.54 | 0.26 |
| r/h | 0.8 | 1.5 | +ve | 3.15 | 0.08 |
| Max P_{Total} | 4559 | | | | |

of design of experiments are employed to find the specific combinations of the parameters which maximize P_{Total} . We have used the L_8 orthogonal array with two levels for each of the parameters for the design of experiments as shown in Tab. 5.6. In this table, ‘-’ and ‘+’ represent the lower value and the upper value of the samples, respectively. In the optimization process, the initial step involves selecting two samples from each attribute within the identified regions R_j , $j = 1, 2, 3$ as derived from the ALE plots associated with the XGBoost model. The initial samples for the optimization of parameters in each of the regions is given in Tab. 5.7. Following this, an augmented L_8 orthogonal table combined with the response variable will be passed through a linear regression model. This aids in determining the directional adjustments needed

for each parameter based on the coefficients and their P -values associated with the student t -test. The student t -test is employed to assess the statistical significance of the coefficients in the linear regression model. The P -values serve to evaluate the significance of the change in the input values of the parameters concerning the response variable. The hypothesis test we have considered is H_0 : the regression coefficient is equal to zero against the alternative hypothesis H_a : the regression coefficient is not equal to zero with a significance level of 0.05. The adjusted parameter values that maximize the P_{Total} will be used as the design parameters for the L_8 orthogonal matrix in the next iteration. The optimal parameter range, sign of the regression coefficient, T Score, and P -Value for the optimal L_8 matrix for each of the three regions R_j , $j = 1, 2, 3$ are given in Tabs. 5.8-5.10. The optimal table is obtained by repeating the optimization procedure discussed above until the significance of the regression coefficient of all the attributes with respect to the P -value associated with the t test is greater than the significance level of 0.05. From Tabs. 5.8-5.10, it is seen that the P -value associated with the parameters of the WEC device is greater than 0.05. Hence, it is to be decided that there is no evidence to reject the H_0 . This leads to the conclusion that the change in the P_{Total} with respect to the samples of the parameters used in the associated L_8 orthogonal matrix is insignificant. Further, it is obtained from the associated L_8 orthogonal matrix that the P_{Total} is higher in the first region R_1 . It is obtained from Tab. 5.8 that the optimal range of the parameters obtained from the RSM is $0.21 \leq l_1/h \leq 0.23$, $-0.08 \leq d_1/h \leq -0.05$, $0.06 \leq g_p/h \leq 0.09$, $-0.19 \leq d_2/h \leq -0.11$, and $0.63 \leq r/h \leq 1.05$ and the optimal combination of the attributes associated with the hybrid OWC-PWEC device is $l_1/h = 0.21$, $d_1/h = -0.08$, $g_p/h = 0.06$, $d_2/h = -0.19$, and $r/h = 0.63$, and the associated optimal P_{Total} is obtained to be 7912 (see Tab. 5.12). The importance of the optimization technique employed in this study can be analyzed by comparing the optimal P_{Total} obtained from the optimization process with the descriptive statistics of the response variable used in the model building (see Tab. 5.11). From the L_8 orthogonal matrix associated with the optimal parameters given in Tab. 5.8, it is evident that each combination of input parameters yields a P_{Total} that is higher than the maximum value of the P_{Total} in the parent dataset (dataset used for training, testing, and validation purpose). This underscores the effectiveness of the optimization technique, which integrates an ML model and interpretable ML approaches with a conventional optimization method (specifically, the Response Surface Methodology (RSM)).

TABLE 5.11: Descriptive statistics of the response variable from the dataset developed in Sec. 5.5. All the units are considered as Wm^{-1} .

| Count | Mean | Std | Min | 50% | 90% | 95% | 99% | Max |
|-------|------|-----|-----|------|------|------|------|------|
| 16807 | 1794 | 974 | 151 | 1507 | 3232 | 3952 | 5063 | 6440 |

TABLE 5.12: L_8 orthogonal matrix associated with the optimal parameters for R_1

| l_1/h | d_1/h | g_p/h | d_2/h | r/h | $P_{Total}(\text{Wm}^{-1})$ |
|---------|---------|---------|---------|-------|-----------------------------|
| 0.21 | -0.08 | 0.06 | -0.19 | 0.63 | 7912 |
| 0.21 | -0.08 | 0.06 | -0.11 | 1.05 | 7149 |
| 0.21 | -0.05 | 0.09 | -0.19 | 0.63 | 7725 |
| 0.21 | -0.05 | 0.09 | -0.11 | 1.05 | 7241 |
| 0.23 | -0.08 | 0.09 | -0.19 | 1.05 | 7469 |
| 0.23 | -0.08 | 0.09 | -0.11 | 0.63 | 7821 |
| 0.23 | -0.05 | 0.06 | -0.19 | 1.05 | 7488 |
| 0.23 | -0.05 | 0.06 | -0.11 | 0.63 | 7873 |

5.10 Summary and concluding remarks

The present study investigates the mathematical modeling, prediction, and optimization of a hybrid WEC device consisting of PWEC and OWC devices. The hydrodynamic problem associated with the total power generation by the WEC device is handled using the BEM-based numerical approach. The database for the ML model building is generated using the LHS technique. After identifying the appropriate ML model to predict the P_{Total} , we employ Spearman's correlation coefficient to assess the correlation strength between the input attributes and the target variable. Subsequently, we leverage an interpretable ML approach, specifically Shapely values, to analyze the importance of features in the database. The optimization of the P_{Total} by the hybrid OWC-PWEC device is carried out using the developed XGBoost model, an interpretable ML approach (namely, the accumulated local effect), and using a conventional optimization technique, namely the response surface methodology. The current investigation results in the subsequent findings:

- The total power generated by the hybrid OWC-PWEC device can be accurately predicted using the proposed XGBoost model with a comparatively smaller error in the test set as MAPE: 0.02%, MAE: 43.05 Wm^{-1} , RMSE: 61.86 Wm^{-1} . Further, the R^2 value is obtained to be 0.9959.
- The feature importance is identified using the XGBoost model and the Shapely values. The most important feature in predicting the P_{Total} is l_1/h , and the subsequent important parameters in feature wise are r/h , d_1/h , g_p/h , and d_2/h , respectively.
- The optimal region of the input space is identified using the XGBoost model, the ALE plots, and the response surface methodology. The optimal range is obtained as $0.21 \leq l_1/h \leq 0.23$, $-0.08 \leq d_1/h \leq -0.05$, $0.06 \leq g_p/h \leq 0.09$, $-0.19 \leq d_2/h \leq -0.11$, and $0.63 \leq r/h \leq 1.05$.

- The exact combination of parameter values which maximizes the P_{Total} is obtained to be $l_1/h = 0.21$, $d_1/h = -0.08$, $g_p/h = 0.06$, $d_2/h = -0.19$, and $r/h = 0.63$, with a maximum $P_{Total} = 7912 \text{ Wm}^{-1}$.

In summary, it is concluded that optimizing the shape parameters of the OWC and PWEC devices and deploying the two devices within the specified gap length can substantially improve the performance of the hybrid OWC-PWEC device.

Chapter 6

Summary and future work

This chapter summarizes the results and findings obtained in the thesis, the limitations of models used in the present research, applications, and the scope of possible extensions of the present study and future investigations.

6.1 Conclusions

The purpose of the thesis is to develop a BEM-based numerical model to study the surface gravity waves interaction with the PWEC and OWC devices to study the performance of the WEC devices. The PWEC device is studied in regular water waves and placed over the undulated seabed, and the OWC device is studied for both the regular and irregular wave climates. Further, we identified suitable machine learning tools based on the maximum accuracy score and minimum error matrix scores for predicting the power generated by the WEC devices. Optimization of the standalone PWEC device parameters in regular wave climate is carried out using the deep learning model, namely the multilayer perceptron model. Moreover, the optimization of the parameters of the standalone OWC device in irregular wave climate and hybrid OWC-PWEC wave energy converter devices under the regular incident wave is carried out using a hybrid optimization approach including machine learning models, interpretable machine learning approaches and using the multivariate statistical optimization method namely the response surface methodology. The salient conclusions and contributions of the present study are the following:

- Chapter 1 presents an in-depth literature review and the mathematical foundation concerning the wave structure interaction problems associated with the piezoelectric plate and oscillating water column wave energy converter devices. A detailed derivation of the boundary conditions of the physical problem is provided under the assumption of linear

wave-structure interaction theory. This thesis employs a numerical solution approach based on the Boundary Element Method to address the hydrodynamics of power generation by the OWC and PWEC devices. The chapter also reviews the background of BEM numerical techniques, specifically focusing on constant and dual boundary elements. Further, a detailed description of the training procedure of the artificial neural network and XGBoost models, interpretable machine learning approaches, and the multivariate statistical optimization technique, namely the response surface methodology, are provided.

- In Chapter 2, a piezoelectric wave energy converter (PWEC) device integrated with an impermeable breakwater placed over an undulated seabed is considered. The PWEC device is composed of a single submerged flexible plate with piezoelectric layers attached to both the faces of the flexible plate. Due to the piezoelectric effect, this piezoelectric plate generates electricity when excited by the incident waves. A detailed analysis is done to investigate the effect of PWEC plate submergence depth, plate length, plate edge conditions, incident wave period, bottom ripple amplitude, and ripple number on the power generation by the PWEC device. It is seen that the PWEC device edge conditions, submergence depth, and plate length play a significant role in the resonating pattern associated with the wave power generation curve. The results demonstrate that the PWEC device having moderate plate length and with free and moored type front edges generates a higher amount of wave power for a wider range of incident wave frequencies.
- In Chapter 2, we have studied the hydrodynamic performance of the PWEC device attached to an impermeable breakwater in the frequency domain. It is to be noted that the study of the plate deflection in the time domain provides more realistic results than in the frequency domain. Hence, it is important to study the performance of a standalone PWEC device in frequency as well as in the time domain.
- In Chapter 3, the power absorption by a submerged piezoelectric wave energy converter (PWEC) in the frequency domain and the time-dependent displacement of the free surface and the PWEC plate deflection are discussed. Further, the prediction of the power generation by the device and the optimization of the device parameters using an artificial neural network model, namely the multilayer perceptron model, are discussed. The problem is studied initially for the case when PWEC plate is situated over an undulated seabed. However, in the parameters optimization process, the seabed is considered uniform in nature as the effect of bottom undulation is negligible. Here, the PWEC plate is considered standalone without attaching the same with an existing breakwater. The boundary element method (BEM) is used to solve the frequency domain problem. Further, the Fourier transform is utilized to convert the frequency domain results into time domain. In time domain analysis, emphasis is given to analyze the the plate deflection and the free surface displacement. The input database for the ANN model building is generated using the latin

hypercube sampling method (LHS), and the corresponding target variable is calculated using the BEM-based numerical tool. After the ANN model building, the optimization of the design parameters of the PWEC device is carried out using a database containing 3000 sample points generated randomly using the LHS method. These generated input samples will be passed through the developed ANN model, and the predicted response variable provides a range for the geometric parameters associated with the PWEC device to optimize the power generation.

- The PWEC device discussed in Chapter 3 is capable of generating electricity to run low-energy electronics such as LEDs, wireless routers, PCs, ocean buoys, and sensors. Further, the resonances in power generation occurs for certain values of the incident wave frequencies. However, ocean waves consists of a wider range of frequencies and therefore, its necessary to design a wave energy converter device which will work efficiently for a wider range of incident wave frequencies and also can generate higher power. In this regard, OWC device can serve the purpose.
- In Chapter 4, we studied the performance of a breakwater-integrated quarter-circle-shaped front wall OWC device under the influence of irregular incident waves. Firstly, the boundary value problem associated with the hydrodynamics of OWC device is handled for a solution using the dual boundary element method (BEM). To examine the complex relationships between all input features and the target variable in a time-efficient manner, supervised machine learning models are developed. Here, two different models: (i) multilayer perceptron (MLP) model based on an artificial neural network, and (ii) a tree ensemble model, namely the XGBoost model are developed. The submergence depth of the front wall of the OWC device, chamber length, rotational speed, and diameter of the turbine blade are considered as input attributes, and the average annual power generated by the OWC device is considered as the output attribute. The MLP model is employed to optimize these input parameters, leveraging the insights provided by the XGBoost model to maximize the annual average power generation. From the dual BEM based numerical results, and using the Latin hypercube sampling technique, 3750 samples were generated to train, validate, and test the machine learning models. Using the XGBoost model with the support of accumulated local effect plots, we find four specific regions of the input space in which the annual average power extraction will be maximum. Hereafter, an extended input database is generated with twenty equally spaced levels for each parameter and the dataset is passed through the developed MLP model to find the optimized values of the parameters of the OWC device which maximizes the power generation. It is obtained that the maximum power generation is attained for $y_0/h = -0.65$, $r/h = 3$, $2.8 \leq D \leq 3$ and $\{70 \leq N \leq 80 \cup 105 \leq N \leq 116\}$.

- In Chapters 2-4, the hydrodynamic performance of the standalone piezoelectric plate and OWC device are studied. However, there is one major shortcoming of the standalone wave energy converter devices, such as the standalone wave energy converter devices are unable to absorb a significant amount of incident wave energy. Hence, in the next chapter, we will study the performance of a hybrid OWC-PWEC device.
- In Chapter 5, we focused on the optimization of the geometric parameters of a hybrid wave energy converter device comprising a piezoelectric plate and an oscillating water column device. Firstly, the boundary element method-based numerical technique is used to solve the hydrodynamic problem associated with the total power generated by the hybrid device. To create the database for the machine learning model building, the input samples are generated using the Latin hypercube sampling technique, and the corresponding values of the target variable are calculated from the solution of the boundary element method. To optimize the device parameters, an appropriate machine learning model is identified from four tree ensemble models and a deep learning model, namely random forest (RF), extreme gradient boosting (XGBoost), light gradient boosting machine (LightGBM), categorical boosting (CatBoost), and multilayer perceptron (MLP). Spearman's correlation coefficient is employed to assess the correlation strength between the input attributes and the target variable, and subsequently, we leverage an interpretable machine learning approach, specifically Shapely values, to analyze the importance of features in the database. Further, using the extreme gradient boosting model along with the interpretable machine learning approaches, we identify the particular areas within the input space that result in optimal power generation. Moreover, the response surface methodology is applied to determine the precise parameters values of the hybrid device, aiming to optimize the total power output extracted by the hybrid device. It is found that the optimal power extraction is attained for $l_1/h = 0.21$, $d_1/h = -0.08$, $g_p/h = 0.06$, $d_2/h = -0.19$, and $r/h = 0.63$, respectively.

Chapters 2-5 are highly advantageous for the engineers and scientists to develop and design efficient piezoelectric and oscillating water column wave energy converter devices. These devices operate effectively when subjected to regular and irregular incident waves. Additionally, the numerical tool employed in this study based on the boundary element method has the potential for extension to analyze a diverse array of challenges related to wave-structure interaction. These challenges are prevalent in coastal and offshore engineering, as well as in interconnected fields of mathematical physics. The current solution methodology is robust and adept at managing complex structural shapes and configurations in an easy manner. Also, the employed ML models will significantly reduce the time complexity and enhance the accuracy of the optimization of the design parameters associated with the wave energy converter devices.

6.2 Major research developments and findings

Chapter 2 illustrates the performance of a submerged PWEC device attached to an impermeable vertical breakwater placed over an undulated seabed and the device performance is analyzed for various parameters associated with the incident waves, PWEC plate, and undulated seabed. Major emphasis is given to analyze the effect of PWEC plate submergence depth, plate length, plate edge conditions, incident wave period, bottom ripple amplitude, and ripple number on the power generation by the PWEC device. The results demonstrated that the overall wave power generated by the PWEC device is significantly higher when the lee side of the PWEC plate is fixed in nature as compared to the moored edge condition. Further, the number of resonating peaks and associated amplitudes are also higher for the PWEC device with a fixed type lee edge. The maximum resonating peak on the wave power generation curve is observed for PWEC devices with fixed-type front edges. In contrast, it is seen that the PWEC device with free and moored type front edges generates moderate wave power for a wider range of incident wave periods. As the length of the PWEC device increases, the number of resonating peaks in the wave power generation curve increases gradually. Further, it is also observed that the PWEC device having moderate length can generate maximum wave power for a wider range of incident wave periods. As the submergence depth of the PWEC device increases, the wave power generated by the PWEC device decreases gradually irrespective of the PWEC device edge conditions. The power generated by the PWEC device doesn't vary much due to the variation in the number of ripples and ripple amplitude of the seabed except at positions where resonances occur. In summary, it is concluded that the plate edge conditions and various parameters associated with the PWEC device can be optimized to generate maximum wave power for a wider range of incident wave frequencies.

Chapter 3 investigates the power generation, the time-dependent free surface displacement and the PWEC plate deflection, and the optimization of the parameters of a submerged PWEC device floating over a sinusoidal seabed under the linear wave-structure interaction theory. The BEM-based numerical method is used to solve the BVP associated with the hydrodynamics of the PWEC device. Various parameters related to the performance of the PWEC device are analyzed. The prediction of the power generated by the PWEC device and optimization of the parameters of the submerged PWEC device to maximize the P_{ext} by the PWEC device are studied using a supervised machine learning algorithm, namely the ANN model. The results demonstrated that the number of resonating peaks increases with an increase in plate length (l/h), and the amplitude of the resonating peak is higher for the moderate values of the plate length (l/h). Further, the amplitude of the resonating peak increases as the submergence depth of the plate decreases. It is noteworthy that, regardless of differences in submergence depth, ripple amplitude, or number of ripples in the seabed, the resonance occurs around the same values of the incident wave period. The amplitude of the resonating peaks increases as the ripple

amplitude decreases in the shortwave regime. On the other hand, an opposite trend is observed for the intermediate and longwave regimes for certain values of the incident wave period. The decrease in the amplitude of the free surface displacement in the transmitted wave from the incident wave pack is due to the power generation by the PWEC device via the interaction of the incident wave pack. Further, the results represent the power-holding behavior of the PWEC device for a longer duration. It is also observed that the power extraction curve attains its maximum when the amplitude of the bottom undulation is negligible. Hence, in the parameter optimization phase, we considered a uniform seabed. For maximum power generation by the PWEC plate, the optimum geometric value for l/h is $2.7 \leq l/h \leq 2.9$ and minimum submergence depth is considered for d/h (the value of d/h is 0.012 chosen in the present study). The mean power generation for this range lies in the interval $[840\text{Wm}^{-1}, 866\text{Wm}^{-1}]$.

In Chapter 4, the performance of a breakwater-integrated quarter-circle-shaped front wall OWC device is studied under the influence of irregular incident waves. By employing the dual BEM, we effectively addressed the associated boundary value problem. We also provided detailed derivations of the physical parameters relevant to the power extraction by the OWC device. The numerical results obtained using the dual BEM demonstrate that the annual average power extraction (P_{ann}) by the OWC device achieves maximum for the following ranges of OWC device and turbine parameters: $2.5 < r/h < 3.0$, $-0.7 < y_0/h < -0.5$, $2 \leq D \leq 3.5$ and $70 \leq N \leq 135$. To shorten these ranges of parameters for maximum power extraction, we employed a supervised machine learning approach based on the ANN model called the MLP model with the support of the tree ensemble model namely, the XGBoost model. Both the MLP model and the XGBoost model were trained, validated, and tested using 3750 input data points in a 60 : 20 : 20 ratio. The optimized MLP architecture consists of five hidden layers comprising of 256, 128, 128, 64, and 32 neurons, respectively, with the ‘‘GELU’’ activation function on each of the hidden layers and the best optimization function is obtained to be ‘‘nadam’’. On the other hand, the architecture of the XGBoost model is also optimized using the genetic algorithm. The R^2 values of the MLP and XGBoost models are obtained to be 0.9995 and 0.9978, respectively. By utilizing the XGBoost model, we have identified four distinct regions of the input space where the maximum annual average power extraction occurs. These high-yield regions of the input space have been determined by studying the highest first-order and second-order ALE scores of the input parameters. Further, in each of the regions, twenty equally spaced samples are selected for all the parameters and then passed through the developed MLP model. Then, the top three combinations of the parameters for which the highest predicted annual average power extraction are chosen for all four regions. Further, the true values of the response variable are also calculated from the dual BEM-based numerical model. It is found that the maximum annual average power extraction by the OWC device occurs when $y_0/h = -0.65$, $r/h = 3$, $2.8 \leq D \leq 3$ and $\{70 \leq N \leq 80 \cup 105 \leq N \leq 116\}$.

In Chapter 5, the mathematical modeling, prediction, and optimization of a hybrid WEC device consisting of PWEC and OWC devices is studied extensively. The hydrodynamic problem associated with the total power generation by the WEC device is handled using the BEM-based numerical approach. The database for the ML model building is generated using the LHS technique. After identifying the appropriate ML model to predict the P_{Total} , we employ Spearman's correlation coefficient to assess the correlation strength between the input attributes and the target variable. Subsequently, we leverage an interpretable ML approach, specifically Shapely values, to analyze the importance of features in the database. The optimization of the P_{Total} by the hybrid OWC-PWEC device is carried out using the developed XGBoost model, an interpretable ML approach (namely, the accumulated local effect), and using a conventional optimization technique, namely the response surface methodology. The current investigation results in the findings: The total power generated by the hybrid OWC-PWEC device can be accurately predicted using the proposed XGBoost model with a comparatively smaller error in the test set as MAPE: 0.02%, MAE: 43.05, RMSE: 61.86. Further, the R^2 value is obtained to be 0.9959. The feature importance is identified using the XGBoost model and the Shapely values. The most important feature in predicting the P_{Total} is l_1/h , and the subsequent important parameters in feature wise are r/h , d_1/h , g_p/h , and d_2/h , respectively. The optimal region of the input space is identified using the XGBoost model, the ALE plots, and the response surface methodology. The optimal range is obtained as $0.21 \leq l_1/h \leq 0.23$, $-0.08 \leq d_1/h \leq -0.05$, $0.06 \leq g_p/h \leq 0.09$, $-0.19 \leq d_2/h \leq -0.11$, and $0.63 \leq r/h \leq 1.05$. The exact combination of parameter values which maximizes the P_{Total} is obtained to be $l_1/h = 0.21$, $d_1/h = -0.08$, $g_p/h = 0.06$, $d_2/h = -0.19$, and $r/h = 0.63$, with a maximum P_{Total} 7912 Wm^{-1} . In summary, it is determined that optimizing the shape parameters of the OWC and PWEC devices and deploying the two devices within the specified gap length can substantially improve the performance of the hybrid OWC-PWEC device.

6.3 Applications

The applications of the study conducted in the research work are as follows

- The analysis conducted in this thesis work is useful for the engineers and scientists working on the research and development, and working on the deployment stage of wave energy converter devices.
- From the qualitative and quantitative results of Chapters 1 – 2, the engineers will gain a comprehensive understanding of the performance of the PWEC device when it is attached to impermeable rigid structures like offshore installations, the pillars of the bridge in the oceans, etc., or when it is deploying standalone.

- Conducting full-scale experiments to assess the efficacy of wave energy converter devices is both expensive and time-consuming. In this context, the numerical results presented in this thesis can significantly alleviate the need for engineers and scientists to perform a large number of experimental analyses, drawing upon the background knowledge provided.
- The machine learning and statistical approaches developed for the prediction and optimization of wave energy converter devices are immensely helpful to the coastal and ocean engineers to design the shapes and structural configurations of wave energy converter devices in real sea conditions. Further, the optimized values of the design parameters and associated power output by WEC devices provide a good estimate of the results a priori to the model tests. The interpretable machine learning models is useful for finding the feature importance and consequently can be used for dimensionality reduction.

6.4 Scope of possible extensions for the future work

A few of the possible extension of the current research work is provided below

- The performance of the PWEC device is studied only in the regular wave climate. This study will be extended to multidirectional and irregular wave climates.
- The current physical problems will be expanded to address the performance of an array of wave energy converter devices with diverse configurations within a wave farm.
- The time domain analysis provided here is merely an introductory analysis of the time-dependent plate deflection and the free surface displacement. This study will be extensively extended to analyze the non-linear behaviors of plate deflection. Further, the study can be extended to estimate the cumulative wave power that can be generated by the wave energy converter device for a specific period of time under suitable wave properties.
- The boundary value problems associated with the power generated by the PWEC device are models using linear wave theory. This can be extended to higher-order water wave theories to obtain better realistic results. Further, the accuracy of the results can be improved by using the higher-order boundary element methods.
- To reduce the computational time and increase the accuracy, a new machine learning model based on the attention mechanism can be developed to accurately predict and consequently to get more accurate optimized input parameters.

References

- [1] A. De O Falcão and R. Rodrigues, “Stochastic modelling of OWC wave power plant performance,” *Applied Ocean Research*, vol. 24, no. 2, pp. 59–71, 2002.
- [2] I. López, J. Andreu, S. Ceballos, I. M. De Alegría, and I. Kortabarria, “Review of wave energy technologies and the necessary power-equipment,” *Renewable and Sustainable Energy Reviews*, vol. 27, pp. 413–434, 2013.
- [3] E. Renzi, “Hydroelectromechanical modelling of a piezoelectric wave energy converter,” *Proceedings of the Royal Society A: Mathematical, Physical and Engineering Sciences*, vol. 472, no. 2195, p. 20160715, 2016.
- [4] F. Buriani and E. Renzi, “Hydrodynamics of a flexible piezoelectric wave energy harvester moored on a breakwater,” in *Proceedings of the 12th European Wave and Tidal Energy Conference (EWTEC 2017), Cork, Ireland*, vol. 27, 2017.
- [5] L. Li, J. Lin, N. Wu, S. Xie, C. Meng, Y. Zheng, X. Wang, and Y. Zhao, “Review and outlook on the international renewable energy development,” *Energy and Built Environment*, vol. 3, no. 2, pp. 139–157, 2022.
- [6] S. Keleş and S. Bilgen, “Renewable energy sources in turkey for climate change mitigation and energy sustainability,” *Renewable and Sustainable Energy Reviews*, vol. 16, no. 7, pp. 5199–5206, 2012.
- [7] S. Sen and S. Ganguly, “Opportunities, barriers and issues with renewable energy development—a discussion,” *Renewable and Sustainable Energy Reviews*, vol. 69, pp. 1170–1181, 2017.
- [8] Y. He, Y. Xu, Y. Pang, H. Tian, and R. Wu, “A regulatory policy to promote renewable energy consumption in China: Review and future evolutionary path,” *Renewable Energy*, vol. 89, pp. 695–705, 2016.
- [9] J. L. Holechek, H. M. Geli, M. N. Sawalhah, and R. Valdez, “A global assessment: can renewable energy replace fossil fuels by 2050?” *Sustainability*, vol. 14, no. 8, p. 4792, 2022.

- [10] BP, “Statistical review of world energy – all data 1965-2019,” BP, 2020, december 2020. [Online]. Available: <https://www.bp.com/>
- [11] C. Ocean, “An overview of wave energy,” Accessed January 11, 2024. [Online]. Available: <https://corppowerocean.com/a-short-history-of-wave-energy/>
- [12] A. D. Craik, “The origins of water wave theory,” *Annual Review of Fluid Mechanics*, vol. 36, pp. 1–28, 2004.
- [13] S. De, “Contributions to the theory of Stokes waves,” in *Mathematical Proceedings of the Cambridge Philosophical Society*, vol. 51, no. 4. Cambridge University Press, 1955, pp. 713–736.
- [14] H. Lamb, *Hydrodynamics*. 6th ed. Cambridge University Press, Cambridge, 1932.
- [15] C. C. Mei, *The applied dynamics of ocean surface waves*. World Scientific Publishing Company, Singapore, 1989, vol. 1.
- [16] R. G. Dean and R. A. Dalrymple, *Water wave mechanics for engineers and scientists*. World Scientific Publishing Company, Singapore, 1991, vol. 2.
- [17] C. M. Linton and P. McIver, *Handbook of mathematical techniques for wave/structure interactions*. Chapman and Hall/CRC, London, 2001.
- [18] F. d. O. Antonio, “Wave energy utilization: A review of the technologies,” *Renewable and Sustainable Energy Reviews*, vol. 14, no. 3, pp. 899–918, 2010.
- [19] H. Polinder, M. Damen, and F. Gardner, “Design, modelling and test results of the AWS PM linear generator,” *European Transactions on Electrical Power*, vol. 15, no. 3, pp. 245–256, 2005.
- [20] T. Belfast, “Islay LIMPET wave power plant, non-nuclear energy programme joule III, CORDIS,” JOR3-CT98-0312, Tech. Rep., 2002.
- [21] Z. Liu, R. Zhang, H. Xiao, and X. Wang, “Survey of the mechanisms of power take-off (PTO) devices of wave energy converters,” *Acta Mechanica Sinica*, vol. 36, pp. 644–658, 2020.
- [22] L. Marquis, M. Kramer, J. Kringelum, J. F. Chozas, and N. Helstrup, “Introduction of wavestar wave energy converters at the Danish offshore wind power plant horns rev 2,” in *4th International Conference on Ocean Energy*. Dublin, Ireland, 2012, p. 6.
- [23] J. P. Kofoed, P. Frigaard, E. Friis-Madsen, and H. C. Sørensen, “Prototype testing of the wave energy converter wave dragon,” *Renewable Energy*, vol. 31, no. 2, pp. 181–189, 2006.

- [24] D. Sarkar, K. Doherty, and F. Dias, "The modular concept of the oscillating wave surge converter," *Renewable Energy*, vol. 85, pp. 484–497, 2016.
- [25] E. Al Shami, R. Zhang, and X. Wang, "Point absorber wave energy harvesters: A review of recent developments," *Energies*, vol. 12, no. 1, p. 47, 2018.
- [26] A. F. d. O. Falcao, "Wave energy utilization: A review of the technologies," *Renewable and Sustainable Energy Reviews*, vol. 14, no. 3, pp. 899–918, 2010.
- [27] B. Drew, A. Plummer, and M. Sahinkaya, "Wave energy converter technology," *Part A: Journal of Power and Energy*, vol. 223, pp. 887–902, 2009.
- [28] B. Czech and P. Bauer, "Wave energy converter concepts: Design challenges and classification," *IEEE Industrial Electronics Magazine*, vol. 6, no. 2, pp. 4–16, 2012.
- [29] D. Evans and R. Porter, "Hydrodynamic characteristics of an oscillating water column device," *Applied Ocean Research*, vol. 17, no. 3, pp. 155–164, 1995.
- [30] T. Heath, "A review of oscillating water columns," *Philosophical Transactions of the Royal Society A: Mathematical, Physical and Engineering Sciences*, vol. 370, no. 1959, pp. 235–245, 2012.
- [31] M. Safaei, H. A. Sodano, and S. R. Anton, "A review of energy harvesting using piezoelectric materials: state-of-the-art a decade later (2008–2018)," *Smart Materials and Structures*, vol. 28, no. 11, p. 113001, 2019.
- [32] O. Farrok, K. Ahmed, A. D. Tahlil, M. M. Farah, M. R. Kiran, M. Islam *et al.*, "Electrical power generation from the oceanic wave for sustainable advancement in renewable energy technologies," *Sustainability*, vol. 12, no. 6, p. 2178, 2020.
- [33] X. Xie, Q. Wang, and N. Wu, "Energy harvesting from transverse ocean waves by a piezoelectric plate," *International Journal of Engineering Science*, vol. 81, pp. 41–48, 2014.
- [34] W. Q. Xie, X. D. and N. Wu, "Potential of a piezoelectric energy harvester from sea waves," *Journal of Sound and Vibration*, vol. 333, no. 5, pp. 1421–1429, 2014.
- [35] N. Wu, Q. Wang, and X. Xie, "Ocean wave energy harvesting with a piezoelectric coupled buoy structure," *Applied Ocean Research*, vol. 50, pp. 110–118, 2015.
- [36] X. Xie and Q. Wang, "A study on an ocean wave energy harvester made of a composite piezoelectric buoy structure," *Composite Structures*, vol. 178, pp. 447–454, 2017.
- [37] J. Zhang, X. Xie, G. Song, G. Du, and D. Liu, "A study on a near-shore cantilevered sea wave energy harvester with a variable cross section," *Energy Science & Engineering*, vol. 7, no. 6, pp. 3174–3185, 2019.

- [38] H. Mutsuda, Y. Tanaka, Y. Doi, and Y. Moriyama, "Application of a flexible device coating with piezoelectric paint for harvesting wave energy," *Ocean Engineering*, vol. 172, pp. 170–182, 2019.
- [39] K. Zhou, H. Dai, A. Abdelkefi, and Q. Ni, "Theoretical modeling and nonlinear analysis of piezoelectric energy harvesters with different stoppers," *International Journal of Mechanical Sciences*, vol. 166, p. 105233, 2020.
- [40] S. Chen, R. Yang, G. Wu, and C. Wu, "A piezoelectric wave-energy converter equipped with a geared-linkage-based frequency up-conversion mechanism," *Sensors*, vol. 21, no. 1, p. 204, 2021.
- [41] S. Zheng, M. Meylan, X. Zhang, G. Iglesias, and D. Greaves, "Performance of a plate-wave energy converter integrated in a floating breakwater," *IET Renewable Power Generation*, vol. 15, no. 14, pp. 3206–3219, 2021.
- [42] H. Ucar, "Patch-based piezoelectric energy harvesting on a marine boat exposed to wave-induced loads," *Ocean Engineering*, vol. 236, p. 109568, 2021.
- [43] L. Qi, H. Li, X. Wu, Z. Zhang, W. Duan, and M. Yi, "A hybrid piezoelectric-electromagnetic wave energy harvester based on capsule structure for self-powered applications in sea-crossing bridges," *Renewable Energy*, vol. 178, pp. 1223–1235, 2021.
- [44] S. Michele, S. Zheng, and D. Greaves, "Wave energy extraction from a floating flexible circular plate," *Ocean Engineering*, vol. 245, p. 110275, 2022.
- [45] Y. Goda, *Random seas and design of maritime structures*. World Scientific Publishing Company, Singapore, 2010, vol. 33.
- [46] C. Josset and A. Clément, "A time-domain numerical simulator for oscillating water column wave power plants," *Renewable Energy*, vol. 32, no. 8, pp. 1379–1402, 2007.
- [47] F. Gouaud, V. Rey, J. Piazzola, and R. Van Hooff, "Experimental study of the hydrodynamic performance of an onshore wave power device in the presence of an underwater mound," *Coastal Engineering*, vol. 57, no. 11-12, pp. 996–1005, 2010.
- [48] F. He, Z. Huang, and A. W.-K. Law, "An experimental study of a floating breakwater with asymmetric pneumatic chambers for wave energy extraction," *Applied Energy*, vol. 106, pp. 222–231, 2013.
- [49] D.-Z. Ning, J. Shi, Q.-P. Zou, and B. Teng, "Investigation of hydrodynamic performance of an OWC (oscillating water column) wave energy device using a fully nonlinear HOBEM (higher-order boundary element method)," *Energy*, vol. 83, pp. 177–188, 2015.

- [50] W. Sheng and A. Lewis, “Wave energy conversion of oscillating water column devices including air compressibility,” *Journal of Renewable and Sustainable Energy*, vol. 8, no. 5, p. 054501, 2016.
- [51] T. Vyzikas, S. Deshoulières, M. Barton, O. Giroux, D. Greaves, and D. Simmonds, “Experimental investigation of different geometries of fixed oscillating water column devices,” *Renewable Energy*, vol. 104, pp. 248–258, 2017.
- [52] K. Rezanejad, C. G. Soares, I. López, and R. Carballo, “Experimental and numerical investigation of the hydrodynamic performance of an oscillating water column wave energy converter,” *Renewable Energy*, vol. 106, pp. 1–16, 2017.
- [53] F. M. Strati, G. Malara, and F. Arena, “Performance optimization of a U-oscillating-water-column wave energy harvester,” *Renewable Energy*, vol. 99, pp. 1019–1028, 2016.
- [54] P. D. Spanos, F. M. Strati, G. Malara, and F. Arena, “An approach for non-linear stochastic analysis of U-shaped OWC wave energy converters,” *Probabilistic Engineering Mechanics*, vol. 54, pp. 44–52, 2018.
- [55] G. Malara and F. Arena, “Response of U-oscillating water column arrays: Semi-analytical approach and numerical results,” *Renewable Energy*, vol. 138, pp. 1152–1165, 2019.
- [56] M. L. Jalón and F. Brennan, “Hydrodynamic efficiency versus structural longevity of a fixed OWC wave energy converter,” *Ocean Engineering*, vol. 206, p. 107260, 2020.
- [57] C. Wang and Y. Zhang, “Wave power extraction analysis for an oscillating water column device with various surging lip-walls,” *Ocean Engineering*, vol. 220, p. 108483, 2021.
- [58] R. Mayon, D. Ning, C. Zhang, L. Chen, and R. Wang, “Wave energy capture by an omnidirectional point sink oscillating water column system,” *Applied Energy*, vol. 304, p. 117795, 2021.
- [59] J. B. Butcher, C. Day, J. Austin, P. Haycock, D. Verstraeten, and B. Schrauwen, “Defect detection in reinforced concrete using random neural architectures,” *Computer-Aided Civil and Infrastructure Engineering*, vol. 29, no. 3, pp. 191–207, 2014.
- [60] K. Kourou, T. P. Exarchos, K. P. Exarchos, M. V. Karamouzis, and D. I. Fotiadis, “Machine learning applications in cancer prognosis and prediction,” *Computational and Structural Biotechnology Journal*, vol. 13, pp. 8–17, 2015.
- [61] M. Mohajane, R. Costache, F. Karimi, Q. B. Pham, A. Essahlaoui, H. Nguyen, G. Laneve, and F. Oudija, “Application of remote sensing and machine learning algorithms for forest fire mapping in a mediterranean area,” *Ecological Indicators*, vol. 129, p. 107869, 2021.

- [62] J. Hegde and B. Rokseth, “Applications of machine learning methods for engineering risk assessment—A review,” *Safety Science*, vol. 122, p. 104492, 2020.
- [63] D. A. Otchere, T. O. A. Ganat, R. Gholami, and S. Ridha, “Application of supervised machine learning paradigms in the prediction of petroleum reservoir properties: Comparative analysis of ANN and SVM models,” *Journal of Petroleum Science and Engineering*, vol. 200, p. 108182, 2021.
- [64] D. Sarkar, E. Contal, N. Vayatis, and F. Dias, “Prediction and optimization of wave energy converter arrays using a machine learning approach,” *Renewable Energy*, vol. 97, pp. 504–517, 2016.
- [65] D. Zhu, J. Zhang, Q. Wu, Y. Dong, and E. Bastidas-Arteaga, “Predictive capabilities of data-driven machine learning techniques on wave-bridge interactions,” *Applied Ocean Research*, vol. 137, p. 103597, 2023.
- [66] L. Li, Z. Yuan, and Y. Gao, “Maximization of energy absorption for a wave energy converter using the deep machine learning,” *Energy*, vol. 165, pp. 340–349, 2018.
- [67] S. Zou, X. Zhou, I. Khan, W. W. Weaver, and S. Rahman, “Optimization of the electricity generation of a wave energy converter using deep reinforcement learning,” *Ocean Engineering*, vol. 244, p. 110363, 2022.
- [68] V. Borisov, T. Leemann, K. Seßler, J. Haug, M. Pawelczyk, and G. Kasneci, “Deep neural networks and tabular data: A survey,” *IEEE Transactions on Neural Networks and Learning Systems*, pp. 1–21, 2022.
- [69] J. Wu, Y. Li, and Y. Ma, “Comparison of XGBoost and the neural network model on the class-balanced datasets,” in *2021 IEEE 3rd International Conference on Frontiers Technology of Information and Computer (ICFTIC)*. IEEE, 2021, pp. 457–461.
- [70] H. D. Nguyen, N. D. Dao, and M. Shin, “Prediction of seismic drift responses of planar steel moment frames using artificial neural network and extreme gradient boosting,” *Engineering Structures*, vol. 242, p. 112518, 2021.
- [71] K. Liu, M. F. Niri, G. Apachitei, M. Lain, D. Greenwood, and J. Marco, “Interpretable machine learning for battery capacities prediction and coating parameters analysis,” *Control Engineering Practice*, vol. 124, p. 105202, 2022.
- [72] A. El Bilali, T. Abdeslam, N. Ayoub, H. Lamane, M. A. Ezzaouini, and A. Elbeltagi, “An interpretable machine learning approach based on DNN, SVR, Extra Tree, and XGBoost models for predicting daily pan evaporation,” *Journal of Environmental Management*, vol. 327, p. 116890, 2023.

- [73] A. George, I.-H. Cho, and M.-H. Kim, "Optimal design of a U-shaped oscillating water column device using an artificial neural network model," *Processes*, vol. 9, no. 8, p. 1338, 2021.
- [74] P. Halder, M. H. Mohamed, and A. Samad, "Wave energy conversion: Design and shape optimization," *Ocean Engineering*, vol. 150, pp. 337–351, 2018.
- [75] K. Trivedi and S. Koley, "Performance of a hybrid wave energy converter device consisting of a piezoelectric plate and oscillating water column device placed over an undulated seabed," *Applied Energy*, vol. 333, p. 120627, 2023.
- [76] H. Li and L. Wang, "Numerical study on self-power supply of large marine monitoring buoys: Wave-excited vibration energy harvesting and harvester optimization," *Energy*, vol. 285, p. 129377, 2023.
- [77] S. Rezaei, A. Rahimi, J. Parvizian, S. Mansourzadeh, and A. Düster, "Dimensional optimization of a two-body wave energy converter using response surface methodology," *Ocean Engineering*, vol. 261, p. 112186, 2022.
- [78] A. Ghaheri, E. Afjei, and H. Torkaman, "Design optimization of a novel linear transverse flux switching permanent magnet generator for direct drive wave energy conversion," *Renewable Energy*, vol. 198, pp. 851–860, 2022.
- [79] D. E. Rumelhart, G. E. Hinton, and R. J. Williams, "Learning representations by back-propagating errors," *Nature*, vol. 323, no. 6088, pp. 533–536, 1986.
- [80] D. Nguyen and B. Widrow, "Improving the learning speed of 2-layer neural networks by choosing initial values of the adaptive weights," in *1990 IJCNN International Joint Conference on Neural Networks*. IEEE, 1990, pp. 21–26.
- [81] P. J. Werbos, "Backpropagation through time: what it does and how to do it," *Proceedings of the IEEE*, vol. 78, no. 10, pp. 1550–1560, 1990.
- [82] I. Goodfellow, Y. Bengio, and A. Courville, *Deep learning*. MIT press, Cambridge, MA, 2016.
- [83] L. Breiman, "Random forests," *Machine Learning*, vol. 45, pp. 5–32, 2001.
- [84] T. Chen and C. Guestrin, "Xgboost: A scalable tree boosting system," in *Proceedings of the 22nd ACM SIGKDD International Conference on Knowledge Discovery and Data Mining*, 2016, pp. 785–794.
- [85] G. Ke, Q. Meng, T. Finley, T. Wang, W. Chen, W. Ma, Q. Ye, and T. Liu, "Lightgbm: A highly efficient gradient boosting decision tree," *Advances in Neural Information Processing Systems*, vol. 30, 2017.

- [86] L. Prokhorenkova, G. Gusev, A. Vorobev, A. V. Dorogush, and A. Gulin, “CatBoost: unbiased boosting with categorical features,” *Advances in Neural Information Processing Systems*, vol. 31, 2018.
- [87] S. H. Schot, “Eighty years of Sommerfeld’s radiation condition,” *Historia Mathematica*, vol. 19, pp. 385–401, 1992.
- [88] G. B. Folland, *Introduction to partial differential equations*. Princeton University Press, Princeton, New Jersey, 1995, vol. 102.
- [89] T. Sahoo, *Mathematical techniques for wave interaction with flexible structures*. CRC Press, Boca Raton, 2012.
- [90] S. Mohapatra, R. Ghoshal, and T. Sahoo, “Effect of compression on wave diffraction by a floating elastic plate,” *Journal of Fluids and Structures*, vol. 36, pp. 124–135, 2013.
- [91] C. A. Brebbia, J. C. F. Telles, and L. C. Wrobel, *Boundary element techniques: theory and applications in engineering*. Springer Science & Business Media, Heidelberg, 2012.
- [92] W. T. Ang, *A beginner’s course in boundary element methods*. Universal-Publishers, Boca Raton, 2007.
- [93] K. C. Ang, “Introducing the boundary element method with MATLAB,” *International Journal of Mathematical Education in Science and Technology*, vol. 39, no. 4, pp. 505–519, 2008.
- [94] K. Trivedi, S. Koley, and K. Panduranga, “Performance of an U-shaped oscillating water column wave energy converter device under oblique incident waves,” *Fluids*, vol. 6, no. 4, p. 137, 2021.
- [95] K. Chen, J. Chen, S. Lin, and Y. Lee, “Dual boundary element analysis of normal incident wave passing a thin submerged breakwater with rigid, absorbing, and permeable boundaries,” *Journal of Waterway, Port, Coastal, and Ocean Engineering*, vol. 130, no. 4, pp. 179–190, 2004.
- [96] J. Chen, C. Yueh, Y. Chang, and C. Wen, “Why dual boundary element method is necessary?” *Engineering Analysis with Boundary Elements*, vol. 76, pp. 59–68, 2017.
- [97] I. A. Basheer and M. Hajmeer, “Artificial neural networks: fundamentals, computing, design, and application,” *Journal of Microbiological Methods*, vol. 43, no. 1, pp. 3–31, 2000.
- [98] D. H. Hubel and T. N. Wiesel, “Receptive fields of single neurones in the cat’s striate cortex,” *The Journal of Physiology*, vol. 148, no. 3, p. 574, 1959.
- [99] D. Hubel and T. Wiesel, “Integrative action in the cat’s lateral geniculate body,” *The Journal of Physiology*, vol. 155, no. 2, p. 385, 1961.

- [100] D. H. Hubel and T. N. Wiesel, "Shape and arrangement of columns in cat's striate cortex," *The Journal of Physiology*, vol. 165, no. 3, p. 559, 1963.
- [101] J. S. Bruner, "Neural mechanisms in perception." *Psychological Review*, vol. 64, no. 6p1, p. 340, 1957.
- [102] D. O. Hebb, "Drives and the CNS (conceptual nervous system)." *Psychological Review*, vol. 62, no. 4, p. 243, 1955.
- [103] N. Rochester, J. Holland, L. Haibt, and W. Duda, "Tests on a cell assembly theory of the action of the brain, using a large digital computer," *IRE Transactions on Information Theory*, vol. 2, no. 3, pp. 80–93, 1956.
- [104] X. Glorot, A. Bordes, and Y. Bengio, "Deep sparse rectifier neural networks," in *Proceedings of the Fourteenth International Conference on Artificial Intelligence and Statistics*. JMLR Workshop and Conference Proceedings, 2011, pp. 315–323.
- [105] Y. LeCun, Y. Bengio, and G. Hinton, "Deep learning," *Nature*, vol. 521, no. 7553, pp. 436–444, 2015.
- [106] A. L. Maas, A. Y. Hannun, A. Y. Ng *et al.*, "Rectifier nonlinearities improve neural network acoustic models," in *Proceedings of the International Conference on Machine Learning*, vol. 30, no. 1. Atlanta, GA, 2013, p. 3.
- [107] A. Nguyen, K. Pham, D. Ngo, T. Ngo, and L. Pham, "An analysis of state-of-the-art activation functions for supervised deep neural network," in *2021 International Conference on System Science and Engineering (ICSSE)*. IEEE, 2021, pp. 215–220.
- [108] S. R. Dubey, S. K. Singh, and B. B. Chaudhuri, "Activation functions in deep learning: A comprehensive survey and benchmark," *Neurocomputing*, vol. 503, pp. 92–108, 2022.
- [109] G. Klambauer, T. Unterthiner, A. Mayr, and S. Hochreiter, "Self-normalizing neural networks," *Advances in Neural Information Processing Systems*, vol. 30, 2017.
- [110] D. Hendrycks and K. Gimpel, "Gaussian error linear units (gelus)," *arXiv preprint arXiv:1606.08415*, 2016.
- [111] N. Srivastava, G. Hinton, A. Krizhevsky, I. Sutskever, and R. Salakhutdinov, "Dropout: a simple way to prevent neural networks from overfitting," *The Journal of Machine Learning Research*, vol. 15, no. 1, pp. 1929–1958, 2014.
- [112] D. Krueger, T. Maharaj, J. Kramár, M. Pezeshki, N. Ballas, N. R. Ke, A. Goyal, Y. Bengio, A. Courville, and C. Pal, "Zoneout: Regularizing RNNs by randomly preserving hidden activations," in *5th International Conference on Learning Representations (ICLR 2017)*. Palais des Congres Neptune, Toulon, France, 2017.

- [113] W. S. McCulloch and W. Pitts, "A logical calculus of the ideas immanent in nervous activity," *The Bulletin of Mathematical Biophysics*, vol. 5, pp. 115–133, 1943.
- [114] D. Elizondo, "The linear separability problem: Some testing methods," *IEEE Transactions on Neural Networks*, vol. 17, no. 2, pp. 330–344, 2006.
- [115] D. P. Kingma and J. Ba, "Adam: A method for stochastic optimization," in *3rd International Conference on Learning Representations, ICLR 2015*. San Diego, CA, USA, 2015.
- [116] T. Dozat, "Incorporating nesterov momentum into adam," in *International Conference on Learning Representations*, 2016, pp. 1–4.
- [117] J. H. Friedman, "Greedy function approximation: A gradient boosting machine," *Annals of Statistics*, vol. 29, pp. 1189–1232, 2001.
- [118] D. W. Apley and J. Zhu, "Visualizing the effects of predictor variables in black box supervised learning models," *Journal of the Royal Statistical Society Series B: Statistical Methodology*, vol. 82, no. 4, pp. 1059–1086, 2020.
- [119] T. Heskes, E. Sijben, I. G. Bucur, and T. Claassen, "Causal shapley values: Exploiting causal knowledge to explain individual predictions of complex models," *Advances in Neural Information Processing Systems*, vol. 33, pp. 4778–4789, 2020.
- [120] G. James, D. Witten, T. Hastie, R. Tibshirani *et al.*, *An introduction to statistical learning*. Springer, New York, 2013, vol. 112.
- [121] T.-T. Wong and P.-Y. Yeh, "Reliable accuracy estimates from k-fold cross validation," *IEEE Transactions on Knowledge and Data Engineering*, vol. 32, no. 8, pp. 1586–1594, 2019.
- [122] M. A. Bezerra, R. E. Santelli, E. P. Oliveira, L. S. Villar, and L. A. Escalera, "Response surface methodology (RSM) as a tool for optimization in analytical chemistry," *Talanta*, vol. 76, no. 5, pp. 965–977, 2008.
- [123] R. H. Myers, D. C. Montgomery, and C. M. Anderson-Cook, *Response surface methodology: process and product optimization using designed experiments (4th)*. New York (Probability and Statistics Series) John Wiley & Sons, 2016.
- [124] S. Koley, K. Panduranga, N. Almashan, S. Neelamani, and A. Al-Ragum, "Numerical and experimental modeling of water wave interaction with rubble mound offshore porous breakwaters," *Ocean Engineering*, vol. 218, p. 108218, 2020.
- [125] S. Koley and T. Sahoo, "Scattering of oblique waves by permeable vertical flexible membrane wave barriers," *Applied Ocean Research*, vol. 62, pp. 156–168, 2017.

- [126] C. A. Brebbia and J. Dominguez, *Boundary elements: an introductory course*. WIT press, Boston, 1994.
- [127] C. C. Mei, M. A. Stiassnie, and D. K.-P. Yue, *Theory and Applications of Ocean Surface Waves: Part 1: Linear Aspects*. World Scientific, New Jersey, 2005.
- [128] S. Koley, “Wave transmission through multilayered porous breakwater under regular and irregular incident waves,” *Engineering Analysis with Boundary Elements*, vol. 108, pp. 393–401, 2019.
- [129] C. D. Wang and M. H. Meylan, “The linear wave response of a floating thin plate on water of variable depth,” *Applied Ocean Research*, vol. 24, no. 3, pp. 163–174, 2002.
- [130] Z. L. Wang, “Catch wave power in floating nets,” *Nature*, vol. 542, no. 7640, pp. 159–160, 2017.
- [131] R. Ahamed, K. McKee, and I. Howard, “Advancements of wave energy converters based on power take off (PTO) systems: A review,” *Ocean Engineering*, vol. 204, p. 107248, 2020.
- [132] V. Vipin, K. Trivedi, and S. Koley, “Performance of a submerged piezoelectric wave energy converter device in time domain,” *Energy Reports*, vol. 8, pp. 309–314, 2022.
- [133] V. Vipin, S. Koley, and K. Trivedi, “Performance of a submerged piezoelectric wave energy converter device floating over an undulated seabed,” *Energy Reports*, vol. 8, pp. 182–188, 2022.
- [134] K. Trivedi and S. Koley, “Mathematical modeling of oscillating water column wave energy converter devices placed over an undulated seabed in a two-layer fluid system,” *Renewable Energy*, vol. 216, p. 119092, 2023.
- [135] V. Vipin and S. Koley, “Mathematical modeling of a submerged piezoelectric wave energy converter device installed over an undulated seabed,” *Renewable Energy*, vol. 200, pp. 1382–1392, 2022.
- [136] K. Trivedi and S. Koley, “Annual mean efficiency of the duct type OWC in regional ocean environments,” *Energy Reports*, vol. 8, pp. 346–351, 2022.
- [137] A. A. M. Rodríguez, K. Trivedi, S. Koley, I. O. Martinez, E. Mendoza, G. P. Vanegas, and R. Silva, “Improved hydrodynamic performance of an OWC device based on a Helmholtz resonator,” *Energy*, vol. 273, p. 127299, 2023.
- [138] K. Trivedi and S. Koley, “Hydrodynamics of an U-shaped OWC device in a two-layer fluid system,” *Energy Reports*, vol. 8, pp. 106–111, 2022.

- [139] S. Koley and T. Sahoo, “Wave interaction with a submerged semicircular porous breakwater placed on a porous seabed,” *Engineering Analysis with Boundary Elements*, vol. 80, pp. 18–37, 2017.
- [140] K. Trivedi and S. Koley, “Mathematical modeling of breakwater-integrated oscillating water column wave energy converter devices under irregular incident waves,” *Renewable Energy*, vol. 178, pp. 403–419, 2021.
- [141] D. Kim, J. Kim, and J. Kim, “Elastic exponential linear units for convolutional neural networks,” *Neurocomputing*, vol. 406, pp. 253–266, 2020.
- [142] M. M. Rahman, M. Shakeri, S. K. Tiong, F. Khatun, N. Amin, J. Pasupuleti, and M. K. Hasan, “Prospective methodologies in hybrid renewable energy systems for energy prediction using artificial neural networks,” *Sustainability*, vol. 13, no. 4, p. 2393, 2021.
- [143] J. Bergstra and Y. Bengio, “Random search for hyper-parameter optimization,” *Journal of Machine Learning Research*, vol. 13, no. 2, 2012.
- [144] D. P. Kingma and J. Ba, “Adam: A method for stochastic optimization,” in *3rd International Conference on Learning Representations, ICLR 2015*. San Diego, CA, USA, 2015.
- [145] M. D. Zeiler, “Adadelta: An adaptive learning rate method,” *ArXiv*, vol. abs/1212.5701, 2012. [Online]. Available: <http://arxiv.org/abs/1212.5701>
- [146] S. M. Lundberg and S.-I. Lee, “A unified approach to interpreting model predictions,” *Advances in Neural Information Processing Systems*, vol. 30, 2017.
- [147] T. Chen, T. He, M. Benesty, V. Khotilovich, Y. Tang, H. Cho, K. Chen, R. Mitchell, I. Cano, T. Zhou *et al.*, “Xgboost: extreme gradient boosting,” *R Package Version 0.4-2*, vol. 1, no. 4, pp. 1–4, 2015.
- [148] S. Masís, *Interpretable Machine Learning with Python: Learn to build interpretable high-performance models with hands-on real-world examples*. Packt Publishing Ltd, Birmingham, 2021.
- [149] A. Babarit, *Ocean wave energy conversion*. Elsevier, Oxford, 2018.
- [150] S. Koley and K. Trivedi, “Mathematical modeling of oscillating water column wave energy converter devices over the undulated sea bed,” *Engineering Analysis with Boundary Elements*, vol. 117, pp. 26–40, 2020.
- [151] J. T. Katsikadelis, *The boundary element method for engineers and scientists: theory and applications*. Academic Press, London, 2016.

-
- [152] H. Behera, R. Kaligatla, and T. Sahoo, “Wave trapping by porous barrier in the presence of step type bottom,” *Wave Motion*, vol. 57, pp. 219–230, 2015.
- [153] S. Koley, “Water wave scattering by floating flexible porous plate over variable bathymetry regions,” *Ocean Engineering*, vol. 214, p. 107686, 2020.
- [154] Y. Li, G. Lei, G. Bramerdorfer, S. Peng, X. Sun, and J. Zhu, “Machine learning for design optimization of electromagnetic devices: Recent developments and future directions,” *Applied Sciences*, vol. 11, no. 4, p. 1627, 2021.
- [155] V. Vipin, K. Trivedi, and S. Koley, “Optimization of parameters of the OWC wave energy converter device using MLP and XGBoost models,” *Results in Physics*, vol. 55, p. 107163, 2023.
- [156] M. Puth, M. Neuhäuser, and G. D. Ruxton, “Effective use of Spearman’s and Kendall’s correlation coefficients for association between two measured traits,” *Animal Behaviour*, vol. 102, pp. 77–84, 2015.
- [157] M. Whitlock and D. Schluter, *The analysis of biological data*. Roberts Publishers Greenwood Village, Colorado, 2015, vol. 768.
- [158] A. Ferraro, A. Galli, V. Moscato, and G. Sperli, “Evaluating eXplainable artificial intelligence tools for hard disk drive predictive maintenance,” *Artificial Intelligence Review*, vol. 56, no. 7, pp. 7279–7314, 2023.

List of Publications

Publication from thesis:

1. Vipin, V., Koley, S. (2022). Mathematical modeling of a submerged piezoelectric wave energy converter device installed over an undulated seabed. *Renewable Energy*, 200, 1382-1392.(SCI, IF-8.7) <https://doi.org/10.1016/j.renene.2022.10.051>
2. Vipin, V., Trivedi, K., Koley, S. (2022). Performance of a submerged piezoelectric wave energy converter device floating over an undulated seabed. *Energy Reports*, 8, 182-188. (SCI, IF-5.2), <https://doi.org/10.1016/j.egyr.2022.05.165>.
3. Vipin, V., Trivedi, K., Koley, S. (2022). Performance of a submerged piezoelectric wave energy converter device in time domain. *Energy Reports*, 8, 309-314. (SCI, IF-5.2), <https://doi.org/10.1016/j.egyr.2022.10.247>
4. Vipin, V., Koley, S. (2023). Design optimization of a submerged piezoelectric wave energy converter device using an artificial neural network model. *Energy Reports*, 9, 322-326. (SCI, IF-5.2), <https://doi.org/10.1016/j.egyr.2023.09.036>
5. Vipin, V., Trivedi, K., Koley, S. (2023). Optimization of parameters of the OWC wave energy converter device using MLP and XGBoost models. *Results in Physics*, 55, 107163. (SCI, IF-5.3), <https://doi.org/10.1016/j.rinp.2023.107163>.
6. Vipin, V., Trivedi, K., Koley, S. Mathematical Modeling, Prediction, and Optimization of Hybrid Oscillating Water Column-Piezoelectric Wave Energy Converter Device using Machine Learning Models. Communicated in *Engineering Applications of Artificial Intelligence*, (SCI, IF-8)

Conferences

1. Vipin, V., Trivedi, K., and Koley, S. (2021,). Mathematical Modeling of a U-shaped OWC Device over the Slanted Sea Bed. *In 2021 3rd International Conference on Control Systems, Mathematical Modeling, Automation and Energy Efficiency (SUMMA)* (pp. 1022-1026). IEEE.
2. Koley, S., and Vipin, V. Water Waves Scattering by A Submerged Thick Porous Breakwater Placed Over Undulated Bottom. *PACE-2021*, Turkey, 20-23 June, 2021.

Other publications:

1. Vipin, V., and Koley, S. (2023). Estimation of Parameters of Some Continuous Distributions Using Frequency Ratio Method Based on Local Information. *In Mathematical Modeling, Computational Intelligence Techniques and Renewable Energy: Proceedings of the Third International Conference, MMCITRE 2022* (pp. 319-327). Singapore: Springer Nature Singapore. (SCOPUS).
2. Vipin, V., Satpathi, D. K., Koley, S., and Haragopal, V. V. (2022). Parameter estimation of log-normal distribution based on local information. *In AIP Conference Proceedings*, vol. 2516, No. 1, AIP Publishing. (SCOPUS).
3. Vipin, V., Panduranga, K., and Koley, S. (2021). Scattering of Water Waves by a Quarter Circular Porous Breakwater Placed on a Porous Foundation. *In Conference on Fluid Mechanics and Fluid Power* (pp. 403-407). Singapore: Springer Nature Singapore. (SCOPUS).
4. Valappil, V., and Koley, S. (2023). Mathematical Modeling of a Piezoelectric Wave Energy Converter Device Integrated with a Vertical Breakwater over a Stepped Seabed. *Miniaturized Electrochemical Devices: Advanced Concepts, Fabrication, and Applications*, 43. (SCOPUS).
5. Koley, S., Trivedi, K., Vipin, V. (2022). Hydroelastic analysis of floating long viscoelastic plate in shallow water. *Materials Today: Proceedings*, 49, 2234-2238, (SCOPUS).
6. Vipin V, Santanu Koley, Power Generation Prediction and Optimization of Parameters of Piezoelectric Wave Energy Converter Device *IEEE Xplore*. Accepted for publication (ID: 24CHCS 7002, SCOPUS).

Biography

Brief Biography of Candidate

Mr. Vipin V completed his Bachelor of Science from Sreekrishnapuram V T Bhattathiripad College, affiliated to the University of Calicut, Kerala, and Master of Science from MPMM SN Trust College Shoranur, affiliated to the University of Calicut, Kerala. He has around three months of academic experience in teaching at MPMM SN Trust College Shoranur, Affiliated to the University of Calicut and four months of academic experience in teaching at Government Arts and Science College Kondotty, Kerala. He qualified CSIR-NET-JRF examination in Mathematical Science in December 2017 examination. Through the junior and senior research fellowships awarded by CSIR, India (File No: 09/1026(0030)/2019-EMR-I), he is working as a full-time Ph.D. scholar in the Dept. of Mathematics, Birla Institute of Technology and Science-Pilani, Hyderabad Campus from 2019-till date under the supervision of Prof. Santanu Koley. He has published 5 SCI, and 8 SCOPUS scientific publications in reputed international journals. He presented his research papers at several national and international conferences held in India and abroad and received the best paper presentation award from ICACER-2022, organized by Universitat Politècnica de Catalunya, BarcelonaTech (UPC), Spain, during April 20-22, 2022. He has received the CSIR Foreign Travel Grant (TG/12139/23- HRD) to attend and present a research paper at ICIAM-2023, Tokyo, Japan, from August 20-25, 2023.

Brief Biography of Supervisor

Prof. Santanu Koley is presently working as Associate Professor in the Department of Mathematics, Birla Institute of Technology and Science-Pilani, Hyderabad Campus. He received his Ph.D. degree from the Indian Institute of Technology Kharagpur in 2016. His main area of research includes Boundary Element Method (Theory & Applications), Mathematical Modeling, Wave Energy Converter Devices, Integral Equations, and Statistical Modeling. He has published 51 SCI papers and 45 SCOPUS papers in the journal of international repute. Prof. Koley has presented several research papers at national and international conferences held in India and abroad. He received a number of prestigious national and international awards like the DST INSPIRE Faculty Award and top cited researcher from EABE, Elsevier, etc. He is currently dealing with two sponsored projects funded by DST, Govt. of India, and SERB, Govt. of India

(Core Research Grant). He has received an international travel support Grant from SERB, India, to attend ICIAM 2019 and ICIAM 2023 conferences. Prior to joining BITS-Pilani, Hyderabad Campus, he worked as INSPIRE Faculty at IISER Bhopal - 2018, Assistant Professor at DA-IICT, Gandhinagar - 2017 to 2018, SERB - National Postdoc Fellow at IIT Ropar - 2016 to 2017, and Research Associate at IIT Kharagpur - 2015 to 2016.